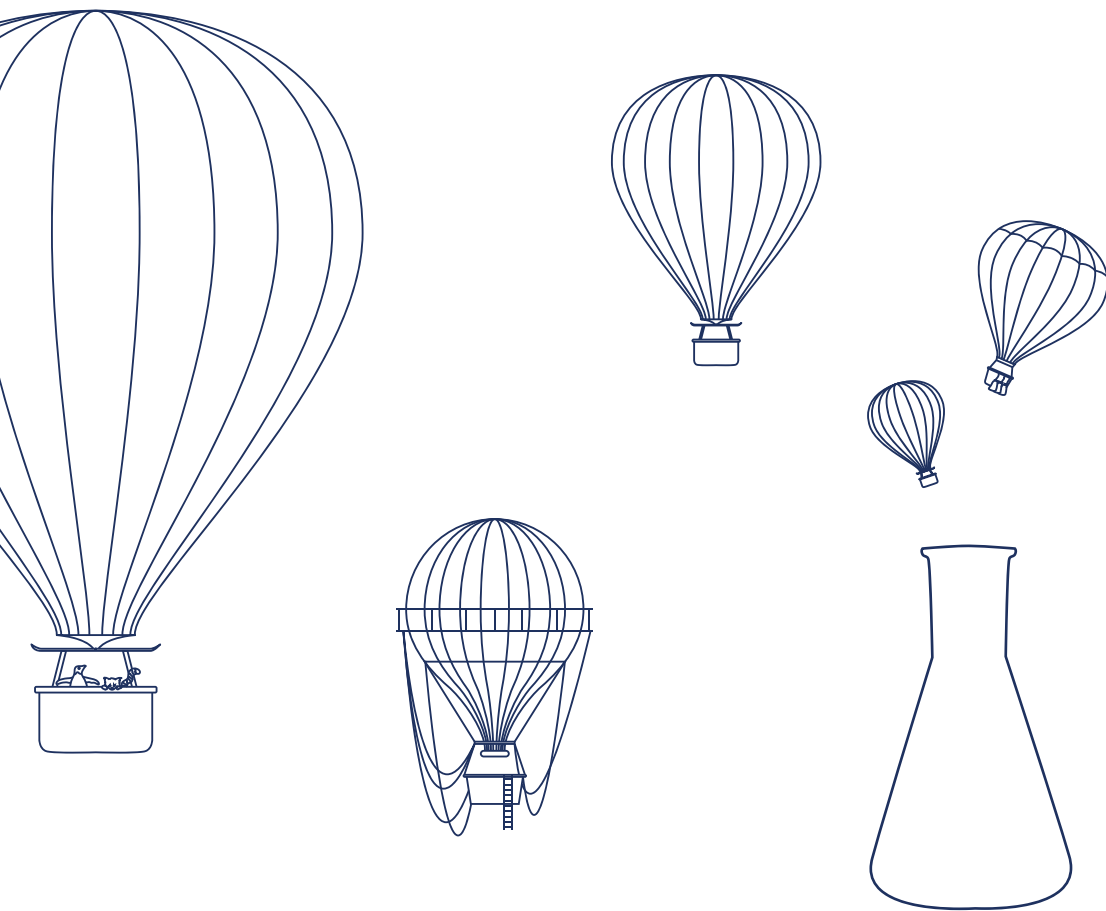


# Luminescent nanoclusters of silver and gold



*“Let us think the unthinkable, let us do the undoable. Let us prepare to grapple with the ineffable itself, and see if we may not eff it after all.”*

— Douglas Adams, *Dirk Gently’s Holistic Detective Agency*

Cover design:     *“Science is an adventure!”*  
                          — Marte van der Linden

Interior artwork:  *“Triptych: places of scientific interest”*  
                          — Marte van der Linden



Luminescent nanoclusters of silver and gold  
PhD thesis

Marte van der Linden  
Universiteit Utrecht

ISBN: 978-90-393-7035-3  
Printed by Gildeprint

---

# Luminescent nanoclusters of silver and gold

---

Luminescente nanoclusters van zilver en goud

(met een samenvatting in het Nederlands)

## Proefschrift

ter verkrijging van de graad van doctor aan de Universiteit Utrecht op gezag van de rector magnificus, prof. dr. H. R. B. M. Kummeling, ingevolge het besluit van het college voor promoties in het openbaar te verdedigen op woensdag 17 oktober 2018 des middags te 2.30 uur

*door*

Marte van der Linden

geboren op 14 april 1989 te Utrecht

Promotor: Prof. dr. F. M. F. de Groot

Copromotor: Dr. J. P. S. Glatzel

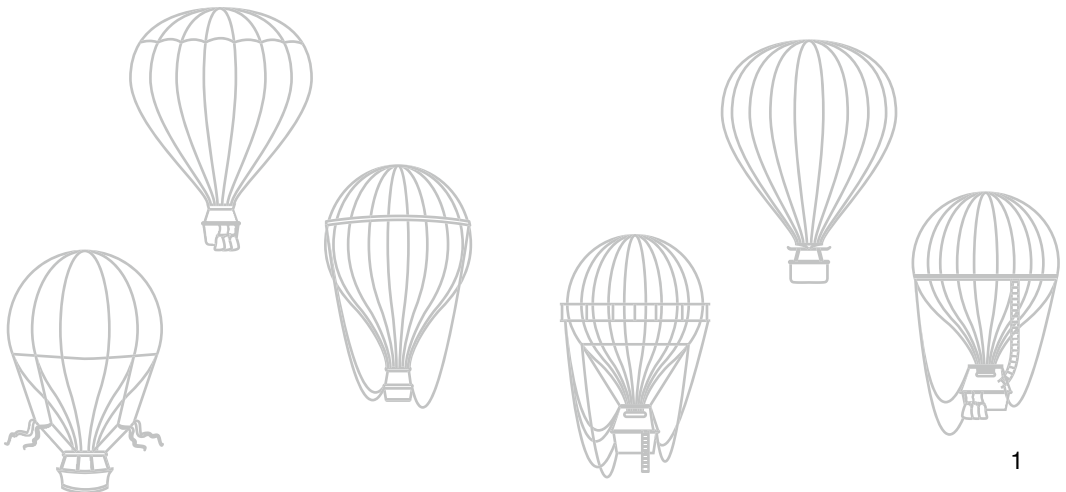
This work was supported through the Debye graduate programme, which was financed jointly by the Netherlands Organisation for Scientific Research (NWO) and the European Synchrotron Radiation Facility (ESRF) in Grenoble, France.

# Contents

1	Introduction	1
<b>I Silver</b>		
2	Characterisation of luminescent Ag <sub>29</sub> clusters	29
3	Synthesis mechanism of Ag <sub>29</sub> clusters	53
	Appendix A Additional spectra; silver clusters	77
<b>II Silver and gold</b>		
4	Single atom doping of monodisperse Ag <sub>29</sub> clusters	81
	Appendix B Additional spectra; bimetallic clusters	109
<b>III Gold</b>		
5	Size tuneability of luminescent Au clusters	115
6	X-ray spectroscopy of Au compounds	139
7	X-ray spectroscopy of Au clusters	157
	Appendix C Additional spectra; gold clusters	181
8	Summary and outlook	185
	Samenvatting voor een algemeen publiek	191
	Acknowledgements	199
	List of publications and conference contributions	204
	About the author	207
	Bibliography	209



# Introduction



*"There are no safe paths in this part of the world.  
Remember you are over the Edge of the Wild now, and  
in for all sorts of fun wherever you go."*

---

— J.R.R. Tolkien, *The Hobbit*

## 1.1 Clusters: small is beautiful

The properties of noble metals are size-dependent, provided the dimensions are on the nanoscale. For larger nanoparticles, with sizes of at least a few hundred or thousand atoms to  $\sim 100$  nm, these properties scale with the particle size. This can be explained from the increasing fraction of surface atoms with decreasing particle size. Surface atoms have a lower coordination number than bulk atoms, and therefore their properties will be different.<sup>1</sup> The lower stability of surface atoms explains the reduction in melting point of Au nanoparticles with decreasing size.<sup>2</sup> Other examples of scaleable properties include electron affinity<sup>3</sup>, catalytic activity<sup>4</sup>, and bond length<sup>5</sup>. Gold and silver nanoparticles also exhibit surface plasmon resonance, which is a collective oscillation of the electrons in the particle. The absorption frequency, and linewidth, depend on the particle size and shape, which is why solutions of Ag and Au nanoparticles of different sizes have different colours.<sup>6,7</sup> The critical size at which a nanoparticle resembles bulk depends on the property in question.<sup>8</sup>

Below a certain size, Au and Ag nanoparticle properties are no longer scaleable. Instead, the addition of even a single atom can drastically alter the particle's properties, as illustrated in Figure 1.1. Such small nanoparticles consist of a few hundred atoms or less and are called *nanoclusters* or simply *clusters*. Their small size induces quantum confinement effects. Au and Ag clusters have unique properties that are not found in bulk or in larger nanoparticles. An example is the structure, which is often not face-centred cubic (fcc) as in bulk. The small number of atoms also results in discrete energy levels, because the spacing between energy levels increases with decreasing size. This means that, in contrast to larger nanoparticles, Au and Ag clusters are not metallic and room temperature conductivity is not possible.<sup>9,10</sup> Instead, clusters have molecular-like electronic properties, such as a large gap between the highest occupied and lowest unoccupied molecular orbitals (HOMO-LUMO gap). This leads to multiple UV-Vis absorption bands<sup>11</sup>, luminescence<sup>12,13</sup>, and magnetic properties<sup>14,15</sup> not found in bulk or larger nanoparticles.

An intriguing question is at which size clusters become nanoparticles. When do the discrete energy levels merge and become (quasi-) continuous bands? When do distinct UV-Vis absorption peaks make way for plasmon resonance? Conductivity

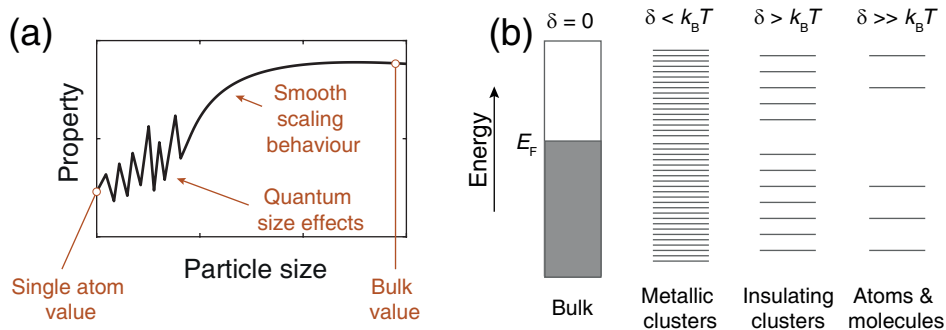


**Figure 1.1** (a) Schematic representation of the variation in an arbitrary property with particle size. (b) Schematic energy level diagrams of bulk metal, metallic clusters and nanoparticles, insulating clusters, and atoms.  $E_F$  is the Fermi level,  $\delta$  is the energy gap at the Fermi level, and  $k_B T$  is the thermal energy. Figures adapted from <sup>16</sup>.

becomes possible when the energy spacing at the Fermi level, the so-called Kubo gap  $\delta$ , is below the thermal energy. That is,  $\delta < k_B T$ . Here,  $k_B$  is Boltzmann's constant and  $T$  the temperature. The gap  $\delta$  is the reciprocal of the density of states at the Fermi level. It can be shown that  $\delta \approx E_F/N$ , where  $E_F$  is the Fermi level and  $N$  the number of atoms. The Fermi level of Au and Ag is  $\sim 5$  eV below the vacuum level, which gives a critical size of 200–300 atoms.<sup>15</sup>

Experimentally, the transition between molecular-like and bulk-like electronic structure was determined to occur between 114 and 152 atoms for Ag<sup>17</sup>, and between 144 and 187 atoms for Au<sup>18</sup>, in both cases by observing how the UV-Vis absorption spectrum changed with size. For the Au clusters, a structural transition was also observed: for  $\geq 187$  Au atoms, the particles had fcc structures, while the smaller particles had icosahedral or Marks decahedral structures. Both studies used clusters capped by thiolate ligands, which will be discussed in more detail below.

A further difference between Ag/Au nanoparticles and clusters is that the latter can be prepared with atomic monodispersity. They do not have an average size with a polydispersity, but can be represented with definite chemical formulas, like organic molecules and organometallic compounds. Clusters are commonly made with Au<sup>11,15</sup> or Ag<sup>12,19</sup>, though metals such as Cu and Pt are also used.<sup>20,21</sup> There has been significant progress in the development of synthesis protocols over the last decades, and a number of Ag and Au clusters can now be prepared on a gram-scale with high purity.<sup>22,23</sup>

**A note on terminology** There is no clear definition of the term *cluster*. It is sometimes used to describe nanoparticles up to 100 nm.<sup>24</sup> In most cases, however, and in this thesis, noble metal *clusters* are defined as nanoparticles with a size below  $\sim 2$  nm, with a discrete electronic structure. The terms *cluster* and *nanocluster* are often used interchangeably. Other terms that can be found in literature include noble metal quantum dot<sup>25</sup>, noble metal molecule<sup>26,27</sup>, and *aspicule*<sup>28</sup>. The latter is formed by combining the words *molecule* and *aspis* (Greek for shield), to stress the importance of ligands for cluster stability and properties. The term *cluster* has also been used to describe species with a constant ligand-to-metal ratio, like Pt-thiolate crowns.<sup>29</sup> These consist of rings with alternating Pt and thiolate ligands. As there are no Pt–Pt bonds, we do not consider these species clusters in this thesis, despite their atomic monodispersity. We define clusters as species with a compact metal core with metal-metal bonds, although this criterion may not hold for the smallest clusters studied, in Chapter 5.

### The magic of cluster stability

The (near) atomic monodispersity of particular clusters can be explained by their high stability when compared to clusters of slightly different sizes.<sup>30</sup> The most stable clusters are termed *magic size clusters* and their stability can have both electronic and geometric origins.<sup>11</sup>

High geometric stability is achieved when the cluster consists of complete shells of atoms, which results in the maximum average coordination number. The number of atoms required to form complete shells depends on the cluster geometry. For tetrahedral clusters, the first four magic numbers are 4, 10, 20 and 35, while for icosahedral clusters they are 13, 55, 147 and 309.<sup>31</sup> Geometric magic numbers are observed for instance in gas phase sodium clusters.<sup>32</sup>

The electronic origins of stability are explained by superatom theory, where the cluster is described as a superatom with a charged nucleus and a certain number of delocalised valence electrons. These occupy superatom orbitals. Superatom orbitals are, in order of increasing energy,  $1S^2$ ,  $1P^6$ ,  $1D^{10}$ ,  $2S^2$ ,  $1F^{14}$ , ... , where the letter denotes the angular momentum in the same way as for atomic orbitals. There is no restriction on the angular momentum quantum number for superatom orbitals.<sup>33</sup> Superatom theory predicts that the most stable clusters are those with filled orbitals, just like the noble gases in the periodic table. Therefore, electronic magic number clusters are those with 2, 8, 18, 20 and 34 electrons. The superatom electrons are the valence electrons of the atoms that make up the cluster. For Na, these are the 3s electrons. For Au and Ag, they are the 6s and 5s electrons, respectively.<sup>34</sup> Since both Ag and Au contribute 1 electron to the superatom orbitals, for a bare, neutral cluster the number of electrons equals the number of atoms.

As early as 1984, the superatom concept was used to explain the high abundance of certain Na cluster sizes in mass spectrometry. Similar observations were later made for K, Cu, Ag and Au.<sup>35,36</sup>

The work in this thesis focuses on ligand-protected Au and Ag clusters, where the ligands are thiolates (abbreviated SR). Electronic and geometric stability are both affected by the presence of ligands. Surface passivation by ligands reduces the need for complete geometric shells while at the same time providing a steric barrier against aggregation. It is important to note that the high stability of certain thiolate-protected Ag and Au clusters is not solely due to there being a high energy barrier for aggregation. These clusters are not rigid, kinetically trapped species; they are highly dynamic. For instance, upon addition of  $\text{Ag}_{25}(\text{SR})_{18}^-$  clusters to  $\text{Au}_{25}(\text{SR})_{18}^-$ , mixed metal  $\text{Au}_{25-x}\text{Ag}_x(\text{SR})_{18}^-$  clusters were formed, via a shortlived adduct  $\text{Au}_{25}\text{Ag}_{25}(\text{SR})_{36}^{2-}$ .<sup>37</sup> Ligand exchange of one thiolate for another is also possible without affecting the cluster size and structure.<sup>38</sup>

**The importance of ligands** To ensure long-term stability, clusters are capped by ligands. These not only prevent aggregation, but can also tune the stability and properties of clusters. It is through the ligand shell that clusters interact, and a better understanding the ligand shell has been the subject of recent studies.<sup>39,40</sup> Noble metal clusters can be stabilised by a variety of ligands, including proteins<sup>41</sup>, DNA<sup>42</sup>, phosphines<sup>43,44</sup> and thiols.<sup>15</sup> The latter are the focus of this thesis. Thiols have a general structure RSH; although they bind as thiolates,  $\text{RS}^-$ .<sup>15,45</sup> In cluster compositions this is usually written SR, hence  $\text{Au}_{25}(\text{SR})_{18}^-$ ,  $\text{Ag}_{44}(\text{SR})_{30}^{4-}$ , and so on. These compositions may be abbreviated  $\text{Au}_{25}$  and  $\text{Ag}_{44}$ , but the ligands are still present.

The introduction of ligands changes the electron count of the cluster.<sup>46</sup> Ligands may be weak Lewis bases, like phosphines, that coordinate without withdrawing electrons from the metal, or they may be electron-withdrawing like thiolates or halides. This changes the electron count  $n$  according to

$$n = xv - y - Z \quad (1.1)$$

where  $x$  is the number of metal atoms, each with  $v$  valence electrons,  $y$  is the number of electron-withdrawing ligands, and  $Z$  is the charge of the cluster. This is a simplistic model, which assumes ligands withdraw either 0 or 1 electrons. Nevertheless, it works surprisingly well, and helps explain the stability of  $\text{Au}_{25}(\text{SR})_{18}^-$ . This has  $25 - 18 - (-1) = 8$  electrons, which is an electronic magic number. Oxidising this cluster to  $\text{Au}_{25}(\text{SR})_{18}^0$  or  $\text{Au}_{25}(\text{SR})_{18}^+$  results in a lower thermal stability.<sup>47</sup> While the anionic cluster has degenerate 1P orbitals, this is not

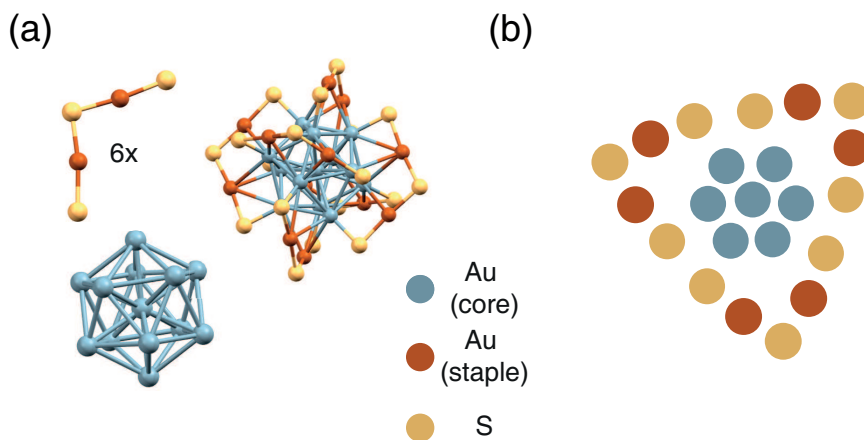


**Figure 1.2** (a) The structure of  $\text{Au}_{25}(\text{SR})_{18}^-$ , from<sup>53</sup>. This cluster consists of an icosahedral  $\text{Au}_{13}$  core capped by six  $\text{SR}-(\text{Au}-\text{SR})_2$  staple motifs. A schematic representation of this structure is shown in (b). For clarity, Au atoms in core and staple sites have been given different colours, and ligand backbones have been omitted.

the case for the cationic cluster. This has a  $1\text{S}^21\text{P}^4$  electron configuration, with the unoccupied  $1\text{P}$  superatom orbital at higher energy due to Jahn-Teller distortion.<sup>48</sup>

Thiolate-protected Ag and Au clusters share some common structural characteristics. They are not cores of metal atoms surrounded by thiolate ligands, but rather, cores of metal atoms surrounded by metal-thiolate complexes.<sup>49–51</sup> For Au clusters, these are often called staple motifs due to their structure; a chain of alternating Au and SR, with SR at either end which connect the structure to the core. A more general term is capping units or capping motifs. Staple motifs were first observed when the structure of  $\text{Au}_{102}(\text{SR})_{44}$  was determined with single crystal X-ray crystallography.<sup>52</sup> Later they were also found in  $\text{Au}_{25}(\text{SR})_{18}^-$ .<sup>53,54</sup> The structure of this cluster is shown in Figure 1.2, along with a schematic representation of it, where it can be clearly seen that Au atoms in capping units are far from the core. Ag clusters have been found to have more complex capping units. For instance,  $\text{Ag}_{44}(\text{SR})_{30}^{4-}$  consists of an  $\text{Ag}_{32}$  core protected by six three-dimensional  $\text{Ag}_2(\text{SR})_5$  units.<sup>23,55</sup> Crown-like  $\text{Ag}_3\text{S}_6$  capping units were observed for  $\text{Ag}_{29}(\text{BDT})_{12}(\text{PR}_3)_4^{3-}$ , where BDT is benzene-1,3-dithiolate (a bidentate ligand) and  $\text{PR}_3$  is a phosphine.<sup>56</sup>

The electronic structure of the cluster can be modified by the ligand. This can influence for instance the catalytic activity of the cluster.<sup>57</sup> Electron-rich ligands were found to increase the luminescence intensity of  $\text{Au}_{25}(\text{SR})_{18}^-$ .<sup>58</sup> The structure of the ligand can also enhance the stability of a particular cluster size. For instance, the three different methylbenzenethiol isomers (ortho-, meta- and para-substituted)

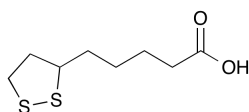


**Figure 1.3** The structure of ( $\pm$ )- $\alpha$ -lipoic acid, LA, the ligand used in this thesis.

resulted in three different Au cluster sizes;  $\text{Au}_{40}(\text{SR})_{24}$ ,  $\text{Au}_{104}(\text{SR})_{41}$  and  $\text{Au}_{130}(\text{SR})_{50}$ , respectively.<sup>59</sup> This is due to decreased steric hindrance in going from ortho- to para-substitution. That steric hindrance may affect cluster size has been known since the 1980s.<sup>60</sup> New sizes prepared using this principle include  $\text{Au}_{64}(\text{SR})_{32}$  with cyclohexanethiolate ligands<sup>61</sup>, and in an extreme case,  $\text{Au}_{41}(\text{SR})_{12}$  clusters, obtained using a bulky arenethiolate as the ligand.<sup>62</sup> The preference of a certain ligand for a certain cluster size may be used to prepare new sizes from existing clusters. In one example,  $\text{Au}_{38}(\text{SR})_{24}$  was treated with a bulky thiolate ligand  $\text{SR}'$ , which induced a structural distortion.<sup>63</sup> Eventually, a tetrahedral  $\text{Au}_{36}(\text{SR}')_{24}$  cluster was obtained from the original biicosahedral structure. Addition of bulky thiolate ligands to  $\text{Ag}_{44}(\text{SR})_{30}^{4-}$  clusters also introduced distortions, eventually leading to the formation of  $\text{Ag}_{25}(\text{SR}')_{18}^-$ . When this was treated with the original thiolate ligand, the  $\text{Ag}_{44}$  clusters formed again.<sup>64</sup> In this way, ligand-exchange reactions may not only modify the ligand shell but also the cluster size and structure.<sup>65</sup>

**Lipoic acid** This thesis focuses on aqueous Au and Ag clusters capped with one ligand; ( $\pm$ )- $\alpha$ -lipoic acid (LA). Its structure is shown in Figure 1.3. As can be seen, LA is chiral. Throughout this thesis we use the racemic mixture. LA is a disulfide rather than a thiol. During synthesis, the disulfide bond breaks and the ligand becomes bidentate.<sup>66</sup> This is commonly associated with enhanced stability<sup>67</sup>, though for small clusters a reduced packing efficiency of bidentate compared to monodentate ligands may in fact make the cluster more susceptible to oxidation and etching.<sup>68</sup> It is clear that by using a dithiolate ligand, clusters with different structures<sup>69</sup> and thus different properties can be obtained.<sup>70</sup> Ligand exchange of  $\text{Au}_{25}(\text{SR})_{18}^-$  with dithiolate has been found to enhance the cluster luminescence.<sup>71</sup> LA can be further functionalised via the carboxylic acid group which is of great interest for potential applications.<sup>72,73</sup>

### Cluster synthesis: kinetics and thermodynamics

In this section we will briefly discuss some common synthesis strategies for the preparation of monodisperse thiolate-protected Ag and Au clusters. First, a gold or

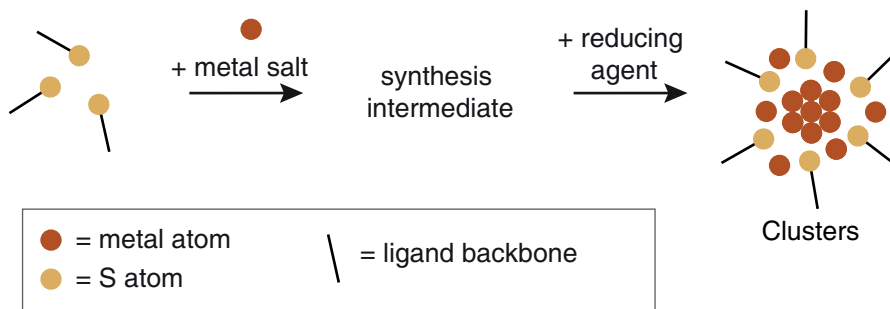


**Figure 1.4** Schematic representation of a typical Au or Ag cluster synthesis. Reactant ratios, solvent, temperature and other parameters may be varied.

silver salt such as  $\text{HAuCl}_4$  or  $\text{AgNO}_3$  is added to a solution containing thiols. The resulting synthesis intermediate may be kept for a certain amount of time before addition of a reducing agent, typically  $\text{NaBH}_4$ . Clusters are then formed, but they may be polydisperse, requiring purification steps to obtain pure, monodisperse clusters. A schematic overview of the synthesis is shown in Figure 1.4.

Some typical synthesis protocols of thiolate-protected Au clusters are based on the Brust-Schiffrin synthesis for Au nanoparticles.<sup>74</sup> This is a two-phase reaction, where the thiols are dissolved in an organic solvent and  $\text{HAuCl}_4$  is dissolved in water. A phase transfer agent is used to transfer  $\text{HAuCl}_4$  to the organic phase, where it reacts with the thiols before  $\text{NaBH}_4$  is added. The mechanism of this reaction is not completely understood; especially the nature of the Au species present before reduction (the synthesis intermediate) is not clear.<sup>13</sup> Nevertheless, this protocol has been successfully employed to prepare  $\text{Au}_{25}(\text{SR})_{18}^-$  clusters.<sup>75,76</sup> Subsequently, protocols have been developed that use one phase, eliminating the need for a phase transfer agent.<sup>77</sup>

Ideally, one would like to obtain monodisperse clusters without extensive purification. To this end, a size focusing method has been developed.<sup>30</sup> This relies on the enhanced stability of certain sizes relative to others. If the initial reaction yields a mixture of cluster sizes, but one size is significantly more stable than the others, then ageing the sample will eventually result in a monodisperse sample containing only the most stable size. The initial size distribution must be narrow enough so that it does not contain multiple stable clusters that can survive the size focusing process. This can be done for instance by varying synthesis parameters such as the solvent or even the stirring speed.<sup>78,79</sup> These parameters have been found to affect the aggregation state of the intermediate, which in turn influenced the size of the clusters. The size focusing method has been described as kinetic

control over the initial size distribution, followed by thermodynamic selection of the most stable product.<sup>80</sup>

### Potential applications and fundamental insights

Noble metal clusters have many potential applications. Their small, monodisperse sizes and well-defined structures make them interesting model systems for catalysis, with potential to explain catalytic activity on the atomic level.<sup>81</sup> The electronic properties of clusters can be tuned by changing metal atoms, ligands, or cluster size and structure, which may then be correlated to catalytic activity.<sup>82,83</sup> Many potential applications of clusters are related to their unique optical properties, in particular luminescence.<sup>84</sup> The luminescence has been shown to be sensitive to the presence of heavy metals such as Hg, and so can be used to detect Hg at nM concentrations<sup>85,86</sup>, even inside living cells.<sup>87</sup> Devices are being developed that can both sense and scavenge heavy metals from contaminated drinking water.<sup>88</sup> Other applications of luminescent clusters include *in vivo* biomedical imaging to localise tumors.<sup>89,90</sup>

The elimination of polydispersity for small Au and Ag clusters has paved the way for extensive studies of their fundamental properties.<sup>91</sup> The emergence of bulk optical properties and crystal structures has already been mentioned. Other fundamental studies focus on the origin of cluster luminescence<sup>92</sup>, or develop ways to enhance it by engineering the ligand shell.<sup>93</sup> It is thought that long capping units may enhance luminescence intensity.<sup>94</sup> Recently, isomerism of clusters such as  $\text{Ag}_{44}(\text{SR})_{30}^{4-}$  has been demonstrated.<sup>95</sup> This was attributed to differences in ligand orientation which changes the overall shape of the cluster. This demonstrates the importance of understanding the ligand layer. Some Au clusters are chiral, and the knowledge of precise structures revealed that it often originates from a chiral arrangement of Au–S bonds at the interface.<sup>96</sup> Chiral clusters may be used in enantioselective catalysis or chiral sensing of biomolecules. Fundamental studies of cluster properties are intimately related to their potential applications.

## 1.2 Characterisation techniques

In this thesis, Au and Ag clusters are characterised using a number of different techniques. These include X-ray spectroscopy, mass spectrometry, and analytical ultracentrifugation. As these may not be familiar to everyone, they are briefly introduced in this section.

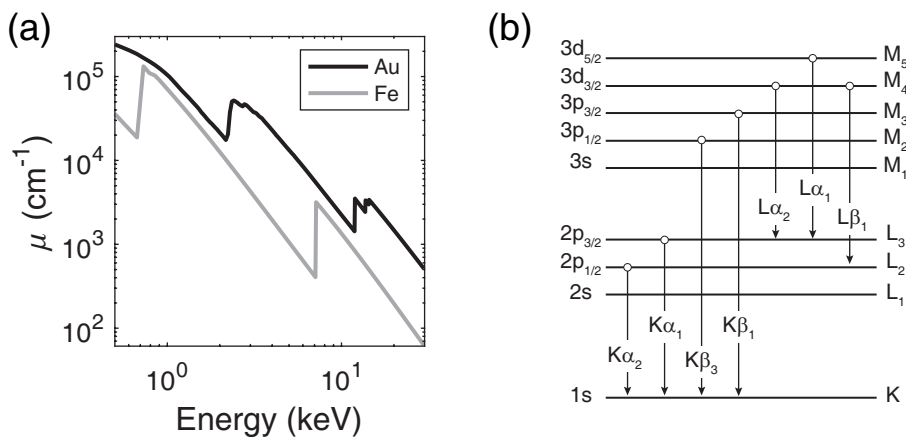


**Figure 1.5** (a) Absorption coefficient  $\mu$  for a heavy (Au) and a light (Fe) element as a function of energy. (b) Naming of absorption edges and emission lines.

### X-ray spectroscopy

X-rays were discovered by Wilhelm Röntgen in 1895.<sup>97</sup> He realised that this "new type of radiation" could penetrate different materials to different extents: while human skin and muscle were transparent, bones were not.<sup>98</sup> In other words, heavy elements absorb X-rays more strongly than light ones. Furthermore, the thicker the material, the stronger the absorption. As in UV-Vis absorption spectroscopy, this can be described with the Beer-Lambert law:

$$I = I_0 e^{-\mu x} \quad (1.2)$$

where  $I_0$  is the incident intensity,  $I$  the intensity after passing through a material with thickness  $x$ , and  $\mu$  is the linear absorption coefficient.

An X-ray absorption spectrum is commonly normalised and the absorption given in arbitrary units. The absorption of a material depends not only on the atomic number  $Z$ , but also on the energy  $E$ , as shown in Figure 1.5. The absorption coefficient decreases with increasing energy, but there are a number of sharp jumps, which occur at different energies for different elements. These jumps are called absorption edges and occur when the energy of the X-ray photon is sufficient to excite a core electron. The edge energies vary with atomic number as  $\sim Z^2$ . A similar dependence on element is observed for X-ray fluorescence; after excitation, each element emits X-rays at characteristic energies. This was first observed by Moseley in 1913<sup>99</sup> and is still a widely used technique for elemental analysis.<sup>100</sup>

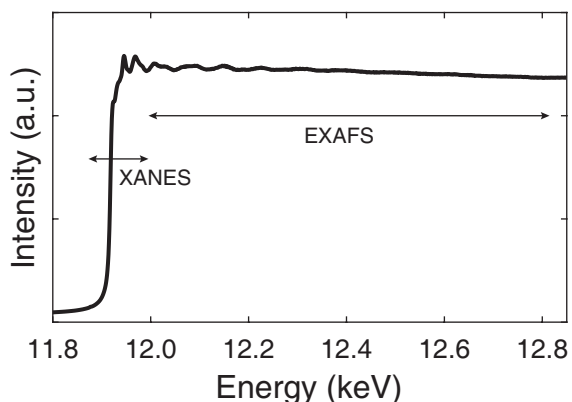


**Figure 1.6** An X-ray absorption spectrum of Au, showing XANES and EXAFS regions.

When the orbital angular momentum  $l$  of the core-hole is non-zero, there will be a large spin-orbit interaction resulting in total angular momentum of  $l + s$  or  $l - s$ , where  $s$  is the spin angular momentum.<sup>101</sup> Thus, there are two edges corresponding to excitation of 2p electrons;  $2p_{1/2}$  and  $2p_{3/2}$ . Similarly, the 3d state splits into  $3d_{3/2}$  and  $3d_{5/2}$ . Absorption edges are named after the principle quantum number of the electron that is excited, according to the Siegbahn notation. Emission lines are similarly named. An overview can be found in Figure 1.5.

The usefulness of X-ray absorption spectroscopy (XAS) goes beyond simple elemental analysis. An absorption edge is not simply a sharp increase in absorption coefficient. It can be highly structured, both around the absorption edge and many hundreds of eV above it. This structure depends on the geometric and electronic properties of the sample.

An X-ray absorption spectrum is divided into two parts as shown in Figure 1.6, the X-ray Absorption Near Edge Structure (XANES) and Extended X-ray Absorption Fine Structure (EXAFS). The XANES region extends to around 50 eV above the edge and also includes the pre-edge region, while EXAFS covers the range from 50 to several hundred eV. From XANES, one can obtain information about the oxidation state of the element in question, as well as its electronic properties and the local symmetry. The oscillations in EXAFS contain structural information about the immediate surroundings of the absorber, and can be used to determine the type of ligand, coordination number, bond length and degree of disorder.<sup>102,103</sup>

X-ray absorption spectra can be measured in transmission if the sample is sufficiently concentrated and with uniform thickness. The element of interest

should make up at least a few percent of the sample. Just as in UV-Vis spectroscopy, the sample must not be too thick or too concentrated, as the intensity of transmitted X-rays must be sufficiently high to measure. For dilute samples, the difference between incident and transmitted intensity will be negligible and the spectrum should be recorded by monitoring the X-ray fluorescence intensity as a function of incident energy. Generally, fluorescence yield is identical to absorption cross section. The fluorescence is typically detected at 90° to the incident beam to suppress elastic scattering. A detector with high energy resolution, ~100 eV, is necessary to avoid fluorescence from other elements in the sample, which may result in a large background signal. The sample must be either very thin and concentrated, or thick and dilute, to avoid over-absorption (or self-absorption) effects, which dampen oscillations in the spectrum.<sup>102</sup>

**EXAFS** In the EXAFS region, the X-ray photon energy far exceeds the binding energy of the electron. The electron is emitted from the atom as a photoelectron with a wavenumber given by:

$$k = \sqrt{2m_e(E - E_0)/\hbar^2} \quad (1.3)$$

where  $E$  is the X-ray energy,  $E_0$  the energy of the edge,  $m_e$  the mass of the electron and  $\hbar$  the reduced Planck constant. The edge energy is typically defined as the maximum of the first derivative of the spectrum.<sup>104</sup> The photoelectron can scatter from electrons in neighbouring atoms and return to the absorber. This will modify its absorption coefficient  $\mu(E)$ :

$$\mu(E) = \mu_0(E)(1 + \chi(E)) \quad (1.4)$$

where  $\mu_0$  is the absorption coefficient of a single isolated atom and  $\chi$  is the fine structure that results from the scattering of the photoelectron. Often simply called "the EXAFS",  $\chi(E)$  (or  $\chi(k)$ ) is proportional to the amplitude of scattered photoelectron at the absorber. Intuitively, one can understand that the photoelectron will be scattered strongly if the absorber has many heavy neighbouring atoms at short distances, leading to a highly structured spectrum. Conversely, no scattering is observed for a single isolated atom. Quantitative analysis of EXAFS was first demonstrated by Sayers, Stern and Lytle in the 1970s.<sup>105</sup> Describing the photoelectron as a spherical wave, which scatters from a neighbouring atom and returns to the absorber, forms the basis of the EXAFS equation:

$$\chi(k) = S_0^2 \sum_j \frac{N_j f_j(k) e^{-2R_j/\lambda(k)} e^{-2k^2\sigma_j^2}}{kR_j^2} \sin [2kR_j + \delta_j(k)] \quad (1.5)$$

The EXAFS is the sum of  $j$  different scattering paths with bond length  $R$  and coordination number  $N$ . The parameter  $\sigma^2$  is the mean-square-displacement in the bond length, also called the Debye-Waller factor. EXAFS is thus sensitive to these geometrical parameters. Chemical information comes from  $f(k)$  and  $\delta(k)$ , the scattering amplitude and phase shift of the neighbouring atom. These parameters are element dependent and can be used to identify the neighbouring atoms. The amplitude reduction factor  $S_0^2$  accounts for intrinsic losses such as many-body excitations, and is considered to be a constant with value 0.7–1. Finally,  $\lambda(k)$  is the photoelectron mean free path. A derivation of the EXAFS equation is given by Newville.<sup>102</sup> Both single scattering and multiple scattering — where the photoelectron scatters from more than one atom — contribute to EXAFS.

The  $1/R^2$  dependency and finite size of the mean free path  $\lambda(k)$  show that EXAFS is a local probe. Information on surrounding atoms can only be obtained up to a few coordination shells, with an upper limit of around 6 Å. A great advantage of EXAFS is that structural information can be obtained regardless of the physical state of the sample. High-quality single crystals are not required, and EXAFS can be done on disordered materials such as glasses and liquids. In this sense, the technique is complementary to X-ray crystallography.

A number of data treatment steps are required to extract the geometrical and chemical parameters of a recorded spectrum  $\mu(E)$ . First,  $\chi(k)$  is obtained by subtracting a smooth background  $\mu_0(E)$  and normalising, according to Equation (1.4), before converting to  $k$ -space (Equation (1.3)). The EXAFS  $\chi(k)$  can then be Fourier transformed to  $\chi(R)$ . Instead of oscillations depending on  $k$ , the data is now represented as peaks at certain distances  $R$ . As a rough approximation,  $\chi(R)$  can be considered as a radial distribution function with each peak corresponding to a coordination shell. However, the bond length is not equal to the precise value of  $R$  where the peak has its maximum, due to the phase shift of the scattered wave. Similarly, the height of the peak does not correspond to the coordination number. Scattering amplitude, distance and disorder can all affect the height of the peak. To extract structural information, calculated phase shifts  $\delta(k)$  and scattering amplitudes  $f(k)$  are used to model the EXAFS  $\chi(k)$  (or its Fourier transform), and the geometrical parameters are varied until a good fit is obtained. These calculations can be done with high accuracy using software such as FEFF.<sup>106</sup> In FEFF, these parameters are calculated for a particular scattering path in a material, thus Au–Au scattering properties will be slightly different depending on whether the material is Au foil or Au<sub>2</sub>S. An advantage of Fourier transforming  $\chi(k)$  is that fitting can be done in a specific range, for example only the first coordination shell.

**XANES** Around the edge, the excited electron is promoted into bound valence states rather than being excited as a photoelectron. In first approximation, XANES probes the empty density of states of a material in the presence of the core-hole. The transition probability in both XANES and EXAFS can be described by the Fermi-Dirac golden rule<sup>107</sup>:

$$W \propto |\langle \Phi_f | T | \Phi_g \rangle|^2 \delta(E_f - E_g - \hbar\Omega) \quad (1.6)$$

where  $\Phi_g$  and  $\Phi_f$  are the ground and final state, respectively,  $T$  is the transition operator and the delta function describes conservation of energy, that is, the final energy  $E_f$  is equal to the ground state energy  $E_g$  and the photon energy  $\hbar\Omega$ .<sup>101</sup> The transition operator can be expanded into a dipole and a quadrupole operator. As a first approximation, we consider only dipole transitions. The ground and final state wavefunctions can be approximated by a core electron and free electron wavefunction, respectively. This assumes all other electrons do not participate in the absorption event. Equation (1.6) can be rewritten as the product of the squared matrix element and the empty density of states.<sup>108</sup> The matrix element is to a good approximation independent of energy, so that the intensity of XAS is proportional to the empty density of states, projected on the absorber.<sup>109</sup> In the dipole approximation, the angular momentum  $l$  of the electron must change by 1 upon excitation. In K-edge XANES, the 1s electrons are excited, thus empty p states can be reached. Quadrupole transitions, such as 1s  $\rightarrow$  3d, also contribute to the X-ray absorption spectrum, although the transition probability is significantly lower than for dipole transitions. For transition metals, these quadrupolar transitions give rise to peaks just below the absorption edge, so-called pre-edges. While pre-edges are usually weak, in certain symmetries the pre-edge intensity can be significantly enhanced. This is due to mixing between (for instance) 3d and 4p states which allows dipole transitions to the pre-edge peak.<sup>110</sup>

At the L<sub>3</sub>-edge of transition metals, the main transition will be 2p<sub>3/2</sub>  $\rightarrow$  nd (where  $n = 3, 4$  or 5 depending on the row in the periodic table). This transition corresponds to the first intense feature in the spectrum<sup>111</sup>, which is called the whiteline. The intensity of the whiteline depends on the number of empty d-states, as demonstrated for 5d<sup>112</sup> as well as 4d and 3d<sup>113</sup> metals. This principle is useful for example in rationalising catalytic activity.<sup>114,115</sup> A further characteristic of XANES is that the energy of the edge shifts with oxidation state<sup>116,117</sup> although the edge energy also depends on the nature of the ligands, the interatomic distance and the spin state<sup>118</sup> of the compound.

At the high energy side of the XANES region, the excited electron will scatter from neighbouring atoms just as in EXAFS. However, the low energy of the

photoelectron ( $E \lesssim 50$  eV) results in a long mean free path, and the process can no longer be described as the sum of a small number of scattering paths. Multiple scattering, where the electron scatters off multiple atoms, becomes increasingly important. Unfortunately, there is no simple XANES equation that can be used to elucidate the structure of a compound. However, significant progress has been made in the understanding and theoretical modelling of XANES.

When the excited electron has weak interactions with the core-hole, the one electron approximation described above is reasonable. The final state wavefunction is calculated in the presence of the core-hole, which is screened by the other electrons in the atom. FEFF, one of the most common codes for XANES calculations, uses a Green's function formalism rather than explicitly calculating all final states which is computationally demanding.<sup>106,119</sup> All possible scattering paths of the photoelectron are considered, therefore the approach is called full multiple scattering. Typically a few hundred atoms must be included around the absorber for an accurate calculation. FEFF uses the muffin-tin approximation, where the potentials of all atoms are considered to be spherical. This is a good approximation for isotropic systems. Another code that is often used is FDMNES.<sup>120</sup> In addition to multiple scattering, this code can be used for calculations using the finite difference method (FDM) where the potentials are allowed to take any shape. This is useful for compounds with a low symmetry or open structure, where the muffin-tin approximation gives poor results.

However, there are cases when the one electron approach is not a valid approximation. Examples include L-edges of 3d metals, where there is a strong overlap of the core and valence wavefunctions. The XAS intensity is then no longer proportional to the density of states. The final states can be found by coupling the 2p and 3d wavefunctions. Depending on the number of 3d electrons and selection rules, there can be dozens of transitions, so-called multiplets. The atoms around the absorber can be included in the calculation by applying a crystal field splitting.<sup>109</sup> Multiplet effects are small for L-edges of Au and Ag. Therefore all XANES calculations in this thesis are done with "one electron, many atom" codes such as FEFF. Another strategy that is often used for XANES analysis is fitting to spectra of reference compounds with known structures, encompassing typical geometries, ligands and oxidation states.<sup>121</sup>

**High resolution fluorescence detection and resonant inelastic X-ray scattering** A downside of XANES is the broadness of the features, which is due to the short lifetime of the core-hole. This may make it hard to distinguish spectra of closely-related compounds especially at high atomic number where lifetime broadening is the greatest.<sup>123</sup> The lifetime broadening can be circumvented by recording High

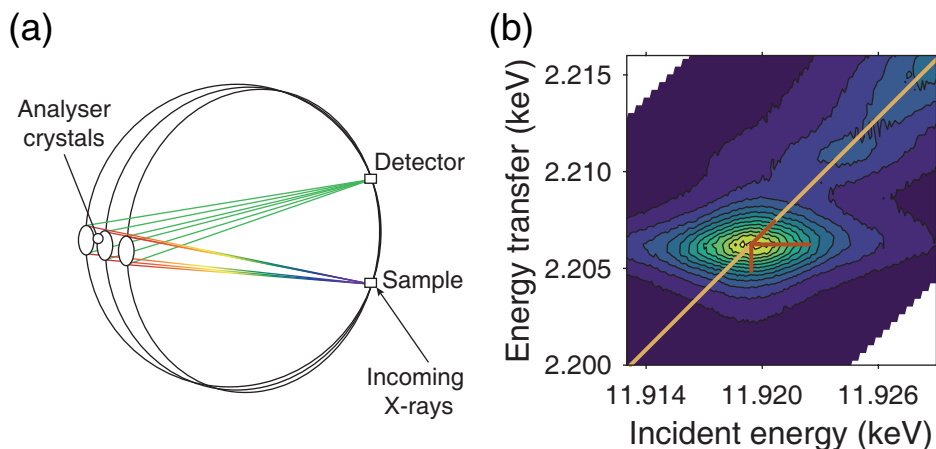


**Figure 1.7** (a) RIXS (and HERFD) setup. Analyser crystals ensure only emitted X-rays of a certain energy reach the detector. Adapted from <sup>122</sup>. (b) RIXS plane of  $\text{HAuCl}_4 \cdot 3 \text{H}_2\text{O}$ . The yellow line is the HERFD experiment, at constant emission energy ( $L\alpha_1$ , 9.71 keV). The red lines indicate lifetime broadening (full width, half maximum) of the intermediate state (horizontal), final state (vertical) and HERFD (diagonal).

Energy Resolution Fluorescence Detected (HERFD) XANES, as first demonstrated by Hämäläinen.<sup>124</sup>

Contrary to conventional fluorescence detected XAS, in HERFD only photons corresponding to a specific emission line of the element of interest are detected with a resolution below the lifetime broadening. This is done by means of Bragg optics, as shown in Figure 1.7. For  $L_3$ -edge HERFD-XANES of Au, measured in this thesis, the intensity of the  $L\alpha_1$  emission at 9.71 keV is recorded. The intermediate state thus has a 2p core-hole, while the final state has a 3d core-hole. The overall lifetime broadening is given by<sup>125</sup>:

$$\Gamma_{\text{all}} \approx 1/\sqrt{(1/\Gamma_{\text{int}}^2) + (1/\Gamma_{\text{fin}}^2)} \quad (1.7)$$

where  $\Gamma_{\text{int}}$  and  $\Gamma_{\text{fin}}$  are the lifetime broadenings of the intermediate and final state, respectively. This is shown graphically in Figure 1.7.

HERFD is a process combining X-ray absorption and emission, and as such it is a general case of Resonant Inelastic X-ray Scattering (RIXS), which is sometimes also referred to as Resonant X-ray Emission Spectroscopy (RXES). Just as absorption spectra, X-ray emission lines are sensitive to the local environment and chemical bonding, making both resonant and non-resonant X-ray emission spectroscopy valuable characterisation tools.<sup>126,127</sup> These techniques can be used to distinguish

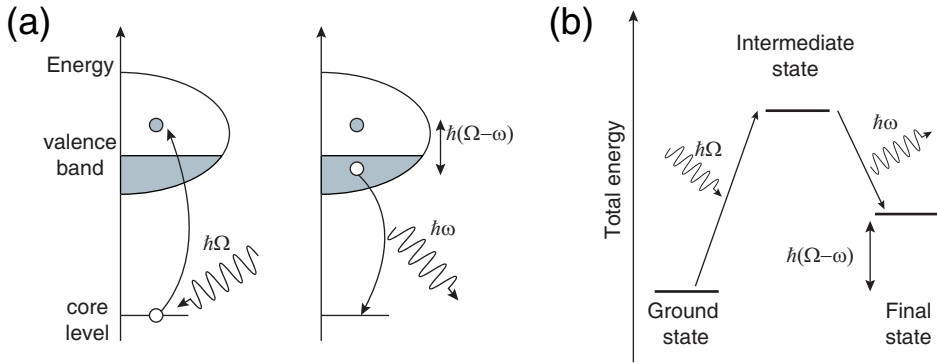


**Figure 1.8** Schematic illustration of RIXS. (a) One-electron picture showing the density of states and (b) total energy scheme. Adapted from<sup>130</sup> and<sup>131</sup>.

between C, N and O neighbouring atoms, which are too similar to be distinguished by EXAFS.<sup>128</sup> RIXS is described by the Kramers-Heisenberg equation<sup>122,129</sup>:

$$F(\Omega, \omega) = \sum_f \left| \sum_i \frac{\langle \Phi_f | T_2 | \Phi_i \rangle \langle \Phi_i | T_1 | \Phi_g \rangle}{E_g - E_i + \hbar\Omega - i \frac{\Gamma_{\text{int}}}{2}} \right|^2 \frac{\Gamma_{\text{fin}}/2\pi}{(E_g - E_f + \hbar\Omega - \hbar\omega)^2 + \frac{\Gamma_{\text{fin}}^2}{4}} \quad (1.8)$$

where  $\Phi_g$ ,  $\Phi_i$  and  $\Phi_f$  are ground, intermediate and final state wavefunctions, with energies  $E_g$ ,  $E_i$  and  $E_f$ ,  $T_1$  and  $T_2$  are the transition operators for absorption and emission. The incoming X-ray photon has energy  $\hbar\Omega$  while the emitted photon has energy  $\hbar\omega$ . The energy transfer is defined as  $\hbar(\Omega - \omega)$ . The energy transfer can be anywhere between several keV, as in the HERFD experiment described above, to below 1 eV. Low energy transfer excitations include phonons and magnons at the meV scale, but also charge transfer and dd excitations of a few eV. Charge transfer and dd excitations are also probed by UV-Vis absorption spectroscopy, but RIXS has the advantage of being element-selective and can also reveal transitions that are optically forbidden.<sup>130</sup>

It is worth noting that HERFD may show features that are not absorption features.<sup>132</sup> This is the case if there are strong interactions between the core-hole and excited electron.<sup>131</sup> In the RIXS plane, this gives off-diagonal features which due to lifetime broadening can have some intensity along the diagonal.<sup>133</sup> When off-diagonal features are not present, as is the case for the RIXS plane in Figure 1.7, HERFD-XANES is a sharpened version of the absorption spectrum and the pronounced spectral features can aid data interpretation.<sup>134,135</sup> In other cases the full RIXS process must be considered for correct interpretation.



**Figure 1.9** The large circular building is the European Synchrotron Radiation Facility (ESRF) in Grenoble.

**Synchrotron radiation** X-ray spectroscopy requires high photon intensity. While there has been progress in laboratory-sized benchtop setups for XAS<sup>136,137</sup>, in most cases synchrotron radiation is used. In a synchrotron, electrons travel at relativistic speeds along the storage ring.<sup>138</sup> The storage ring consists of straight and curved sections. The curved sections contain bending magnets, which guide the electrons along the circular orbit. This change in direction causes the electrons to emit X-rays tangential to the orbit. The radiation from a bending magnet covers a wide range of energies, from infrared to X-ray photons. The average energy depends on the magnetic field and the energy of the electron beam. The energy that the electrons lose upon emitting radiation is compensated in radio frequency cavities in the straight sections, which also contain focusing magnets to ensure that the orbit is maintained. Furthermore, the straight sections contain insertion devices such as undulators. An undulator consists of a periodic array of magnets. Electrons travelling through the undulator follow an undulating trajectory due to the alternating magnetic field. The radiation cones produced at each bend overlap and interfere with each other, so that certain wavelengths are enhanced. This results in a spectrum with harmonic peaks with a brilliance that is orders of magnitude higher than that produced by bending magnets.

Each bending magnet or insertion device is linked to an experimental station called a beamline, where X-ray optics are used to focus the X-ray beam and select the energy required for the experiment. The beamline also contains the equipment needed to control the sample environment, as well as detector systems. The XAS experiments described in this thesis were performed at the European Synchrotron Radiation Facility (ESRF), shown in Figure 1.9. HERFD-XANES and RIXS experiments were done at ID26, an undulator beamline, while EXAFS was measured at the bending magnet beamline BM26A.

## Mass spectrometry

With mass spectrometry (MS), one can determine the mass-to-charge ratio ( $m/z$ ) of a species of interest. The technique is used to study everything from small organic molecules to entire proteins, and in addition to  $m/z$  it can provide information on molecular structure and intermolecular interactions.<sup>139,140</sup> Mass spectrometry is one of the most common techniques for the analysis of noble metal clusters.<sup>141</sup> An accurate analysis will provide not only the cluster mass but also its composition: the number of metal atoms, the number of ligands, and the cluster charge, if any.

In a mass spectrometer, samples are ionised to generate molecular ions, which are then separated according to their  $m/z$ . A mass spectrum shows the abundance of each species with a particular  $m/z$ . Fragmentation may occur during ionisation, which can produce multiple peaks (called *ion signals*) even if the sample contains only one species. To determine the mass associated with a particular ion signal, one must first determine the charge (see below). In MS experiments, the mass is often given in units of dalton (1 Da =  $1.66 \times 10^{-27}$  kg). The mass of an ion in Da is numerically equivalent to the molar mass in  $\text{g mol}^{-1}$ . The charge is given in units of elementary charge.

**Ionisation and separation** There are multiple ways to ionise an analyte.<sup>142</sup> One example is electron ionisation, also called electron impact ionisation, in which molecules in the gas phase are bombarded with high energy electrons. The impact results in the loss of an electron from the molecule, creating a radical cation. This unstable ion can then fragment further. Which bonds break depends on the functional groups in the molecule, and electron ionisation is therefore typically used to elucidate structures of small organic molecules.<sup>143</sup> The fragmentation makes it less useful for clusters. A milder ionisation technique is matrix-assisted laser desorption ionisation (MALDI), where the analyte is mixed with a matrix of organic molecules containing conjugated bonds. The matrix absorbs strongly in the UV, so that when a pulsed laser is used to irradiate the sample, the matrix vaporises and carries with it the analyte molecules. Because the matrix absorbs most of the laser energy, fragmentation of the analyte itself is limited. This has allowed MALDI to be highly useful in the study of clusters; from the identification of new bimetallic clusters<sup>144</sup> to the study of ligand exchange<sup>145</sup> or size focusing<sup>146</sup> reactions.

Perhaps the mildest ionisation technique is electrospray ionisation (ESI).<sup>142</sup> In ESI, an analyte solution is sprayed from a capillary. A high voltage is applied between the tip of the capillary and a counter-electrode a short distance away. This causes the liquid to emerge as a fine spray of charged droplets. The solvent evaporates, leaving intact gas phase ions. ESI can yield multiply-charged species if

the analyte can undergo multiple (de)protonations. This is especially useful for large species, because it means they can be detected at low  $m/z$  where the resolution is highest.<sup>147</sup> ESI-MS played an important role in the early characterisation studies of thiolate-protected Au clusters.<sup>148–150</sup> It is used in this thesis for the study of Ag, Au and bimetallic clusters.

Separation of ions with different  $m/z$  is done using electric or magnetic fields. In this thesis, a time-of-flight (ToF) setup is used. This consists of a tube of length  $L$ , which the ions enter as they are accelerated by application of a voltage  $V$ . The kinetic energy is equivalent to:

$$E_{\text{kin}} = zV = \frac{mv^2}{2} \quad (1.9)$$

where  $v$  is the ion velocity. The time spent traversing the flight tube is given by:

$$t = \left(\frac{m}{2zV}\right)^{1/2} L \quad (1.10)$$

A standard ToF has limited resolution, but it can be improved by the use of a reflectron, an electrostatic mirror.<sup>142</sup> In a ToF, an ion with high  $m/z$  will traverse the tube more slowly than a low  $m/z$  ion.

**Isotope signals and ion adducts: determining charge and mass** There are several ways to deduce the charge of a species from a mass spectrum so that its mass can be determined. We use ESI-MS in negative mode, meaning only anions are detected. Some clusters are already anions because the cluster is charged (the charge is located on the Au/Ag and S atoms). In addition to this core charge, one or more of the LA ligands — each of which has a carboxylic acid group — can be deprotonated. The overall cluster charge is the sum of the core charge and the ligand charge. We typically observe clusters with overall charge states between 1– and 5–.

Multiple ion signals can be detected even for one single species in one overall charge state. This is due to the presence of different isotopes, for instance,  $^{12}\text{C}$  and  $^{13}\text{C}$ ,  $^{32}\text{S}$  and  $^{34}\text{S}$ ,  $^{107}\text{Ag}$  and  $^{109}\text{Ag}$ . The molecular formula of LA is  $\text{C}_8\text{H}_{14}\text{O}_2\text{S}_2$ , thus a sample of LA will contain both  $(^{12}\text{C})_8\text{H}_{14}\text{O}_2(^{32}\text{S})_2$ ,  $(^{12}\text{C})_7(^{13}\text{C})\text{H}_{14}\text{O}_2(^{32}\text{S})_2$ ,  $(^{12}\text{C})_8\text{H}_{14}\text{O}_2(^{32}\text{S})(^{34}\text{S})$ , etc, in a ratio that depends on the natural abundances of the isotopes. The more atoms a species consists of, the more possible combinations there are (though some have very low abundance). This is illustrated in Figure 1.10. Isotope patterns can be calculated<sup>151</sup> and compared to experimental spectra to help assign ion signals to clusters. Due to the presence of  $^{12}\text{C}$  and  $^{13}\text{C}$  there will always be a so-called  $M + 1$  ion signal (with mass 1 Da more than the main signal).

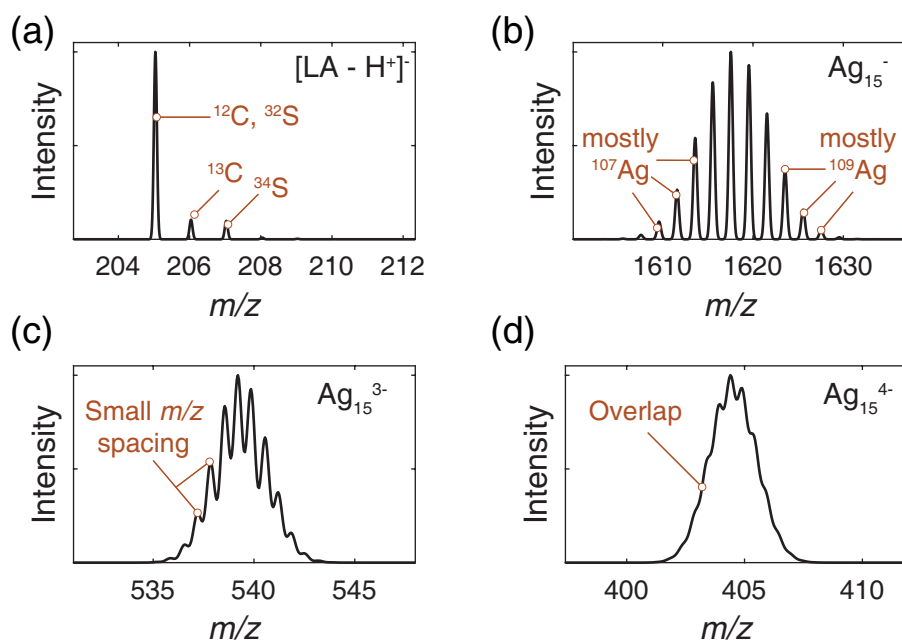


**Figure 1.10** Theoretical mass spectra, or isotope distributions, calculated with ChemCalc.<sup>151</sup> (a) Deprotonated LA ( $C_8H_{13}O_2S_2^-$ ) has multiple ion signals due to the presence of  $^{12}C$  and  $^{13}C$ ,  $^{32}S$  and  $^{34}S$ . (b) An  $Ag_{15}^-$  cluster contains both  $^{107}Ag$  and  $^{109}Ag$ , at 52 : 48 ratio, yielding a large number of ion signals. (c) and (d), the same cluster but now with  $z = 3^-$  and  $z = 4^-$  charge, respectively, which decreases the  $m/z$  spacing between adjacent signals.

The spacing in  $m/z$  between these two signals depends on the overall charge  $z$ , meaning the charge of a species can be determined if the individual isotope signals are resolved. If the overall charge is high, adjacent isotope signals can overlap because the  $m/z$  spacing is below the spectrometer resolution. Instead of multiple isotope signals, a single broad signal is observed and a different method must be used to determine the charge.

Proteins contain many acidic and basic groups and can therefore undergo multiple (de)protonations. Each time, the mass changes only by 1 Da, but the charge changes by  $\pm 1$  and together this gives a large change in  $m/z$ . For a neutral protein with mass  $m$  that becomes positively charged due to protonation, adjacent ion signals can be found at  $m/z(1) = (m + nH^+)/n$  and  $m/z(2) = (m + [n + 1]H^+)/[n + 1]$ . This can be used to determine number of protonations  $n$ , which is equal to the charge  $z$ , and hence the mass of the protein.<sup>142</sup> A similar approach can be used for clusters that are found in different charge states. The clusters

in this thesis are capped by LA, which has a carboxylic acid group that can be deprotonated. Different degrees of deprotonation of LA ligands can yield different charge states for the same cluster.

After deprotonation of LA, we often observe the addition of  $\text{Na}^+$ . This is called  $\text{H}^+/\text{Na}^+$  exchange, and the new ion signals are called  $\text{Na}^+$  adduct signals. The charge of the cluster does not change as a result of  $\text{H}^+/\text{Na}^+$  exchange, but its mass increases by 22 Da. The difference in  $m/z$  depends on the charge and can therefore be used to determine  $z$ . Each LA can undergo one  $\text{H}^+/\text{Na}^+$  exchange, meaning that for one particular cluster we observe a series of ion signal groups, where each group consists of many isotope ion signals. If the  $\text{Na}^+$  concentration is not too high, the ion signal with 0  $\text{Na}^+$  will be intense, so it is easy to observe where the series of signals begins. For higher  $\text{Na}^+$  concentrations, the ion signal with 0  $\text{Na}^+$  might be less obvious which can result in inaccurate mass determinations. A further disadvantage of high salt concentration is that it can complicate the measurement due to background noise and low stability of the capillary spray. If there are many clusters present, the adduct signals can overlap and it may be hard to determine which adduct signals belong to which cluster species.

**Determining the composition of a cluster: trial and error** If the mass of the cluster species can be unequivocally determined, it is often not too hard to determine the cluster composition. In this thesis, clusters consist of Au/Ag atoms and LA molecules ( $\text{C}_8\text{H}_{14}\text{O}_2\text{S}_2$ ), with possibly one or more deprotonations (deprotonated LA is  $\text{C}_8\text{H}_{13}\text{O}_2\text{S}_2$ ). The overall charge on the cluster,  $z$ , is the sum of deprotonations and the intrinsic cluster charge, which is located on the Ag/Au and S atoms. The average masses of Au, Ag and LA are 197, 107.9 and 206.3 Da, respectively. An ion signal can thus be from an Au cluster if the mass is a multiple of  $\sim 200$  Da, or from an Ag cluster if the mass is a multiple of  $\sim 100$  Da. Large deviations from this could mean that the ion signal is not the first in the series of  $\text{Na}^+$  adducts, or that the species is not a cluster but contains LA, salts, or compounds used in the purification of the clusters (methanol and butanol).

The cluster composition is determined by calculating theoretical isotope distributions for a number of trial species  $\text{Au}_x(\text{LA})_y$  or  $\text{Ag}_x(\text{LA})_y$ . This is done for all possible number of  $\text{H}^+/\text{Na}^+$  exchanges. The intrinsic cluster charge, and thus number of deprotonated LA, is tweaked until the theoretical spectrum overlaps with the experimental one and all  $\text{Na}^+$  adduct signals are explained by the composition. Trial species are chosen so that  $x$  and  $y$  give a likely metal-to-ligand ratio and the intrinsic charge is not unreasonably high. For small clusters with low overall charge, individual isotope signals may be observed, which facilitates the identification. This is the case for small Au clusters as described in Chapter 5 .

### Analytical ultracentrifugation

Analytical ultracentrifugation (AUC) is a powerful method for the analysis of clusters in solution and can be used to determine their mass and demonstrate monodispersity.<sup>152</sup> The technique dates back nearly a century and was developed by Svedberg, who was awarded the Nobel Prize for chemistry in 1926.<sup>153</sup> In AUC, a solution of the compound of interest is placed in a sample cell which is centrifuged at high speed. Changes in the distribution of sample in the cell are then monitored, typically by measuring the absorbance of the sample at a specific wavelength at each position in the cell. There are almost no restrictions on the type of sample that can be measured. The molecular mass can be anywhere in the range  $10^2$ – $10^8$  Da and any solvent can be used, although the absorbance of the sample must not be too high or too low, just as in UV-Vis spectroscopy. In principle, there is also no restriction on the concentration of sample or of any contaminants, meaning AUC can for example be used to study samples under biologically relevant conditions.<sup>154</sup> It should be noted that there may be interactions between the species of interest.<sup>155,156</sup> For charged particles, counterions must be considered which may influence the interpretation of the data, especially at low ionic strength.<sup>157</sup>

There are two types of AUC experiments; sedimentation velocity (SV) and sedimentation equilibrium (SE). The latter will be discussed only very briefly, as it is not used to any great extent in this thesis.

SV-AUC experiments are done at high centrifugation speeds and are therefore fast, taking only a few hours. During a SV-AUC experiment, three forces act on a sedimenting particle. The first is the force due to centrifugation, which is  $m_p\omega^2r$ , where  $m_p$  is the mass of the particle,  $\omega$  the rotor speed in radians per second and  $r$  the rotor distance. The second force is the buoyant force which acts in the opposite direction,  $m_s\omega^2r$ , where  $m_s$  is the mass of the displaced solvent. Finally, there is the frictional force, which also opposes sedimentation,  $fv$ , where  $f$  is the frictional coefficient and  $v$  the velocity. During the experiment, the forces are balanced, and the sedimentation velocity of the particle can be determined from:

$$s \equiv \frac{v}{\omega^2r} = \frac{m_b}{f} \quad (1.11)$$

where the particle buoyant mass has been defined as  $m_b = m_p - m_s = m_p(1 - \bar{v}_p\rho_s)$ , with  $\rho_s$  the solvent density and  $\bar{v}_p$  the partial specific volume of the particle, which is the inverse of its density ( $\bar{v}_p^{-1} = \rho_p$ ). The sedimentation coefficient,  $s$ , is defined as the ratio of the sedimentation velocity to applied acceleration. Sedimentation coefficients are related to the size, shape and density of a species, and the unit is svedberg ( $1\text{ S} = 1 \times 10^{-13}\text{ s}$ ).

The frictional coefficient is related to the diffusion coefficient  $D$  via the Einstein relation,  $D = RT/N_a f$ , where  $R$  is the gas constant,  $T$  the temperature and  $N_a$  Avogadro's number. Taken together with Equation (1.11), this yields the well-known Svedberg equation:

$$\frac{s}{D} = \frac{M_b}{RT} \quad (1.12)$$

where the molar buoyant mass of the particle  $M_b = m_b N_a$  is used. The sedimentation and diffusion coefficients are obtained by fitting the data to the Lamm equation:

$$\frac{\partial c}{\partial t} = D \left[ \frac{\partial^2 c}{\partial r^2} + \frac{1}{r} \frac{\partial c}{\partial r} \right] - s \omega^2 \left[ r \frac{\partial c}{\partial r} + 2c \right] \quad (1.13)$$

which describes how the concentration,  $c$ , of a species changes over time  $t$  and with rotor distance  $r$ . There is no analytical solution to the Lamm equation, but there are numerical approaches to extract  $s$  and  $D$  from the measured data,  $c(r, t)$ . In this thesis, the  $c(s)$  method is used.<sup>158</sup> It is assumed that all species within one sample have the same shape, and thus the same frictional ratio  $f/f_0$ , where  $f_0$  is the frictional coefficient of a perfect sphere. With this approach, there is a scaling relationship between  $s$  and  $D$  which can be used in the fitting. The result is a sedimentation coefficient distribution function  $c(s)$ , which is useful for determining sample homogeneity. The main advantage of SV-AUC in characterisation of clusters is thus its ability to determine whether a sample is monodisperse or polydisperse, and how many species are present in the sample, while removing the need for extensive purification which may damage or otherwise affect the sample.<sup>157-159</sup>

With some assumptions, it is possible to estimate molar masses of the species.<sup>152</sup> A first assumption is that the particles are spherical, so that their diffusion coefficient can be calculated from the Stokes-Einstein relation:

$$D = \frac{k_B T}{3\pi\eta_s d_H} \quad (1.14)$$

where  $d_H$  is the particle hydrodynamic diameter,  $k_B$  Boltzmann's constant and  $\eta_s$  the solvent viscosity. We further assume that the hydrodynamic diameter equals the particle diameter,  $d_H = d_p$ , which is used to calculate the partial specific volume of the particle,  $\bar{v}_p$ . Equation (1.14) can be combined with Equation (1.12) to give a number of useful equations:

$$d_p = \sqrt{\frac{18\eta_s s}{\bar{v}_p^{-1} - \rho_s}} = \sqrt{\left( \frac{18\eta_s s}{\rho_p - \rho_s} \right)} \quad (1.15)$$

$$M_p = \frac{sRT}{D} \left(1 - \frac{\rho_s}{\rho_p}\right)^{-1} \quad (1.16)$$

Equation (1.15) can be further rearranged to give:

$$\rho_p = \rho_s + 18\eta_s s \left(\frac{1}{D} \frac{k_B T}{3\pi\eta_s}\right)^{-2} \quad (1.17)$$

Equations (1.15) to (1.17) will be used in Chapter 5 to estimate sedimentation coefficients of clusters based on their molar mass and estimated density. Further derivations for this purpose are introduced in Section 5.2.

Finally, we briefly discuss SE-AUC experiments. At lower centrifugation speeds, sedimentation of particles is exactly balanced by diffusion. An equilibrium concentration gradient is obtained, which for an ideal species is given by<sup>157</sup>:

$$c(r) = c_0 \exp \left[ \frac{M_b \omega^2}{RT} \frac{r^2 - r_0^2}{2} \right] \quad (1.18)$$

where  $c_0$  is the concentration at a reference distance  $r_0$ . SE-AUC experiments can thus be used to determine the molar mass of a species with very high accuracy. However, due to the lower centrifugation speed, the experiment can easily take multiple days. Ideally, the sample must be measured at different wavelengths, centrifugation speeds and concentrations to rule out interactions between particles which can change the apparent molar mass. For a good measurement, the sample must be stable at different concentrations over several days. This is not the case for the clusters described in this thesis, as will be demonstrated in Chapter 2.

### 1.3 Scope and outline of this thesis

In this thesis we discuss Au and Ag clusters capped with LA, which show red and near-infrared luminescence. The thesis is divided in three parts; the first focusing on silver, the second on silver and gold, and the third on gold. The clusters are characterised to determine their composition, and we also investigate the synthesis process in more detail.

In **Chapter 2** the synthesis of luminescent silver clusters with LA is described. The clusters are characterised with mass spectrometry and analytical ultracentrifugation, and found to be monodisperse without any purification steps. The composition was determined to be  $\text{Ag}_{29}(\text{LA})_{12}$ , with a charge of 3<sup>-</sup> on the silver and sulfur atoms. The clusters emit red luminescence with quantum yield of ~3%.

They are stable for up to 18 months, and once degraded can be regenerated by repeating the reduction step.

**Chapter 3** describes the synthesis mechanism of the  $\text{Ag}_{29}$  clusters in more detail. Using mass spectrometry, optical spectroscopy and X-ray spectroscopy, we find that particles of  $\sim 100$  atoms are formed after an initial burst of nucleation. These large particles subsequently decrease in size until only  $\text{Ag}_{29}$  clusters remain. No other stable sizes are observed in this process.

In **Chapter 4** we move away from pure silver clusters. A small amount of gold is introduced in the synthesis, resulting in bimetallic clusters,  $\text{Au}_y\text{Ag}_{29-y}$ . With a few percent Au, cluster luminescence and stability are both enhanced. There is a strong preference for monodoping, and X-ray spectroscopy was used to determine that the central position in the cluster is preferentially occupied by Au.

The third and final part of this thesis is about gold. **Chapter 5** describes the synthesis and characterisation of Au with LA. In contrast to  $\text{Ag}_{29}$ , the Au clusters are not atomically monodisperse but show size distributions. The average cluster size can be tuned by varying the NaOH concentration during synthesis. The NaOH concentration was also found to impact the composition of the synthesis intermediates.

Before the characterisation of Au clusters with LA is discussed in more detail, **Chapter 6** presents an X-ray spectroscopy study of five Au reference compounds. X-ray absorption spectra and resonant inelastic X-ray spectra are presented, as well as results from calculations. In **Chapter 7**, X-ray spectroscopy of LA-capped Au clusters is discussed. X-ray absorption spectra of the clusters are similar to the spectrum of an Au(I)-thiolate reference compound, suggesting the samples may consist of complexes rather than clusters. However, we found that  $\text{Au}_{25}(\text{SR})_{18}^-$  has similar spectral features. Calculated X-ray spectra of this and other clusters of similar size show these features are common for thiolate-protected Au clusters, and result from the small particle size and large surface-to-volume ratio.

The work presented in this thesis is summarised in **Chapter 8**, which also gives some suggestions for future work.

**PART I**





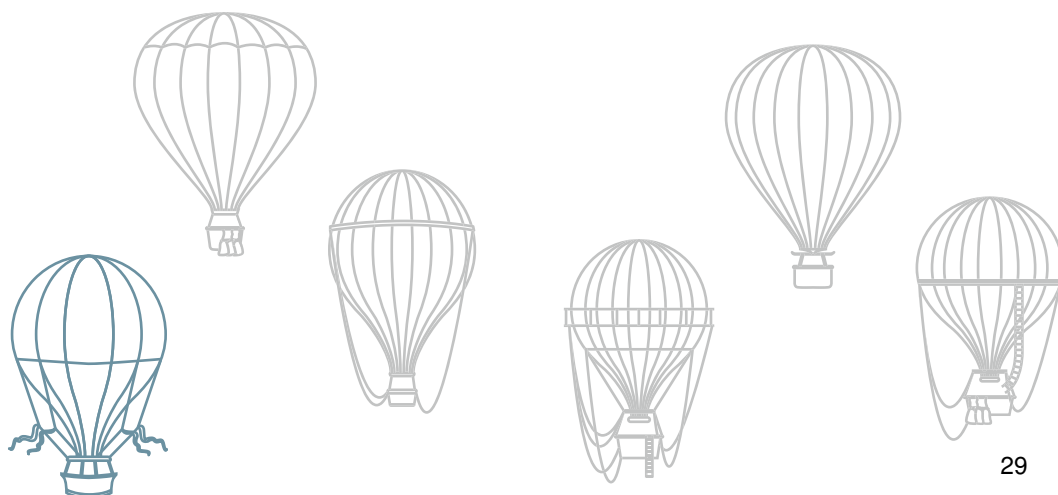
## Characterisation, degradation and regeneration of luminescent Ag<sub>29</sub> clusters in solution

---

### Abstract

Luminescent Ag clusters are prepared with lipoic acid (LA) as the ligand. Using a combination of mass spectrometry, optical spectroscopy and analytical ultracentrifugation, the clusters are found to be highly monodisperse with mass 5.6 kDa. We assign the chemical composition Ag<sub>29</sub>(LA)<sub>12</sub><sup>3-</sup> to the clusters, where LA likely binds in a bidentate fashion. The Ag<sub>29</sub> clusters show slow degradation, retaining their deep red emission for at least 18 months if stored in the dark. Purification or exposure to light results in faster degradation. No other cluster species are observed during the degradation process. Once degraded, the clusters could easily be regenerated using NaBH<sub>4</sub>, which is not usually observed for thiolate-capped Ag clusters.

---



*“Go back? No good at all! Go sideways? Impossible!  
Go forward? Only thing to do! On we go.”*

— J. R. R. Tolkien, *The Hobbit*

## 2.1 Introduction

Many thiolate-protected Au and Ag clusters with known structures luminesce weakly or not at all. Examples are Ag<sub>44</sub>(SR)<sub>30</sub><sup>4-</sup> and Au<sub>25</sub>(SR)<sub>18</sub><sup>-</sup>, both with a reported quantum yield of only ~ 0.01%.<sup>58,160</sup> The luminescence intensity of clusters can be enhanced in a number of ways. It has been shown to depend on the oxidation state of the cluster and the electronic properties of the ligand: ligands containing electron-rich groups are particularly effective.<sup>58,161,162</sup> Furthermore, it has been shown that treating Au<sub>25</sub>(SR)<sub>18</sub> with Au(I)-thiolate results in additional thiolate groups on the surface, and an increased quantum yield of almost 2%.<sup>163</sup> This suggests that the surface structure is also important for cluster luminescence.

By using dithiolate rather than thiolate ligands to cap clusters, clusters with different surface structures and thus different properties can be obtained. Indeed, several studies have shown changes in luminescence properties during ligand exchange of thiols with dithiols.<sup>71,164</sup> Recent work has also led to the structure elucidation of a dithiolate Ag cluster.<sup>56</sup> A promising ligand is lipoic acid (LA), a disulfide, which has been used to prepare luminescent clusters of both Au<sup>72,87,165,166</sup> and Ag<sup>73,86,167-170</sup>. Advantages of LA include its solubility in water, the possibility of functionalisation of its carboxylic acid terminated tail<sup>72,73</sup> and the straightforward synthesis of LA-protected clusters. We have previously reported on the synthesis of LA-protected Ag clusters with strong red luminescence, and on the influence of pH, solvent and presence of poly(ethylene glycol) on the luminescence properties.<sup>168</sup>

However, different sizes have been reported for this cluster, and the monodispersity has not been verified. Adhikari *et al.*, who first prepared these clusters, report the presence of Ag<sub>4</sub> and Ag<sub>5</sub> in their mass spectra (size <1 nm), while simultaneously showing TEM images of 2–3 nm nanoparticles with clear crystal lattices.<sup>86</sup> We have also observed 2–3 nm nanoparticles with TEM<sup>168</sup>, as have our co-workers<sup>171</sup>. Particles of this size would have several hundred Ag atoms.<sup>18,172</sup> This suggests that the synthesis does not yield monodisperse clusters. An alternative explanation was offered by Chen *et al.*, who propose that these nanoparticles act as a scaffold for a luminescent Ag<sub>8</sub> species.<sup>167</sup> In a recent study, Russier-Antoine *et al.* report the size as Ag<sub>29</sub>(LA)<sub>12</sub> (no core charge) and find no larger nanoparticles.<sup>170</sup> It is clear that extensive characterisation of LA-capped Ag clusters is needed to explain these inconsistencies and correctly identify all species present. Ideally, characterisation should be done at different times after synthesis or purification, as the cluster

composition and properties can change for example by removal of excess ligands and salts<sup>173</sup> or oxidation following exposure to air and light.<sup>174</sup>

In this chapter, we combine sedimentation velocity analytical ultracentrifugation (SV-AUC) experiments with electrospray ionisation mass spectrometry (ESI-MS) and optical spectroscopy to investigate the monodispersity and composition of LA-capped Ag clusters. We show here that the cluster composition is most likely  $\text{Ag}_{29}(\text{LA})_{12}^{3-}$  (not  $\text{Ag}_{25}(\text{LA})_{14}$  as we reported earlier<sup>168</sup>). The monodispersity of the clusters is confirmed by SV-AUC experiments; thus it is expected that the 2–3 nm particles observed with TEM are formed by cluster aggregation during TEM sample preparation. Our experiments indicate bidentate bonding of LA to the Ag cluster. The clusters are found to be remarkably stable in solution, remaining luminescent for  $\geq 18$  months if stored in the dark, although purification was found to decrease the cluster stability significantly. We do not observe different cluster species as a result of purification or cluster ageing. Degradation over time of as-synthesised clusters results in aggregation and possibly oxidation. However, this degradation is reversible upon addition of  $\text{NaBH}_4$ , which is not observed for other thiolate-capped Ag clusters.

## 2.2 Experimental methods

### Chemicals

$\text{AgNO}_3$  (laboratory reagent grade) was obtained from Fisher Scientific.  $\text{NaBH}_4$  (99%), ( $\pm$ )- $\alpha$ -lipoic acid ( $\geq 99\%$ ) and methanol ( $\geq 99.9\%$ ) were purchased from Sigma Aldrich. 1-Butanol (99.5%) and Nile Blue A were obtained from Acros. Water was of Milli-Q quality, purified using a Millipore Direct-Q 3 water purification system. 4-(dicyanomethylene)-2-methyl-6-(4-dimethylaminostyryl)-4H-pyran (DCM dye) was obtained from Exciton.

### Synthesis

The synthesis of the Ag clusters is adapted from the literature.<sup>86</sup> In a standard synthesis, 19 mg lipoic acid (92  $\mu\text{mol}$ ) and 7 mg  $\text{NaBH}_4$  (185  $\mu\text{mol}$ ) were placed in a 40 or 20 mL glass vial with 14 mL water. This was stirred (using a magnetic stirring bean) until all LA had dissolved. Next, 700  $\mu\text{L}$  25 mM  $\text{AgNO}_3$  (17.5  $\mu\text{mol}$ ) was added (the solution turned turbid), followed by 10 mg  $\text{NaBH}_4$  (264  $\mu\text{mol}$ ) in 2 mL water. The vial was wrapped in aluminium foil to minimise the exposure of the clusters to light, and stirring was continued overnight. The synthesis was performed at room temperature. Samples were stored in the dark at room temperature.

In the standard synthesis, the Ag : LA ratio is 1 : 5.3. The synthesis was also performed with other Ag : LA ratios (from 1 : 0.6 to 1 : 28) by changing the amount of LA (and  $\text{NaBH}_4$  in the first step) while the Ag concentration was kept constant. Unless stated otherwise, clusters with Ag : LA ratio of 1 : 5.3 are used for the experiments described.

To investigate whether clusters would behave as classical seeds for formation of larger nanoparticles, the synthesis was performed in the presence of existing Ag<sub>29</sub>. A synthesis of Ag clusters was done on ½ scale. Just before addition of AgNO<sub>3</sub> and NaBH<sub>4</sub> solutions, half of a previously prepared sample was added to it. The resulting sample had exactly the same overall concentrations of Ag, LA and reducing agent as a sample prepared according to the standard protocol.

### Optical spectroscopy

UV-Vis spectra were recorded using a Perkin Elmer Lambda 950, a Perkin Elmer Lambda 40 or a Varian Cary 50 spectrometer. Emission spectra were recorded with a Spex 1680 (0.22 m) double beam spectrofluorometer equipped with a liquid nitrogen cooled Acton Research SpectraPro 300i CCD camera. The CCD camera was equipped with a 150 lines/mm grating blazed at 800 nm. The excitation wavelength was typically 425 nm. Emission spectra were corrected for the spectral response of the equipment. Luminescence lifetimes were recorded with a time-correlated single photon counting card (TimeHarp 260 PC, PicoQuant) with a laser (Opolette HE 355-II, Opotec Inc) operating at 500 nm as excitation source. Excitation spectra were recorded using a Jasco FP8300 Spectrofluorometer. For optical spectroscopy measurements, the cluster solution was diluted with water. The dilution factor varied between 4–10×, but the dilution was the same when comparing different samples for the same experiment.

**Quantum yield determination** The quantum yield of Ag clusters was determined using DCM dye and Nile Blue A in ethanol as references. A Varian Cary 50 spectrometer was used to record UV-Vis absorption spectra. Emission spectra were recorded on a Jasco FP8300 Spectrofluorometer. The excitation wavelengths used were 485 and 550 nm. At 485 nm only the DCM dye reference and the Ag clusters were measured. Ag clusters, Nile Blue A and DCM dye were diluted with water to prepare five samples with absorbance ≤ 0.1 at 485 nm. The integrated emission intensity of each spectrum scales linearly with the absorbance at 485 nm, see Figure 2.1, the slopes of the lines are proportional to the quantum yield. The quantum yield of DCM dye in ethanol is 43.5%<sup>175</sup>, that of Nile Blue A in ethanol is 27%.<sup>176</sup> The quantum yield of the Ag clusters can be calculated according to Equation (2.1), where  $m$  is the slope from Figure 2.1,  $n$  is the solvent refractive index and  $\Phi$  is the quantum yield. In each case, the subscript R refers to the reference dye. Values for the solvent refractive index are  $n = 1.33336$  and  $n_R = 1.3611$  for water and ethanol, respectively.<sup>177</sup>

$$\Phi = \Phi_R \frac{m}{m_R} \frac{n^2}{n_R^2} \quad (2.1)$$

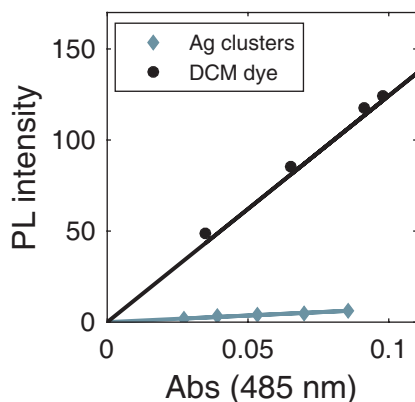


**Figure 2.1** Integrated emission intensity as a function of absorbance at 485 nm for Ag clusters and DCM dye. The lines are a fit through the points.

### Analytical ultracentrifugation

Sedimentation velocity experiments have been performed on XL-I and XL-A Analytical ultracentrifuges (Proteomelab and Optima XL-A, Beckman Coulter) using absorbance optics. Samples were centrifuged in 12 mm path length double-sector Aluminium centrepieces with sapphire windows in an An60-Ti rotor; the reference sector was filled with Milli-Q water. All measurements were performed at 50 000 and 60 000 rpm at 20 °C. Changes in solute concentrations were detected by 300–500 absorbance scans measured at 528 nm (undiluted samples) or 423 nm (diluted samples). Analysis and fitting of the data was performed using the program Sedfit v 14.3.<sup>158</sup> A continuous  $c(s)$  distribution model was fitted to the data. The resolution was set to 200 over a sedimentation coefficient range of 0.0–10.0 S. The meniscus and the bottom were kept at fixed values, and the frictional coefficient, the baseline and the raw data noise were floated in the fitting. Degraded clusters were measured at 60 000 rpm and 395 nm, and fitted using a sedimentation coefficient range of 0.0–20.0 S or 0.0–50.0 S.

### Mass spectrometry

MS measurements were performed in negative ion mode using an electrospray ionisation time-of-flight (ESI-ToF) instrument (LC-T; Micromass, Manchester, U.K.) equipped with a Z-spray nano-electrospray ionisation source. Needles were made from borosilicate glass capillaries (Kwik-Fil, World Precision Instruments, Sarasota, FL) on a P-97 puller (Sutter Instruments, Novato, CA), coated with a thin gold layer by using an Edwards Scancoat (Edwards Laboratories, Milpitas, CA) six Pirani 501 sputter coater. After purification, the sample was sprayed into the mass spectrometer. The applied voltage on the needle was between 1200 and 1100 V and the sample cone voltage was varied between –7 and 0 V for measurements of intact clusters. All spectra were mass calibrated in negative ion

mode, using an aqueous solution of phosphoric acid (0.1 % v/v). Theoretical mass spectra were calculated using ChemCalc<sup>151</sup> with full width at half maximum = 1. In calculating theoretical mass spectra, we assume that neither of the two S-atoms in LA is present as a thiol (thus LA is C<sub>8</sub>H<sub>14</sub>O<sub>2</sub>S<sub>2</sub>). To assign cluster compositions from mass spectra, theoretical mass spectra of many different clusters were calculated. All had approximate mass of 5.6 kDa and were in the overall  $z = 5-$  charge state, with compositions between Ag<sub>11</sub>(LA)<sub>21</sub> and Ag<sub>37</sub>(LA)<sub>8</sub>. Spectra were calculated with and without core charges, for all possible H<sup>+</sup>/Na<sup>+</sup> exchanges and for clusters with either all LA ligands or all HLA ligands (HLA is assumed to have one –SH group thus making it 1 Da heavier than LA). Cluster compositions were rejected if there were unexplained ion signals (or missing ion signals) and/or a large shift between experimental and theoretical spectra.

Matrix-assisted laser desorption ionisation mass spectrometry (MALDI-MS) of Ag clusters was unsuccessful. Attempts were made to characterise the Ag cluster samples in both positive and negative mode, using four different matrices (3,5-dimethoxy-4-hydroxycinnamic acid, 3-hydroxypicolinic acid, 2,5-dihydroxybenzoic acid,  $\alpha$ -cyano-4-hydroxycinnamic acid).

**Purification of samples** It was necessary to purify the sample before mass spectrometry analysis. The main purification method uses 1-butanol (BuOH) to extract water, containing excess ligands and other possible contaminants, until the clusters sediment, after which they are washed with a small amount of methanol (MeOH) and redispersed in water. This is done by mixing 300  $\mu$ L cluster solution, 400  $\mu$ L BuOH and 100  $\mu$ L MeOH in an Eppendorf vial. The vial was briefly centrifuged to speed up phase separation, and the upper colourless organic layer was removed. Next, 300  $\mu$ L BuOH was added, the vial was shaken and centrifuged, and the organic layer was again removed. This was repeated until the clusters just sedimented. Typically, 3–5 extractions with BuOH were needed. After removing the final organic layer and washing with MeOH (50–100  $\mu$ L), the clusters were redispersed in water (50–100  $\mu$ L). This purification method could easily be scaled up (we used up to 12 mL cluster solution, although the amount of MeOH for washing was kept to a minimum as the clusters are somewhat soluble in MeOH). This allowed for characterisation of the purified clusters with optical spectroscopy. The amount of water for cluster redispersion was chosen so that the absorbance of as-synthesised and purified clusters was similar.

An alternative purification method with 3 kDa molecular mass cutoff filters (Amicon, Millipore) was also used. 400  $\mu$ L cluster solution was centrifuged at 10 000 rpm for 25 min. The clusters remained on the filter and were washed 2 $\times$  with water. For regenerated clusters, 500  $\mu$ L cluster solution was purified and washed 4 $\times$  with water. The final concentrated, washed cluster solution (volume approximately 60  $\mu$ L) was clear and orange.

### Transmission electron microscopy

Transmission electron microscopy (TEM) images were recorded using a FEI Tecnai F30ST microscope in high-angle annular dark field (HAADF) mode operated at an acceleration voltage of 300 kV. Sample purification was done with a 3 kDa cutoff filter. A drop of the purified solution was placed on a carbon coated copper (400-mesh) TEM grid.

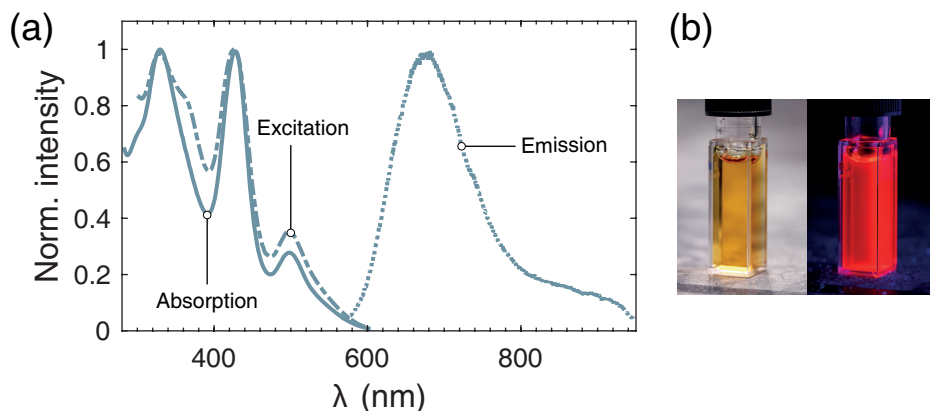


**Figure 2.2** (a) Absorption, excitation and emission spectrum of Ag cluster solution. For excitation, the emission wavelength was 680 nm, and for emission, the excitation wavelength was 425 nm. (b) Photographs of the clusters under normal and UV-light.

## 2.3 Results and discussion

### Optical properties of Ag clusters

The as-synthesised clusters (Ag : LA = 1 : 5.3) have the same optical properties as reported earlier<sup>168</sup>, with a bright orange colour and strong red luminescence that is easily visible using a handheld UV-lamp. Absorption and excitation spectra are similar (Figure 2.2). There are three distinct peaks at 500, 425 and 330 nm and a shoulder at 310 nm. The emission maximum is at 680 nm with a shoulder extending into the near-infrared (NIR, ~800 nm). Normalised excitation spectra of the main peak and the shoulder are near-identical and show only a few percent intensity variation in the UV region. Typically, pronounced absorption peaks indicate the presence of small clusters with high monodispersity.<sup>11,19</sup> Assuming a 100 % yield of Ag<sub>29</sub>, the molar extinction coefficient of the clusters was determined to be  $8.9 \times 10^4 \text{ M}^{-1} \text{ cm}^{-1}$  at 425 nm. This is in good agreement with values found for other monodisperse clusters. It is slightly lower than the  $2 \times 10^5 \text{ M}^{-1} \text{ cm}^{-1}$  below 550 nm reported for Ag<sub>44</sub><sup>160</sup> but higher than that of Au<sub>25</sub> ( $3.4 \times 10^3 \text{ M}^{-1} \text{ cm}^{-1}$  at 510 nm).<sup>178</sup>

The quantum yield of the clusters was determined to be 2.1–3.6 % using 4-(dicyanomethylene)-2-methyl-6-(4-dimethylaminostyryl)-4H-pyran (DCM dye) or Nile Blue A as a reference. This is somewhat lower than what was reported previously (5 % using Nile Blue A as a reference<sup>168</sup>) which may be explained by

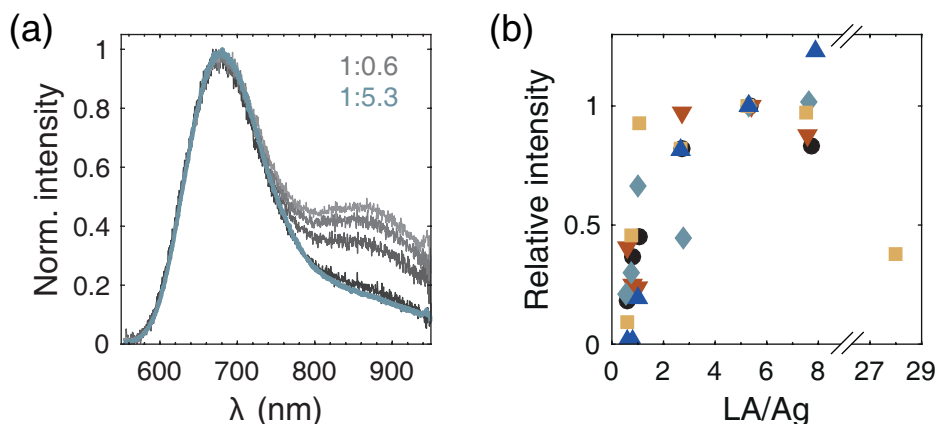


**Figure 2.3** (a) Normalised emission spectra of different samples with low ligand concentration (Ag : LA = 1 : 0.6, greyscale) and a standard sample (Ag : LA = 1 : 5.3, in blue). (b) Maximum emission intensity for samples with various Ag : LA ratios, relative to samples with Ag : LA = 1 : 5.3. Different markers represent samples prepared on different days.

the improved methodology that involved preparing a series of samples of clusters, DCM dye and Nile Blue A with different concentrations to make a calibration curve, rather than just comparing one cluster sample with one reference sample.

The quantum yield of the Ag clusters is also lower than that typically observed for clusters capped with polymers (19 %<sup>179</sup>), DNA strands (64 %<sup>180</sup>) or proteins (11 %<sup>181</sup>). However, these ligands are large, can bind to the cluster in multiple ways and can have an inherent polydispersity, all of which makes accurate cluster size determination and structure elucidation challenging. Of Ag-thiolate clusters, those capped with glutathione show especially high quantum yields, 0.8–7% for clusters with known composition and sizes between Ag<sub>10</sub>(SR)<sub>5</sub> and Ag<sub>32</sub>(SR)<sub>19</sub>.<sup>161,182,183</sup> An extraordinarily high quantum yield of 68% was also found for glutathione-capped Ag clusters, although the size and monodispersity of these clusters are unknown.<sup>184</sup> The highly monodisperse Ag<sub>44</sub>, in contrast, only has a quantum yield of 0.01%.<sup>160</sup>

The cluster synthesis can easily be scaled up (at least 5× without adapting the synthesis protocol), and works for different Ag : LA ratios (Figure 2.3). If low ligand concentrations (LA/Ag < 1) are used, the samples have weak (sometimes no) luminescence, although the NIR shoulder has a relatively high intensity. It is possible that the NIR emission originates from a surface state that is not fully passivated by ligands.

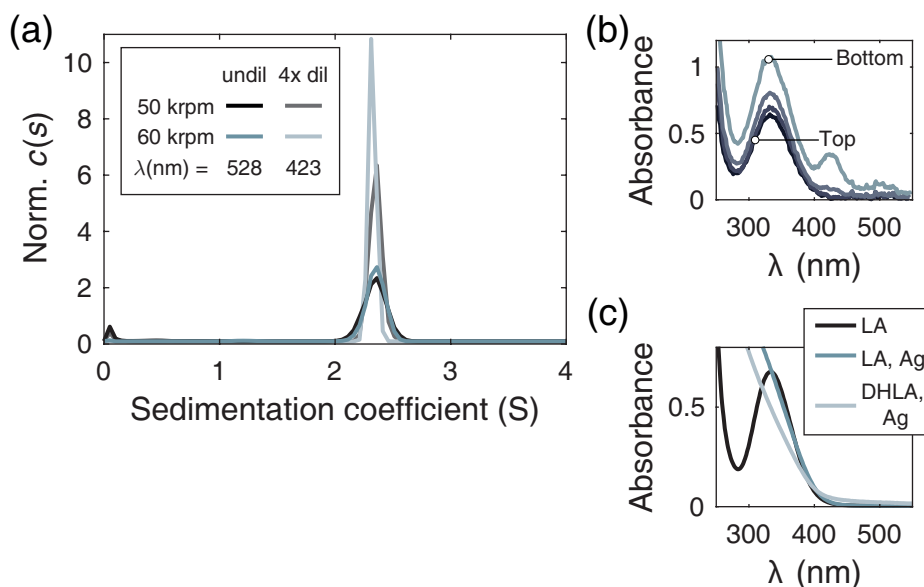


**Figure 2.4** (a) The highly monodisperse distribution of sedimentation coefficients for Ag clusters is virtually independent of dilution (undiluted and 4× diluted), centrifugation speed (50 000 and 60 000 rpm) and absorption wavelength (423 and 528 nm). At higher S-values no significant peaks were observed. The small peak close to 0 S probably originates from free ligands, as demonstrated by recording UV-Vis absorption spectra (b) in the cell after sedimentation. The pathlength of the cells for absorption is 1.2 cm. (c) UV-Vis absorption spectra of LA, LA with AgNO<sub>3</sub> and DHLA (reduced LA) with AgNO<sub>3</sub>, for comparison. The LA and DHLA samples with AgNO<sub>3</sub> have been diluted; respectively 4× and 10× relative to the LA concentration in cluster samples.

### Determination of cluster size

**Analytical ultracentrifugation** Sedimentation velocity analytical ultracentrifugation (SV-AUC) measurements were performed to study the monodispersity of the Ag clusters. Cluster solutions were measured without purification at different absorption wavelengths and rotation speeds, and with different dilution factors. The obtained distributions of sedimentation coefficients are shown in Figure 2.4. The clusters have a uniform sedimentation coefficient of 2.32–2.38 S (average 2.34 S, standard deviation 0.014 S), indicating a monodisperse species. The contribution of larger species (4–10 S) was negligible at below 1%. We expect the 2–3 nm particles previously observed with TEM to have sedimentation coefficients in this range; these are thus not present in the cluster solution but likely result from aggregation during TEM sample preparation, which involves removal of excess ligands and drying.<sup>185</sup> For all SV-AUC experiments, the frictional ratio  $f/f_0$  was 1.2–1.3, mean-

ing the clusters are not perfectly spherical. We also observed a species with an extremely low sedimentation coefficient (close to 0 S) in SV-AUC experiments. By recording absorption spectra of the upper part of the centrifugation cell at the end of the experiment, we identified this species as free LA (see Figure 2.4) and not small Ag clusters or complexes with LA or DHLA (dihydrolipoic acid, reduced LA). It can therefore be concluded that all Ag clusters are present as the 2.34 S species.

To determine the particle molar mass, we performed sedimentation equilibrium (SE) measurements of undiluted, 2× and 4× diluted Ag cluster solution at three different speeds (23 000, 35 000 and 43 000 rpm at 423, 485 and 528 nm). For undiluted samples, the data could be fitted to a single species model with one component. This species was found to have a molar mass of 6.6 kDa. For 2× and 4× diluted samples, a model with two components was used. One species was the same as for the undiluted sample, with a molar mass of 6.6–6.7 kDa. The second species was found to have a molar mass of 15.2 kDa or 26.0 kDa for 2× and 4× diluted samples, respectively. These were found to be the result of cluster aggregation due to lower stability of clusters in diluted samples (see Figure A.1 for absorption spectra of diluted clusters over time). These larger species are not present in the as-synthesised, undiluted sample. Dilution of the sample decreases the concentration of free LA which can lead to desorption of ligands from the cluster<sup>186</sup>, resulting in lower cluster stability. Indeed, we found that purified clusters, where the excess of free LA has been removed, are less stable than as-synthesised clusters (see Figure 2.13).

**Mass spectrometry** The mass of the cluster is 5604 Da, determined using electrospray ionisation (ESI) MS. This is in reasonable agreement with the 6.6 kDa determined from SE-AUC measurements. The difference could be due to the estimated value of the particle density for SE-AUC. The clusters may have a hydration layer which is observed in SE-AUC but not ESI-MS. Mass spectra, Figure 2.5, were recorded of clusters purified with 1-butanol (BuOH) and show the same features as reported earlier.<sup>168</sup> Two groups of broad ion signals, around  $m/z$  1130 and 1420, originate from the same 5.6 kDa species in the  $z = 5-$  and  $z = 4-$  charge states, respectively.

We previously identified the 5.6 kDa cluster as neutral Ag<sub>25</sub>(LA)<sub>14</sub> on the basis of good agreement of theoretical mass and observed mass of the base peak in the deconvoluted spectrum. However, a subsequent detailed analysis of the spectrum before deconvolution has shown that a more likely composition is Ag<sub>29</sub>(LA)<sub>12</sub><sup>3-</sup>. This cluster carries a charge of 3- on the core (which we define here as the S and Ag atoms and thus excludes any charges on the ligands themselves due

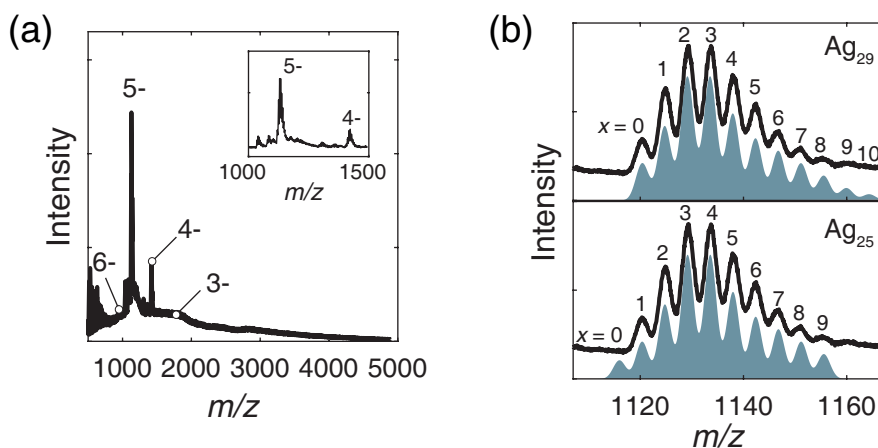


**Figure 2.5** (a) ESI-MS spectrum of Ag clusters purified with BuOH. The most intense signal is from a  $z = 5^-$  species with mass 5.6 kDa. The  $z = 6^-$ ,  $4^-$  and  $3^-$  species (around  $m/z$  930, 1400 and 1870) are also marked. A weak feature around  $m/z$  2800 could be the cluster in  $z = 2^-$  charge state. The inset shows a close-up of the  $z = 5^-$  and  $4^-$  species. (b) Experimental (black) and theoretical (colour) mass spectra of (top)  $[\text{Ag}_{29}(\text{LA})_{12}]^{3-} - (2+x)\text{H}^+ + x\text{Na}^+ ]^{5-}$  and (bottom)  $[\text{Ag}_{25}(\text{LA})_{14} - (5+x)\text{H}^+ + x\text{Na}^+ ]^{5-}$  clusters. The theoretical spectrum is shown for all possible  $x$ , where  $x$  is the number of  $\text{H}^+/\text{Na}^+$  exchanges. Theoretical spectra for each possible  $x$  have been manually scaled. Note the absence of the  $m/z$  1116 signal for  $\text{Ag}_{25}$ .

to deprotonation). Deprotonation of the carboxylic acid group and subsequent association with  $\text{Na}^+$ , termed  $\text{H}^+/\text{Na}^+$  exchange, results in the observation of multiple ion signals for the same cluster with the same overall charge. Figure 2.5 shows the theoretical mass spectrum of the cluster for all possible  $\text{H}^+/\text{Na}^+$  exchanges  $x$ , in the overall charge state  $z = 5^-$ . The total composition of this cluster can be written as  $[\text{Ag}_{29}(\text{LA})_{12}]^{3-} - (2+x)\text{H}^+ + x\text{Na}^+ ]^{5-}$ . There is excellent agreement with the experimental spectrum, while for the previously proposed composition  $[\text{Ag}_{25}(\text{LA})_{14} - (5+x)\text{H}^+ + x\text{Na}^+ ]^{5-}$  there is no experimental ion signal for the cluster with  $x = 0$  at  $m/z$  1116. Since species with low  $x$  dominate, it is unlikely that the species with  $x = 0$   $\text{Na}^+$  is not observed experimentally. To confirm the assignment of the cluster as  $\text{Ag}_{29}(\text{LA})_{12}^{3-}$ , mass spectra of clusters purified with 3 kDa centrifugal cutoff filters (Figure 2.6) were recorded. We expect that purification with the rather apolar solvent BuOH does not remove excess salts from the cluster solution, whereas purification with 3 kDa filters will, thus the two techniques should show different distributions of  $x$ . Indeed, the intensity of ion signals with low  $x$  increased when 3 kDa filters were used for purification, with the most intense ion signal at  $m/z$  1120 ( $z = 5^-$  species), which corresponds to the

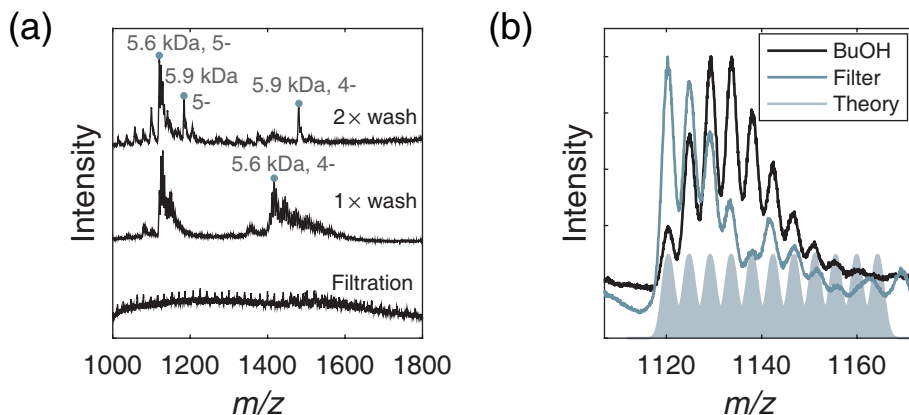


**Figure 2.6** (a) Mass spectra of clusters purified with cutoff filters, after filtration and two subsequent washing steps. (b) Close-up of the  $z = 5^-$  group of the 5.6 kDa species, after two washing steps (dark blue) compared to a BuOH purified sample (black). Also shown is the theoretical mass spectrum of  $[\text{Ag}_{29}(\text{LA})_{12}^{3-} - (2 + x)\text{H}^+ + x\text{Na}^+]^{5-}$  for all  $x$  (filled graph), without scaling of peaks for different  $x$ . The sample purified with filters shows an increase in intensity for ion signals with low  $x$ , consistent with the washing away of excess salts.

Ag<sub>29</sub> cluster with  $x = 0$  H<sup>+</sup>/Na<sup>+</sup> exchanges. No signal was observed at  $m/z$  1116 (Ag<sub>25</sub>,  $x = 0$ ). Therefore we conclude that the Ag cluster is indeed Ag<sub>29</sub>.

Note that purification with cutoff filters yields more ion signals than the BuOH purification (Figure 2.6). During purification, a number of other heavier species (up to 6.4 kDa) are also observed. After two washing steps, the 5.6 kDa species dominates but there is also a significant amount of a 5.9 kDa species. Furthermore, in the  $z = 5^-$  charge state, there appears to be a second distribution of ion signals at  $m/z$  1135–1155 where the agreement with the theoretical spectrum is not as good. It is possible that the cutoff filter method causes aggregation and/or fragmentation of the clusters.

Our assignment broadly agrees with the study of Russier-Antoine *et al.* of LA-capped Ag clusters, which were identified as neutral Ag<sub>29</sub>(LA)<sub>12</sub>.<sup>170</sup> The cluster with 3<sup>-</sup> core shows better agreement with our mass spectra than a cluster with neutral core (regardless of whether we compare with the  $z = 5^-$ , 4<sup>-</sup> or 3<sup>-</sup> overall charge states or the deconvoluted spectrum). Not only is there a slight shift between the neutral theoretical and experimental spectrum, but the ion signal at  $m/z$  1155.5 (and possibly 1160) cannot be satisfactorily explained if the cluster is neutral. The mass difference between the neutral and 3<sup>-</sup> charged core Ag<sub>29</sub>

clusters is 3 Da, which for the overall  $z = 5-$  charge state is a difference in  $m/z$  of 0.6. The resolution of the mass spectrometer (2800) is sufficiently high to resolve this. In a recently published study, Black *et al.* provided further confirmation of the 3- core charge.<sup>187</sup> The cluster has 8 electrons and is thus a magic number cluster with a closed electron shell.<sup>46</sup>

The  $\text{Ag}_{29}(\text{LA})_{12}^{3-}$  cluster also shows similarities with the recently discovered  $\text{Ag}_{29}(\text{BDT})_{12}(\text{TPP})_4^{3-}$ , where BDT is the dithiolate ligand 1,3-benzenedithiol and TPP the labile ligand triphenylphosphine.<sup>56</sup> Besides almost identical compositions and equal core charge, this cluster and our  $\text{Ag}_{29}(\text{LA})_{12}^{3-}$  have comparable absorption and emission spectra. We therefore deem it very likely that  $\text{Ag}_{29}(\text{LA})_{12}^{3-}$  has a similar structure as  $\text{Ag}_{29}(\text{BDT})_{12}(\text{TPP})_4^{3-}$ , namely an icosahedral core capped with Ag-ligand units (four  $\text{Ag}_3\text{S}_6$  crowns and four  $\text{Ag}_1\text{S}_3\text{P}_1$  units). However, in contrast to the BDT-capped cluster,  $\text{Ag}_{29}(\text{LA})_{12}^{3-}$  does not require additional stabilisation by phosphines, so the capping units might be slightly different or distorted to protect all Ag atoms. The increased stability of LA-capped clusters compared to BDT-capped clusters could be due to the presence of the carboxylic acid-terminated alkyl chain of LA, which provides additional steric and electrostatic stabilisation. Moreover, thiolate ligands may protect the metal core of a cluster in more ways than just via metal-thiolate bonding.<sup>39</sup> In Au clusters capped with 3-mercaptopbenzoic acid, weak  $-\text{OH}\cdots\text{Au}$  bonds and  $\pi-\text{Au}$  interactions were found, with a strength similar to that of a hydrogen bond. Due to these additional stabilisation effects, clusters with remarkably low ligand-to-metal ratio and stability under ambient conditions could be prepared.

The ligand-to-metal ratio is very low for these  $\text{Ag}_{29}$  clusters. Recently, a scaling law ( $L = mN^{2/3}$ ) was proposed for Au clusters to relate the number of ligands ( $L$ ) to the number of metal atoms ( $N$ ).<sup>188</sup> The coefficient  $m$  was found to be 2.08 for Au-thiolate clusters (1.82 for stable Au-thiolate clusters) while a higher coefficient (2.41) was found for  $\text{Ag}_{44}(\text{SR})_{30}^{4-}$ .<sup>189</sup> For  $\text{Ag}_{29}(\text{LA})_{12}^{3-}$ , the coefficient is extremely low (1.27), however this ignores the fact that LA can bind bidentate. If we assume bidentate bonding of all LA, the clusters can be considered as  $\text{Ag}_{29}(\text{SR})_{24}^{3-}$  with  $m = 2.54$ , which is in good agreement with what was found for  $\text{Ag}_{44}$ . In  $\text{Ag}_{29}(\text{BDT})_{12}(\text{TPP})_4^{3-}$ , bidentate bonding of all BDT ligands was observed. While this is not necessarily the case for our LA-capped clusters, the ligand-to-metal ratio indicates at least a significant fraction of bidentate ligands to ensure complete capping of the Ag surface. If the structure of the LA-capped cluster is indeed comparable to that of the BDT-capped  $\text{Ag}_{29}$  and all LA bind bidentate, this means there are 16 Ag- and 24 S-atoms in the capping layer surrounding the icosahedral core.

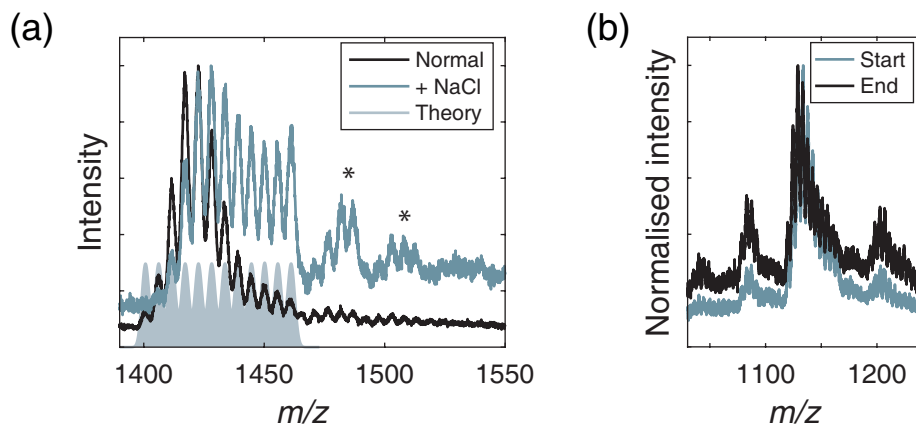


**Figure 2.7** (a) Mass spectra in the  $z = 4^-$  region of Ag clusters after purification with BuOH (black), and the same sample after addition of NaCl solution (dark blue), corresponding to an increase in  $\text{Na}^+$  concentration of 15.3 mM. The theoretical spectrum of  $\text{Ag}_{29}(\text{LA})_{12}^{3-}$  for all possible  $\text{H}^+/\text{Na}^+$  exchanges is shown in solid blue. The difference in  $\text{Na}^+$  adduct peak distribution can be clearly seen, and a number of new, heavier species are marked with an asterisk. (b) Scans at the start of the MS measurement have a higher relative intensity of the  $\text{Ag}_{29}$  signal ( $m/z$  1120–1160) than those at the end.

We occasionally observe what appears to be bidispersity, with two species showing  $\text{H}^+/\text{Na}^+$  exchange in the range  $m/z$  1120–1160. Theoretically all these ion signals could originate from  $\text{Ag}_{29}(\text{LA})_{12}^{3-}$  as they show the same  $m/z$  as this cluster. In some spectra, lighter and heavier cluster species are observed which could not be explained from the  $\text{Ag}_{29}(\text{LA})_{12}^{3-}$  composition (5.7–5.9 kDa). It is unlikely that clusters slightly bigger or smaller than  $\text{Ag}_{29}(\text{LA})_{12}^{3-}$  are present in the original sample, as size focusing would convert them to the most stable size;  $\text{Ag}_{29}$ . Therefore we expect that the observed polydispersity is to a large extent due to fragmentation or aggregation of the clusters, during purification or ionisation.

Indeed, we found that the concentration of  $\text{Na}^+$  in the purified sample affects the spectrum. This concentration may vary from sample to sample due to the purification technique, which involves extraction of water with BuOH followed by washing with methanol before the clusters are redispersed in water. Small variations in this process can result in different final  $\text{Na}^+$  concentrations. By adding  $\text{Na}^+$  in the form of NaCl solution after the purification, we investigated the effect of  $\text{Na}^+$  concentration on the spectrum (Figure 2.7). Higher  $\text{Na}^+$  concentration shifts the distribution of  $\text{Na}^+$  adduct peaks from Gaussian-like to a broader, almost bidisperse distribution. In addition, a number of heavier species appear. Recently,

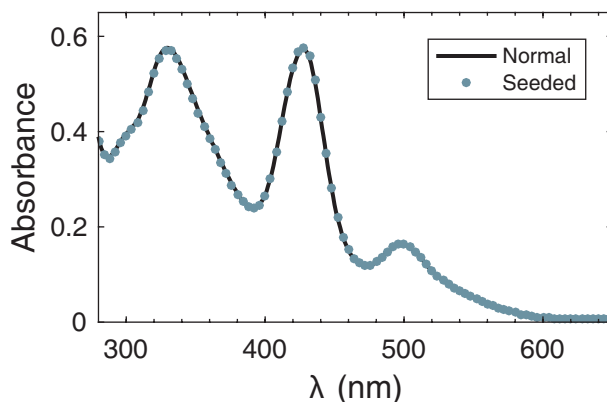


**Figure 2.8** UV-Vis spectra of a batch of clusters synthesised in the presence of existing clusters (markers) and a normal batch of clusters (line). Spectra are indistinguishable.

it was discovered that two isomers of LA-capped  $\text{Ag}_{29}$  may exist in solution<sup>187</sup>, which may be related to different ligand conformations.<sup>95</sup> Each isomer may have a different affinity for  $\text{Na}^+$ , resulting in the apparent bidispersity.

The mass spectrum also changes slightly during a measurement, which typically consists of around hundred scans. Over time, the signal-to-noise ratio usually decreased while the relative intensity of lighter and heavier species than  $\text{Ag}_{29}$  increased (Figure 2.7). The influence of heat, light or high voltage could cause degradation of the clusters in the capillary needle.

### Cluster stability, degradation and regeneration

The as-synthesised clusters are stable for many months if stored in the dark, with observable luminescence present after 18 months for some samples. The stability of the as-synthesised clusters is comparable to those prepared by Bakr *et al.*<sup>160</sup>, which were later shown to be the ultrastable and atomically monodisperse  $\text{Ag}_{44}(\text{SR})_{30}^{4-}$ , a magic number cluster with 18 electrons.<sup>23,189</sup> The stability of these  $\text{Ag}_{44}$  clusters was demonstrated by synthesising them in the presence of existing  $\text{Ag}_{44}$ .<sup>23</sup> We performed a similar experiment with our Ag clusters with the same result: rather than acting as seeds for nanoparticle growth, the pre-existing Ag clusters were inert under reductive (synthesis) conditions. The clusters prepared in presence of Ag clusters had the same absorption profile as a reference batch prepared simultaneously (see Figure 2.8). This illustrates the high stability of these clusters and how different they are from classical nanoparticles.

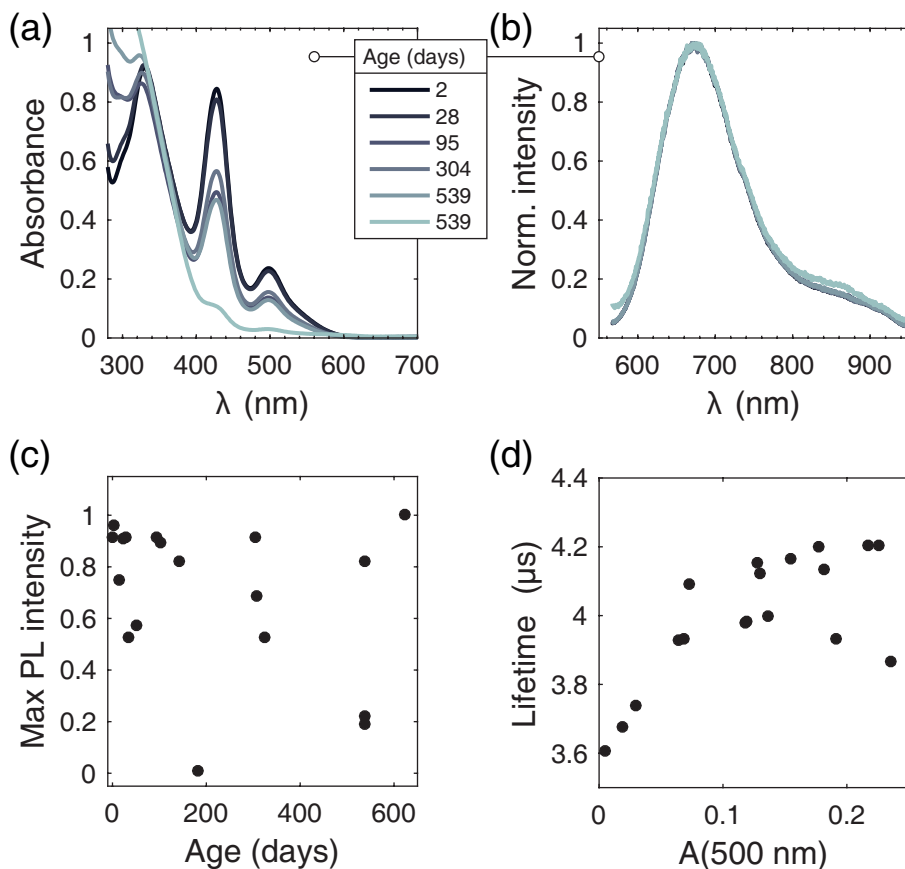


**Figure 2.9** (a) Absorption and (b) normalised emission spectra of Ag clusters at various times after synthesis (during degradation). (c) Maximum emission (PL) intensity for samples at various times after the synthesis. (d) Dependence of luminescence lifetime on the sample absorbance. Fresh samples have higher absorbance and longer luminescence lifetimes than partially degraded samples. Quenching occurs from  $A = 0.15$ .

We further investigated the stability of the  $\text{Ag}_{29}\text{LA}_{12}^{3-}$  clusters by studying their degradation over time. Fully degraded cluster solutions are clear, very pale yellow and non-luminescent. Full cluster degradation can take anything between 4 and more than 18 months, depending on the sample. We found that exposure to light and oxygen (opening the vial often) has a negative effect on sample stability, with these samples showing the shortest degradation times of just a few months.

During degradation, the luminescence intensity decreases and the peaks in the absorption spectrum become less pronounced (Figure 2.9). The shape of the emission spectrum is the same regardless of sample age, and apart from a small blueshift of the 330 nm peak, the absorption features do not shift and no new features appear during degradation. We therefore conclude that no other dominant cluster species are formed as the clusters age. UV-Vis spectra of fully degraded clusters show a decrease in absorbance with increasing wavelength which is characteristic of metal-thiolate complexes.<sup>150,190</sup> The spectrum shows no sharp absorption features (indicating monodisperse clusters) or a surface plasmon absorption (indicating plasmonic Ag nanoparticles).

The degradation coincides with a shortening in luminescence lifetime. The lifetime at 680 nm is fitted to a single exponential. We use the absorbance at 500 nm as a measure for the extent of sample degradation rather than sample age, since the latter does not take into account faster degradation due to exposure to light and air. Clusters with pronounced absorption features have luminescence lifetimes of around 4.1  $\mu\text{s}$ , while for almost fully degraded clusters the luminescence lifetime is 0.5  $\mu\text{s}$  shorter.

SV-AUC experiments (Figure 2.10) show that degraded clusters are polydisperse and larger than as-synthesised clusters, with sedimentation coefficients in the range 5–20 S. The species with 2.34 S is not observed, meaning the clusters are fully aggregated. We also performed SV-AUC experiments of an old cluster sample that was not fully degraded, and found a broad distribution around 7 S as well as a sharper distribution at 2.34 S, shown to originate from the  $\text{Ag}_{29}$  clusters. This is in excellent agreement with the UV-Vis absorption spectra where the not fully degraded clusters show the same absorption features as fresh clusters, but with lower absorbance. There is no evidence of Ag clusters that are slightly bigger or smaller than  $\text{Ag}_{29}$ . The large size,  $\sim 5$  nm, of degraded clusters is confirmed with TEM and by purification with 3 kDa centrifugal cutoff filters, where the yellow species remained on the filter. The exact composition of degraded clusters remains unknown; we could find no clear ion signals indicating the presence of species with Ag with ESI-MS.

Degraded clusters could be regenerated by the addition of  $\text{NaBH}_4$  (a similar amount as was used during the last step of the synthesis). It is thus likely

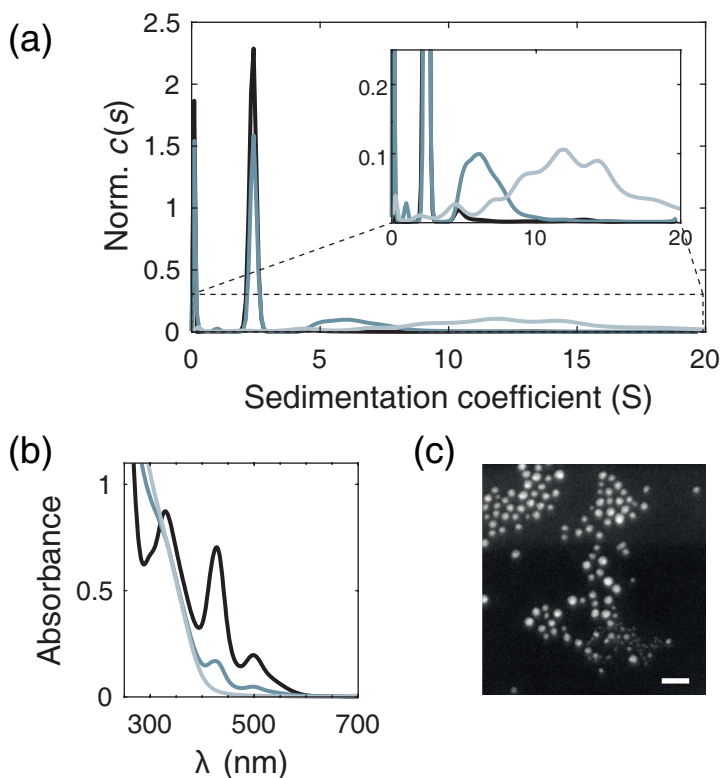


**Figure 2.10** (a) Sedimentation coefficient distributions (60 000 rpm, 395 nm) of Ag clusters at various stages during degradation. The species with sedimentation coefficient close to 0 S is free LA. Corresponding UV-Vis spectra are shown in (b); a lighter colour corresponds to a more degraded sample. (c) HAADF TEM image of fully degraded clusters. Clearly, large nanoparticles/aggregates are present. The scale bar is 20 nm.

that degraded clusters are oxidised (for example aggregates of Ag(I)-thiolates). Alternatively, degradation could be due to ligand desorption and subsequent cluster aggregation: addition of NaBH<sub>4</sub> reduces free LA to its dithiol form which could induce a size reduction for example via etching.

Regenerated clusters have the same absorption and emission features as freshly prepared clusters and similar size distributions (Figure 2.11). Regenerated clusters were characterised with SV-AUC and ESI-MS. SV-AUC shows that regenerated clusters have the same sedimentation coefficient and narrow size distribution as fresh clusters. We were unable to purify regenerated clusters with BuOH for ESI-MS. Once the last water had been extracted with BuOH and the clusters sedimented, they became brownish and could not be redispersed in water. However, mass

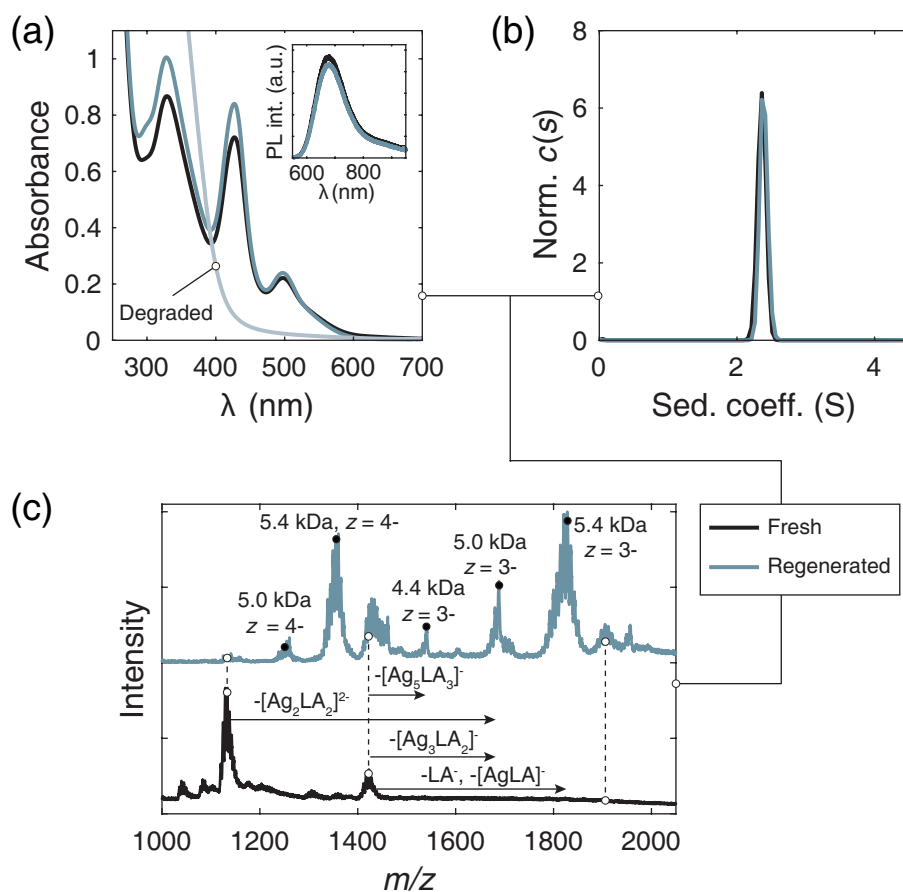


**Figure 2.11** Comparison of optical properties and size distributions of freshly prepared and regenerated clusters. (a) UV-Vis absorption spectra, showing also the spectrum of a fully degraded sample (inset: emission spectra, excitation wavelength 420 nm). (b) Sedimentation coefficient distributions (60 000 rpm, 528 nm) (c) Mass spectra (fresh clusters were purified using BuOH, regenerated clusters with 3 kDa filters).  $\text{Ag}_{29}(\text{LA})_{12}^{3-}$  clusters, mass 5.6 kDa, in  $z = 5-$ ,  $4-$  and  $3-$  overall charge states are marked with vertical dashed lines. A number of lighter species are also observed (marked with black circles). The arrows and text show how these lighter species can be formed from the  $\text{Ag}_{29}$  cluster (the species with  $z = 4-$  are the same, but for clarity arrows are only shown for  $z = 3-$ ).

spectra of regenerated clusters purified with 3 kDa filters confirm the presence of Ag<sub>29</sub>(LA)<sub>12</sub><sup>3-</sup>. In addition, we observe a number of slightly lighter species (around 5.0 and 5.4 kDa, identified in Figure A.2). Fresh clusters appeared more polydisperse in ESI-MS when purified with 3 kDa filters than with BuOH (Figure 2.6), so it is possible that these lighter species are formed during purification.

While the initial synthesis of the Ag<sub>29</sub> clusters involves reduction of AgNO<sub>3</sub>, cluster regeneration appears to proceed via a top-down route by reducing larger, oxidised species. The same luminescent species are formed in both cases which is evidence for the stability of our clusters and high affinity of LA for Ag. The strong bonding of LA to Ag (and also to Au) has been demonstrated in several studies where luminescent Ag (or Au) clusters are prepared from nanoparticles ( $\approx 5$  nm) which are etched to clusters by addition of LA,<sup>73,191,192</sup> a process which could be similar to the regeneration of our degraded clusters. The initial synthesis of Ag<sub>29</sub> will be discussed in more detail in Chapter 3.

Regeneration has been demonstrated earlier for DNA-capped Ag clusters<sup>180</sup> and selenolate-capped Ag<sub>44</sub> clusters.<sup>193</sup> Interestingly, the authors of the latter study report that regeneration was not successful for thiolate-capped Ag<sub>44</sub> clusters and that larger nanoparticles were formed instead. We could find no reports in the literature of any fully reversible degradation of thiolate-capped Ag clusters, suggesting that LA-capped clusters could be unique in this respect. The high LA/Ag ratio ( $\approx 5$ ) could be a contributing factor to the success of regeneration. When LA/Ag < 1, the cluster stability is decreased and the samples become non-luminescent within weeks. Degraded clusters with such a low LA concentration were somewhat darker than the standard degraded clusters. While regeneration by NaBH<sub>4</sub> is still possible, optical properties of regenerated clusters appear not to be fully recovered, although this might be partially attributed to the lack of reproducibility of cluster synthesis with low LA concentration. If regeneration is performed with both NaBH<sub>4</sub> and LA, the optical properties resemble that of a freshly prepared Ag : LA = 1 : 5.3 batch. Addition of only LA is not sufficient for cluster regeneration. Absorption and emission spectra are shown in Figure 2.12.

**Stability of purified clusters.** Purification of clusters with BuOH affects their stability. Absorption, emission and mass spectra of the clusters were recorded before and at several times after purification, see Figure 2.13. Shortly after purification, there are no changes in the emission spectrum and the absorption spectrum shows only minor differences (comparable to differences between different batches of clusters). Thus, the luminescent species is not influenced directly by the purification and this method is suitable for purification of samples for MS.

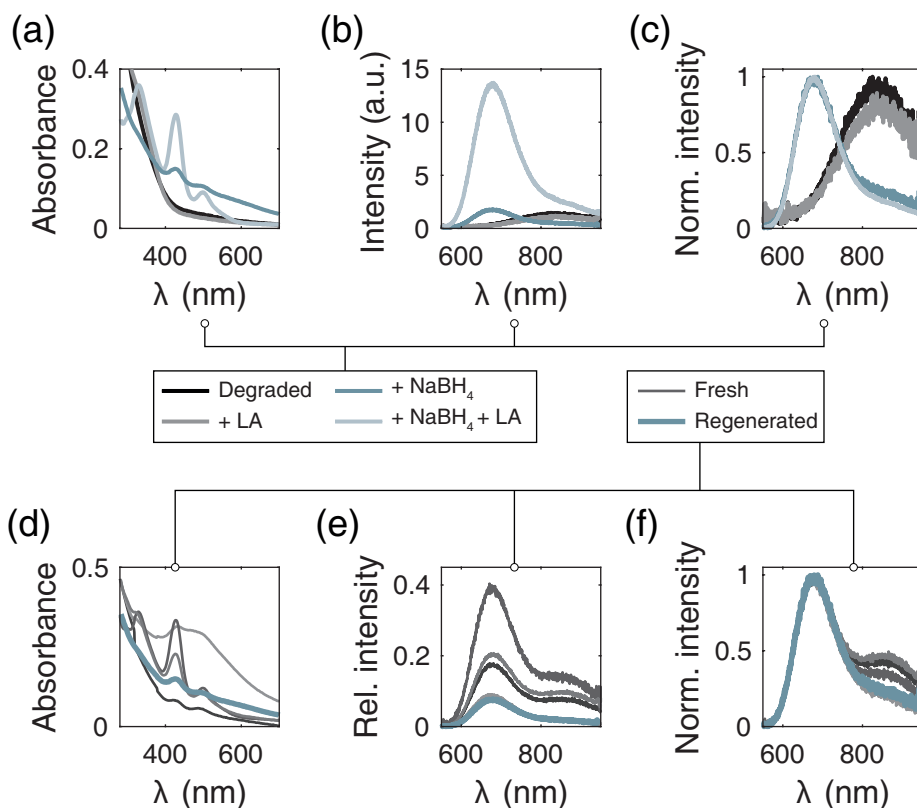


**Figure 2.12** (a) Absorption, (b) emission and (c) normalised emission spectra of degraded clusters with Ag : LA = 1 : 0.6, and these clusters after regeneration with respectively LA, NaBH<sub>4</sub>, and LA + NaBH<sub>4</sub>. The integration time of the CCD detector was 10× as long for degraded clusters and degraded clusters with LA than for the other two samples. The optical properties of clusters regenerated with just NaBH<sub>4</sub> are in reasonable agreement with those of freshly prepared Ag : LA = 1 : 0.6 clusters, as shown in (d), (e) and (f) which show absorption, emission and normalised emission spectra, respectively. Emission spectra (e) are divided by the emission maximum of a freshly prepared Ag : LA = 1 : 5.3 sample prepared on the same day to account for any variations in lamp intensity or differences in measurement protocol. Spectra of the freshly prepared Ag : LA = 1 : 0.6 clusters are plotted in greyscale, while spectra of regenerated clusters are shown in colour with a thicker line.

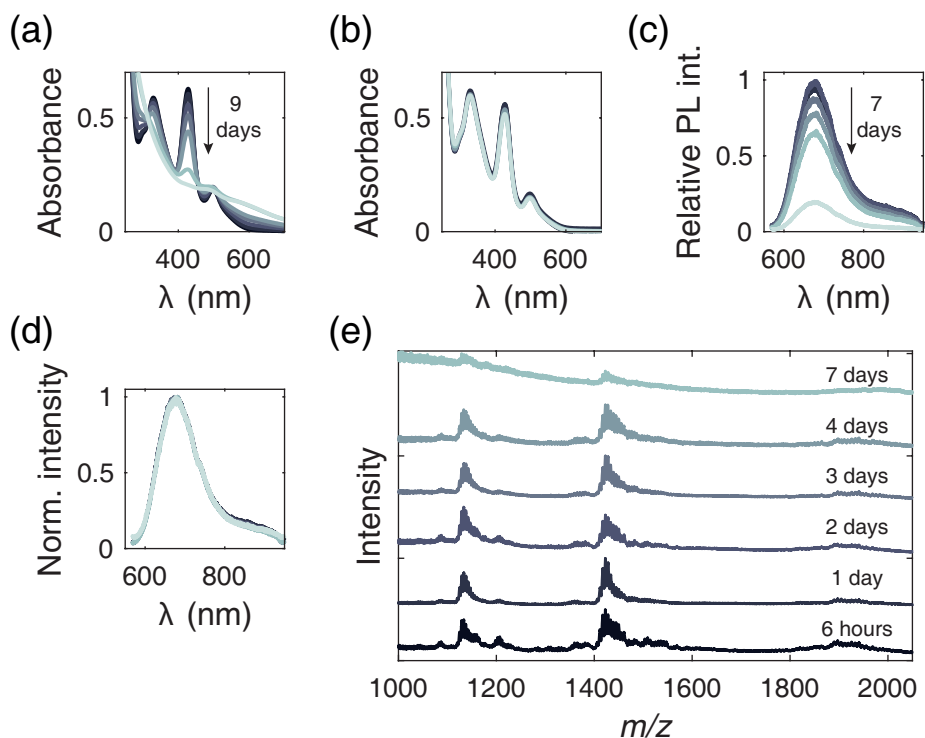


**Figure 2.13** UV-Vis absorption spectra of (a) BuOH purified and (b) as-synthesised clusters, recorded each day after purification. (c) Emission intensity of purified clusters over time, relative to that of an as-synthesised sample measured on the same day. The intensity decreases, but the shape of the emission peak (d) does not change. (e) Mass spectra of Ag cluster sample at various times after purification, shifted vertically for clarity. The signal of the 5.6 kDa clusters ( $m/z= 1120$  and  $1400$ ) is almost gone after 1 week.

Within a few days, the purified cluster solution turns brown and the pronounced peaks in the absorption spectrum gradually disappear. This coincides with a drop in emission intensity, to around 20% of the original value after one week. However, the shape of the emission peak does not change. This is strong evidence for the presence of a single luminescent species and thus high monodispersity of the clusters, as was also found with SV-AUC.

Along with the disappearance of characteristic optical properties, the relative intensity of the ion signals corresponding to  $\text{Ag}_{29}(\text{LA})_{12}^{3-}$  increases at first but then it decreases and is barely discernible over the background after 1 week. This is further evidence that  $\text{Ag}_{29}(\text{LA})_{12}^{3-}$  is the luminescent species. However, it is not possible to directly correlate a decrease in MS signal intensity to the changes

in optical properties, as mass spectrometry is not a quantitative technique and various factors such as the stability of the capillary spray varied from day to day. Note that we have been unable to identify the product of the degradation process of the purified clusters with ESI-MS, although we expect the formation of larger species as observed for as-synthesised clusters. The lower stability of purified clusters can be explained by an equilibrium between bound and free LA. Removal of excess ligands would thus lead to ligand desorption.

## 2.4 Conclusions

In conclusion, we have prepared stable, luminescent Ag clusters with high monodispersity. The combination of mass spectrometry, optical spectroscopy and analytical ultracentrifugation has allowed us to unequivocally identify a 5.6 kDa species (assigned to  $\text{Ag}_{29}(\text{LA})_{12}^{3-}$ ) as the luminescent cluster. We found no evidence of other cluster sizes at different times after synthesis or purification. Over time, the clusters degraded resulting in loss of luminescence, but the luminescent clusters could easily be regained by addition of  $\text{NaBH}_4$ . The reversibility of cluster degradation has not been previously observed for thiolate-capped Ag clusters. The high monodispersity and quantum yield of the  $\text{Ag}_{29}$  cluster makes it a candidate for both fundamental studies into the origin of luminescence<sup>91</sup> and for potential applications<sup>194</sup>, for example in bioimaging.

## 2.5 Acknowledgements

We thank Dominique Thies-Weesie for analytical ultracentrifugation measurements and data analysis, Arjan Barendregt for help with mass spectrometry measurements, and Marcel Verheijen for recording TEM images of degraded clusters. Andries Meijerink and Patrick Chin are thanked for useful discussions. This work was financially supported by the Debye Graduate Programme (The Netherlands Organisation for Scientific Research, NWO, project 022.004.016), and ESRF Graduate Programme; the mass spectrometry research was performed within the framework of NWO and supported by the large scale proteomics facility Proteins@Work (project 184.032.201) embedded in The Netherlands Proteomics Centre.



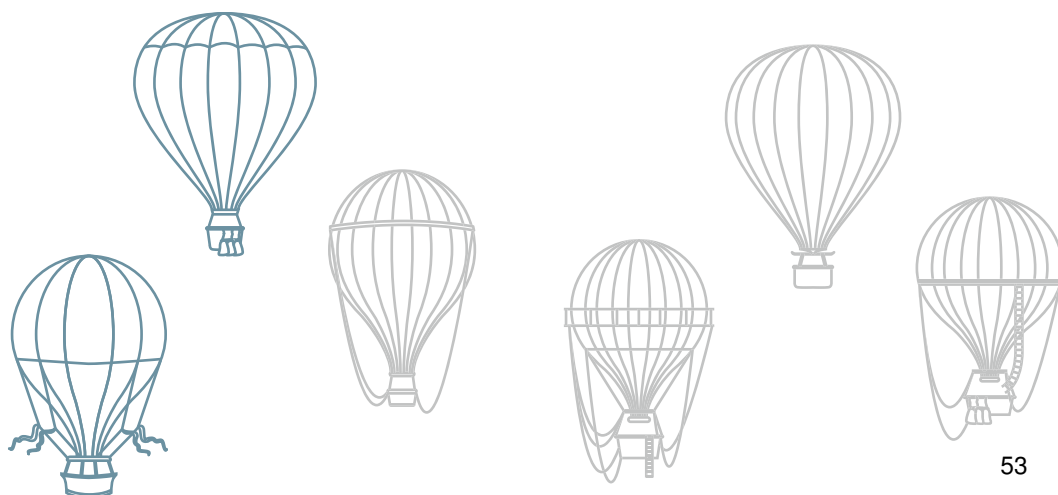
## Synthesis mechanism of Ag<sub>29</sub> clusters

---

### Abstract

Ag<sub>29</sub> clusters capped with lipoic acid can be prepared according to a simple synthesis protocol without any additional purification to achieve atomic monodispersity. Using optical spectroscopy, mass spectrometry and X-ray spectroscopy, it was determined that the synthesis involves a rapid nucleation and growth to species with up to a few hundred Ag atoms. From these larger species, Ag<sub>29</sub> clusters are formed and their concentration increases steadily over time. Oxygen plays an important role in the etching of large particles to Ag<sub>29</sub>. No other stable Ag cluster species are observed at any point during the synthesis.

---



*"Scientific progress goes boink?"*

---

— Bill Waterson, *Calvin & Hobbes*:  
*Scientific Progress goes boink*

### 3.1 Introduction

It is of great interest to prepare atomically monodisperse clusters in bulk quantities and with high yields, preferably without resorting to multi-step reactions or extensive purification protocols. To date, this has been achieved for a number of highly stable magic number gold and silver clusters, notably Ag<sub>44</sub><sup>23,55,195</sup> and Au<sub>25</sub><sup>22,77</sup>. New synthesis protocols are constantly being developed and improved so that increasingly, also less stable sizes can be more easily obtained. For example, the cluster Au<sub>18</sub>(SR)<sub>14</sub> was at first only prepared in a mixture with multiple different sizes and had to be isolated using gel electrophoresis.<sup>150</sup> More recently, a pH controlled reduction method was developed, which directly yielded the monodisperse cluster in high quantities.<sup>196</sup> Knowledge of the mechanisms of cluster synthesis have made this progress possible.

Studies of cluster synthesis have focused on Au, while less is known about the synthesis mechanisms of Ag clusters. For Au clusters, there are a number of factors that can influence the product(s) obtained from a reaction. These include reaction temperature<sup>76</sup>, solvent<sup>78,197,198</sup> and even stirring speed<sup>79,199</sup>. While at first glance this may seem like the development of a good synthesis protocol is more art than science, some general principles have been established.

It is commonly accepted that the synthesis of clusters proceeds via a kinetically controlled reduction reaction. The precursor for cluster synthesis is usually a simple metal salt such as AgNO<sub>3</sub> or HAuCl<sub>4</sub> which is mixed with thiols in solution. For Au clusters, it has been shown that a reaction occurs already at this step to give a synthesis intermediate. This is thought to consist of aggregates of Au(I)-thiolates<sup>30,76,200–202</sup>, although recent work has suggested that [Au(I)X<sub>2</sub>]<sup>-</sup> complexes, where X is a halide, are more likely to form in organic solvents.<sup>203</sup>

After formation of the synthesis intermediate, a reducing agent (often NaBH<sub>4</sub>) is added to reduce the metal ions. Nucleation occurs, followed by growth. A large number of different cluster and nanoparticle species may be formed. The solution is then aged to obtain the final product. This may involve a change in synthesis conditions such as a change of solvent and addition of a different ligand to etch clusters to the desired size.<sup>197</sup> During ageing, thermodynamics becomes of great importance. Some species are inherently less stable than others, and due to the dynamical nature of clusters they will slowly convert to the more stable species.

These are the final products of the reaction. This spontaneous process is called size focusing.<sup>30,80,204</sup> To obtain a different product, the initial size distribution of clusters can be changed. This can be done for example by changing the solvent, temperature or stirring speed. These parameters influence the rate of the reduction, but also (for gold) the extent of aggregation of the Au(I)-thiolate intermediate.<sup>76</sup>

In this chapter, we investigate the synthesis of Ag clusters with lipoic acid (LA), identified as  $\text{Ag}_{29}(\text{LA})_{12}^{3-}$  in Chapter 2. Its straightforward, highly reproducible synthesis which achieves atomic monodispersity without any purification makes it an ideal candidate for a detailed investigation. Once the synthesis starts, there are no further changes to the reaction mixture. These clusters can be formed via a bottom-up approach using  $\text{AgNO}_3$ , as shown in Chapter 2, but also via a top-down method by etching larger nanoparticles with excess LA.<sup>73</sup> It may be that similar size focusing mechanisms occur in both cases.

The formation of  $\text{Ag}_{29}(\text{LA})_{12}^{3-}$  is studied using optical spectroscopy, mass spectrometry and X-ray absorption spectroscopy (XAS). XAS is found to be an especially useful technique, as it is element-specific and does not require extensive sample purification which may affect the compositions of the clusters. A XAS spectrum is usually divided in two regions; the Extended X-ray Absorption Fine Structure (EXAFS) and X-ray Absorption Near Edge Structure (XANES). From EXAFS, one can identify the nature of ligands, their coordination number and bond lengths. XANES gives information about the electronic structure, including oxidation numbers.<sup>102,103</sup> Both techniques are used to study the formation of  $\text{Ag}_{29}$  clusters in this chapter.

The nucleation and initial growth are too rapid to observe with any detail. However, we determine that within minutes of reduction, large clusters or nanoparticles with a hundred or more Ag atoms are present. Size focusing to  $\text{Ag}_{29}$  then occurs, possibly via  $\text{Ag}_{28}$  and  $\text{Ag}_{26}$ . The remarkable stability of  $\text{Ag}_{29}$  clusters is an important factor in their successful synthesis. The conversion of  $\text{Ag}_{\sim 100}$  to  $\text{Ag}_{29}$  likely proceeds via an etching mechanism where oxygen plays an important role.

## 3.2 Experimental methods

### Chemicals

$\text{AgNO}_3$  was obtained from Fisher Scientific (laboratory reagent grade) or Sigma Aldrich ( $\geq 99.0\%$ ).  $\text{NaBH}_4$  (99%), ( $\pm$ )- $\alpha$ -lipoic acid ( $\geq 99\%$ ), methanol ( $\geq 99.9\%$ ), Ag powder ( $\geq 99.9\%$ ) and silver diethyldithiocarbamate (99%) were purchased from Sigma Aldrich. 1-Butanol (99.5%) was obtained from Acros. Water was of Milli-Q quality, purified using a Millipore Direct-Q 3 water purification system.

### Synthesis

The synthesis of the Ag clusters is adapted from the literature.<sup>86</sup> 19 mg lipoic acid (92  $\mu\text{mol}$ ) and 7 mg NaBH<sub>4</sub> (185  $\mu\text{mol}$ ) were placed in a 40 or 20 mL glass vial with 14 mL water. This was stirred (using a magnetic stirring bean) until all LA had dissolved. Next, 700  $\mu\text{L}$  25 mM AgNO<sub>3</sub> (17.5  $\mu\text{mol}$ ) was added (the solution turned turbid), followed by 10 mg NaBH<sub>4</sub> (264  $\mu\text{mol}$ ) in 2 mL water. The vial was wrapped in aluminium foil to minimise the exposure of the clusters to light. The synthesis was performed at room temperature and magnetic stirring was continued throughout. For X-ray spectroscopy experiments, the synthesis was scaled up 5 $\times$  without any further modifications to the protocol.

### Optical spectroscopy

UV-Vis spectra were recorded using a Perkin Elmer Lambda 950, a Perkin Elmer Lambda 40 or a Varian Cary 50 spectrometer. Emission spectra were recorded with a Spex 1680 (0.22 m) double beam spectrofluorometer equipped with a liquid nitrogen cooled Acton Research SpectraPro 300i CCD camera. The CCD camera was equipped with a 150 lines/mm grating blazed at 800 nm.

### Mass spectrometry

MS measurements were performed in negative ion mode using an electrospray ionisation time-of-flight (ESI-ToF) instrument (LC-T; Micromass, Manchester, U.K.) equipped with a Z-spray nano-electrospray ionisation source. Needles were made from borosilicate glass capillaries (Kwik-Fil, World Precision Instruments, Sarasota, FL) on a P-97 puller (Sutter Instruments, Novato, CA), coated with a thin gold layer by using an Edwards Scancoat (Edwards Laboratories, Milpitas, CA) six Pirani 501 sputter coater. After purification, the sample was sprayed into the mass spectrometer. The applied voltage on the needle was 1180 V and the sample cone voltage was varied between  $-5$  and 0 V to measure intact clusters. All spectra were mass calibrated in negative ion mode, using an aqueous solution of phosphoric acid (0.1 % v/v). Theoretical mass spectra were calculated using ChemCalc<sup>151</sup> with full width at half maximum = 1. In calculating theoretical mass spectra, we assume that neither of the two S-atoms in LA is present as a thiol (thus LA is C<sub>8</sub>H<sub>14</sub>O<sub>2</sub>S<sub>2</sub>).

For mass spectrometry, samples were purified using 1-butanol (BuOH) to extract water, containing excess ligands and other possible contaminants, until the clusters sediment, after which they are washed with a small amount of methanol (MeOH) and redispersed in water. This is done by mixing 300  $\mu\text{L}$  cluster solution, 400  $\mu\text{L}$  BuOH and 100  $\mu\text{L}$  MeOH in an Eppendorf vial. The vial was briefly centrifuged to speed up phase separation, and the upper colourless organic layer was removed. Next, 300  $\mu\text{L}$  BuOH was added, the vial was shaken and centrifuged, and the organic layer was again removed. This was repeated until the clusters just sedimented. Typically, 3–5 extractions with BuOH were needed. After removing the final organic layer and washing with MeOH (50–100  $\mu\text{L}$ ), the clusters were redispersed in water (50–100  $\mu\text{L}$ ).

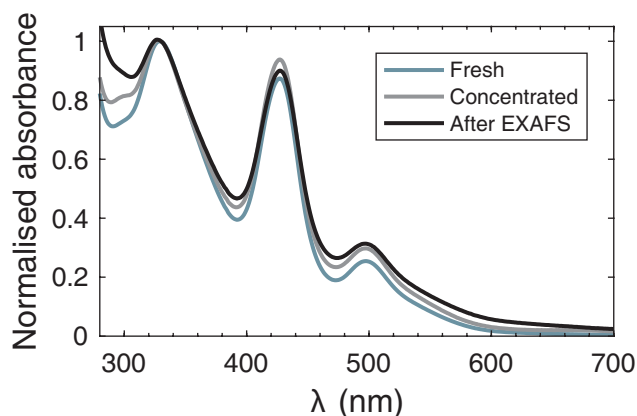


**Figure 3.1** UV-Vis absorption spectra of freshly prepared  $\text{Ag}_{29}$  clusters (blue) compared to clusters that have been concentrated with cutoff filters and exposed to X-rays (black), and clusters that have only been concentrated (grey). Damage to clusters due to X-ray exposure or concentration is limited. Spectra are normalised at 330 nm.

### EXAFS

Ag K-edge EXAFS (25.51 keV) was measured at BM26A (DUBBLE) of the European Synchrotron Radiation Facility.<sup>205</sup> The incident beam was selected using a Si(111) monochromator. The measurements were performed in fluorescence mode using an 8 element Ge detector. Samples were measured in capillaries (Hilgenberg, 2 mm outside diameter, article no. 4007620).

To accurately determine the coordination numbers of as-synthesised Ag clusters, we recorded EXAFS of concentrated Ag cluster solution prepared a few days before the measurement. The clusters were concentrated around  $5\times$  using 3 kDa cutoff filters (Amicon, Millipore), then measured for 30–60 min (4 scans). After this, a new sample was prepared and measured. This was done in order to avoid radiation damage. The final spectrum was averaged over 25 spectra taken from seven freshly concentrated aliquots of the same batch of clusters.

After recording EXAFS, we removed one sample from the capillary and recorded a UV-Vis absorption spectrum to determine the extent of radiation damage. To distinguish between the influence of the concentration process and the exposure to X-rays, we also recorded an absorption spectrum of clusters that had been concentrated and then stored in the lab for around an hour. Results are shown in Figure 3.1. It is clear that both concentration and X-ray exposure make the absorption peaks only slightly less pronounced, so we consider radiation damage to be limited.

EXAFS during synthesis was recorded by taking aliquots at regular intervals. Each aliquot was measured for no more than 60 min. As the synthesis is ongoing, the sample

compositions will change somewhat during this time, and this is the reason we did not measure for longer times. In combination with the low Ag concentration (1 mM), this means the EXAFS data are rather noisy. To check for radiation damage, the aliquots were kept after EXAFS measurement. Around 9 h after addition of NaBH<sub>4</sub>, when the synthesis is finished, all aliquots were found to luminescence red under a UV-lamp, showing that luminescent Ag<sub>29</sub> clusters were formed despite exposure to X-rays.

**EXAFS analysis** EXAFS analysis was done using VIPER<sup>206</sup>, and the Athena and Artemis<sup>207</sup> software packages. Scattering phases and amplitudes were calculated using FEFF for a number of different compounds, including Ag and Ag<sub>2</sub>S, coordinates of which were obtained from the Inorganic Crystal Structure Database<sup>208</sup> (numbers 44387 and 44507, respectively), as well as Ag<sub>29</sub>(BDT)<sub>12</sub>(TPP)<sub>4</sub><sup>56</sup>, with TPP (triphenylphosphine) ligands removed and BDT (1,3-benzenedithiol) replaced by LA. A geometry optimisation of this structure was done in Avogadro<sup>209</sup>, keeping Ag and S atoms frozen, to ensure reasonable C–C and C–H bond lengths and angles.

One Ag–Ag and one Ag–S path were used in the fit. Typical fit parameters for as-synthesised clusters were:  $k = 3.0\text{--}12.5 \text{ \AA}^{-1}$ ,  $R = 1.0\text{--}3.2 \text{ \AA}$ , using a Hanning window ( $dk = 1 \text{ \AA}^{-1}$ ) for the Fourier Transformation. Fitting was done using  $k = 3$  weighting in VIPER and  $k = 1, 2, 3$  weighting in Artemis. The compound from which the scattering path was calculated had a minor effect on the fit, as had the fitting software and parameters. Clusters during synthesis were measured over a shorter  $k$ -range,  $k = 3.0\text{--}8.15 \text{ \AA}^{-1}$ , and  $R = 1.0\text{--}3.45 \text{ \AA}$ . To determine coordination numbers during synthesis, a number of parameters of the two scattering paths were fixed to that of as-synthesised clusters; such as bond lengths or Debye-Waller factors, or both.<sup>210</sup> A number of fits showed unreasonable parameters, such as negative Debye-Waller factors or extremely short bond lengths. These fits were discarded and excluded from further analysis. Regardless of whether none, two or four parameters were fixed in the fit, the results show similar trends.

The amplitude reduction factor  $S_0^2$  was not explicitly taken into account during fitting (that is,  $S_0^2 = 1$  was used). However, from fitting a reference Ag sample, it may be estimated,  $S_0^2 = 0.9$ .

## XANES

Ag L<sub>3</sub>-edge XANES (3.35 keV) was recorded at beamline ID26 at the European Synchrotron Radiation Facility. The incident beam was selected using the (111) reflection from a double Si crystal monochromator. X-ray fluorescence was collected at a 90° angle using a silicon drift diode detector (Ketek).

The synthesis (5× normal scale) was carried out in a vial from which liquid was pumped through a 1.5 mm capillary to form a free-standing liquid jet which was placed in the focus of the beam. Below the jet, the liquid was collected and returned to the synthesis vial. To avoid attenuation of X-rays through air, the jet was run through a chamber filled with helium. The chamber had a kapton window on one side for the incoming X-ray beam, and

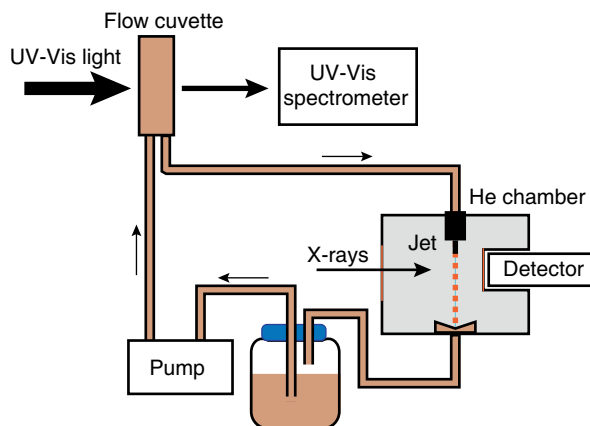


**Figure 3.2** Liquid jet setup with continuous flow for recording X-ray absorption spectroscopy in a He atmosphere. The sample is pumped from the reservoir first through a flow cuvette to record UV-Vis spectroscopy, then through a capillary nozzle to form a freestanding jet in a chamber with He, where X-ray spectroscopy can be measured. Note that this was done in fluorescence mode, at an angle of  $90^\circ$  to the incoming beam.

another where the detector was placed. Pumping and purging with He was required to avoid absorption by argon present in air (K-edge 3.21 keV). The slight overpressure of He in the chamber resulted in saturation of the Ag cluster solution with He, which we believe was beneficial in preventing radiation damage.

To monitor sample changes, we also recorded UV-Vis absorption spectroscopy by pumping the solution through a Hellma 3-in-1 flow cuvette (product nr 176-766-15-40, 2 mm path length) which was built into the circuit just before the capillary. The excitation source was an Ocean Optics DH-2000-BAL lamp equipped with an Ocean Optics FVA-UV fibre optic variable attenuator, and transmitted light was detected using an Ocean Optics Maya 2000 Pro spectrometer. The attenuator was positioned between the lamp and flow cuvette to decrease the intensity of UV-Vis light, which was necessary to avoid saturation of the spectrometer. By recording a blank and dark spectrum, the absorbance of the sample was immediately calculated by the software (SpectraSuite). A schematic figure of the setup is shown in Figure 3.2.

Despite exposure to X-rays for 7 h, the change in UV-Vis absorption spectra was minimal. This was in contrast to what was observed when the same liquid jet setup was used without He chamber, in an attempt to record Ag K-edge EXAFS (25.51 keV). Then, the sample darkened noticeably and absorption features had all but disappeared after the same time.

Reference compounds were measured as solids. They were mixed with boron nitride, using around 15 mg compound for 40 mg boron nitride for  $\text{AgNO}_3$ ,  $\text{Ag}_2\text{O}$  and silver diethyldithiocarbamate. Ag was diluted twice as much. After mixing, the samples were spread thinly on kapton tape before being measured in a cryostat (KONTI, CryoVac) cooled with liquid He. The typical operating temperature was 40 K. Sample preparation and

measurement of Ag<sub>2</sub>S was done by mixing 4 mg of the compound with 50 mg cellulose and pressing it into a 13 mm diameter pellet. The spectrum was recorded at room temperature in the He chamber. No significant radiation damage was observed, but nevertheless as a precaution, multiple spots on each sample were measured.

**XANES analysis** Detectors for XAS may suffer from loss of counts due to detector deadtime; a period of time after the arrival of a photon where the detector is inactive and does not process any other incoming photons. The outgoing count rate (OCR) of the detector is therefore lower than the incoming count rate (ICR), giving an observed intensity  $I_{\text{obs}}$  that is lower than the true intensity. The detector deadtime is energy dependent and can therefore change the spectral shape. All XANES spectra were corrected for deadtime to obtain the corrected intensity  $I_{\text{corr}}$ , according to<sup>211</sup>:

$$I_{\text{corr}} = I_{\text{obs}} \frac{\text{ICR}}{\text{OCR}} \quad (3.1)$$

Scans with a high deadtime,  $(\text{ICR} - \text{OCR})/\text{OCR} \geq 25\%$ , were not used, as the correction method becomes increasingly inaccurate. In addition, all spectra were normalised for incident intensity.

The experimental spectrum of Ag<sub>29</sub> clusters was compared to spectra of reference compounds, as well as spectra calculated using FEFF 9.6<sup>106</sup> and FDMNES<sup>120</sup>. The structure of the cluster was taken from that of Ag<sub>29</sub> protected with BDT<sup>56</sup>, where the phosphine ligands were removed and the BDT was replaced by LA. A geometry optimisation of this structure was done in Avogadro<sup>209</sup>, keeping Ag and S atoms frozen, to ensure reasonable C–C and C–H bond lengths and angles. For FDMNES, the calculation was done of all 29 Ag atoms in the cluster, using a radius of 6 Å for each calculation. Atomic potentials, Fermi level, and charge transfer were calculated self-consistently and the finite difference method was used to calculate potentials.<sup>212,213</sup> Relativistic effects were taken into account. The spectrum was convoluted to apply an energy-dependent broadening, using default parameters (an arctangent function). The width of the core-hole was decreased slightly to 1.50 eV to better match the experimental data. FEFF calculations were done for four different Ag atoms in the cluster; the central atom (1 site), one in the icosahedral shell (12 sites), one in an Ag<sub>3</sub>S<sub>6</sub> crown (12 sites) and one external Ag atom (4 sites). The final spectrum was taken as the weighted average of these. Calculations were done using a screened (FSR) core-hole, Hedin-Lundquist exchange model, full multiple scattering (FMS, radius 6 Å) and self-consistently calculated potentials (SCF, radius 4 Å). For both FEFF and FDMNES calculations, only dipole transitions are considered ( $\Delta l = \pm 1$ ). The individual contributions to the spectrum of d and s final states,  $\Delta l = +1$  and  $-1$ , respectively, were also calculated with FDMNES, using the *lplus1* and *lminus1* cards.

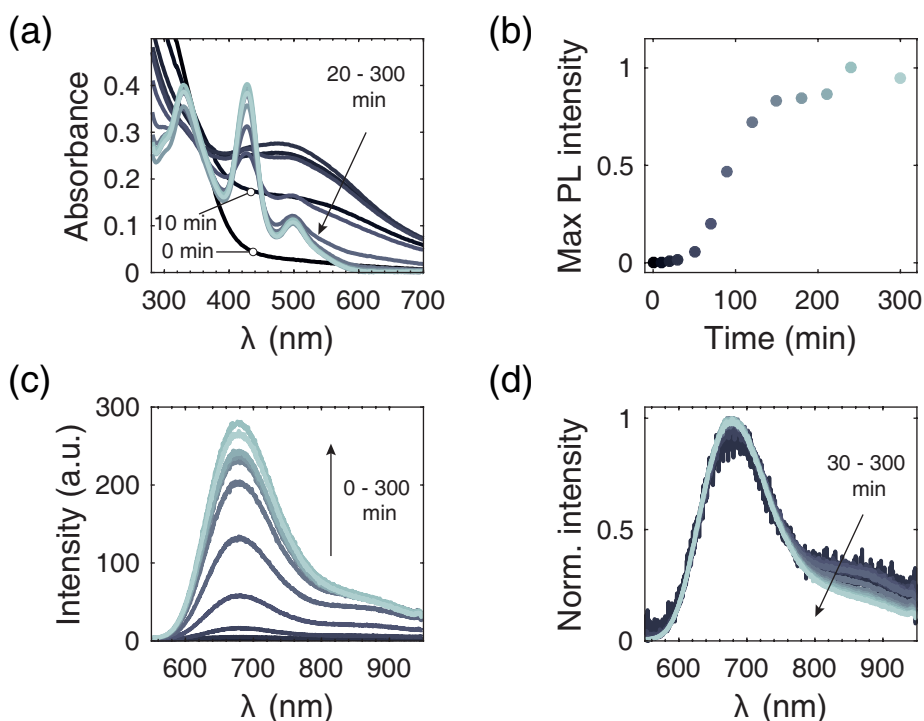


**Figure 3.3** Optical properties of Ag<sub>29</sub> clusters during synthesis. At  $t = 0$ , NaBH<sub>4</sub> is added. (a) UV-Vis absorption spectra. (b) Maximum emission intensity over time. (c) Emission spectra (excitation wavelength 420 nm). (d) Normalised emission spectra. The first appearance of characteristic absorption features of Ag<sub>29</sub> (at 330, 425 and 500 nm, after 50 min) coincides with the emergence of red luminescence. During the synthesis, the relative intensity of the NIR shoulder decreases.

### 3.3 Results and discussion

#### Synthesis of Ag<sub>29</sub> studied with optical spectroscopy

The synthesis process of Ag<sub>29</sub> clusters involves the addition of AgNO<sub>3</sub> to an aqueous solution of LA and NaBH<sub>4</sub>; the latter being added to deprotonate LA and reduce it to dihydrolipoic acid (DHLA), thus making it water-soluble. This solution is pale yellow and turbid. Subsequently, more NaBH<sub>4</sub> was added to reduce the silver ions. Within minutes of this, the solution turned dark, then gradually lightened to bright, reddish orange. The final cluster solution shows strong red luminescence and characteristic absorption features at 330, 425 and 500 nm. In total, the synthesis process takes  $\sim 6$  h, although there is some variation between samples.

Absorption and emission spectra of Ag clusters during synthesis were recorded by taking aliquots at regular intervals. Spectra are shown in Figure 3.3. The initial dark solution is not luminescent and shows only a broad absorption feature around 480 nm, which may indicate the presence of particles larger than 29 atoms, with a broad size distribution.<sup>17,73,160,214</sup> Luminescence appears after around 50 min, which coincides with the lightening of the sample and the emergence of the absorption features at 330, 425 and 500 nm. From the normalised luminescence spectra, it can be seen that the shape of the emission peak hardly changes after the first appearance. There is only a slight decrease in relative intensity of the near-infrared (NIR) luminescence. Possibly this NIR luminescence originates from clusters that are not fully protected by ligands (it was also observed for clusters with lower LA concentrations, see Chapter 2). The Ag<sub>29</sub> cluster is clearly present in low concentration in the first hour of the synthesis. Its concentration increases in time until virtually all Ag is present as Ag<sub>29</sub>, as is clear from its characteristic optical properties (see Chapter 2).

The observed changes in optical properties are consistent with earlier reports of the synthesis of Ag clusters capped with LA or LA functionalised with poly(ethylene glycol).<sup>73,86,168</sup> The synthesis process also appears similar to that of Ag<sub>44</sub>(SR)<sub>30</sub><sup>4-</sup>.<sup>160</sup> It is not, however, a general process that occurs for all Ag clusters; Ag<sub>30</sub>(SR)<sub>18</sub> does not show a broad absorption feature during synthesis, but instead a steady increase in absorbance of all its characteristic absorption features.<sup>215</sup>

### Mass spectrometry study of Ag<sub>29</sub> clusters during synthesis

Mass spectra of the Ag clusters during synthesis were recorded by taking aliquots which were purified with 1-butanol (BuOH). Purification took 5–10 min, after which the sample was measured for around 15 min to collect sufficient scans. Mass spectra are shown in Figure 3.4.

Our mass spectrometry data confirm the results of optical spectroscopy, namely that the Ag<sub>29</sub> cluster appears early in the synthesis and that its concentration (signal/noise ratio) increases with time. For a number of the spectra (140, 208 and 298 min), the intensities of Na<sup>+</sup> adducts appear to show a bidisperse distribution and additional species are present. These are particularly evident in the  $z = 4$ –overall charge state around  $m/z$  1500. We believe this to be an effect of a slightly higher Na<sup>+</sup> concentration, either in the final purified aliquot or at some stage during the purification, which results in cluster degradation (see also Figure 2.7).

A number of other cluster species were also observed, with sizes close to the main cluster: Ag<sub>29</sub>(LA)<sub>11</sub><sup>2-</sup>, Ag<sub>28</sub>(LA)<sub>11</sub><sup>2-</sup> and some Ag<sub>26</sub>(LA)<sub>10</sub><sup>2-</sup>. Interestingly, these were also observed in the mass spectrum of regenerated clusters (Chapter 2), where it was proposed that they were formed during the purification process. The

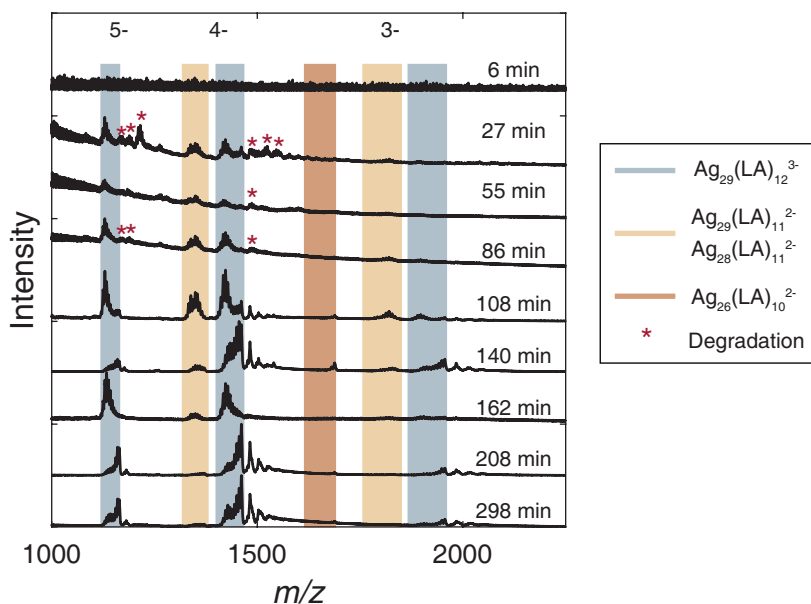


**Figure 3.4** Mass spectra of Ag clusters at various times after NaBH<sub>4</sub> addition. The ion signals of Ag<sub>29</sub>(LA)<sub>12</sub><sup>3-</sup> are marked in blue; those of the other observed clusters in red and yellow. Charges in the legend are the cluster core charges (on Ag and S atoms). The overall charge state, which includes deprotonation, is given at the top of the figure. Ion signals marked with a red asterisk are found to increase in intensity during the mass spectrometry measurement, indicating they are formed by degradation due to light, heat or high voltage. The given time is when the aliquot was taken.

ion signals of these clusters become less prominent as the synthesis progresses. A number of other ion signals are also observed but these increased in intensity during one measurement, suggesting degradation inside the capillary needle. Therefore they are not analysed further. These degradation products are marked with a red asterisk in Figure 3.4. We find no small cluster species such as Ag<sub>5</sub>(LA)<sub>3</sub><sup>-</sup> or Ag<sub>6</sub>(LA)<sub>3</sub> that were previously observed upon fragmentation of Ag<sub>29</sub>(LA)<sub>12</sub><sup>3-</sup> during tandem MS or when applying a high sample cone voltage.<sup>216</sup> These small species evidently do not play an important role during the synthesis. Nor do we observe any ion signals at higher *m/z* values, although the source pressure of the mass spectrometer was kept to a minimum, which limits the ionisation of larger species.

It appears that the first initial burst of nucleation results in the formation of species that are not observed in our mass spectra. Within half an hour these are

then converted to a mixture of Ag<sub>26</sub>, Ag<sub>28</sub> and Ag<sub>29</sub>, and over time size focusing makes the distribution more and more monodisperse.

The initial species may be unobserved due to its high  $m/z$ , the high Na concentration or because it does not survive the purification protocol. Indeed, the BuOH purification method was seen to have some influence on the synthesis. Around 6 h after the start of the synthesis, when the reservoir solution was bright reddish orange, the purified aliquots were held under a UV-lamp to check for luminescence. The first four aliquots (taken between 0 and 86 min) were brown and non-luminescent. Aliquot 5 was lighter in colour and showed weak luminescence, while aliquots 6-9 were orange and strongly luminescent. This indicates that purification in the first 1–2 h removed species that are necessary for a good reaction (for example NaBH<sub>4</sub>, or an excess of free LA). After 2 h the composition of the sample is such that complete purification will still yield clusters.

Mass spectrometry studies during synthesis of noble metal clusters are rare due to the challenging nature of such experiments. However, some studies have been done on Au<sub>25</sub>. These indicate that the exact reaction pathway depends on synthesis conditions. An early study was of Au<sub>25</sub> in tetrahydrofuran with phenylethanethiol as ligand and NaBH<sub>4</sub> as reducing agent.<sup>217</sup> It was found that the initial rapid nucleation and growth stage yielded a number of different cluster sizes up to Au<sub>102</sub>. Magic sizes (Au<sub>25</sub>, Au<sub>38</sub> and Au<sub>102</sub>) were noticeably present. Over the course of several days, the larger sizes were gradually converted to Au<sub>25</sub>. A second study was done of aqueous Au<sub>25</sub> clusters at high pH, capped with 3-mercaptopbenzoic acid and using CO as a reducing agent.<sup>218</sup> Two growth stages were identified. The first stage involved reduction of the Au(I)-thiolate intermediate to give a narrow size distribution of clusters. In the second stage, size focusing converted these clusters into the thermodynamically most stable cluster; Au<sub>25</sub>. The main difference with the study using NaBH<sub>4</sub> lies in the cluster sizes present after the first stage. For the clusters reduced with CO, these were significantly smaller, with fewer than 25 Au atoms. CO is a much slower, milder reducing agent than NaBH<sub>4</sub>. It appears to be a general trend that mild reducing agents yield smaller initial species.<sup>80</sup>

As our Ag<sub>29</sub> clusters are prepared with NaBH<sub>4</sub>, it is not unlikely that the first stage of the synthesis involves rapid reduction and growth to larger nanocluster cores, much as in the case of Au<sub>25</sub> reduced by NaBH<sub>4</sub>.

### EXAFS of Ag<sub>29</sub> clusters, and during synthesis

To confirm that the synthesis of Ag<sub>29</sub> involves larger nanoparticles, we performed X-ray absorption spectroscopy. X-ray spectroscopy is element-selective and does not require sample purification. This makes it an ideal tool to investigate the synthesis of Ag<sub>29</sub> clusters in further detail. As a first step, we characterised

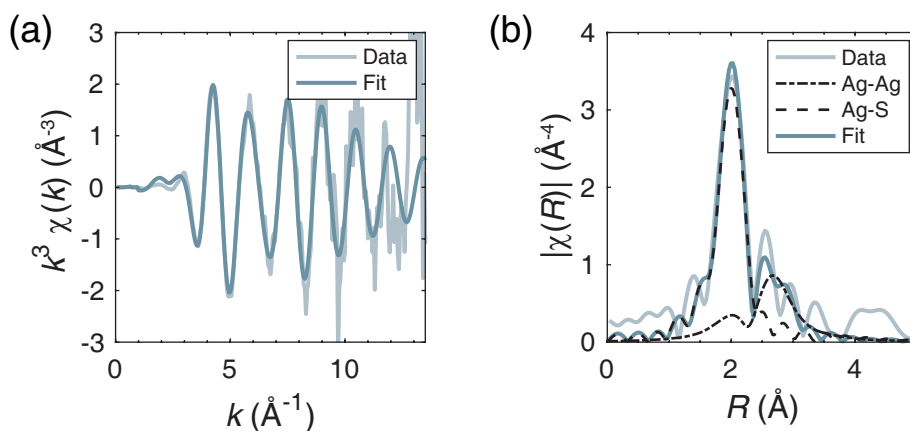


**Figure 3.5** EXAFS of Ag cluster solution in (a)  $k$  and (b)  $R$ -space. The fit was done using scattering paths from Ag metal and  $\text{Ag}_2\text{S}$ . The contributions of each path are also shown in (b). The results of the fit are given in Table 3.1.

the as-synthesised  $\text{Ag}_{29}$  clusters with EXAFS to determine average coordination numbers and bond lengths. The cluster solution was concentrated ( $\sim 5\times$ ) using 3 kDa molecular mass cutoff filters to increase the signal-to-noise ratio and ensure accurate analysis. The spectrum was fitted to one Ag–S and one Ag–Ag scattering path. A typical fit is shown in Figure 3.5, with the results of the fit in Table 3.1. The Ag–Ag coordination number was found to vary slightly depending on the fitting software and on the compound used to calculate the scattering paths, including which site was taken as the absorber for  $\text{Ag}_{29}$  with BDT (see Figure 3.6). Typical values of the Ag–Ag coordination number are between 2 and 5. The Ag–S coordination number does not change as much. Using two Ag–Ag scattering paths (one long and one short) did not improve the fit.

The low Ag–Ag coordination number indicates a small particle size of perhaps several tens of atoms.<sup>219,220</sup> However, due to the presence of ligands an estimate that assumes a perfectly icosahedral or cuboctahedral shape will be inaccurate. The ubiquitous staple motif present in nanoclusters results in a significant fraction of metal atoms with bonds only to ligands, thus increasing the metal-ligand and lowering the metal-metal coordination numbers when compared to a perfectly icosahedral cluster with the same number of atoms.<sup>221–223</sup>

Our coordination numbers are similar to those found for  $\text{Au}_{25}(\text{SR})_{18}$ .<sup>222,223</sup> Furthermore, the similarities in composition and optical properties between  $\text{Ag}_{29}(\text{LA})_{12}^{3-}$  and  $\text{Ag}_{29}(\text{BDT})_{12}(\text{TPP})_4^{3-}$  and the latter’s known structure<sup>56</sup> allow a more direct comparison between our experimental results and the expected

**Table 3.1** Structural parameters of Ag clusters from EXAFS analysis. CN is the coordination number,  $R$  the bond length,  $\sigma^2$  the Debye-Waller factor and  $E_0$  the energy shift. The fit is shown in Figure 3.5. The amplitude reduction factor is not taken into account ( $S_0^2 = 1$ ) for the values in the table. From fitting of Ag it was estimated to be 0.9.

Parameter	Ag-S	Ag-Ag
CN	$1.30 \pm 0.17$	$3.29 \pm 1.37$
$R$ (Å)	$2.46 \pm 0.01$	$2.83 \pm 0.04$
$\sigma^2$ ( $10^{-3}$ Å <sup>2</sup> )	$4.55 \pm 1.40$	$24.7 \pm 7.6$
$E_0$ (eV)	$3.6 \pm 1.6$	$1.7 \pm 2.5$

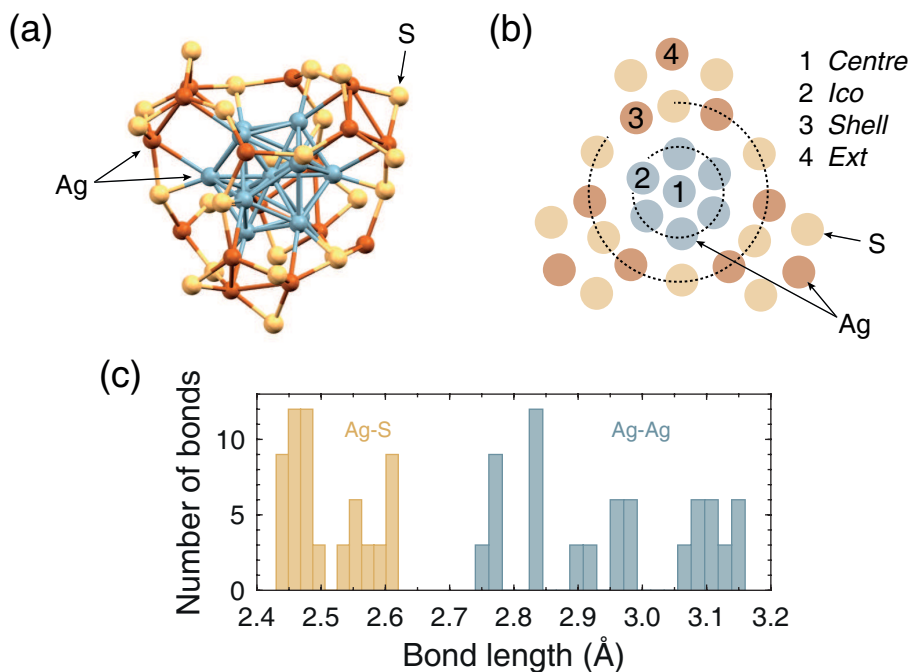


**Figure 3.6** (a) The structure of Ag<sub>29</sub>(BDT)<sub>12</sub>(TPP)<sub>4</sub><sup>3-</sup>.<sup>56</sup> Only Ag and S atoms are shown. For clarity, Ag atoms are given two different colours; blue for those in the icosahedral Ag<sub>13</sub> core, red for those in capping units (*shell* and *ext* sites). S atoms are in yellow. (b) Schematic representation of the cluster, showing the different Ag sites. (c) shows bond length distributions for Ag-S and Ag-Ag bonds in the cluster.

coordination numbers.  $\text{Ag}_{29}(\text{BDT})_{12}(\text{TPP})_4^{3-}$  has an icosahedral  $\text{Ag}_{13}$  core surrounded by four  $\text{Ag}_3\text{S}_6$  crowns, with the remaining four Ag atoms capped by triphenylphosphine (TPP) situated between these crowns.

A histogram of the Ag–Ag and Ag–S bond lengths in  $\text{Ag}_{29}(\text{BDT})_{12}(\text{TPP})_4^{3-}$  is shown in Figure 3.6. The shortest bonds (up to 2.78 Å) are the 12 bonds from the central atom to those in the shell of the icosahedron. Next are the bonds between the atoms of the icosahedral shell, 12 bonds around 2.85 Å, 6 around 2.92 Å and a further 12 bonds of around 2.97 Å. Finally there are 24 long bonds of 3.05–3.16 Å that connect the Ag atoms in the crowns to each other and to the icosahedral surface. All in all, there are 42 bonds below 3.0 Å, which corresponds to an average Ag–Ag coordination number of 2.9.

The distribution of Ag–S bond lengths in BDT-capped  $\text{Ag}_{29}$  shows a group of short and one of longer bonds. The 36 shorter bonds, below 2.5 Å, are those linking the  $\text{Ag}_3\text{S}_6$  crowns to the icosahedral surface and most of the bonds within the crowns themselves. The longer Ag–S bonds are mainly those binding to the four external Ag atoms, which are capped by TPP ligands in the  $\text{Ag}_{29}(\text{BDT})_{12}(\text{TPP})_4^{3-}$  cluster. Considering only the 36 shorter bonds, the average Ag–S coordination number is 2.5.

These theoretical coordination numbers are in good agreement with our results. The Ag–S coordination number is perhaps slightly lower than expected. This may be due to a slightly different structure of our  $\text{Ag}_{29}$  clusters compared to the  $\text{Ag}_{29}(\text{BDT})_{12}(\text{TPP})_4^{3-}$ , as our clusters do not have the additional TPP ligands which may result in some distortion. A small amount of cluster degradation/aggregation can also not be completely excluded as the cutoff filters are known to cause some cluster degradation (see Chapter 2). However, UV-Vis absorption spectra recorded before and after EXAFS show that radiation damage is limited. The experimental Ag–Ag and Ag–S bond lengths are in good agreement with expected values, and Debye-Waller factors are reasonably similar to those found for  $\text{Au}_{25}(\text{SR})_{18}$ .<sup>222</sup>

To investigate the synthesis mechanism of  $\text{Ag}_{29}$  clusters, EXAFS was recorded of aliquots taken from the synthesis solution at various times after addition of  $\text{NaBH}_4$ . Due to the low Ag concentration and limited time for measurements, spectra were recorded over a short  $k$ -range and are noisy. Calculated EXAFS of  $\text{Ag}_{29}(\text{LA})_{12}$  is shown in Figure A.3 for the short  $k$ -range used here as well as the longer  $k$ -range used for previously synthesised  $\text{Ag}_{29}$  clusters. While the shorter  $k$ -range results in the loss of some detail, overall the features in  $R$ -space EXAFS are similar.

To obtain good fits of EXAFS recorded during synthesis, we fixed Debye-Waller factors and bond lengths to the values of the as-synthesised cluster.<sup>210</sup> Figure 3.7 presents the EXAFS of the aliquots taken during the synthesis. The Ag–Ag and

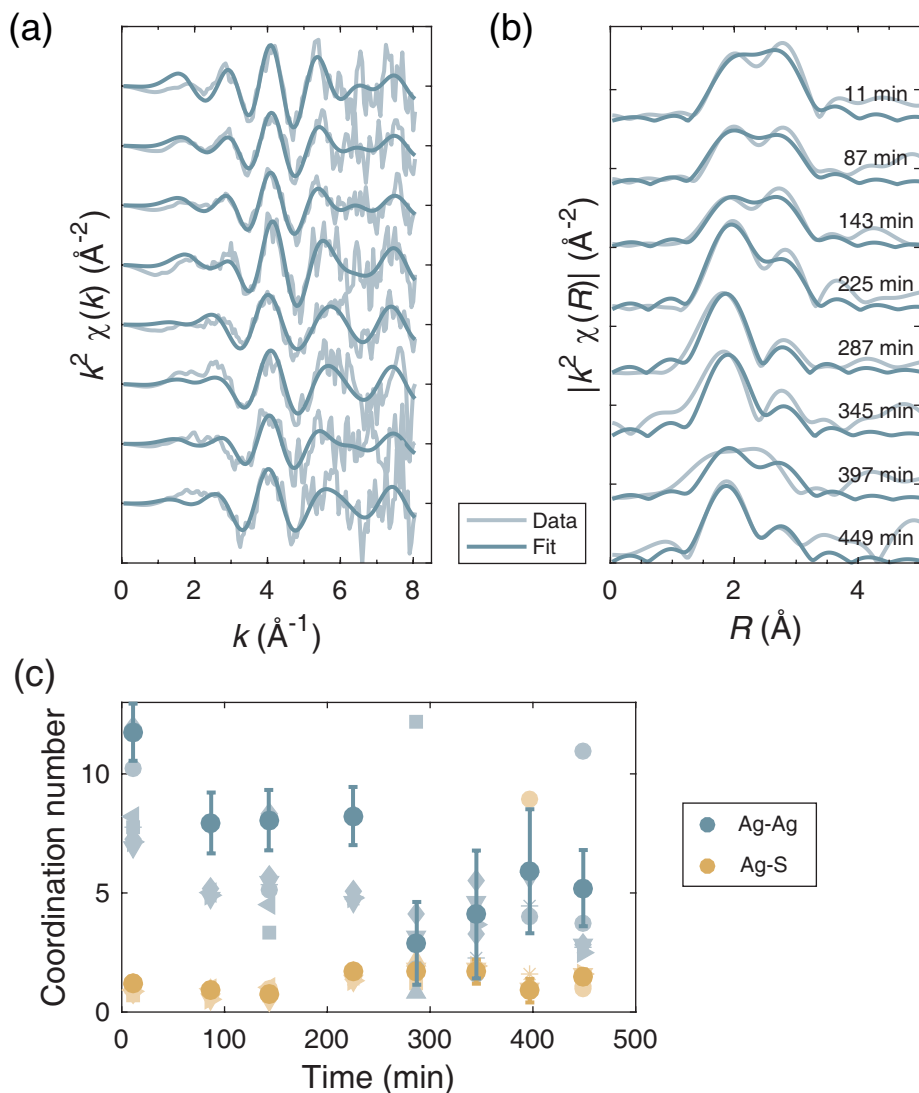


**Figure 3.7** EXAFS of Ag clusters during synthesis in (a)  $k$  and (b)  $R$ -space. The fit was done using scattering paths from Ag metal and Ag<sub>2</sub>S, with Debye-Waller factors and bond lengths fixed to that of as-synthesised clusters. The fitted coordination numbers are plotted in (c) using dark colours. Lighter colours are results of other fits, using fewer constraints, different software or scattering paths calculated from different materials. The times are the start of each EXAFS measurement, measured from the addition of NaBH<sub>4</sub> to the synthesis mixture.

Ag–S coordination numbers of these fits are shown in Figure 3.7, together with results of fits using no or different constraints (only Debye-Waller factors or only bond lengths fixed). The error bars of each point are large, as is expected from the noisy data. However, the general trend is clear: the Ag–Ag coordination number decreases over time while the Ag–S coordination number is fairly constant, with perhaps a slight increase. After 5 h, the coordination numbers are similar to those found for the as-synthesised sample, with little change during the rest of the synthesis. The initial high Ag–Ag coordination number is similar to that of Au<sub>144</sub>(SR)<sub>60</sub> (Au–Au coordination number 7.2)<sup>222</sup> and so consistent with a particle of a hundred to a few hundred atoms. That monodisperse Ag<sub>29</sub> is formed from such large species indicates that no other larger Ag cluster has a similar stability. In the size focusing process from Ag<sub>~100</sub> to Ag<sub>29</sub> many medium-sized clusters may be formed but none have sufficient stability to be present in the final solution. Neither are any medium-sized clusters observed in ESI-MS.

### XANES of Ag<sub>29</sub> clusters

The Ag<sub>29</sub> clusters were further studied by recording L<sub>3</sub>-edge X-ray absorption spectra, focusing on the near-edge structure. The cluster solution was measured as a liquid jet in a chamber with He-atmosphere to avoid unnecessary attenuation of X-rays. Ag L<sub>3</sub>-edge X-ray absorption spectra of freshly prepared Ag<sub>29</sub> clusters in solution are shown in Figure 3.8, together with spectra of reference compounds Ag powder, Ag<sub>2</sub>S, AgNO<sub>3</sub> and silver diethyldithiocarbamate (Ag(I)-thio).

In L<sub>3</sub>-edge XAS, transitions from 2p<sub>3/2</sub> to predominantly s- and d-states are observed, according to the dipole selection rule. In silver, the 2p → 5s transition is weaker by an order of magnitude than the 2p → 4d transition, thus the latter will dominate.<sup>224</sup> The first peak in the spectrum is called the whiteline, and for 4d metals its intensity is related to the number of empty 4d states.<sup>113</sup> Metallic silver has electron configuration 4d<sup>10</sup>5s<sup>1</sup>, while ionic Ag<sup>+</sup> compounds also have a 4d<sup>10</sup> state with no d-holes. Nevertheless, strong whitelines are observed, notably in AgNO<sub>3</sub> and Ag<sub>2</sub>O. It has been found that the strong whiteline transition in these compounds is due to s-d hybridisation, which results in 4d<sup>10-δ</sup>5s<sup>δ</sup> states. Hybridisation becomes stronger with increased covalency of the Ag-ligand bond.<sup>225</sup> This is different from the general interpretation of whiteline intensities due to electron-withdrawal by ligands which would create 4d<sup>9</sup>5s<sup>0</sup> states, that is, Ag<sup>2+</sup>. For bulk Ag, the features up to around 20 eV above the edge were assigned to pd states, while weak features close to the edge were due to excitations to 5s.<sup>226</sup>

The spectrum of Ag<sub>29</sub> clusters shows two features just above the edge (3.358 and 3.363 keV), in addition to a shoulder on the edge, and some weak, broad features far above the edge. There are significantly fewer and weaker features than

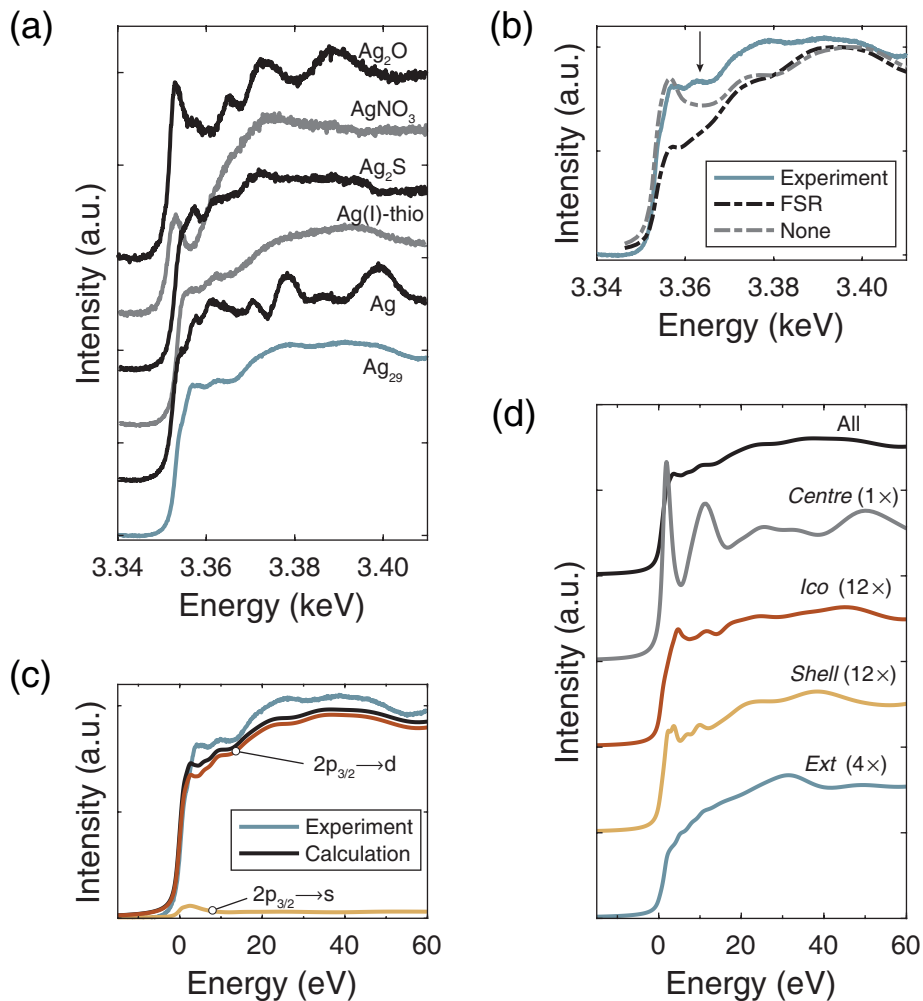


**Figure 3.8** (a) XANES of Ag<sub>29</sub> clusters together with spectra of reference compounds. (b) The Ag<sub>29</sub> spectrum together with the results of FEFF calculations, done with (FSR) and without (None) core-hole. The arrow indicates a feature that is missing in the calculations. (c) FDMNES calculations, of all 29 Ag sites, using the dipole selection rules  $\Delta l = \pm 1$  (s+d final states, black),  $\Delta l = +1$  (d final states, red) and  $\Delta l = -1$  (s final states, yellow). (d) FDMNES calculations of the entire Ag<sub>29</sub> cluster (black) and of four representative sites, as given by Figure 3.6. In parentheses, the number of atoms for each site in the cluster is given.

for Ag metal, as expected for clusters with a small number of atoms and lack of long-range order.<sup>227</sup> We further observe that the strong whiteness of AgNO<sub>3</sub> does not appear in the Ag<sub>29</sub> spectrum; clearly this precursor is not present in the solution at any significant concentration. The spectrum of Ag<sub>29</sub> resembles somewhat that of the Ag(I)-thio and Ag<sub>2</sub>S, in particular the former. The structure of Ag(I)-thio has been shown to consist of bridged hexameric units [AgS<sub>2</sub>CN(C<sub>2</sub>H<sub>5</sub>)<sub>2</sub>]<sub>6</sub> where each Ag atom is connected to either 1 Ag and 4 S or 2 Ag and 3 S.<sup>228</sup> It is thus not unreasonable to compare this to the surface atoms of the Ag clusters. All in all, the observed spectral features of Ag<sub>29</sub> are in accordance with (i) the small size of Ag<sub>29</sub>, (ii) capping by thiolate ligands and (iii) absence of any AgNO<sub>3</sub> precursor in the cluster solution.

The spectral features of the Ag<sub>29</sub> XANES spectrum could be reproduced with reasonable accuracy with FEFF calculations. These were done using two different core-hole treatments; the final state rule (FSR) and no core-hole (None). In the first case the core-hole is self-consistently screened. In the second case it is ignored; this has been found to more accurately reproduce the intensity just above the L<sub>3</sub>-edge for 3d metals<sup>229</sup>, but also for Pt nanoparticles<sup>135</sup> and Au (see Chapter 6). While the calculation without a core-hole gave a more accurate intensity, it does not reproduce the two features above the edge. Instead, only one is observed. FEFF uses the muffin-tin approximation, where potentials are assumed to be spherically symmetrical. This approximation may break down for anisotropic systems. We therefore also performed FDMNES calculations where the potential is allowed to take any shape.<sup>230</sup> This shows good agreement with the experimental spectrum, including features and intensity around the edge.

Further information about the nature of the transitions in the spectrum can be obtained from FDMNES calculations using different selection rules. The default is the dipole selection rule  $\Delta l = \pm 1$ , that is, from 2p<sub>3/2</sub> to d and to s final states. Calculations were done considering  $l \rightarrow l + 1$  and  $l \rightarrow l - 1$  transitions separately. As can be seen, most spectral features can be assigned to 2p<sub>3/2</sub>  $\rightarrow$  d transitions. However, the whiteness intensity is partially due to a transition to 5s. The spectra of four representative sites in Ag<sub>29</sub> were also calculated separately. The cluster is assumed to have the same structure as Ag<sub>29</sub>(BDT)<sub>12</sub>(TPP)<sub>4</sub><sup>3-56</sup>, shown in Figure 3.6. For the calculations, TPP is removed as it is not present in our clusters, and BDT is replaced with LA. As can be seen from Figure 3.8, both *ico* and *shell* sites have a spectrum that is in good agreement with the experiment. The *centre* site has an intense whiteness, while the *ext* spectrum is nearly featureless, probably due to the long distance to the nearest ligands.

**XANES during the synthesis of Ag<sub>29</sub>** We attempted to record XANES of the Ag<sub>29</sub> cluster synthesis *in situ* using the liquid jet setup. However, the synthesis was unsuccessful despite several attempts. The sample colour turned from light yellow to black upon addition of NaBH<sub>4</sub> to the LA + AgNO<sub>3</sub> solution, with a broad absorption feature around 480 nm, but then did not change any further. It appears the initial nucleation and growth stage occurs similarly to when the synthesis is done in the lab, but the later size focusing stage of reaction is hindered. The liquid jet setup differs from the standard reaction setup in a number of ways, most notably the exposure to X-rays and saturation of the synthesis solution with He, which may interfere with the required conditions for size focusing. This is discussed in more detail later.

Nevertheless, despite difficulties in performing the synthesis, we were able to record XANES of the solution at different stages during synthesis. If the synthesis was started in the lab and the solution transferred to the liquid jet setup after a certain amount of time, the synthesis stopped at this stage (there were no changes in the UV-Vis absorption spectrum for several hours). By repeating this for a number of different waiting times, we were able to record pseudo *in situ* XANES during synthesis. These spectra are shown in Figure 3.9, together with the corresponding UV-Vis spectra. Even under laboratory conditions there is some variation in the synthesis time. Therefore the times given in Figure 3.9 are approximate.

A number of observations can be made from the spectra. First, there is no sign of AgNO<sub>3</sub> in any of the spectra. Second, the edge features reminiscent of Ag(I)-thio are not present early in the synthesis. Third, the features far above the edge around 3.38 and 3.40 keV become broader and less prominent over time. Weak, broad post-edge features are commonly associated with smaller particles due to lack of long-range order, as observed in various studies including L<sub>3</sub>-edge XANES of Au nanoparticles during synthesis<sup>231–233</sup>, L<sub>3</sub>-edge XANES of Ag nanoparticles of various sizes<sup>227</sup>, and L<sub>3</sub>-edge XANES of Au nanoparticles, either ligand-capped<sup>234</sup> or supported on oxides<sup>115</sup>. XANES thus shows a decrease in particle size over time during the synthesis. The results agree very well with those of EXAFS and optical spectroscopy. The spectra during synthesis were fitted to the spectrum of the previously prepared, finished clusters and that of the initial large species (first and last spectra in Figure 3.9). Results of the fits are given in Table 3.2 and show around 50–70 % of Ag is present as Ag<sub>29</sub> in the synthesis solution when characteristic UV-Vis absorption features begin to appear.

The very first stage of the synthesis is not observed with XANES (nor with EXAFS). In this stage, AgNO<sub>3</sub> is reduced and rapid nucleation and growth occur to give the large Ag nanoparticles. This occurs within 10 min of addition of the reducing agent, and probably also to some extent before. The synthesis

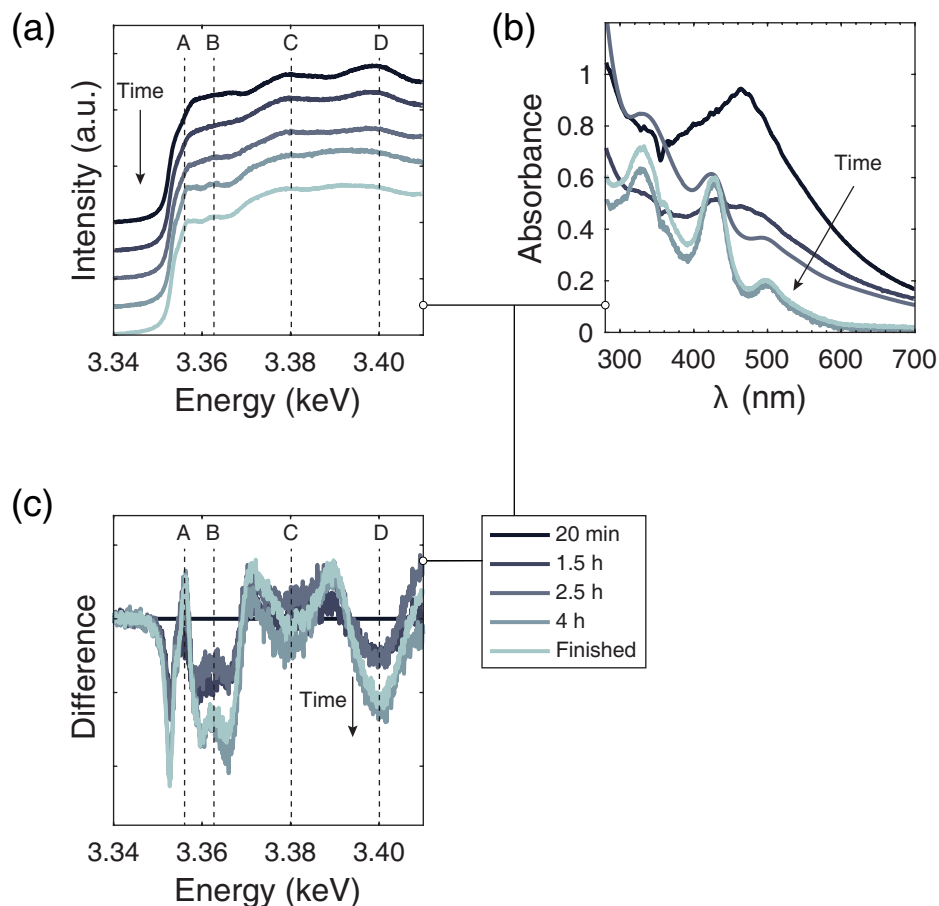


**Figure 3.9** (a) XANES of  $\text{Ag}_{29}$  clusters at various stage of the synthesis. (b) UV-Vis spectra of these stages. The first XANES spectrum (black) is of a sample where the synthesis was attempted directly in the liquid jet setup. The next two spectra are of batches where the synthesis was done in the lab until characteristic UV-Vis absorption features were just starting to appear and correspond to the system somewhere in the middle of the synthesis. The fourth spectrum is of a batch that was kept in the lab until the sample colour was orange, and corresponds to a system towards the end of the synthesis. The times in the legend indicate approximate progress of the synthesis from the moment of  $\text{NaBH}_4$  addition. The final spectrum shows previously synthesised, finished  $\text{Ag}_{29}$  for comparison. In (c), the difference between each XANES spectrum and the first spectrum is plotted. Some characteristic features are marked using dashed vertical lines.

intermediate solution (LA + AgNO<sub>3</sub>) already contains some NaBH<sub>4</sub> that was used to make LA water-soluble. Some Ag<sub>29</sub> clusters will form in this solution even without further addition of NaBH<sub>4</sub>.

**Table 3.2** Fractions of previously prepared Ag<sub>29</sub> clusters ('Finished') and large Ag species present early in the synthesis synthesis ('20 min'), as obtained by linear combination fitting of XANES spectra.

Spectrum	Fraction '20 min'	Fraction 'Finished'	R-factor
1.5 h	0.53	0.47	0.000 79
2.5 h	0.32	0.68	0.000 39
4 h	0.13	0.87	0.001 60

### The importance of oxygen during size focusing

We propose that the synthesis cannot proceed without a small amount of oxygen, and that it is the saturation of the solution with He rather than exposure to X-rays which prevents successful synthesis in the liquid jet setup used for XANES. When the synthesis was performed in the setup with He but without recording XANES, Ag<sub>29</sub> clusters were not formed. The UV-Vis absorption spectrum only showed the broad

the Ag<sub>29</sub> clusters did not appear. In laboratory setting (without He) it was observed, though not systematically studied, that opening the vial briefly a few times during synthesis increased the rate of size focusing and led to faster appearance of the bright orange colour and characteristic absorption features. In addition, when a small aliquot was transferred to a larger vial (containing more air) shortly after reduction with NaBH<sub>4</sub>, it turned orange and luminescent faster than the parent sample.

It has been shown that oxygen plays an important role in etching to obtain monodisperse Au clusters. Au<sub>25</sub> clusters can be prepared in tetrahydrofuran with tetra-*n*-octylammonium bromide, a phase transfer agent, provided there is some oxygen present.<sup>235</sup> Etching of larger nanoparticles to clusters with excess thiols was similarly only observed when oxygen was present.<sup>236</sup> It was proposed that the synthesis of Au<sub>25</sub> proceeds via larger, polydisperse nanoparticles that are etched with excess thiols. Thiols can react with oxygen to give thiyl radicals (RS•) which homolytically cleave Au–S bonds of the nanoparticles, resulting in Au• species which were experimentally observed with electron paramagnetic resonance (EPR) spectroscopy. The overall proposed mechanism for etching results in a layer-by-layer stripping of Au from the nanoparticle, until magic size clusters are obtained. Under inert atmosphere, no Au<sub>25</sub> was obtained unless also radical

initiators were added, confirming the importance of the diradical nature of oxygen. Similar observations were made for aqueous Au clusters, where in the absence of oxygen or radical initiators larger nanoparticles were formed instead of atomically monodisperse Au<sub>25</sub> or Au<sub>102</sub>.<sup>237</sup> Clearly, the role of oxygen in size focusing is of great importance both in organic and in aqueous solutions.

To the best of our knowledge, no similar studies have been performed on Ag clusters, although a method involving multiple reduction and oxidation steps has been shown to obtain a stable cluster of unknown composition.<sup>238</sup> Another study found highly luminescent Ag could be formed after the reduction of a decomposed and initially polydisperse cluster sample.<sup>239</sup> In both these cases multiple reduction steps are used and size focusing does not yield the desired product by direct ageing after the initial reduction.

The etching mechanism proposed for Au clusters involves both oxygen (or radical initiator) and excess thiols. If a similar mechanism is responsible for the etching to Ag<sub>29</sub>, it is clear why clusters prepared with low LA concentrations (Figures 2.3 and 2.12) show weak luminescence and less pronounced absorption features when compared to the standard clusters; there is less ligand available for etching.

### 3.4 Conclusions

The synthesis process of Ag<sub>29</sub>(LA)<sub>12</sub><sup>3-</sup> clusters was studied using optical spectroscopy, mass spectrometry and X-ray spectroscopy. Upon addition of NaBH<sub>4</sub> to the synthesis intermediate solution of LA with AgNO<sub>3</sub>, rapid nucleation and growth occurs resulting in the formation of Ag particles consisting of a few hundred atoms. How these nanoparticles are formed is still unknown, as none of the techniques were able to observe the nucleation process. From this polydisperse mixture of larger species, Ag<sub>29</sub> clusters are formed and their concentration increases steadily over time. The etching process to obtain Ag<sub>29</sub> requires oxygen and cannot proceed in inert atmosphere. Clusters with composition Ag<sub>29</sub>(LA)<sub>11</sub><sup>2-</sup>, Ag<sub>28</sub>(LA)<sub>11</sub><sup>2-</sup> and Ag<sub>26</sub>(LA)<sub>10</sub><sup>2-</sup> are observed in mass spectrometry during synthesis and may be intermediates in this process. No heavier cluster species are observed, proving that Ag<sub>29</sub> is by far the most stable species in the range Ag<sub>29</sub> to Ag<sub>~100</sub> under the synthesis conditions.

### 3.5 Acknowledgements

We thank Blanka Detlefs and Alessandro Longo for beamline support; Mario Delgado-Jaime, Hebatalla Elnaggar, Ties Haarman, Naud van Bunningen, Boyang

Liu and Ru-Pan Wang for their help during the beamtimes; and Arjan Barendregt for help with mass spectrometry measurements. The ESRF and NWO are thanked for providing beamtime (proposals CH4969 and 26-01-1044). This work was financially supported by the Debye Graduate Programme (NWO project 022.004.016), and ESRF Graduate Programme; the mass spectrometry research was performed within the framework of NWO and supported by the large scale proteomics facility Proteins@Work (project 184.032.201) embedded in The Netherlands Proteomics Centre.

## Additional spectra; silver clusters

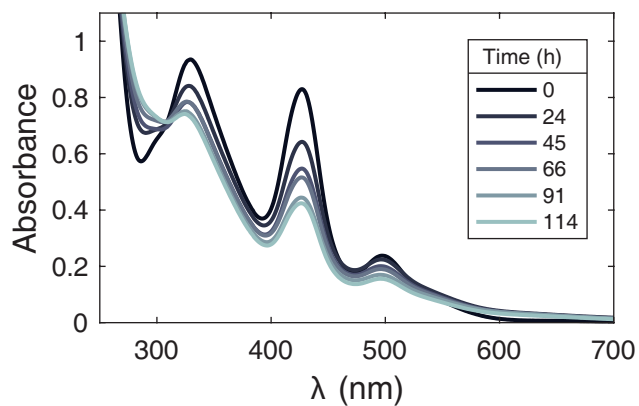


**Figure A.1** Absorption spectra of Ag clusters at various times after dilution (4 $\times$ ). The absorption peaks gradually disappear, which indicates aggregation (see also Figure 2.10). The timescale of one week is similar to that of the SE-AUC experiment.

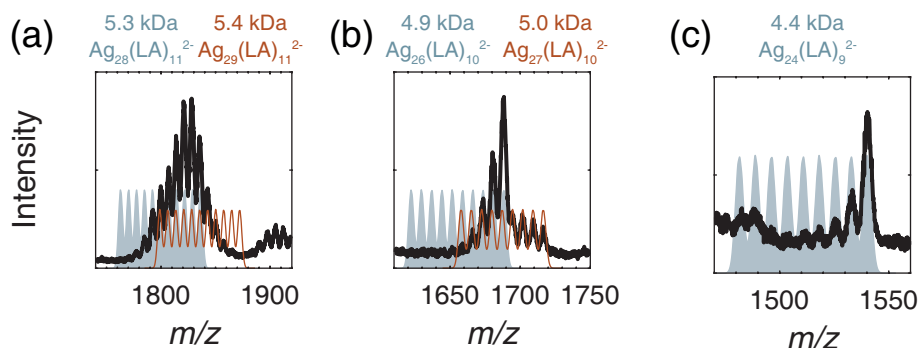


**Figure A.2** Identification of new species from the mass spectrum of regenerated clusters (Figure 2.11). The experimental spectrum is in black, theoretical spectra are in colour. (a) The 5.3–5.4 kDa species, a combination of  $\text{Ag}_{29}(\text{LA})_{11}^{2-}$  and  $\text{Ag}_{28}(\text{LA})_{11}^{2-}$ . (b) The 4.9–5.0 kDa species, a combination of  $\text{Ag}_{26}(\text{LA})_{10}^{2-}$  and  $\text{Ag}_{27}(\text{LA})_{10}^{2-}$ . (c) The 4.4 kDa species,  $\text{Ag}_{24}(\text{LA})_9^{2-}$ . The overall charge state is  $z = 3^-$ , but the same species are also observed for  $z = 4^-$  (these have one additional deprotonation).

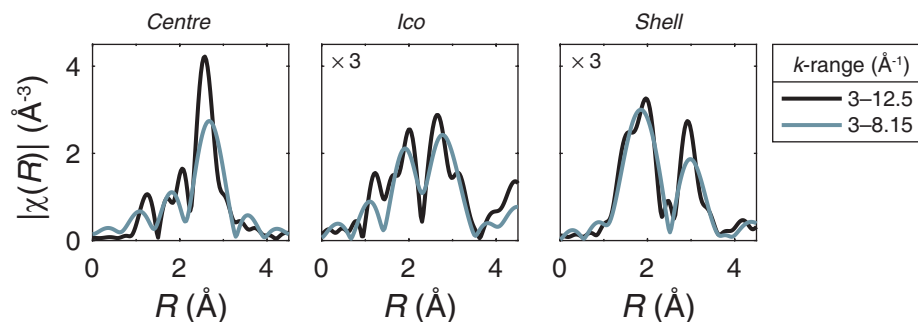


**Figure A.3** Calculated EXAFS of  $\text{Ag}_{29}(\text{LA})_{12}$  in  $R$ -space, for three different sites in the cluster. From left to right, the Ag–Ag coordination number decreases, and the Ag–S coordination number increases (see also Table 4.3). The  $k$ -ranges are those used in Figures 3.5 and 3.7. Spectra were calculated with FEFF and processed with Athena, using parameters as described in Section 3.2. An overall Debye-Waller factor of  $0.010 \text{ \AA}^2$  was added using the SIG2 card.

# PART II



SILVER AND GOLD ▶



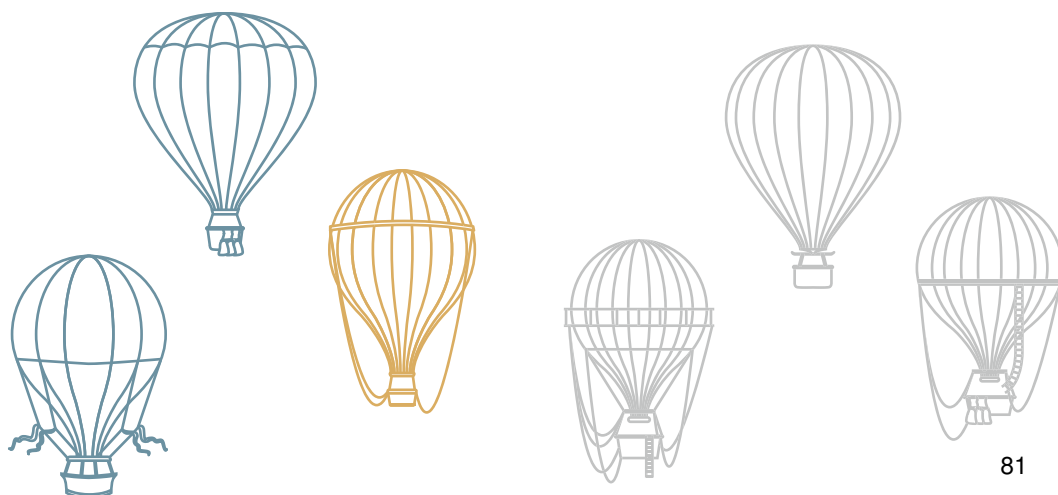
## Single atom doping of monodisperse Ag<sub>29</sub> clusters

---

### Abstract

Doping of Ag<sub>29</sub> with Au has a profound effect on the properties of the cluster. With a few percent Au, highly stable bimetallic clusters are formed. The Au-doped Ag clusters show enhanced resistance to heat and bleaching with UV-light compared to pure Ag<sub>29</sub> clusters. The optical properties are also affected, with blueshifts in absorption and emission spectra. The luminescence quantum yield increases by almost a factor 4, to around 8%. The increase in quantum yield was explained by an increase in the rate of radiative decay, as shown by a decrease in luminescence lifetime. With mass spectrometry, the Au-doped clusters are found to consist predominantly of Au<sub>1</sub>Ag<sub>28</sub>, with 12 ligands just as for the monometallic cluster. X-ray absorption spectroscopy of the Au L<sub>3</sub>-edge was done to determine that the dopant is preferentially located in the centre of the cluster.

---



*“Scientists have calculated that the chances of something so patently absurd actually existing are millions to one. But magicians have calculated that million-to-one chances crop up nine times out of ten.”*

— Terry Pratchett, *Mort*

## 4.1 Introduction

The properties of a noble metal cluster depend on its exact composition. Adding a single metal atom may reduce a cluster's stability, enhance its luminescence or increase its catalytic activity. Likewise, changing one atom for an atom of another metal may profoundly affect the cluster properties. Bimetallic clusters offer new avenues of exploration into fundamental properties, but also a vastly greater range of parameters that can be tuned to obtain clusters with desired properties. The addition of a second metal can drastically enhance the quantum yield<sup>240</sup>, which is of great importance for many potential applications such as sensing<sup>241</sup> and bioimaging<sup>242</sup>. With two metals it is also possible to tune the composition and structure of the cluster surface which may be beneficial for catalysis.<sup>243</sup>

Bimetallic nanoparticles are not new, and have been studied extensively to prepare alloyed or core-shell architectures to tune plasmonic properties.<sup>244</sup> However, the small size and high monodispersity of clusters allows one to understand the changes in optical and electronic properties at the single-atom level.<sup>245</sup> An example is the core charge; which is neutral for the bimetallic clusters Pt<sub>1</sub>Au<sub>24</sub>(SR)<sub>18</sub><sup>0</sup> and Pd<sub>1</sub>Au<sub>24</sub>(SR)<sub>18</sub><sup>0</sup> but negative for the monometallic Au<sub>25</sub>(SR)<sub>18</sub><sup>1-</sup>.<sup>144,246</sup> The decrease in charge density on the cluster core of Pd<sub>1</sub>Au<sub>24</sub> compared to Au<sub>25</sub> resulted in a greatly enhanced rate of ligand exchange.<sup>247</sup> Furthermore, the increased stability of the bimetallic clusters could be attributed to bond length contraction<sup>248,249</sup> and strong interactions<sup>250</sup> between Pd or Pt and the rest of the cluster.

The terms doping and alloying are both used when discussing bimetallic clusters. The former usually describes clusters with a specific number of heteroatoms, while alloying refers to clusters with a distribution of heteroatoms that depends on the ratio of the two metals in the synthesis.<sup>245</sup> Whether alloying or doping occurs depends on the relative stabilities of the possible clusters, although the method used to prepare the clusters may help tune the obtained compositions.<sup>251</sup> As with monometallic clusters, there are different ways to prepare bimetallic clusters. The most straightforward is co-reduction, where two metal salts are reduced together in the presence of ligands.<sup>252</sup> Alternatively, the second metal can be incorporated later, for example during an etching step.<sup>253</sup> The second metal may be deposited on the surface and interact with the capping units or ligands, thus increasing the overall number of atoms in the cluster,<sup>254,255</sup> but it can also be

fully incorporated into the clusters by replacing<sup>251</sup> an atom of the first metal without changing the overall cluster size. Two different monometallic clusters can react together to give bimetallic clusters, demonstrating that clusters are dynamic, reactive species.<sup>37,256,257</sup>

Recent advances have resulted in a better understanding of bimetallic clusters, to explain why some clusters can be easily doped while others form alloys. Due to its high stability, robust synthesis protocols and early structural characterisation, work on bimetallic clusters has focused on alloying or doping of  $\text{Au}_{25}(\text{SR})_{18}$ .<sup>245</sup> While introduction of Pt or Pd led to monodoping and increased stability, the addition of Cu resulted in alloy clusters  $\text{Cu}_y\text{Au}_{25-y}$  with  $y \leq 5$ . Due to the small size of Cu atoms, the alloyed clusters had a distorted geometry and lower stability than  $\text{Au}_{25}$ .<sup>258,259</sup> Introduction of Ag also resulted in alloys, but these were stable over time.<sup>259</sup> The electronic structure and optical properties of the clusters were found to be sensitive to the number of Ag atoms.<sup>252,260</sup> Alloying is also observed in other cluster sizes, such as  $\text{Ag}_y\text{Au}_{38-y}(\text{SR})_{24}$ <sup>261</sup>,  $\text{Ag}_y\text{Au}_{144-y}(\text{SR})_{60}$ <sup>262</sup>,  $\text{Ag}_y\text{Au}_{18-y}(\text{SR})_{14}$ <sup>263</sup> and  $\text{Ag}_y\text{Au}_{130-y}(\text{SR})_{50}$ <sup>264</sup>.

There has been some work on bimetallic clusters using common Ag clusters as a starting point, such as  $\text{Ag}_{25}(\text{SR})_{18}$ ,  $\text{Ag}_{44}(\text{SR})_{30}^{4-}$  and  $\text{Ag}_{29}(\text{BDT})_{12}(\text{TPP})_4^{3-}$  (BDT is 1,3-benzenedithiol, TPP is triphenylphosphine). For  $\text{Ag}_{29}$ , up to 5 Au atoms could be incorporated.<sup>265</sup> For  $\text{Ag}_{44}$ , either a distribution of different alloy clusters<sup>266</sup> or a cluster doped with 12 Au atoms<sup>55</sup> could be prepared, depending on synthesis protocol. The same was found for  $\text{Ag}_{25}$ ; it was obtained either as a distribution of alloyed clusters<sup>266</sup> or a singly doped<sup>251</sup> cluster.  $\text{Ag}_{25}$  could also be doped with Pt or Pd, giving the stable singly doped clusters  $\text{PtAg}_{24}$  and  $\text{PdAg}_{24}$ .<sup>267</sup> In contrast with doped  $\text{Au}_{25}$ , however, these clusters had a core charge of 2– thus retaining the total electron count of 8. This difference between Ag and Au clusters upon doping is intriguing.

In this chapter we study the changes in  $\text{Ag}_{29}(\text{LA})_{12}^{3-}$  properties upon doping with Au. We find that high concentrations of Au destabilise the cluster, but with just a few percent Au, a stable bimetallic species is formed. Using mass spectrometry, this is identified as mostly  $\text{Au}_1\text{Ag}_{28}(\text{LA})_{12}^{3-}$ . Some pure  $\text{Ag}_{29}$  is also present, but the fraction of  $\text{Au}_2\text{Ag}_{27}$  is low even at high Au concentrations, and clusters with 3 or more Au atoms are not observed. X-ray absorption spectroscopy is used to demonstrate that the Au atom is preferentially located in the centre of the cluster. This is in agreement with preferential sites typically observed for Au and Ag in bimetallic clusters. We further find that the bimetallic cluster has a higher quantum yield than the monometallic cluster, with blueshifts in both emission and absorption spectra. Studies of the luminescence lifetime indicate that doping with Au causes an increase in the rate of radiative decay.

## 4.2 Experimental methods

### Chemicals

AgNO<sub>3</sub> (laboratory reagent grade) was obtained from Fisher Scientific. NaBH<sub>4</sub> (99 %), (±)- $\alpha$ -lipoic acid ( $\geq 99\%$ ), methanol ( $\geq 99.9\%$ ), HAuCl<sub>4</sub> · 3 H<sub>2</sub>O ( $\geq 99.9\%$ ), Cu(NO<sub>3</sub>)<sub>2</sub> · 3 H<sub>2</sub>O (99 %), Zn(NO<sub>3</sub>)<sub>2</sub> · xH<sub>2</sub>O (99.999 %), Ni(NO<sub>3</sub>)<sub>2</sub> · 6 H<sub>2</sub>O and PtCl<sub>4</sub> (99.99 %) were purchased from Sigma Aldrich. 1-Butanol (99.5 %) was obtained from Acros. Water was of Milli-Q quality, purified using a Millipore Direct-Q 3 water purification system. 4-(dicyanomethylene)-2-methyl-6-(4-dimethylaminostyryl)-4H-pyran (DCM dye) was obtained from Exciton.

### Synthesis

The synthesis of the clusters is adapted from a protocol for Ag clusters.<sup>86</sup> 19 mg lipoic acid (92  $\mu$ mol) and 7 mg NaBH<sub>4</sub> (185  $\mu$ mol) were placed in a 40 or 20 mL glass vial with 14 mL water. This was stirred (using a magnetic stirring bean) until all LA had dissolved. Next, 25 mM AgNO<sub>3</sub> and HAuCl<sub>4</sub> · 3 H<sub>2</sub>O solutions were added, with a combined volume of 700  $\mu$ L (corresponding to 17.5  $\mu$ mol in total). The AgNO<sub>3</sub> solution was always added first, and the addition of HAuCl<sub>4</sub> · 3 H<sub>2</sub>O was followed by 10 mg NaBH<sub>4</sub> (264  $\mu$ mol) in 2 mL water. The vial was wrapped in aluminium foil to minimise the exposure of the clusters to light, and stirring was continued overnight. The synthesis was performed at room temperature. For synthesis with Pt, Zn, Ni or Cu, the HAuCl<sub>4</sub> solution was replaced by 25 mM solutions of PtCl<sub>4</sub>, Zn(NO<sub>3</sub>)<sub>2</sub> · xH<sub>2</sub>O, Ni(NO<sub>3</sub>)<sub>2</sub> · 6 H<sub>2</sub>O, or Cu(NO<sub>3</sub>)<sub>2</sub> · 3 H<sub>2</sub>O.

Post-synthesis modification was done by preparing Ag<sub>29</sub> according to the standard procedure. After a day, 25 mM HAuCl<sub>4</sub> · 3 H<sub>2</sub>O solution was added to a total Au concentration of 2.9 or 7.1 %, followed by the addition of 10 mg NaBH<sub>4</sub> in solid form. The solution was stirred overnight. All samples were stored in the dark at room temperature.

### Optical spectroscopy

UV-Vis spectra were recorded using a Perkin Elmer Lambda 950, a Perkin Elmer Lambda 40 or a Varian Cary 50 spectrometer. Room temperature emission spectra were recorded with a Jasco FP8300 Spectrofluorometer or a Spex 1680 (0.22 m) double beam spectrofluorometer equipped with a liquid nitrogen cooled Acton Research SpectraPro 300i CCD camera. The CCD camera was equipped with a 150 lines/mm grating blazed at 800 nm. Emission spectra were corrected for the spectral response of the equipment. Emission and excitation spectra at 4 K were recorded using an Edinburgh Instrument FLS920, with a Hamamatsu R928 photomultiplier as detector and a 450 W Xenon lamp as excitation source. The setup was equipped with an Oxford Instruments cryostat for liquid helium. Room temperature luminescence lifetimes were recorded using a Hamamatsu R928 photomultiplier with a time-correlated single photon counting card (TimeHarp 260 PC, PicoQuant), and a laser (Opolette HE 355-II, Opotec Inc.) operating at 500 nm, or a 441.4 nm pulsed diode laser (Edinburgh Instruments EPL-445) as excitation source. At low temperature, luminescence lifetimes were recorded with a slightly modified version of this setup. A Hamamatsu H7422

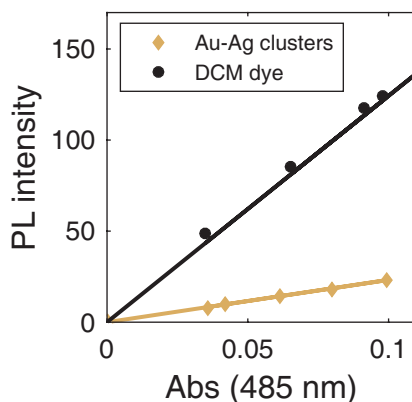


**Figure 4.1** Integrated emission intensity as a function of absorbance at 485 nm for Au-doped Ag clusters and DCM dye. The lines are a fit through the points.

photomultiplier was used as detector, and the excitation source was a laser (Opolette HE 355-II, Opotec Inc.) operating at 420, 460 or 490 nm. For optical spectroscopy measurements, the cluster solution was diluted 4–10× with water; the dilution was the same when comparing different samples for the same experiment.

**Quantum yield determination** The quantum yield of doped Ag clusters with 2.9% Au was determined using DCM dye in ethanol as reference. A Varian Cary 50 spectrometer was used to record UV-Vis absorption spectra. Emission spectra were recorded on a Jasco FP8300 Spectrofluorometer. The excitation wavelengths used were 485 and 550 nm. Au-doped Ag clusters and DCM dye were diluted with water or ethanol to prepare five samples with absorbance  $\leq 0.1$  at 485 nm. The integrated emission intensity of each spectrum scales linearly with the absorbance at 485 nm (Figure 4.1); the slopes of the lines are proportional to the quantum yield. The quantum yield of DCM dye in ethanol is 43.5%.<sup>175</sup> The quantum yield of the Au-doped Ag clusters can be calculated according to:

$$\Phi = \Phi_R \frac{m}{m_R} \frac{n^2}{n_R^2} \quad (4.1)$$

where  $m$  is the slope from Figure 4.1,  $n$  is the solvent refractive index and  $\Phi$  is the quantum yield. In each case, the subscript R refers to the reference dye. Values for the solvent refractive index are  $n = 1.33336$  and  $n_R = 1.3611$  for water and ethanol, respectively.<sup>177</sup>

### Stability tests

The stability of cluster solution to UV-light was tested by placing samples by a UVP UVGL-58 handheld UV-lamp (365 nm excitation wavelength, 6 W) while minimising the influence of other light sources. UV-Vis absorption spectra were recorded at regular intervals. To test the stability against heat, cluster solutions were placed on a hotplate at 80 °C for 6 h.

### Mass spectrometry

MS measurements were performed in negative ion mode using an electrospray ionisation time-of-flight (ESI-ToF) instrument (LC-T; Micromass, Manchester, U.K.) equipped with a Z-spray nano-electrospray ionisation source. A nano ESI quadrupole ToF instrument (Micromass, Manchester, U.K.) was used for tandem mass spectrometric analysis. Needles were made from borosilicate glass capillaries (Kwik-Fil, World Precision Instruments, Sarasota, FL) on a P-97 puller (Sutter Instruments, Novato, CA), coated with a thin gold layer by using an Edwards Scancoat (Edwards Laboratories, Milpitas, CA) six Pirani 501 sputter coater. After purification, the sample was sprayed into the mass spectrometer. The applied voltage on the needle was between 1200 and 1100 V and the sample cone voltage was varied between  $-7$  and  $0$  V. All spectra were mass calibrated in negative ion mode, using an aqueous solution of phosphoric acid ( $0.1\%$  v/v).

Samples were purified using 1-butanol (BuOH) to extract water until the clusters sediment, after which they were washed with a small amount of methanol (MeOH) and redispersed in water. This was done by mixing  $300\ \mu\text{L}$  cluster solution,  $400\ \mu\text{L}$  BuOH and  $100\ \mu\text{L}$  methanol in an Eppendorf vial. The vial was briefly centrifuged to speed up phase separation, and the upper colourless organic layer was removed. Next,  $300\ \mu\text{L}$  BuOH was added, the vial was shaken and centrifuged, and the organic layer was again removed. This was repeated until the clusters just sedimented. Typically, 3–5 extractions with BuOH were needed. After removing the final organic layer and washing with MeOH ( $50$ – $100\ \mu\text{L}$ ), the clusters were redispersed in water ( $50$ – $100\ \mu\text{L}$ ).

**Data analysis** Theoretical mass spectra were calculated using ChemCalc<sup>151</sup> with full width at half maximum =  $0.5$ . In calculating theoretical mass spectra, we assume that neither of the two S-atoms in LA is present as a thiol (thus LA is  $\text{C}_8\text{H}_{14}\text{O}_2\text{S}_2$ ). The  $5-$  overall charge state was considered, as this is the most intense in our spectra. Each LA has one carboxylic acid group which can be deprotonated. Two LA must be deprotonated without any  $\text{Na}^+$  association to keep the overall  $5-$  charge state. Clusters with 3 or more Au atoms are not observed, so were ignored in this analysis. The composition of a cluster can therefore be written as  $[\text{Au}_y\text{Ag}_{29-y}(\text{LA})_{12}]^{3-} - (2+x)\text{H}^+ + x\text{Na}^+ ]^{5-}$ , where  $y = 0$ – $2$  and  $x = 0$ – $10$ . For the fit, it was assumed that each of the clusters with different  $y$  has the same intensity distribution of  $\text{Na}^+$  adduct peaks (with different  $x$ ). The total intensity of the spectrum is then given by:

$$I = n_0 \sum_{x=0}^{10} a_x I_x^{(0)} + n_1 \sum_{x=0}^{10} a_x I_x^{(1)} + n_2 \sum_{x=0}^{10} a_x I_x^{(2)} + C \quad (4.2)$$

where  $n_0$ ,  $n_1$  and  $n_2$  are the abundances of the cluster with  $y = 0$ ,  $1$  or  $2$  Au atoms,  $a_x$  the abundances of the species with  $x$   $\text{H}^+/\text{Na}^+$  exchanges,  $I_x^{(y)}$  the spectrum of that species and  $C$  a constant background intensity. The experimental spectrum was normalised and the fit parameters  $a_x$  were constrained between  $0$  and  $1$ . Further constraints were added if needed to ensure a reasonable distribution of  $a_x$  values (monodisperse or bidisperse depending on the spectrum).

The theoretically expected abundance of clusters with  $y$  Au atoms as a function of Au fraction  $\chi_{\text{Au}}$ , assuming Au is randomly distributed over all clusters, is given by:

$$n_y = (1 - \chi_{\text{Au}})^{(29-y)} \chi_{\text{Au}}^y \binom{29}{y} \quad (4.3)$$

### X-ray spectroscopy

Au L<sub>3</sub>-edge XAS (11.92 keV) was recorded at beamline ID26 at the European Synchrotron Radiation Facility. For XANES, the incident beam was selected using the (311) reflection from a double Si crystal monochromator. The spectrometer was equipped with a set of four Ge(555) analyser crystals to record High Energy Resolution Fluorescence Detected (HERFD) XANES. Masks were used to increase the resolution. The L $\alpha_1$  fluorescence channel was monitored (9.71 keV). For EXAFS, the (111) reflection of the monochromator was used. A liquid jet setup was used to minimise radiation damage. The sample (prepared at 5 $\times$  the standard scale) was placed in a vial from which liquid was pumped through a capillary to form a free-standing liquid jet which was placed in the focus of the beam. Below the jet, the liquid was collected and returned to the vial. The setup is shown in Figure 4.2.

Ag L<sub>3</sub>-edge XANES (3.35 keV) was recorded at beamline ID26 at the European Synchrotron Radiation Facility. The incident beam was selected using the (111) reflection from a double Si crystal monochromator. X-ray fluorescence was collected at a 90° angle using a silicon drift diode detector (Ketek). Samples of pure Ag<sub>29</sub> and Au-doped Ag<sub>29</sub> cluster solutions were concentrated  $\sim$ 5 $\times$  using 3 kDa molecular mass cutoff filters (Amicon, Millipore), then measured in a cryostat (KONTI, CryoVac) cooled with liquid He. The typical operating temperature was 40 K.

**EXAFS analysis** EXAFS analysis was done using VIPER<sup>206</sup>, and the Athena and Artemis software packages.<sup>207</sup> Scattering phases and amplitudes were calculated using FEFF for Ag<sub>29</sub>(BDT)<sub>12</sub>(TPP)<sub>4</sub><sup>56</sup>, with TPP (triphenylphosphine) ligands removed and BDT (1,3-benzenedithiol) replaced by LA. A geometry optimisation of this structure was done in Avogadro<sup>209</sup>, keeping Ag and S atoms frozen, to ensure reasonable C–C and C–H bond lengths and angles. One of the Ag atoms in the icosahedral shell was replaced by Au to model an average environment with both Au–Ag and Au–S paths that were used in the fit. Typical fit parameters were:  $k = 3.0\text{--}12.0 \text{ \AA}^{-1}$ ,  $R = 1.15\text{--}3.3 \text{ \AA}$ , using a Hanning window ( $dk = 1 \text{ \AA}^{-1}$ ) for the Fourier Transformation. Fitting was done using  $k = 3$  weighting in VIPER and  $k = 1, 2, 3$  weighting in Artemis. The amplitude reduction factor  $S_0^2$  was not explicitly taken into account during fitting (that is,  $S_0^2 = 1$  was used). However, from fitting a reference Au sample, it may be estimated to be between 0.95 and 1.0.

**XANES analysis** The experimental spectrum was compared to calculations using the FDMNES code.<sup>120</sup> The structure of the cluster was taken from that of Ag<sub>29</sub> protected with BDT<sup>56</sup>, where the phosphine ligands were removed and the BDT was replaced by LA.

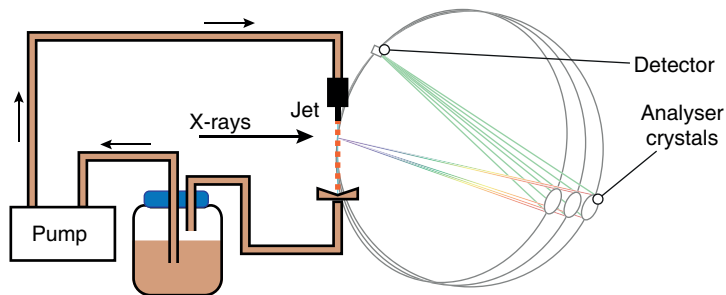


**Figure 4.2** Liquid jet setup with continuous flow. The sample is pumped from the reservoir through a capillary nozzle to form a freestanding jet, where X-ray spectroscopy can be measured.

A geometry optimisation of this structure was done in Avogadro<sup>209</sup>, keeping Ag and S atoms frozen, to ensure reasonable C–C and C–H bond lengths and angles. The FDMNES calculations were done for all Ag atoms in the clusters Ag<sub>29</sub>(LA)<sub>12</sub> and Au<sub>1</sub>Ag<sub>28</sub>(LA)<sub>12</sub>, and for one Au atom in each inequivalent site in Au<sub>1</sub>Ag<sub>28</sub>(LA)<sub>12</sub>. A radius of 6 Å was used for each calculation. Atomic potentials, Fermi level, and charge transfer were calculated self-consistently and the finite difference method was used to calculate potentials.<sup>212,213</sup> Relativistic effects were taken into account. The spectra were convoluted to apply an energy-dependent broadening, using default parameters (an arctangent function). The width of the core-hole was decreased slightly to 1.50 eV for Ag and 0.50 eV for Au, which was further broadened with a 1.0 eV Gaussian, to better match the experimental data.

### 4.3 Results and discussion

#### Synthesis and optical properties of Au-doped Ag clusters

The bimetallic clusters are made according to the same protocol as Ag<sub>29</sub> clusters, by simply replacing some of the AgNO<sub>3</sub> solution with HAuCl<sub>4</sub>. Similar colour changes are observed as during Ag<sub>29</sub> synthesis. UV-Vis absorption spectra of samples with low Au concentrations show blueshifts of all absorption features compared to pure Ag<sub>29</sub>. A marked increase in luminescence intensity is also observed, along with a slight blueshift of emission wavelength and a decrease in near-infrared (NIR) emission. The reproducibility of the synthesis is not as high as for Ag<sub>29</sub>, therefore to ensure the accuracy of the observed trend, multiple samples were prepared and emission spectra of all were recorded. Optical properties of bimetallic clusters are summarised in Figure 4.3. Attempts were also made to incorporate Cu, Ni, Zn or Pt, but preliminary results suggest this is not possible (Figure B.1), therefore the focus of this chapter is on Au-doped Ag<sub>29</sub>.

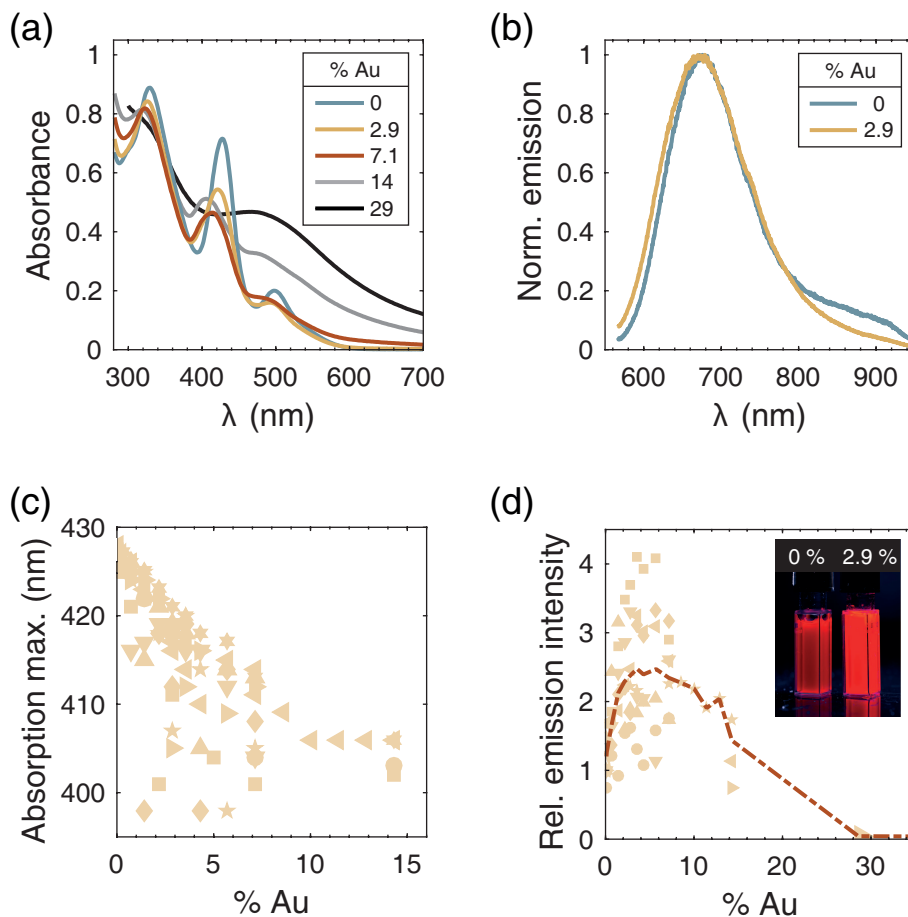


**Figure 4.3** Optical properties of  $\text{Ag}_{29}$  clusters doped with Au. (a) UV-Vis absorption spectra for samples with Au concentrations from 0–29%. (b) Normalised emission spectra of pure  $\text{Ag}_{29}$  and  $\text{Au}_y\text{Ag}_{29-y}$  clusters with 2.9%, showing a slight blueshift of the emission peak and decrease in relative NIR emission intensity. (c) Wavelength of maximum absorption (in the range 390–440 nm). (d) Emission intensity of samples as a function of Au concentration, relative to a pure  $\text{Ag}_{29}$  sample prepared and measured on the same day. All emission spectra were measured at 480 and 500 nm and the intensities were averaged. The inset shows a photograph of clusters with 0 and 2.9% Au under UV-light.

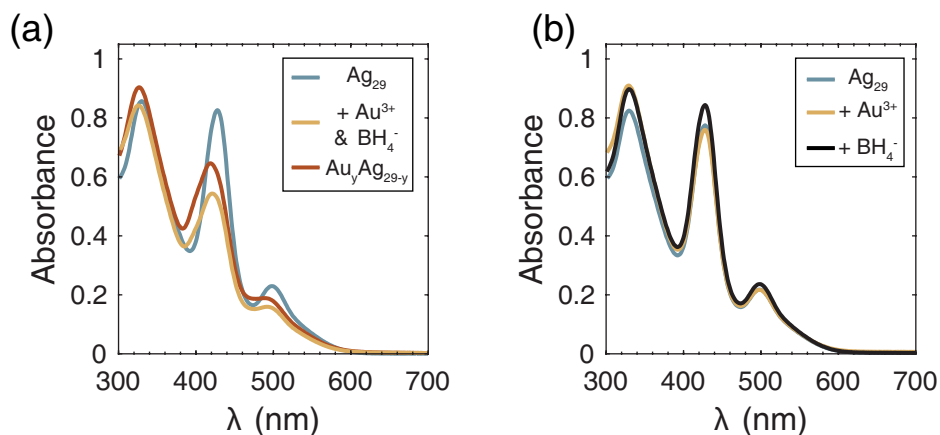


**Figure 4.4** (a) UV-Vis absorption spectra of Ag cluster samples before (blue) and after addition of HAuCl<sub>4</sub> and NaBH<sub>4</sub> (yellow), as well as that of a reference sample prepared according to the standard procedure (red), for 2.9% Au. (b) Absorption spectra of Ag clusters when only HAuCl<sub>4</sub> or only NaBH<sub>4</sub> is added. Apart from small changes in absorbance, spectra are identical.

There appears to be an optimal Au concentration of around 3–5%, above which the emission intensity decreases again. We attribute the initial increase in intensity and blueshifts in absorption and emission to the incorporation of Au into the Ag<sub>29</sub> cluster, giving a general cluster formula Au<sub>y</sub>Ag<sub>29-y</sub>. The decrease in emission can then be explained if there is no formation of stable clusters with high *y*. This is also apparent from the absorption spectra. For 0–7.1% Au, there is a smooth blueshift and decrease in absorbance. At around 14% Au, absorption features are less pronounced, and they disappear entirely at even higher Au concentrations, instead showing only a single broad absorption feature. The optimal Au concentration lies far below that found for the organosoluble cluster Ag<sub>29</sub>(BDT)<sub>12</sub>(TPP)<sub>4</sub><sup>3-</sup> (BDT, 1,3-benzenedithiol; TPP, triphenylphosphine). Here, up to 40% Au could be incorporated, with a 26-fold enhancement in quantum yield. These Au-doped clusters also showed a blueshift in absorption, but their emission spectrum was redshifted.<sup>265</sup> For Ag<sub>25</sub>(SR)<sub>18</sub><sup>-</sup>, the incorporation of a single Au atom (yielding Au<sub>1</sub>Ag<sub>24</sub>)<sup>254</sup> or a single Pd or Pt atom<sup>268</sup>, resulted in a blueshift both in absorption and in emission.

A second way to prepare the bimetallic clusters is by post-synthesis modification of pure Ag clusters. This is done by addition of HAuCl<sub>4</sub> to a solution of Ag<sub>29</sub> clusters, followed by reduction with NaBH<sub>4</sub>. The sample then darkens and turns brown, but after several hours of stirring the orange colour returns. UV-Vis

absorption spectra show that the final sample has similar absorption features as Au-doped Ag clusters prepared according to the standard procedure (Figure 4.4). Post-synthesis modification was successful for samples with 2.9 and 7.1 % Au. When only  $\text{HAuCl}_4$  or only  $\text{NaBH}_4$  is added, there is only a slight change in absorbance but no shift in absorption wavelength, even after two weeks. Thus, Au is not incorporated into the cluster unless both Au salt and reducing agent are added.

Based on the redox potentials of  $\text{AuCl}_4^- / \text{Au}$  and  $\text{Ag}^+ / \text{Ag}$ , one would expect a redox reaction to occur and Au to be incorporated into the cluster in a galvanic exchange reaction when only  $\text{Au}^{3+}$  is added. This was observed in the synthesis of thiolate-protected  $\text{Ag}_7\text{Au}_6$  clusters, which were made from  $\text{Ag}_7$  and  $\text{Ag}_8$  by adding  $\text{AuCl}_4^-$ .<sup>269</sup> However, the small size of the clusters and the presence of ligands can influence such reactions. An anti-galvanic exchange reaction was observed for  $\text{Au}_{25}(\text{SC}_2\text{H}_4\text{Ph})_{18}$ , which reacted with  $\text{Ag}^+$  to form bimetallic species such as  $\text{Ag}_2\text{Au}_{23}$  and  $\text{Ag}_3\text{Au}_{22}$ <sup>270</sup>, although the reaction did not occur when glutathione was used as a ligand.<sup>271</sup> Interestingly, the only way to prepare monodisperse  $\text{Ag}_1\text{Au}_{24}(\text{SR})_{18}^-$  clusters is by galvanic exchange, using  $\text{Ag}_{25}(\text{SR})_{18}^-$  and  $\text{Au}^{3+}$ .<sup>251</sup> A direct synthesis from Ag and Au salts instead gave a range of alloy clusters  $\text{Au}_y\text{Ag}_{25-y}(\text{SR})_{18}^-$ , as also demonstrated in a number of other studies.<sup>260,272,273</sup>

The sample with 2.9 % Au, prepared using the direct synthesis protocol, was investigated further. This has on average 0.85 Au atoms per cluster. The quantum yield of this cluster was determined to be 7.9 % relative to DCM dye, when excited at 485 nm. Upon excitation at 550 nm, a significantly lower quantum yield of 1.7 % is measured, similar to that of pure Ag clusters (2.1 %) measured with the same reference dye and with the same excitation wavelength. This can be explained if the 2.9 % Au sample still contains some pure  $\text{Ag}_{29}$  clusters. These are the only clusters excited at 550 nm, because the Au-doped clusters have blueshifted absorption.

The blueshifts in absorption and excitation wavelengths are more easily observed at low temperature. A series of emission spectra at different excitation wavelengths was recorded of samples with 0 and 3.6 % Au at 4 K. They are presented in Figure 4.5 as 2D maps. The 3.6 % Au sample shows four features, two at emission wavelength 660 nm and the others at 675 nm. The latter two have excitation wavelengths that are in good agreement with room temperature excitation and absorption spectra of pure Ag clusters. Indeed, a similar 2D map recorded of pure Ag clusters show that these features originate from  $\text{Ag}_{29}$ . The two additional features present in the 3.6 % Au sample, with excitation wavelengths 400 and 460 nm and emission wavelength 660 nm, thus originate from  $\text{Au}_y\text{Ag}_{29-y}$  clusters. As both have the same emission wavelength, it is likely that the sample contains only one other species in addition to  $\text{Ag}_{29}$ .

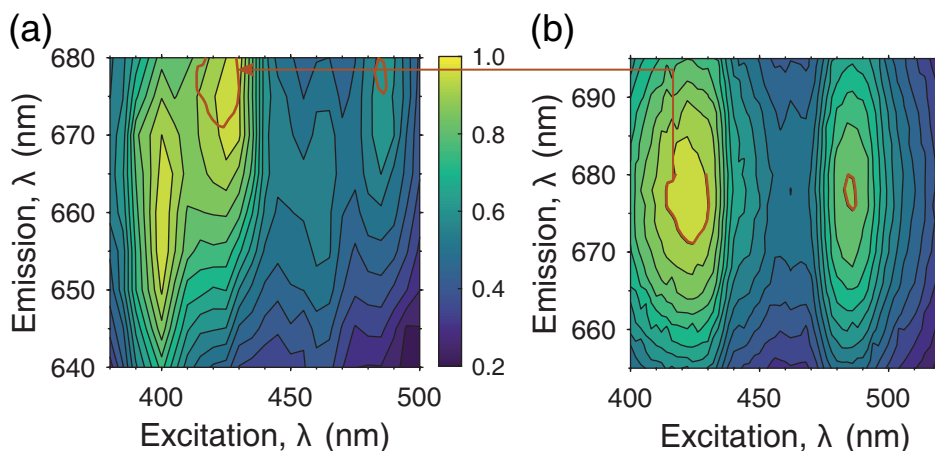


**Figure 4.5** 2D emission and excitation maps of (a) clusters with 3.6 % Au and (b) pure Ag clusters, recorded at 4 K. Both have been normalised to the maximum intensity. Note the slightly different ranges of emission and excitation wavelengths. The highest contour lines of the features of the pure Ag clusters are shown in red in the spectrum of clusters with 3.6 % Au. These two features thus originate from Ag<sub>29</sub>.

**Luminescence lifetime** The room temperature luminescence lifetime was found to decrease with increasing Au doping, from around 4  $\mu$ s for pure Ag clusters to 2.6  $\mu$ s for clusters with 14 % Au, see Figure 4.6. Lifetimes are fitted according to Equation (4.4) for  $i = 1$  component, where  $I$  is the recorded luminescence intensity at delay time  $t$ ,  $c$  is a constant background intensity, and  $\tau_i$  and  $a_i$  are lifetime and pre-exponential factor of the  $i^{\text{th}}$  component, respectively.

$$I(t) = \left( \sum_i a_i \exp(-t/\tau_i) \right) + c \quad (4.4)$$

The Ag<sub>29</sub> and Au<sub>y</sub>Ag<sub>29-y</sub> clusters absorb and emit at different wavelengths. Therefore, we expect to see some variation in the luminescence decay as these parameters are varied and we probe different species. This effect is especially noticeable at 4 K (Figure 4.7). At low temperatures, the non-radiative decay rate decreases resulting in longer lifetimes and higher luminescence intensity. The decay curve of pure Ag<sub>29</sub> is similar to that of a 3.6 % Au sample emitting at 680 nm and excited at 490 nm. These wavelengths correspond to the emission feature assigned to Ag<sub>29</sub> in Figure 4.5. When excitation and emission wavelengths of 460 and 640 nm are used, corresponding to the Au<sub>y</sub>Ag<sub>29-y</sub> cluster, the decay is significantly faster.

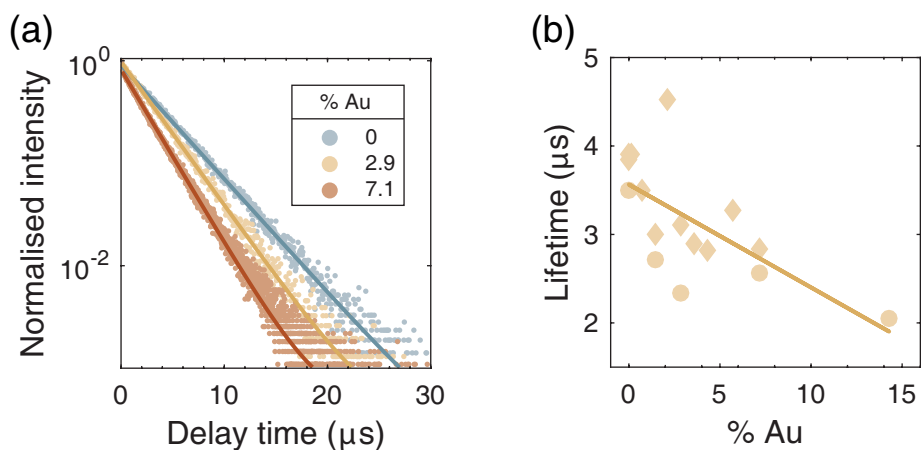


**Figure 4.6** (a) Room temperature luminescence decay curves of clusters with three different Au concentrations, recorded with emission wavelength of 680 nm. Solid lines are fits to mono-exponential decay. The luminescence lifetimes of samples with 0, 2.9 and 7.1 % Au are respectively 3.9, 3.1 and 2.6  $\mu\text{s}$ . (b) The luminescence lifetime decreases with increasing Au concentration.

The luminescence decay shows multi-exponential behaviour even for pure  $\text{Ag}_{29}$  clusters. This does not necessarily mean there are multiple emitting species. Different environments or conformations of the emitter can influence the rates of decay, leading to an ensemble of emitters with different luminescence lifetimes.<sup>274</sup> There may for example be small differences in ligand coordination. While the data may be fitted with multiple exponentials according to Equation (4.4), interpretation of the fit may not be straightforward. Pre-exponential factors  $a_i$  and lifetimes  $\tau_i$  are correlated, meaning there may be many solutions to Equation (4.4), which can be hard to distinguish from each other especially if the signal-to-noise ratio is low.<sup>275</sup> Furthermore, the small, finite number of luminescence lifetimes obtained from such a fit may not accurately reflect the shape of the entire distribution actually present in the sample.

The luminescence decay curves at 4 K were fitted with two or three exponentials, with the latter yielding slightly better fits. The tri-exponential fits are shown in Figure 4.7, and components are given in Table 4.1. The pure Ag sample and 3.6 % Au sample measured at  $\text{Ag}_{29}$  excitation and emission wavelengths (490 and 680 nm) show very similar lifetimes, but the pre-exponential factors differ, which may be due to a different distribution of decay rates in the sample. The 3.6 % Au sample at  $\text{Au}_y\text{Ag}_{29-y}$  excitation and emission wavelengths (460 and 640 nm) shows shorter lifetimes and different pre-exponential factors suggesting an overall distribution of

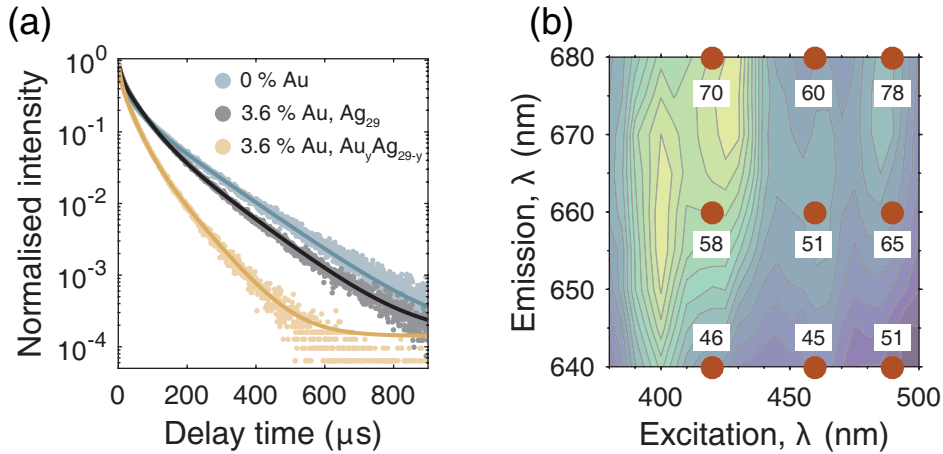


**Figure 4.7** (a) Luminescence decay curves at 4 K of clusters with 0 and 3.6 % Au. Emission and excitation wavelengths are respectively 490 and 680 nm (blue and grey) and 460 and 640 nm (yellow). Grey and yellow luminescence decay curves are thus recorded at wavelengths corresponding to mostly Ag<sub>29</sub> and mostly Au<sub>y</sub>Ag<sub>29-y</sub>, respectively. Solid lines are tri-exponential fits to the data. (b) The 2D emission-excitation map from Figure 4.5 with red dots indicating wavelengths where luminescence decay was recorded. Numbers are average lifetimes  $\tau_{\text{avg}}$  in  $\mu\text{s}$ .

**Table 4.1** Results of tri-exponential fit of luminescence decay curves, recorded at different excitation ( $\lambda_{\text{ex}}$ ) and emission ( $\lambda_{\text{em}}$ ) wavelengths.

% Au	$\lambda_{\text{ex}}$ (nm)	$\lambda_{\text{em}}$ (nm)	$\tau_1$ ( $\mu\text{s}$ )	$\tau_2$ ( $\mu\text{s}$ )	$\tau_3$ ( $\mu\text{s}$ )	$a_1$	$a_2$	$a_3$	$\tau_{\text{avg}}$ ( $\mu\text{s}$ )
0	490	680	130	40	5	0.22	0.28	0.45	100
3.6	490	680	121	47	9	0.16	0.44	0.35	78
3.6	460	640	77	30	6	0.11	0.45	0.40	45

faster decay. For further analysis, we calculated the average lifetimes according to  $\tau_{\text{avg}} = \sum_i I_i t_i / \sum_i I_i$ .<sup>274</sup>

This equation removes the need for fitting, so was used to calculate average lifetime for a number of excitation and emission wavelengths and superimposed on the 2D map in Figure 4.7. Lower average lifetimes coincide with wavelengths preferentially probing the  $\text{Au}_y\text{Ag}_{29-y}$  clusters. Even at wavelengths where we expect mostly  $\text{Ag}_{29}$ , the average lifetime is shorter than for pure Ag clusters, meaning there is probably still some  $\text{Au}_y\text{Ag}_{29-y}$  absorbing and emitting due to the overlap of broad emission and excitation peaks. The two clusters can not be fully distinguished and it is therefore not possible to conclusively determine the average lifetime of pure  $\text{Au}_y\text{Ag}_{29-y}$ .

**Luminescence mechanisms** Overall, the luminescence of noble metal clusters remains rather poorly understood, and the changes in luminescence behaviour upon doping even more so. Ligand-to-metal charge transfer has been proposed as a mechanism for the luminescence of  $\text{Au}_{25}(\text{SR})_{18}^-$ , which showed increased quantum yield with strongly electron-donating ligands.<sup>58</sup> Such a charge transfer mechanism was also suggested for monodoped  $\text{M}_1\text{Ag}_{24}(\text{SR})_{18}$  clusters, where the dopant was located in the centre of the cluster.<sup>268</sup> The dopants (Pd, Ag, Pt and Au) were found to give different quantum yields which could be related to electron affinity of the dopant and bond lengths from the capping units to the icosahedral core of the clusters. Both factors could influence the ligand-to-metal charge transfer. In contrast, theoretical studies of the luminescence of  $\text{Au}_{25}$ ,  $\text{Ag}_{25}$  and  $\text{Au}_1\text{Ag}_{24}$  found that luminescence involves only superatomic orbitals of the cluster and charge-transfer states are not involved.<sup>92,276</sup>

Nevertheless, we can qualitatively explain some of the differences in luminescence behaviour between  $\text{Ag}_{29}$  and  $\text{Au}_y\text{Ag}_{29-y}$ . Upon doping with Au, the quantum yield increases and the luminescence lifetime decreases. This is in contrast to the Au-doped  $\text{Ag}_{29}$  capped by BDT<sup>265</sup> and  $\text{Au}_1\text{Ag}_{24}(\text{SR})_{18}^-$ <sup>251</sup> clusters. In both these cases, a higher quantum yield and a longer lifetime were observed upon incorporation of Au. This suggests different mechanisms may be responsible for the increase in quantum yield upon doping Ag clusters with Au, and may depend for example on the exact nature of the ligands or structure of the cluster.

The lifetime is the inverse sum of all rates of decay from the excited state, which for simplicity's sake we group into one overall radiative rate  $k_r$  and one overall non-radiative rate  $k_{\text{nr}}$ . The quantum yield is defined as the ratio between emitted and absorbed photons, or, alternatively, the ratio between  $k_r$  and  $k_r + k_{\text{nr}}$ . For  $\text{Au}_1\text{Ag}_{24}$  and Au-doped  $\text{Ag}_{29}$  with BDT, a decrease in non-radiative decay rate is consistent with experimental observations. A decrease in non-radiative decay rate

means the system spends longer in the excited state and a larger fraction will decay via the radiative pathway, as observed for BDT-capped Ag<sub>29</sub> doped with Au.<sup>265</sup> A recent study of rod-shaped Au<sub>25</sub> clusters showed that, when doped with Ag to give Ag<sub>13</sub>Au<sub>12</sub>, the quantum yield increased which was attributed to stabilisation of the LUMO and enhanced rigidity of the cluster.<sup>277</sup> With increased rigidity, vibrational and rotational motion can be suppressed which decreases the non-radiative decay. This phenomenon is known from organic molecules as aggregation-induced emission<sup>278</sup> and has also been demonstrated for clusters.<sup>254,279</sup> In contrast, the changes in luminescent behaviour we observe upon doping our Ag<sub>29</sub> clusters with Au are consistent with an increase in radiative decay rate. This results in an increase in quantum yield and also means the system spends less time in the excited state, giving a shorter luminescence lifetime. Both our Ag<sub>29</sub> and Au<sub>y</sub>Ag<sub>29-y</sub> clusters have long  $\mu$ s luminescence lifetimes which are characteristic for spin-forbidden transitions.<sup>280</sup> This selection rule can be relaxed through spin-orbit coupling<sup>281</sup>, which is greater for heavier elements such as Au.<sup>282</sup>

### Stability of bimetallic clusters

We further find that doping with gold increases the stability of the Ag<sub>29</sub> clusters. This was demonstrated by exposing samples with 0, 2.9 and 7.1 % Au to UV-light, as shown in Figure 4.8. Over time, the characteristic absorption features disappear for all samples, but bleaching is fastest for the pure Ag clusters. The pure Ag sample showed only a slight blueshift of the absorption features (3 nm). With 2.9 and 7.1 % Au, the blueshifts were 13 and 6 nm, respectively. The large blueshift observed for the 2.9 % Au sample can be explained by the different stabilities of the species present in this sample; Ag<sub>29</sub> and Au<sub>y</sub>Ag<sub>29-y</sub>. The pure Ag clusters are bleached more rapidly than Au<sub>y</sub>Ag<sub>29-y</sub>. Thus, over time, the relative concentration of Au<sub>y</sub>Ag<sub>29-y</sub> increases and its blueshifted absorption features dominate the spectrum. The difference in stability between pure Ag and Au-doped clusters was also observed when 0 and 7.1 % Au clusters were exposed to heat.

An increase in stability was also found for BDT-capped Ag<sub>29</sub> upon doping with Au or Pt.<sup>265,283</sup> Similarly, Pt<sub>1</sub>Au<sub>24</sub><sup>246</sup>, Pd<sub>1</sub>Au<sub>24</sub><sup>144</sup>, and Au<sub>1</sub>Ag<sub>24</sub><sup>251</sup> were found to be more stable than their monometallic counterparts. Alloying Au<sub>25</sub> with Cu, on the other hand, reduced the stability of the clusters.<sup>258,259</sup> This is attributed to the small size of Cu (atomic radius 1.28 Å) compared to Au (1.44 Å) which leads to distortions of the structure. For clusters with both Au and Ag, alloying rather than doping is typically observed due to the similar sizes of these atoms.<sup>252,259,261</sup> It has also been observed that Au-Ag alloy clusters are less stable than pure Au clusters.<sup>261,262</sup> This can be explained by bond strengths, which in bulk are found to be Au-Au > Au-Ag > Ag-Ag.<sup>244</sup> Conversely, doping a Ag cluster with a small amount of Au will introduce a number of strong Ag-Au bonds.

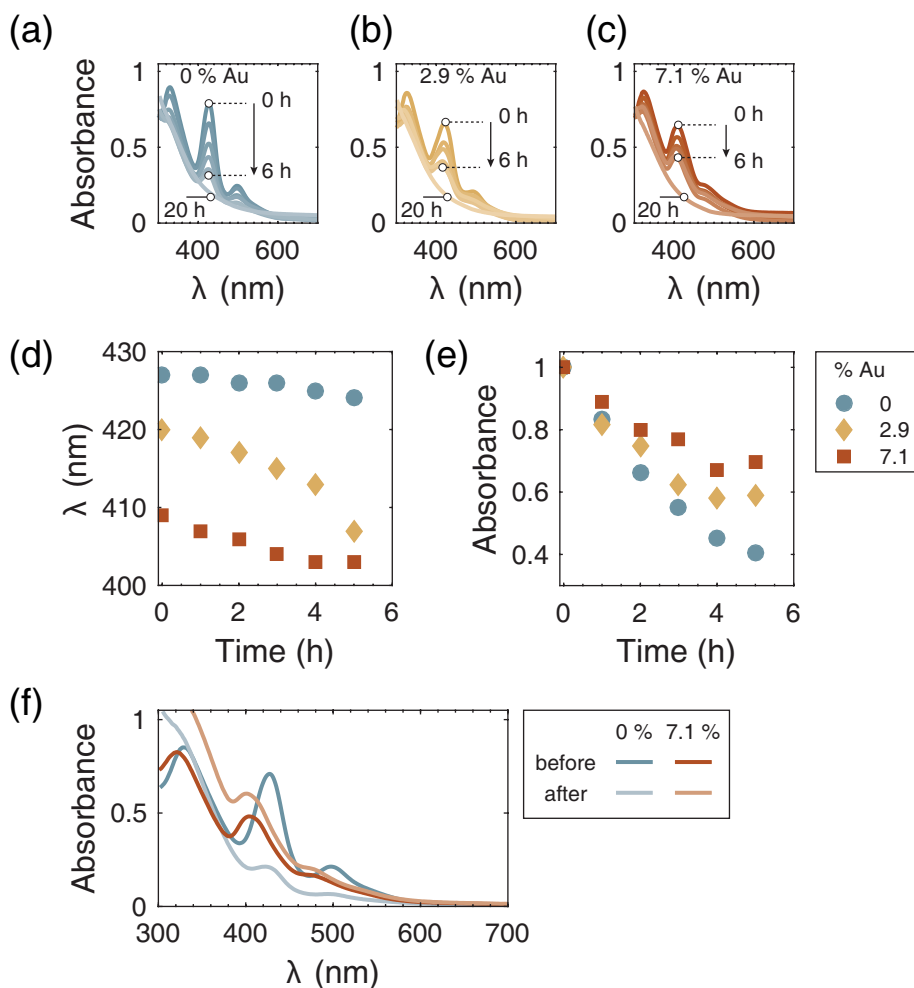


**Figure 4.8** (a)-(e) UV-Vis absorption spectra show a decrease in absorbance for all absorption features upon exposure to UV-light (355 nm). Figures (a), (b) and (c) are of samples with 0, 2.9 and 7.1 % Au, respectively. Figure (d) shows how the wavelength of the second absorption peak changes over time, and in (e) the absorbance at this wavelength is shown (normalised to the absorbance before exposure to UV-light). (f) UV-Vis absorption spectra of samples with 0 and 7.1 % Au, before and after exposure to heat. Absorption features of the pure Ag clusters have nearly disappeared, those of the 7.1 % Au clusters remain prominent.

### Composition of bimetallic clusters

Electrospray ionisation mass spectrometry was used to determine the size of the Au-doped clusters and confirm the successful incorporation of Au. From our previous experiments (Chapter 2), it is known that the pure Ag clusters are Ag<sub>29</sub>(LA)<sub>12</sub><sup>3-</sup> with near atomic monodispersity. Deprotonation of LA can give higher overall charge states, while deprotonation and association with Na<sup>+</sup> gives multiple ion signals in the same charge state with mass difference 22 Da. Thus, the mass spectrum of the pure Ag<sub>29</sub> clusters already contains multiple ion signals. As in Chapter 2, we consider only the species in the overall 5- charge state, as these ion signals are the most intense.

Figure 4.9 shows mass spectra of clusters with 0, 2.9 and 7.1 % Au as well as theoretical spectra of Ag<sub>29</sub>, Au<sub>1</sub>Ag<sub>28</sub> and Au<sub>2</sub>Ag<sub>27</sub> in the overall  $z = 5-$  charge state and with all possible H<sup>+</sup>/Na<sup>+</sup> exchanges. Spectra of a larger range of samples are shown in Figure B.2. The full composition of Au-doped Ag<sub>29</sub> clusters can be written as [Au<sub>y</sub>Ag<sub>29-y</sub>(LA)<sub>12</sub><sup>3-</sup> - (2 + x)H<sup>+</sup> + x Na<sup>+</sup>]<sup>5-</sup> in the overall  $z = 5-$  charge state. The mass difference upon Ag/Au exchange is 89 Da, which is nearly identical to that of 4 H<sup>+</sup>/Na<sup>+</sup> exchanges. This means we expect significant overlap between spectra of Ag<sub>29</sub> and Au<sub>y</sub>Ag<sub>29-y</sub>. The number of H<sup>+</sup>/Na<sup>+</sup> exchanges,  $x$ , can take values between 0 and 10; with the two last LA always deprotonated without any Na<sup>+</sup> association to keep the overall 5- charge state. The number of Au atoms can be anywhere from 0 to 29. However, based on the changes in optical properties with increasing Au concentration, we expect that clusters with high  $y$  are not formed due to their low stability and thus Ag clusters with only a few Au atoms will dominate.

It is clear from the spectra that the sample with 2.9 % Au contains mostly Au<sub>1</sub>Ag<sub>28</sub>. There is a small amount of Ag<sub>29</sub> visible (first four ion signals,  $m/z$  1120 to 1143) and no contribution from Au<sub>2</sub>Ag<sub>27</sub> (as seen by the lack of intense ion signals in the region  $m/z$  1187 to 1200). For samples with 7.1 % Au (on average 2.1 Au atoms per cluster), we again observe mostly Au<sub>1</sub>Ag<sub>28</sub> with minor contributions of Ag<sub>29</sub> and Au<sub>2</sub>Ag<sub>27</sub>. There appears to be a preference for monodoped clusters.

To estimate concentrations of each cluster is challenging due to the overlapping ion signals. Experimental spectra are therefore fitted to a weighted sum of theoretical spectra, for each combination of  $x$  and  $y$ . It is assumed that each cluster has the same distribution of Na<sup>+</sup> adduct peaks. In other words, each number of Au atoms  $y$  has the same intensity distribution for the eleven values of  $x$ . As the H<sup>+</sup>/Na<sup>+</sup> exchange takes place on the ligands far away from the metal atoms, this is a valid assumption. Even with these constraints, there are still a large number of fit parameters. Assuming contributions from Ag<sub>29</sub>, Au<sub>1</sub>Ag<sub>28</sub> and Au<sub>2</sub>Ag<sub>27</sub>, there

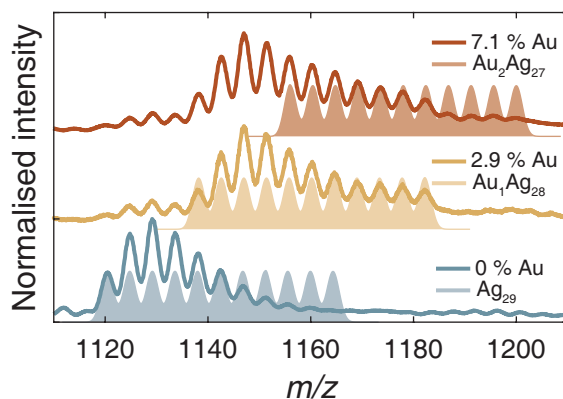


**Figure 4.9** Mass spectra of samples with 0, 2.9 and 7.1 % Au, which corresponds to average compositions of  $\text{Ag}_{29}$ ,  $\text{Au}_{0.8}\text{Ag}_{28.2}$  and  $\text{Au}_{2.1}\text{Ag}_{26.9}$ , respectively. Theoretical spectra of  $\text{Ag}_{29}$ ,  $\text{Au}_1\text{Ag}_{28}$  and  $\text{Au}_2\text{Ag}_{27}$  are shown in lighter colours for comparison. For the mass spectra of these samples, there is a clear preference for the monodoped cluster  $\text{Au}_1\text{Ag}_{28}$  for both 2.9 and 7.1 % Au. See also Figure B.2.

are 15 fit parameters (3 for the concentrations of clusters, 11 for the intensity of each  $\text{Na}^+$  adduct signal, and 1 parameter to estimate the non-zero background intensity). If no ion signals are observed in the range  $m/z$  1187 to 1200 (where only  $\text{Au}_2\text{Ag}_{27}$  appears),  $y = 2$  is ignored. Adduct signal intensities were always constrained between 0 and 1. If a particular  $\text{Na}^+$  adduct signal distribution was observed, for example bidisperse, additional constraints were imposed such as a minimum intensity for the last few adduct signals.

The fit does not give absolute intensities of each cluster, but rather ratios. These are compared to the theoretically expected ratios of  $\text{Ag}_{29}$  and  $\text{Au}_2\text{Ag}_{27}$  to  $\text{Au}_1\text{Ag}_{28}$ , assuming a completely random distribution of Au in Ag clusters. Experimental intensities and theoretically expected values are shown Figure 4.10 together with an example of a fit. In all cases the experimental intensities lie far below the theoretically expected values, indicating that the distribution of Au is not random but there is instead a preference for  $\text{Au}_1\text{Ag}_{28}$ .

We estimate the accuracy of the fit results to be around 10%. This is based on the results of fits to three spectra of pure  $\text{Ag}_{29}$  clusters, where the fitting procedure nevertheless found small contributions of  $\text{Au}_1\text{Ag}_{28}$  because of the non-flat background near the ion signals of the cluster. For samples with low Au concentrations (below 5%), the total observed ratio of gold to silver is different from the ratio in the sample, up to 20%. In some cases there appears to be an

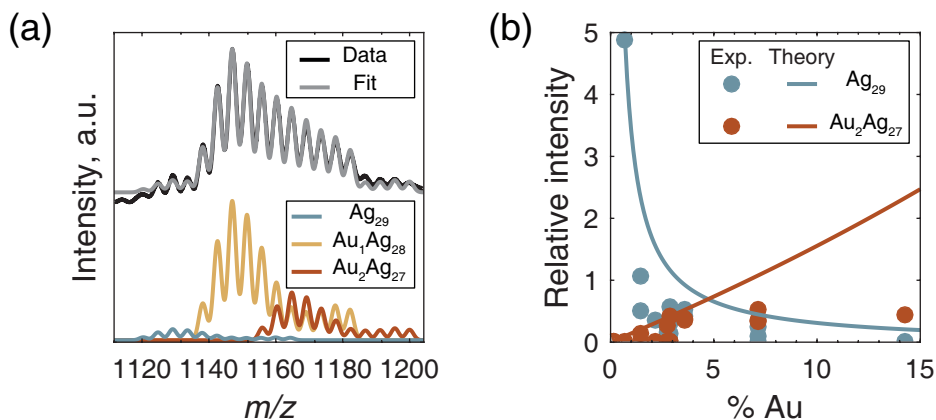


**Figure 4.10** (a) Mass spectrum of sample with 7.1 % Au (black) and the fit of theoretical spectra (grey). The contribution of each theoretical spectrum is shown below in colour. Note the identical intensity distributions for the H<sup>+</sup>/Na<sup>+</sup> exchange ion signals. (b) Intensity of Ag<sub>29</sub> and Au<sub>2</sub>Ag<sub>27</sub> relative to Au<sub>1</sub>Ag<sub>28</sub> for different Au concentrations. Fit results of experimental data are shown as circles. Solid lines indicate the theoretically expected intensity, assuming a completely random distribution of Au throughout the clusters, calculated according to Equation (4.3). Relative intensities of Ag<sub>29</sub> and Au<sub>2</sub>Ag<sub>27</sub> are lower than expected for all Au concentrations, meaning there is a preference for the monodoped clusters, Au<sub>1</sub>Ag<sub>28</sub>.

excess of Au, in others an excess of Ag, but there is no clear trend. It may be dependent on many factors in sample preparation, purification and ionisation. For higher concentrations of Au, the difference between fit result and theoretically expected concentrations far exceeds this, with 40–70 % less Au than expected from the sample composition. Pure Au clusters with LA (see Chapter 5) are not observed in any of the mass spectra, so it is unknown where the missing Au is. Clusters with different numbers of Au atoms may not behave the same upon ionisation and purification. A preference for monodoped clusters during synthesis may be further enhanced by high stability of Au<sub>1</sub>Ag<sub>28</sub> compared to Ag<sub>29</sub>, Au<sub>2</sub>Ag<sub>27</sub> and Au<sub>3</sub>Ag<sub>26</sub> during purification or ionisation. The less stable clusters suffer more degradation, and the resulting species may remain undetected, much like degraded Ag<sub>29</sub>.

Samples prepared via post-synthesis modification, by addition of Au<sup>3+</sup> to Ag<sub>29</sub> followed by reduction, also show a preference for monodoped clusters. Due to the two reduction steps with NaBH<sub>4</sub>, the Na<sup>+</sup> concentration is much higher in this sample and a bidisperse distribution of Na<sup>+</sup> adduct signals is observed. The preference for monodoping with gold, both via a direct synthesis and post-synthesis modification, appears to be unique for Ag<sub>29</sub> with LA. For BDT-capped

Ag<sub>29</sub>, direct synthesis with Au yielded a distribution of different compositions with 1–7 Au atoms, although one that shows a preference for clusters with a low number of dopants.<sup>265</sup> Doping with Pt yielded only a small fraction of Pt<sub>1</sub>Ag<sub>28</sub> when direct synthesis was done.<sup>283</sup> For Au-doped Ag<sub>25</sub>, direct synthesis also resulted in a mixture of clusters with different number of Au atoms, while the monodoped cluster was only obtained via post-synthesis modification.<sup>251</sup>

### Location of the Au atom

The bimetallic clusters were further studied with X-ray absorption spectroscopy. This has been successfully used in the study of bimetallic clusters and nanoparticles<sup>284</sup>, for example to determine the preferential position of dopants in Au<sub>25</sub><sup>248,285</sup> and larger clusters<sup>286</sup>, as well as studying reactions<sup>287</sup> between Au<sub>25</sub> and Pd<sup>2+</sup> and Ag<sup>+</sup>.

To determine the position of the Au atom in the bimetallic cluster, we recorded EXAFS. A 2.9% Au sample was used without any additional purification or concentration. Mass spectrometry and optical spectroscopy do not exclude the presence of small Au–LA complexes or clusters in the samples after synthesis, and the lack of purification ensures all Au species are taken into account. Due to the low Au concentration in the samples (30 μM), multiple EXAFS spectra were recorded over a total time period of 4 h. Despite the use of a liquid jet setup, radiation damage was observed during this time, resulting in a colour change of the sample from orange to brown and a disappearance of prominent UV-Vis absorption features (see Figure B.3).

For a first analysis, the radiation damage was ignored and all EXAFS scans were averaged. The averaged spectrum was fitted to two scattering paths, one Au–S and one Au–Ag. The spectrum is shown together with the fit in Figure 4.11. The results of the fit are given in Table 4.2. The Au–Ag coordination number, 7.8, is significantly higher than the average Ag–Ag coordination number in pure Ag<sub>29</sub> which was around 3 (see Chapter 3). Clearly, the Au atom does not occupy a random position in each doped cluster. We assume that the clusters have a similar structure as Ag<sub>29</sub>(BDT)<sub>12</sub>(TPP)<sub>4</sub><sup>3-</sup>, which is a reasonable assumption as cluster composition and optical properties are similar.<sup>56</sup> The structure of this cluster is shown in Figure 4.12. There are four unique sites the Au atom may occupy; in the centre of the icosahedron (*centre*), on the outer icosahedral positions (*ico*), in the capping units, bound to LA (*shell*), and on the external positions bound only to phosphines (*ext*). Note that the LA-capped clusters do not have the phosphines, so these sites may not exist with the same coordination geometry. The lack of phosphines may also distort the rest of the surface, giving slightly different

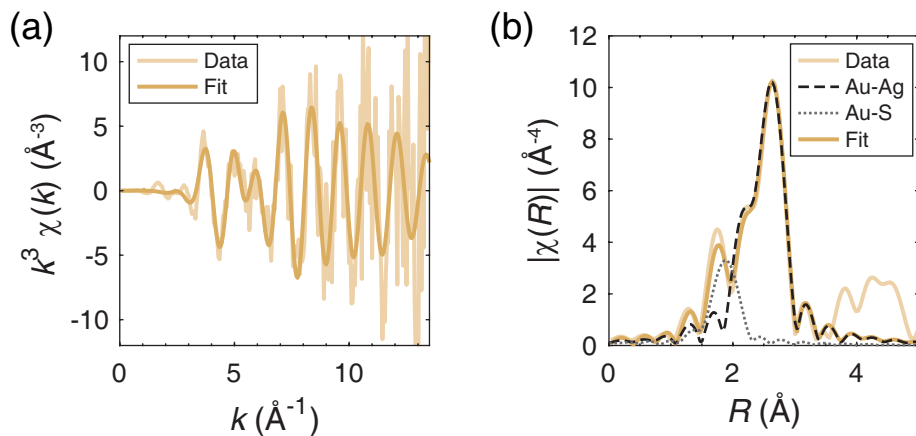


**Figure 4.11** EXAFS of Au-doped Ag<sub>29</sub> cluster solution in (a)  $k$  and (b)  $R$ -space. The fit was done using scattering paths Au–S and Au–Ag of Au<sub>1</sub>Ag<sub>28</sub><sup>56</sup>, where the Au atom occupies one of the outer positions of the icosahedron (*ico*). The contributions of each path are also shown in (b). The results of the fit are given in Table 4.2. For this figure, all EXAFS scans are averaged together (even though we observe some radiation damage).

**Table 4.2** Structural parameters of Au-doped Ag<sub>29</sub> clusters from EXAFS analysis. CN is the coordination number,  $R$  the bond length,  $\sigma^2$  the Debye-Waller factor and  $E_0$  the energy shift. The fit is shown in Figure 4.11. For this fit, R-factor = 0.024 and reduced  $\chi^2 = 48$ . The amplitude reduction factor is not taken into account ( $S_0^2 = 1$ ) for the values in the table. From fitting of Au foil it was estimated to be between 0.95 and 1.0.

Parameter	Au–S	Au–Ag
CN	$1.16 \pm 0.61$	$7.82 \pm 1.55$
$R$ (Å)	$2.29 \pm 0.04$	$2.78 \pm 0.01$
$\sigma^2$ ( $10^{-3}$ Å <sup>2</sup> )	$5.05 \pm 5.46$	$8.98 \pm 1.42$
$E_0$ (eV)	$3.8 \pm 5.8$	$4.2 \pm 1.3$

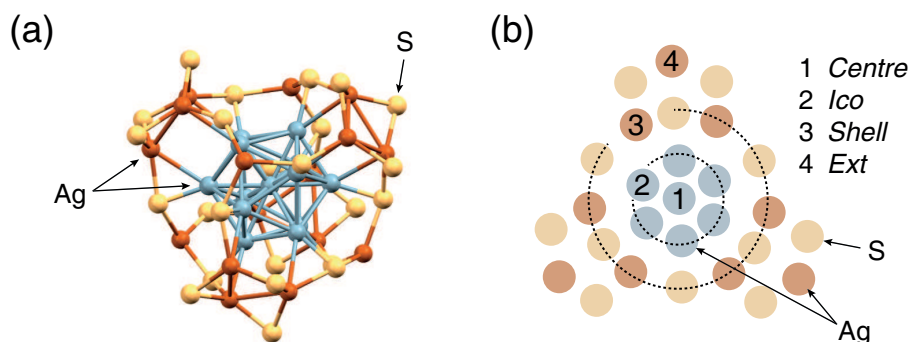


**Figure 4.12** (a) The structure of  $\text{Ag}_{29}(\text{BDT})_{12}(\text{TPP})_4^{3-}$ .<sup>56</sup> Only Ag and S atoms are shown. For clarity, Ag atoms are given two different colours; blue for those in the icosahedral  $\text{Ag}_{13}$  core, red for those in capping units. S atoms are in yellow. (b) Schematic representation of the cluster, showing the four different Ag sites.

coordination numbers for *shell* sites. Expected coordination numbers can be found in Table 4.3.

The Au–Ag coordination number of 7.8 can only be explained if a significant fraction of Au occupies a *centre* or *ico* position, in particular the former. Furthermore, we observe an Au–S bond length of 2.29 Å, which is shorter than the 2.46 Å Ag–S bond present in pure  $\text{Ag}_{29}$  clusters (Chapter 3). It is, however, consistent with typical bond lengths of Au–S bonds in Au clusters<sup>222,223,288</sup> and gold thiolates<sup>289,290</sup>. Thus, Au in *shell* or *ext* sites would cause a significant surface distortion. Alternatively, the Au–S bonds may be present in Au clusters or Au-thiolate complexes, rather than in  $\text{Au}_1\text{Ag}_{28}$ .

From colour changes, and by comparing UV-Vis absorption spectra before and after EXAFS, it is clear there is radiation damage. This may affect the analysis

**Table 4.3** Expected coordination numbers (CN) of Au in different sites, assuming the clusters have the same structure as  $\text{Ag}_{29}(\text{BDT})_{12}(\text{TPP})_4^{3-}$ .<sup>56</sup> Only Au–Ag bonds shorter than 3 Å are considered, except where explicitly noted.

Site	CN (Au–S)	CN (Au–Ag)
<i>Centre</i>	0	12
<i>Ico</i>	1	6
<i>Shell</i>	3	2*
<i>Ext</i>	3	0

\* These bonds are slightly longer, around 3.1 Å.

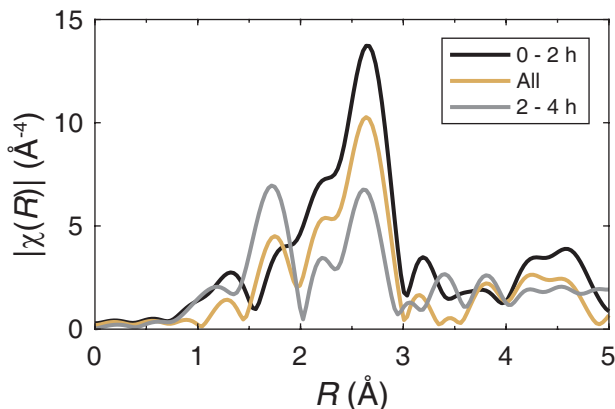


**Figure 4.13** Effect of radiation damage on FT-EXAFS of Au-doped Ag<sub>29</sub>. When only the first 2 h of measurements are used (black), the intensity of the Au–Ag scattering peak is higher than when only the last 2 h of measurements, corresponding to more damaged sample, are considered (grey). The average of all scans, measured over 4 h, is used in Figure 4.11.

and obtained results. To monitor radiation damage more closely, XANES was recorded every 25 min between EXAFS scans. There are minor changes in XANES over time, most notably a slight decrease in whiteline intensity. The changes occur gradually over time, thus it is not possible to conclusively select a number of EXAFS scans that correspond to an undamaged sample. It is possible to get a better understanding of the damage process by comparing the first and second half of the EXAFS scans (Figure 4.13). Due to the lower signal-to-noise ratio when only half the scans were considered, fitting was more challenging and in some cases required the use of constraints for parameters of the Au–S scattering path. The first half of the scans could also be successfully fitted using only the Au–Ag scattering path. In the first half of the EXAFS scans, the Au–Ag coordination number is around 10, while in the second half it decreases to around 7. In contrast, the Au–S coordination number shows a slight increase to around 1.5 in the second half. Radiation damage thus either causes the Au to migrate to the surface of the cluster, or results in cluster degradation yielding gold thiolate species. The high Au–Ag coordination number before extensive radiation damage shows a strong preference for Au in the *centre* site, in the middle of the cluster.

The high resolution Au L<sub>3</sub>-edge XANES of Au-doped Ag<sub>29</sub> (Figure 4.14) shows a strong whiteline and a number of well-resolved post-edge features. The agreement with a calculated spectrum of Au<sub>1</sub>Ag<sub>28</sub> is excellent when Au occupies the *centre*

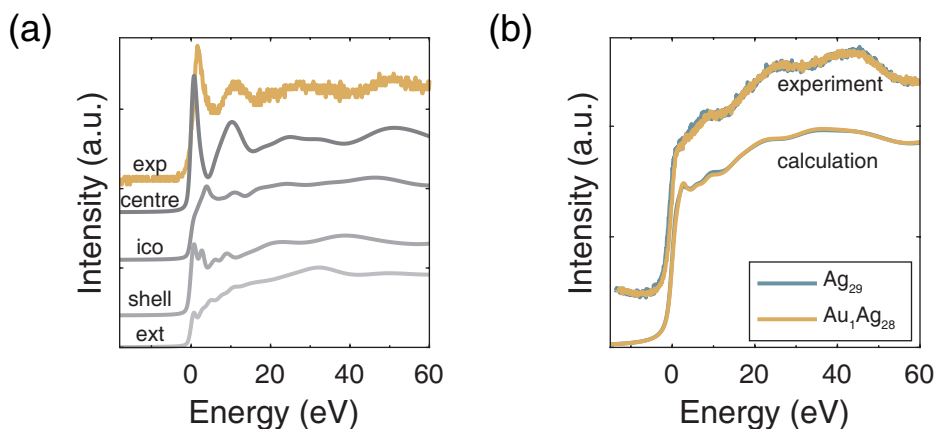


**Figure 4.14** (a) Experimental Au  $L_3$ -edge XANES of Au-doped Ag clusters, together with results of FDMNES calculations for an Au atom in each of the four possible locations in  $Ag_{29}$ . There is good agreement between the experimental spectrum and the calculation for the *centre* position. (b) Ag  $L_3$ -edge XANES of pure  $Ag_{29}$  and Au-doped  $Ag_{29}$  are nearly identical (top), which is confirmed with FDMNES calculations (bottom).

position. With Au in other locations, the spectrum lacks the whiteline. As will be shown in Chapter 7, both Au(I)-thiolate compounds and LA-capped Au clusters have an intense whiteline, but for both these cases the other post-edge features are weaker. XANES presents an intriguing addition to EXAFS for the analysis of bimetallic clusters to determine dopant location. It has lower detection limits than EXAFS, which allows for the study of dilute samples. It is also less critical for the spectra to have high signal-to-noise ratio. This is beneficial for the study of radiation-sensitive compounds. XANES is sensitive to the number and identity of ligands, as well as that of next-nearest neighbours. A downside is that the analysis is less straight-forward than for EXAFS, and may require comparison to reference spectra of compounds with known structure, together with calculations of spectra for expected structures.<sup>291,292</sup>

Ag  $L_3$ -edge XANES was also recorded of the Au-doped clusters, and compared to the spectrum of pure  $Ag_{29}$  clusters (Figure 4.14). Both samples were concentrated using 3 kDa molecular mass cutoff filters and measured in a cryostat at 40 K. We found no difference between the two spectra. Calculations confirm that the Ag  $L_3$ -edge XANES hardly changes upon incorporation of Au into the  $Ag_{29}$  cluster.

A preference for monodoping in the centre of clusters is also observed for  $Pd^{249}$  and  $Pt^{248}$  in  $Au_{25}$ . Monodoping can be rationalised when a cluster doped in the *centre* position exhibits a significantly higher stability than a cluster with

dopants in other locations, or an undoped or multidoped cluster. The Au–Ag bond is stronger than the Ag–Ag bond.<sup>244</sup> When an Au atom occupies the *centre* position in Ag<sub>29</sub>, the number of Au–Ag bonds is maximised, which explains the preference for *centre* doping. In Au clusters, alloying with Ag results in Ag at *ico* sites in Au<sub>25</sub><sup>273,285</sup> and similar sites in Au<sub>144</sub><sup>293,294</sup>. The same is observed for Ag<sub>44</sub> doped with Au.<sup>55</sup> Clearly, *ico* sites are more favourably occupied by Ag than Au. We further propose that Au atoms can't go into the capping layer of Ag<sub>29</sub> (*shell* and *ext* sites) as this would result in significant structural distortions and thus a lower stability due to change in bond length from Ag–S to Au–S. Changes in capping unit metal are rare in AgAu alloy clusters.<sup>295</sup> In BDT-capped Ag<sub>29</sub>, it was found that also the *ext* sites could be replaced with Au<sup>265</sup>, but the presence of phosphines may help stabilise these doped clusters due to the strong Au–P bond.<sup>296,297</sup>

#### 4.4 Conclusions

The introduction of dopants is a promising method for tuning nanocluster properties. In this chapter, the effects of introducing Au into Ag<sub>29</sub>(LA)<sub>12</sub><sup>3-</sup> clusters were investigated. Au atoms can be incorporated both via direct synthesis or by post-synthesis modification, with both methods yielding clusters with similar properties. Doping with Au results in enhanced stability to heat and UV-light. The optical properties of the cluster are also affected, with blueshifts in both absorption and emission spectra. The quantum yield increases by a factor of 3–4. This coincides with a decrease in luminescence lifetime. Together, these observations indicate an increase in radiative decay rate for the doped cluster which may be due to enhanced spin-orbit coupling of Au. The optical properties suggest one major Au-doped Ag<sub>29</sub> species. This species was identified as Au<sub>1</sub>Ag<sub>28</sub>(LA)<sub>12</sub><sup>3-</sup> with electrospray ionisation mass spectrometry. X-ray absorption spectroscopy was used to determine that the Au atom occupies the central position in the cluster. Our experiments also suggest that clusters with Au atoms located on surface sites would cause structural distortions and therefore be less stable. This may explain the strong preference for monodoped species.

#### 4.5 Acknowledgements

We would particularly like to thank Naud van Bunningen for his many contributions to this work, which were part of his master's research project. The European Synchrotron Radiation Facility (ESRF) is thanked for beamtime (proposals CH4593 and CH4969). Lucia Amidani and Blanka Detlefs are thanked for providing beamline support, and Maarten Bransen, Naud van Bunningen, Hebatalla Elnaggar,

Ties Haarman and Mario Delgado-Jaime are thanked for their participation and help during the beamtimes. Arjan Barendregt is thanked for help with mass spectrometry measurements, which was performed within the framework of The Netherlands Organisation for Scientific Research (NWO) and supported by the large scale proteomics facility Proteins@Work (project 184.032.201) embedded in The Netherlands Proteomics Centre. This work was financially supported by the Debye Graduate Programme (NWO project 022.004.016), and ESRF Graduate Programme.

#### 4 | Single atom doping of monodisperse Ag<sub>29</sub> clusters

## Additional spectra; bimetallic clusters

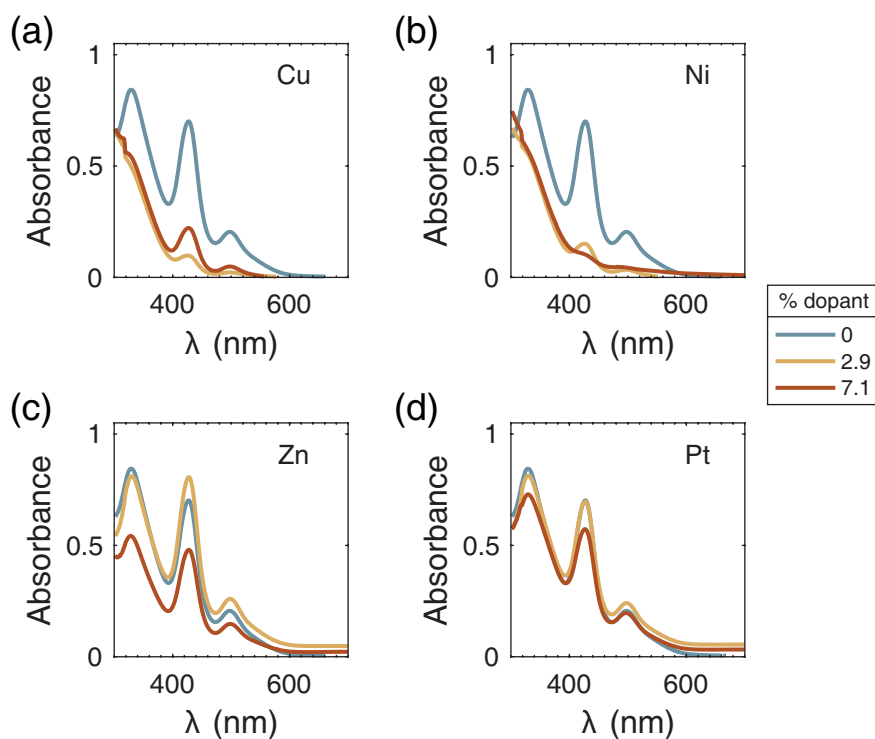


**Figure B.1** UV-Vis spectra of Ag clusters synthesised with (a) Cu, (b) Ni, (c) Zn and (d) Pt. There is no shift in absorption features for any of these metals. For Cu and Ni, characteristic absorption features of  $\text{Ag}_{29}$  are very weak, suggesting these metals may interfere with the synthesis.

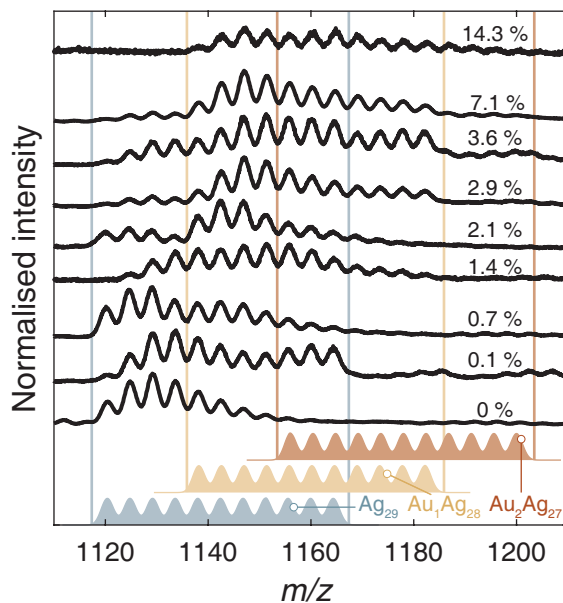


**Figure B.2** Mass spectra of Au-doped Ag<sub>29</sub> clusters with Au concentrations of 0–14.3 %, shown for the overall  $z = 5^-$  charge state. Theoretical spectra of Ag<sub>29</sub> (blue), Au<sub>1</sub>Ag<sub>28</sub> (yellow) and Au<sub>2</sub>Ag<sub>27</sub> (orange) with all possible number of H<sup>+</sup>/Na<sup>+</sup> exchanges are shown for comparison. The vertical lines mark the boundaries of the *m/z* ranges. The Au<sub>1</sub>Ag<sub>28</sub> cluster is detected from the 0.7% Au sample, while Au<sub>2</sub>Ag<sub>27</sub> is present from 7.1% (although different samples of the same Au concentration show somewhat different contributions). Even for 14.3% Au, which has an average composition of Au<sub>4</sub>Ag<sub>25</sub>, the cluster Au<sub>1</sub>Ag<sub>28</sub> dominates the spectrum.

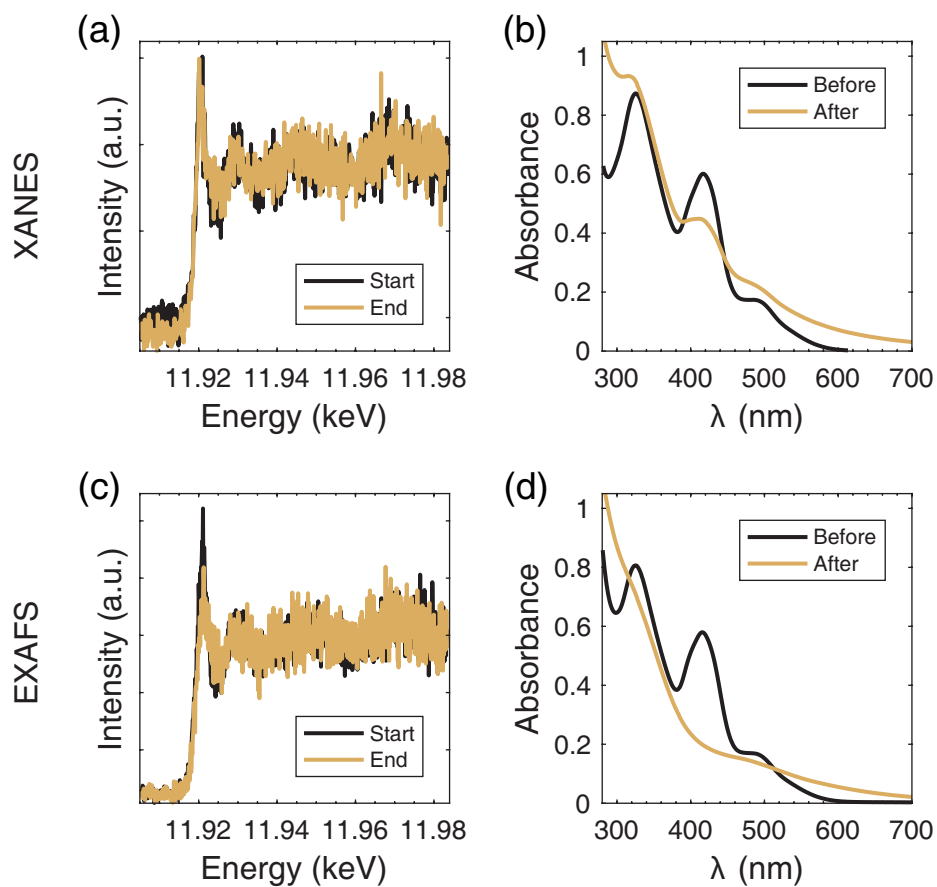


**Figure B.3** Effect of radiation damage during XAS measurements. (a) XANES spectra at the start and end of the experiment. (b) UV-Vis absorption spectra before and after recording XANES. In (c) and (d), the same is shown for the sample used for EXAFS measurements. Radiation damage is more severe for EXAFS than for XANES.



# PART III





## Size tuneability of luminescent Au clusters

---

### Abstract

In contrast to Ag clusters, which were found to be atomically monodisperse, Au clusters capped with lipoic acid (LA) show polydispersity. However, the size distribution and optical properties can be tuned by varying the NaOH concentration during synthesis. From UV-Vis spectroscopy, three regimes were identified. Mass spectrometry identified cluster sizes from Au<sub>2</sub> to Au<sub>~25</sub>. Larger species were identified with analytical ultracentrifugation, up to Au<sub>~45</sub>. Despite this discrepancy, both techniques show that a low NaOH concentration favours large clusters. The NaOH concentration also affects the size distribution or composition of the synthesis intermediates, which are formed by addition of HAuCl<sub>4</sub> to LA solution. Based on their optical properties, the intermediates are identified as Au(I) species with different degrees of aggregation, although the presence of Au(III) could not be excluded. At low NaOH concentrations, the reaction between LA and HAuCl<sub>4</sub> initially results in the rapid formation of large Au nanoparticles with surface plasmon absorption. However, these nanoparticles are highly unstable and disappear within seconds.

---



*“We demand rigidly defined areas of doubt and uncertainty!”*

— Douglas Adams, *The Hitchhiker’s Guide to the Galaxy*

## 5.1 Introduction

Lipoic acid (LA) is a promising ligand for the preparation of luminescent noble metal clusters. Its carboxylic acid group allows for functionalisation which can be used to tune cluster solubility and reactivity as well as luminescence colour and intensity.<sup>72,73,298–300</sup> As discussed in previous chapters, LA-capped Ag clusters are monodisperse and highly stable. Doping with a few percent Au increases stability and luminescence intensity, but a higher Au concentration has a detrimental effect on the optical properties. Nevertheless, even pure Au clusters with LA show luminescence.<sup>165,191</sup> This makes them promising candidates for biomedical applications such as fluorescence imaging, which has already been demonstrated for LA-capped Au to detect Hg<sup>2+</sup> inside cells<sup>87</sup> and to determine intracellular temperature<sup>301</sup>.

Despite numerous studies of Au clusters capped with LA<sup>87,165,191,301,302</sup> or functionalised LA<sup>298,299,303</sup>, accurate size characterisation is lacking. The complexity of many functionalised LA-ligands may contribute to the difficulty in obtaining high quality mass spectra.<sup>72</sup> In one case, a broad size distribution around 7–10 kDa was observed.<sup>304</sup> However, zwitterionic functionalisation of the ligands gave rise to electrostatic interactions that may result in multiple ligand layers.

In this chapter, we describe the synthesis of LA-capped Au clusters from HAuCl<sub>4</sub>, and the characterisation of the clusters. The protocol used for preparation of monodisperse Ag<sub>29</sub> clusters (see Chapter 2) does not yield well-defined Au clusters. Typical synthesis protocols for LA-capped Au clusters use a small amount of NaOH to dissolve LA, rather than reducing it with NaBH<sub>4</sub>.<sup>165</sup> Recent work has highlighted the role of NaOH in the successful, rapid synthesis of aqueous Au<sub>25</sub>(SR)<sub>18</sub><sup>–22</sup> and in the tuning of cluster size of glutathione-capped Au clusters.<sup>196,305</sup> Inspired by this, we investigated the role of NaOH in the synthesis of LA-capped Au clusters and found that the optical properties of the clusters could be tuned by varying the NaOH concentration.

A certain amount of NaOH is required to ensure ligands and clusters do not sediment. Beyond this, additional NaOH results in changes in the UV-Vis absorption spectra of the clusters. All clusters show red and near-infrared luminescence, with a quantum yield of 0.2–0.3%. Interestingly, despite differences in absorption spectra, the excitation spectra of all samples show the same features. This suggests

all samples contain one dominating luminescent species, in addition to a distribution of non-luminescent (or weakly luminescent) clusters. The polydispersity of the samples was confirmed with analytical ultracentrifugation, which found broad distributions of sedimentation coefficients, and with mass spectrometry, from which a large number of cluster species were identified with sizes  $\text{Au}_2$  to  $\text{Au}_{\geq 25}$ . While both techniques agree that the sample with lowest NaOH concentration contains the largest clusters, analytical ultracentrifugation finds larger clusters than mass spectrometry. This discrepancy has not yet been fully resolved.

We further investigated the synthesis procedure of the clusters by characterising the synthesis intermediates, which contain ligand and  $\text{HAuCl}_4$  but no reducing agent. Synthesis intermediates of thiolate-protected Au clusters are aggregates or polymers, and tailoring their size and structure is a common strategy to obtain different sizes of Au clusters.<sup>204</sup> The composition of the polymers is often thought to be  $(\text{Au(I)}-\text{SR})_n$ <sup>30,76,200–202</sup>, where aggregation occurs due to Au(I)–Au(I) aurophilic interactions or van der Waals interactions between ligands.<sup>204</sup> Recent work suggests  $(\text{Au(I)}-\text{SR})_n$  may only be formed when water is present or at large excess of thiols.<sup>203,306,307</sup> It is reasonable to assume that synthesis intermediate composition also depends on whether the ligand is a thiol or a disulfide such as LA.

The synthesis intermediates of LA-capped Au clusters were characterised with the same techniques as the clusters. No Au-containing species could be identified with mass spectrometry, but based on optical properties we identify the intermediates as Au(I) species. Sedimentation coefficient distributions of the intermediates were found to depend on NaOH concentration, suggesting that the degree of aggregation of the intermediate may determine the final cluster size. We also present evidence that at low NaOH concentrations, the initial reaction between  $\text{HAuCl}_4$  and LA results in the formation of large Au nanoparticles with surface plasmon absorption. These nanoparticles are highly unstable and disappear within minutes, possibly due to a comproportionation reaction with remaining Au(III).

## 5.2 Experimental methods

### Chemicals

$\text{HAuCl}_4 \cdot 3\text{H}_2\text{O}$  ( $\geq 99.9\%$ ),  $\text{NaBH}_4$  (99%), ( $\pm$ )- $\alpha$ -lipoic acid ( $\geq 99\%$ ) and methanol ( $\geq 99.9\%$ ) were purchased from Sigma Aldrich. NaOH ( $\geq 99.0\%$ ) was obtained from Merck. 1-Butanol (99.5%) and Nile Blue A were obtained from Acros. Water was of Milli-Q quality, purified using a Millipore Direct-Q 3 water purification system. 4-(dicyanomethylene)-2-methyl-6-(4-dimethylaminostyryl)-4H-pyran (DCM dye) was obtained from Exciton.

### Synthesis

10 mg lipoic acid (49  $\mu\text{mol}$ ) was placed in a 20 mL glass vial with water and a small amount of NaOH solution, with a total volume of 10.5 mL. Three concentrations of NaOH were investigated in detail; 8.9, 12 and 89 mM. This corresponds to 0.5 mL 0.2 M, 0.7 mL 0.2 M and 0.5 mL 2 M NaOH in the synthesis. While stirring, 0.25 mL 68 mM  $\text{HAuCl}_4 \cdot 3 \text{H}_2\text{O}$  was added (17  $\mu\text{mol}$ ) giving the synthesis intermediate. After 15 min, the synthesis intermediate was reduced with  $\text{NaBH}_4$  (1.7 mg in 0.5 mL water). Vials were wrapped in aluminium foil, kept closed except when adding reagents, and stirred throughout the synthesis, which was done at room temperature. Clusters were used without additional purification (except where explicitly noted), after stirring overnight. The synthesis intermediates were also studied. When describing these samples, the NaOH concentrations in the final sample volume are used.

### Optical spectroscopy

UV-Vis absorption spectra were recorded using a Perkin Elmer Lambda 40 or a Varian Cary 50 spectrometer. Fast UV-Vis spectra during formation of the synthesis intermediate were recorded using an Avantes AvaSpec 2048 spectrometer and a QX Hellma 1.000 UV-Vis probe. The lamp was a DH-2000 CAL from Ocean Optics. The integration time was set to 1.05 ms, and repetition rate of the setup was 30–60 ms. Emission spectra were recorded on a Jasco Spectrofluorometer FP-8300. The typical excitation wavelength was 580 nm. Room temperature luminescence lifetimes at 750 nm were recorded using a Hamamatsu R928 photomultiplier with a time-correlated single photon counting card (TimeHarp 260 PC, PicoQuant), and a laser (Opolette HE 355-II, Opotec Inc.) operating at 500 nm as excitation source. All absorption and emission spectra were recorded of undiluted samples.

**Quantum yield** The quantum yield of Au clusters (8.9 mM NaOH) was determined using DCM dye and Nile Blue A in ethanol as references. A Varian Cary 50 spectrometer was used to record UV-Vis absorption spectra. Emission spectra were recorded on a Jasco FP8300 Spectrofluorometer. The excitation wavelength used was 550 nm. Au clusters, Nile Blue A and DCM dye were diluted with water or ethanol to prepare five samples with absorbance  $\leq 0.1$  at 550 nm. The integrated emission intensity of each spectrum scales linearly with the absorbance at 550 nm (Figure 5.1); the slopes of the lines are proportional to the quantum yield. The quantum yields of Nile Blue A and DCM dye in ethanol are 27 and 43.5%, respectively.<sup>175,176</sup> The quantum yield of the Au clusters can be calculated according to:

$$\Phi = \Phi_{\text{R}} \frac{m}{m_{\text{R}}} \frac{n^2}{n_{\text{R}}^2} \quad (5.1)$$

where  $m$  is the slope from Figure 5.1,  $n$  is the solvent refractive index and  $\Phi$  is the quantum yield. In each case, the subscript R refers to the reference dye. Values for the solvent refractive index are  $n = 1.33336$  and  $n_{\text{R}} = 1.3611$  for water and ethanol, respectively.<sup>177</sup>

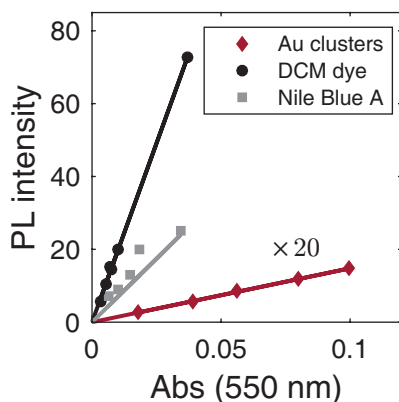


**Figure 5.1** Integrated emission intensity as a function of absorbance at 550 nm for Au clusters (multiplied by 20), Nile Blue A and DCM dye. The lines are a fit through the points.

### Mass spectrometry

MS measurements were performed in negative ion mode using an electrospray ionisation time-of-flight (ESI-ToF) instrument (LC-T; Micromass, Manchester, U.K.) equipped with a Z-spray nano-electrospray ionisation source. Needles were made from borosilicate glass capillaries (Kwik-Fil, World Precision Instruments, Sarasota, FL) on a P-97 puller (Sutter Instruments, Novato, CA), coated with a thin gold layer by using an Edwards Scancoat (Edwards Laboratories, Milpitas, CA) six Pirani 501 sputter coater. After purification, the sample was sprayed into the mass spectrometer. The applied voltage on the needle was typically 1180 V and the sample cone voltage was varied between  $-7$  and  $0$  V for measurements of clusters, and increased up to  $-40$  V for synthesis intermediates. All spectra were mass calibrated in negative ion mode, using an aqueous solution of phosphoric acid ( $0.1\%$  v/v).

**Sample purification** For mass spectrometry, cluster samples were purified using 1-butanol (BuOH) to extract water, containing excess ligands and other possible contaminants, until the clusters sediment, after which they are washed with a small amount of methanol (MeOH) and redispersed in water. This was done by mixing  $300\ \mu\text{L}$  cluster solution,  $400\ \mu\text{L}$  BuOH and  $100\ \mu\text{L}$  MeOH in an Eppendorf vial. The vial was briefly centrifuged to speed up phase separation, and the upper colourless organic layer was removed. Next,  $300\ \mu\text{L}$  BuOH was added, the vial was shaken and centrifuged, and the organic layer was again removed. This was repeated until the clusters just sedimented. Typically, 2–4 extractions with BuOH were needed. After removing the final organic layer and washing with MeOH ( $50$ – $100\ \mu\text{L}$ ), the clusters were redispersed in water ( $50$ – $100\ \mu\text{L}$ ).

**Data analysis** Analysis and quantification of the data was done in two steps. The first involved identification of cluster species. Theoretical spectra of numerous possible species were calculated using ChemCalc<sup>151</sup> with full width at half maximum = 0.1 and compared with the experimental spectra. In calculating theoretical mass spectra, we assume that neither of the two S-atoms in LA is present as a thiol (thus LA is  $C_8H_{14}O_2S_2$ ). Not all ion signals could be assigned. Especially at high  $m/z$ , overlap of  $Na^+$  adduct signals belonging to different species complicates the assignment. In the second step, an  $m/z$  range was chosen for each cluster and the intensity of each species was determined by integrating this area of the spectrum. Where ion signals of two species overlap, the ranges were shortened if the overlap was minor. If the overlap was significant, the species with lowest intensity was ignored.

### Analytical ultracentrifugation

Sedimentation velocity experiments have been performed on XL-I and XL-A Analytical ultracentrifuges (Proteomelab and Optima XL-A, Beckman Coulter) using absorbance optics. All measurements were performed at 20 °C. Samples were centrifuged in 12 mm path length double-sector Aluminium centrepieces with sapphire windows in an An60-Ti rotor; the reference sector was filled with Milli-Q water. Changes in solute concentrations were detected at absorption wavelengths of 380 and 484 nm. Synthesis intermediates were measured undiluted, at 380 nm, and using centrifugation speed of 60 000 rpm. Clusters were measured at 380 and 484 nm and using centrifugation speeds of 40 000 and 60 000 rpm. Samples were undiluted for measurements at 484 nm and diluted 1 : 1 with water at 380 nm. Fresh samples were prepared for each experiment.

Analysis and fitting of the data was performed using the program Sedfit v 14.3.<sup>158</sup> A continuous  $c(s)$  distribution model was fitted to the data. The resolution was set to 200 over a sedimentation coefficient range typically up to 20S. The meniscus and the bottom were kept at fixed values, and the frictional coefficient, the baseline and the raw data noise were floated in the fitting. All sedimentation coefficient distributions are normalised to area.

**Calculations of sedimentation coefficients** Results were compared with data from literature. Where a different solvent such as toluene was used for the experiment, the sedimentation coefficient in water was calculated using Equation (1.15), which relates a particle's size and density to its sedimentation coefficient. It is assumed that the particle size and density do not change when the solvent changes from 1 (toluene) to 2 (water), giving the following relation:

$$s_2 = s_1 \frac{\eta_1}{\eta_2} \frac{\rho_p - \rho_2}{\rho_p - \rho_1} \quad (5.2)$$

where  $\eta$  is the viscosity,  $\rho$  the density and the subscript p refers to the particle. This equation can also be used to calculate the sedimentation coefficient of a particle p1 from the known sedimentation coefficient and density of another particle, p2, with the same size, in which case it reduces to:

$$s_{p1} = s_{p2} \frac{\rho_{p1} - \rho_s}{\rho_{p2} - \rho_s} \quad (5.3)$$

where  $\rho_s$  is the density of the solvent.

Sedimentation coefficients can also be calculated by combining Equations (1.16) and (1.17), which relate the sedimentation coefficient to molar mass and density. The density of the cluster must be known. Assuming that the volume of a cluster is the sum of total ligand and gold volumes, this is given by:

$$\rho_p^{-1} M_p = \rho_{Au}^{-1} N_{Au} M_{Au} + \rho_{LA}^{-1} N_{LA} M_{LA} \quad (5.4)$$

where  $M$  is the molar mass,  $N$  the number of Au atoms or LA molecules and  $\rho$  is the density and subscripts p, Au, LA refer to particle, gold and lipoic acid respectively.

Values for viscosity and density of water are:  $\rho = 1.00 \text{ g mL}^{-1}$  and  $\eta = 1.00 \text{ mPa s}$ .<sup>308</sup> For toluene, the values are:  $\eta = 0.59 \text{ mPa s}$  and  $\rho = 0.867 \text{ g mL}^{-1}$ .<sup>309</sup> Furthermore, the molar mass of Au and LA are 197 and 206.33  $\text{g mol}^{-1}$ , respectively. The densities are respectively 19.3 and 1.2  $\text{g cm}^{-3}$ , where the last is an estimate.<sup>152,177</sup>

## 5.3 Results and discussion

### Synthesis, optical properties and stability

The synthesis of LA-capped Au clusters proceeds in two steps. First,  $\text{HAuCl}_4$  solution is added to a solution of LA and NaOH to form a synthesis intermediate. This is pale yellow to colourless, with higher NaOH concentrations giving a lighter colour. After 15 min, the synthesis intermediate is reduced to form clusters by addition of  $\text{NaBH}_4$ . The first step is discussed in more detail later in this chapter. The reduction step is rapid, with a colour change within minutes. The final NaOH concentration was 7.1–89 mM while LA and Au concentrations were kept constant at 4.3 and 1.5 mM, respectively. The final colour of the cluster solution depends on the NaOH concentration, and varies from pale brown to reddish brown. All samples are used directly without any purification, so that the effect of NaOH on cluster properties can be studied without any additional changes to the sample composition. The use of high NaOH concentration was inspired by a synthesis protocol for aqueous  $\text{Au}_{25}(\text{SR})_{18}$ , where NaOH was used to increase the etching ability of the thiol ligands and decrease the reduction ability of  $\text{NaBH}_4$ , resulting in rapid formation of clusters.<sup>22</sup> For LA-capped clusters, we find that NaOH can be used to tune the optical properties.

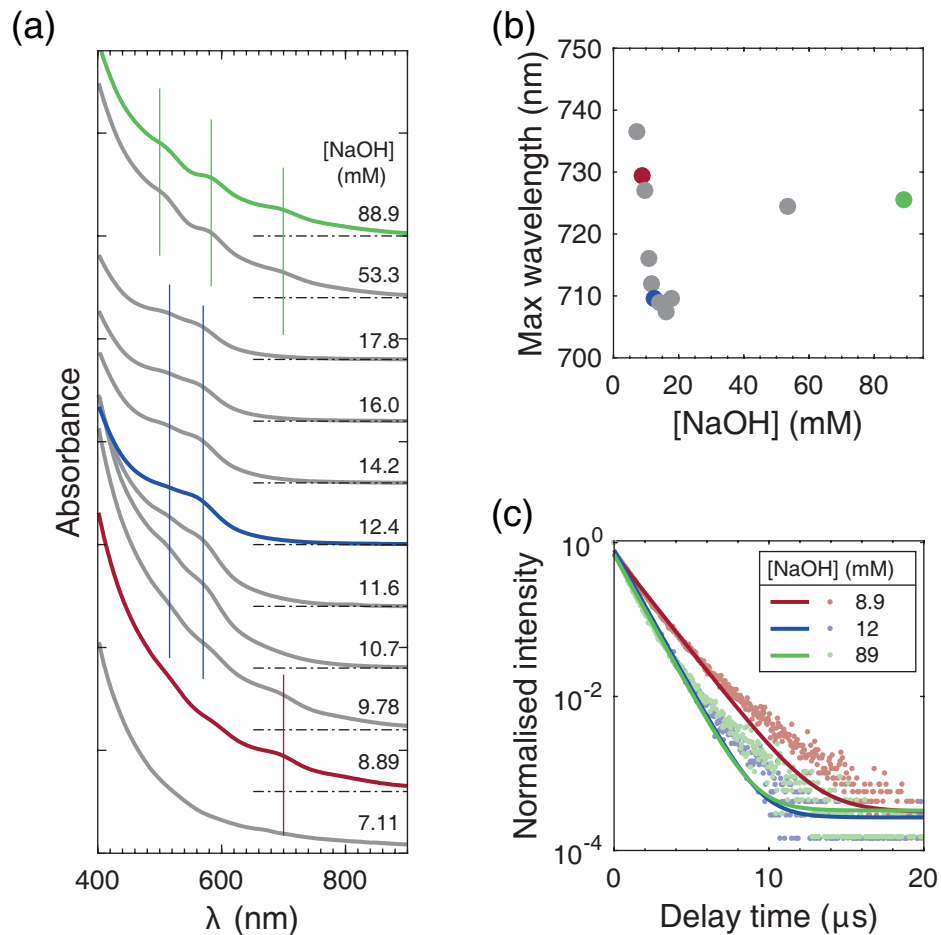


**Figure 5.2** Optical properties of Au clusters capped with LA. (a) UV-Vis absorption spectra for samples with NaOH concentrations from 7.1–89 mM. Vertical lines mark characteristic absorption features. (b) Maximum emission wavelength, for excitation at 580 nm. (c) Luminescence decay curves for three samples. Solid lines are fits of monoexponential decay, with lifetimes 1.7, 1.2 and 1.2  $\mu\text{s}$  for clusters with 8.9, 12 and 89 mM NaOH, respectively.

From the UV-Vis absorption spectra of clusters with different NaOH concentrations, shown in Figure 5.2, we make a number of observations. First, a certain amount of NaOH is needed for a successful synthesis. At just 7.1 mM NaOH, no pronounced absorption features are observed in UV-Vis spectra, the luminescence is weak, and the sample appears turbid. The synthesis intermediate of this sample contained large flakes of sediment. The NaOH concentration was not sufficient to deprotonate all LA, which is required for water-solubility. Note that  $\text{HAuCl}_4$  is acidic and will also react with NaOH.

Second, optical properties of LA-capped Au clusters depend on the NaOH concentration. At low NaOH concentrations (8.9–9.8 mM), a pronounced absorption feature is observed around 680 nm. The emission spectra have a maximum around 730 nm. At medium NaOH concentrations (11–18 mM), absorption features around 505 and 580 nm appear, with an emission maximum at 710 nm. Both absorbance and emission intensity decrease with increasing NaOH concentration. Finally, at high NaOH concentrations (53–89 mM), there are three peaks in the absorption spectrum at 505, 580 and 690 nm, and the emission maximum is at 725 nm. Optical properties resemble those of clusters with low NaOH concentration, but absorption features below 600 nm are more pronounced. There are thus three different regimes of clusters with different optical properties. At certain NaOH concentrations, there is a switch from one regime to the next. However, within one regime, an increase in NaOH concentration simply causes a decrease in absorbance and emission intensity, with little effect on wavelength.

A third observation is that clusters with the highest NaOH concentrations are unstable, with a strong decrease in absorbance after a couple of days. To limit cluster degradation, all characterisation was done on samples the day after synthesis. For potential applications, this is of course a major downside, although there is sufficient evidence to suggest high stability can be obtained after purification for example with molecular mass cutoff filters.<sup>87,165,191,298</sup>

Red luminescence is visible for all samples using a handheld UV-lamp, although it is weaker than for  $\text{Ag}_{29}(\text{LA})_{12}^{3-}$  clusters. The quantum yield (QY) was determined for the sample with 8.9 mM NaOH, and found to be 0.2–0.3% using 4-(dicyanomethylene)-2-methyl-6-(4-dimethylaminostyryl)-4H-pyran (DCM dye) or Nile Blue A as a reference. The luminescence of LA-capped Au clusters shows multi-exponential decay (Figure 5.2). The average luminescence lifetimes<sup>274</sup>,  $\tau_{\text{avg}} = \sum_i I_i t_i / \sum_i I_i$ , of clusters with 8.9, 12 and 89 mM NaOH are 1.8, 1.2 and 1.3  $\mu\text{s}$ , respectively. There is little dependence on emission wavelength, and the long lifetime indicates that the luminescence is due to a forbidden transition which explains the low intensity.

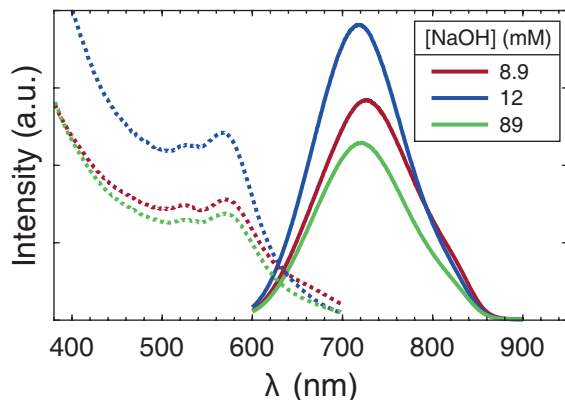


**Figure 5.3** Emission (solid) and excitation (dashed) spectra of Au clusters capped with LA, with three different NaOH concentrations.

The luminescence and the multiple absorption features are strong evidence of cluster-sized species in each of the samples. Furthermore, there is a clear absence of a pronounced surface plasmon absorption. The absorption features of all clusters are weak and significantly less pronounced than those of LA-capped Ag clusters, suggesting polydispersity. It is interesting to note that, while absorption spectra and maximum emission wavelength depend on NaOH concentration, the excitation spectra of all samples have identical features, see Figure 5.3. This suggests that there may be one dominant luminescent species which is present in all samples, but at different concentrations and together with other non-luminescent species.

The excitation spectrum resembles that of  $\text{Au}_{22}(\text{SG})_{18}$  (where SG is glutathione).<sup>162</sup> This similarity in optical properties has been noted before and was used to assign a cluster size of  $\text{Au}_{22}(\text{LA})_{12}$ , where the number of ligands was deduced from studies on ligand oxidation.<sup>165,310</sup>  $\text{Au}_{22}(\text{SG})_{18}$  was found to have a QY of 8%, an order of magnitude higher than our clusters.<sup>162</sup> If this highly luminescent  $\text{Au}_{22}$  is indeed the luminescent species in our samples, it can only be a minor component. Non-luminescent species dominate, and it is their absorption features that determine the UV-Vis spectrum of the sample.

The absorption spectra of the three different NaOH concentration regimes can be compared with those of atomically monodisperse Au clusters with known compositions. The absorption spectrum of our clusters with 12 mM NaOH resembles those of clusters in the size range  $\text{Au}_{15}(\text{SR})_{13}$  to  $\text{Au}_{23}(\text{SR})_{16}$ , and the 8.9 mM NaOH sample resembles  $\text{Au}_{24}(\text{SR})_{20}$  to  $\text{Au}_{38}(\text{SR})_{24}$ .<sup>11</sup> For clusters capped with glutathione, the absorption onset shifts to lower wavelength with decreasing cluster

size.<sup>150</sup> This suggests 12 mM NaOH clusters are smaller than those with 8.9 mM NaOH. Note that all these clusters from the literature have monothiolate ligands, and bidentate bonding of LA can give different metal-to-ligand ratios, surface structures and optical properties. For instance, Au<sub>22</sub> can be obtained with 16, 17 and 18 glutathione ligands, and the first two are only weakly luminescent with QY around 0.2%.<sup>150</sup> The number of ligands is expected to have a large influence on the surface structure.<sup>162</sup>

Attempts were made to prepare Au clusters using the same protocol as for LA-capped Ag clusters (see Chapter 2). However, this resulted in Au clusters with weak luminescence intensity and no pronounced absorption features. We also briefly investigated other parameters in the synthesis of LA-capped Au clusters. In all cases, the clusters with 8.9 mM NaOH were studied. Varying the waiting time between HAuCl<sub>4</sub> and NaBH<sub>4</sub> addition had a negligible effect on the UV-Vis spectrum, while increasing the NaBH<sub>4</sub> concentration led to a minor decrease in the absorbance at 680 nm. Finally, we studied the effect of NaOH addition after the synthesis is complete. Only a minor decrease in UV-Vis absorbance was observed and the clusters were not converted to a different size regime.

### Cluster size and composition

Different optical properties of clusters are often due to their different sizes.<sup>11</sup> We used a combination of electrospray ionisation mass spectrometry (ESI-MS) and sedimentation velocity analytical ultracentrifugation (SV-AUC) to characterise the clusters further. Three cluster samples were chosen for detailed characterisation, with 8.9, 12 and 89 mM NaOH.

**Sedimentation velocity analytical ultracentrifugation (SV-AUC)** Sedimentation coefficient distributions of the samples are shown in Figure 5.4. Measurements at 484 nm were done for two different centrifugation speeds, 40 000 and 60 000 rpm, with little differences in distributions. Therefore only 60 000 rpm data is shown. Frictional ratios  $f/f_0$  are close to 1 for the 8.9 and 12 mM NaOH samples, meaning these clusters are to a good approximation spherical. For the 89 mM NaOH sample, a frictional ratio of 1.7 is obtained, indicating an asymmetrical shape.<sup>311</sup> Changing the absorption wavelength to 380 nm resulted in different distributions, especially for the 12 and 89 mM NaOH samples. For this experiment, the samples were diluted 1 : 1 with water, but UV-Vis spectra do not show any changes over time. We therefore conclude that the observed differences reflect actual differences in species probed at different wavelengths and not degradation caused by instability upon dilution.

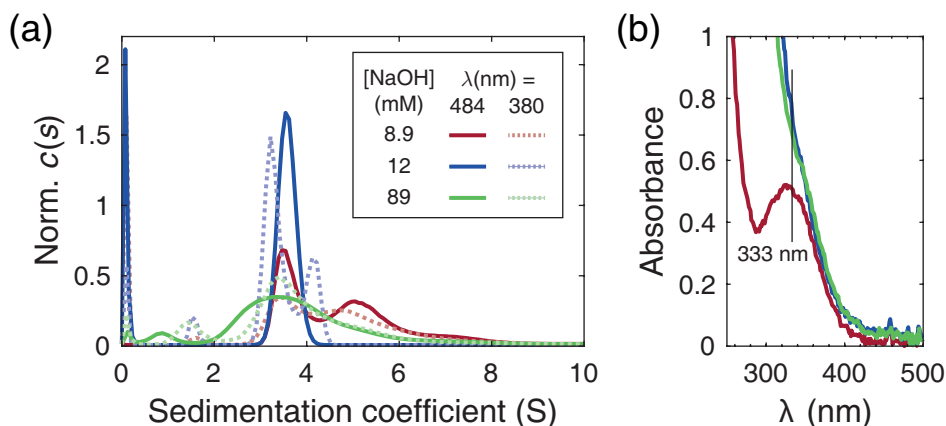


**Figure 5.4** (a) Sedimentation coefficient distributions for Au clusters with 8.9, 12 and 89 mM NaOH, recorded at 380 and 484 nm (dashed and solid lines, respectively). The centrifugation speed was 60 000 rpm. (b) UV-Vis absorption spectra recorded in the cell after sedimentation, near the bottom of the cell. The black line indicates 333 nm, the absorption maximum of LA.

We focus on the 484 nm measurements, as this wavelength is closest to the characteristic absorption and excitation features of the clusters. The three samples show different distributions, all of which are broad, indicating polydisperse species. The sample with 12 mM NaOH has the sharpest distribution, centred around 3.5 S. This species appears to be present in the other two samples as well, although for the 89 mM NaOH sample the distribution is very broad, and the 8.9 mM NaOH sample additionally contains 5.0 and 7.1 S species. UV-Vis absorption spectra recorded near the bottom of the cell after sedimentation show that the 8.9 mM NaOH sample contains free LA, while the other two probably still contain Au–LA complexes (see also Figure 5.9). This suggests an incomplete reduction in the latter case.

To estimate the size of the clusters from SV-AUC, we can compare with sedimentation coefficients of clusters with known size. One example is undecagold,  $(\text{Ar}_3\text{P})_7\text{Au}_{11}\text{I}_3$ , where  $\text{Ar}_3\text{P}$  is 4,4',4''-phosphinidynetri(benzenemethanamine), which was found to have sedimentation coefficient of 2.4 S.<sup>44</sup> The LA-capped clusters are bigger than  $\text{Au}_{11}$ . The sedimentation coefficients of three atomically monodisperse Au clusters,  $\text{Au}_{25}(\text{SR})_{18}$ ,  $\text{Au}_{38}(\text{SR})_{24}$  and  $\text{Au}_{144}(\text{SR})_{60}$ , were determined to be 6.8, 9.6 and 27.1 S, respectively.<sup>152</sup> The ligand was the monothiol 2-phenylethanethiol. However, these experiments were performed in toluene so they can not be directly compared to our results. To calculate sedimentation

**Table 5.1** Calculated densities and sedimentation coefficients of LA-capped Au clusters.

Cluster	Mass (kDa)	Density (g mL <sup>-1</sup> )	Sedimentation coefficient (S)
Au <sub>2</sub> (LA) <sub>2</sub>	0.81	2.21	0.74
Au <sub>6</sub> (LA) <sub>4</sub>	2.01	2.68	1.7
Au <sub>16</sub> (LA) <sub>8</sub>	4.80	3.12	3.4
Au <sub>22</sub> (LA) <sub>12</sub>	6.81	2.98	4.1
Au <sub>26</sub> (LA) <sub>11</sub>	7.39	3.43	4.9
Au <sub>29</sub> (LA) <sub>12</sub>	8.19	3.47	5.3
Au <sub>36</sub> (LA) <sub>14</sub>	9.98	3.60	6.1
Au <sub>45</sub> (LA) <sub>16</sub>	12.2	3.79	7.3

coefficients of these clusters in water, we use Equation (5.2). The cluster densities are (from smallest to largest cluster) 1.95, 2.43 and 4.51 g mL<sup>-1</sup>.<sup>152</sup> This gives sedimentation coefficients of 3.5, 5.2 and 15.4 S for the three clusters, respectively.

The LA-capped Au clusters thus have similar sedimentation coefficients as Au<sub>25</sub> and Au<sub>38</sub>. However, due to the bidentate nature of LA, the ligand-to-gold ratio is expected to be lower; thus the density and sedimentation coefficients may be different for clusters with dithiolate or monothiolate ligands but the same number of Au atoms.

To the best of our knowledge, there have been no SV-AUC studies of dithiolate-protected Au clusters. However, we can also compare the sedimentation coefficient of LA-capped Ag clusters. As demonstrated in Chapter 2, Ag<sub>29</sub>(LA)<sub>12</sub><sup>3-</sup> clusters are monodisperse with mass 5.6 kDa and a uniform sedimentation coefficient of 2.34 S. The density of this cluster can be determined by combining Equations (1.16) and (1.17), which relate the sedimentation coefficient to molar mass and density, and using known values for the density and viscosity of water. This yields a density of  $\rho_p = 2.01$  g mL<sup>-1</sup> for the Ag<sub>29</sub> cluster. This can be used to calculate the expected sedimentation coefficient for a hypothetical cluster Au<sub>29</sub>(LA)<sub>12</sub><sup>3-</sup> (mass 8.2 kDa) which we assume has exactly the same shape and size as its silver equivalent. The density of this Au<sub>29</sub> is then 2.94 g mL<sup>-1</sup>. The sedimentation coefficient of Au<sub>29</sub>(LA)<sub>12</sub><sup>3-</sup>, calculated using Equation (5.3), is 4.6 S.

Sedimentation coefficients were also calculated for other (hypothetical) Au<sub>z</sub>(LA)<sub>y</sub> clusters by combining Equations (1.16) and (1.17). Calculated cluster masses, densities (Equation (5.4)) and sedimentation coefficients for a number of Au<sub>z</sub>(LA)<sub>y</sub> clusters are given in Table 5.1. The compositions of these clusters are taken from mass spectrometry (see below), from the proposed composition Au<sub>22</sub>(LA)<sub>12</sub><sup>310</sup>, or from hypothetical compositions with a ligand-to-gold ratio calculated from the scaling law described in Chapter 2 for Ag<sub>29</sub>(LA)<sub>12</sub><sup>3-</sup>. Note that the Au<sub>29</sub> cluster

has a slightly different density and thus sedimentation coefficient than estimated using Equation (5.3). Densities and sedimentation coefficients in Table 5.1 are calculated assuming spherical particles, while Equation (5.3) takes into account the frictional ratio of 1.2–1.3 determined for Ag<sub>29</sub>.

Overall, a cluster size of around 16 Au atoms is consistent with the 3.5 S species, while the heavier 5.0 and 7.1 S species present in the 8.9 mM NaOH sample may be Au<sub>≥25</sub> and Au<sub>~45</sub>.

**Electrospray ionisation mass spectrometry (ESI-MS)** The Au cluster samples are further characterised using ESI-MS. As with LA-capped silver and bimetallic clusters (Chapters 2 and 4), multiple ion signals are observed even for one cluster in one overall charge state. This is due to deprotonation of LA and subsequent association with Na<sup>+</sup>, which increases the mass by 22 Da but keeps the charge constant. The general composition of a cluster can be written as [Au<sub>z</sub>(LA)<sub>y</sub><sup>a-</sup> - (b + x)H<sup>+</sup> + x Na<sup>+</sup>]<sup>(a+b)-</sup>, where a<sup>-</sup> is the core charge (on Au and S atoms), and (a + b)<sup>-</sup> is the overall charge state which includes charges due to deprotonated ligands without associated Na<sup>+</sup> atoms.

Mass spectra were recorded of samples with and without purification. These show similar ion signals, although the signal-to-noise ratio is significantly improved with purification. All spectra contain multiple ion signals which are assigned to different species, from small species such as Au<sub>2</sub>(LA)<sub>2</sub><sup>2-</sup> to larger species like Au<sub>24</sub>(LA)<sub>11</sub><sup>4-</sup>. Especially for the larger clusters, there are many ion signals due to H<sup>+</sup>/Na<sup>+</sup> exchange, and overlap between ion signals of adjacent clusters makes assignment challenging. The compositions for species with ≥ 20 Au atoms are therefore approximate. For smaller species, ion signals are well separated and isotopic resolution was obtained in some cases, so the composition could be determined with high accuracy. Spectra of some cluster species are shown in Figure 5.5.

To quantify the mass spectrometry results, the intensity of each cluster ion signal per sample was determined. Mass spectra of samples with 8.9, 12 and 89 mM are shown in Figure 5.6, as are histograms of the cluster intensities. Mass spectra were also recorded of samples with a larger range of NaOH concentrations, see Figure 5.7, which also shows the reproducibility of ESI-MS analysis. In general, as the NaOH concentration increases, the contribution of smaller clusters increases. Furthermore, we observe very few clusters with 11–15 Au atoms. There also appears to be a strong preference for clusters with an even number of Au atoms. Bare clusters are known to be more stable when the number of atoms is even, due to electronic stabilisation effects.<sup>312–314</sup> Especially for the smaller species, the fact that LA is bidentate may also help stabilise even-numbered clusters.

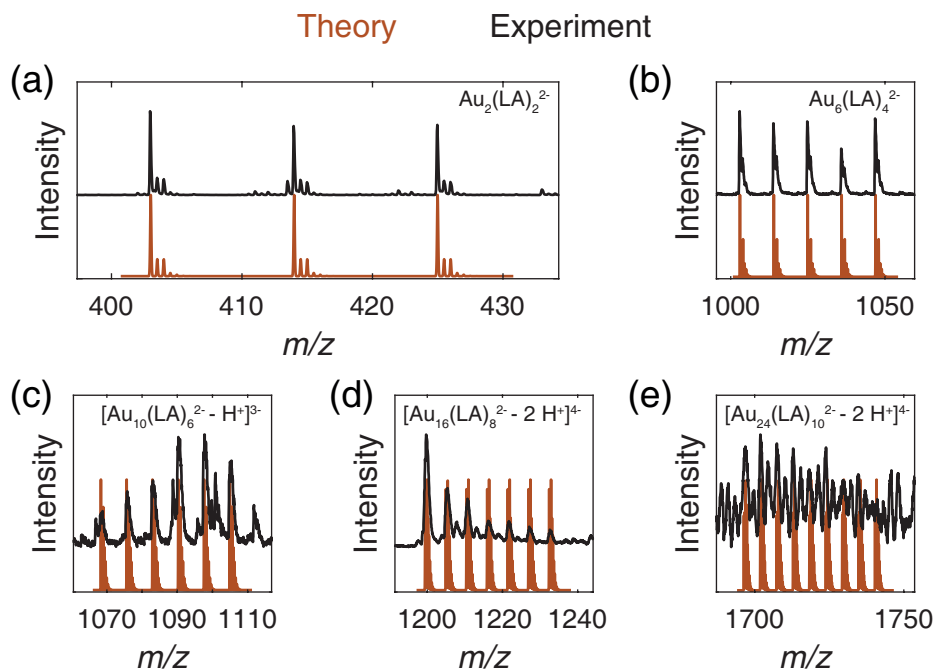


**Figure 5.5** Experimental (black) and theoretical (red) ESI-MS spectra of purified Au clusters, showing a number of identified species. Each cluster has multiple groups of ion signals due to  $\text{H}^+/\text{Na}^+$  exchange. The given composition is for the first ion signal. (a-c) have 12 mM NaOH, (d-e) have 8.9 mM NaOH. In (a), the individual isotope peaks within each of the three groups can be observed.

While insightful, Figure 5.7 may not accurately represent the actual size distributions in the samples. The intensity in mass spectrometry is related to the concentration in solution, but it also depends on how easily a species is ionised, and how stable it is once ionised. Apart from these experimental considerations, the analysis protocol itself may also skew the interpretation of the results, as only ion signals which could be assigned with reasonable certainty to a cluster composition were taken into account. For samples with 89 mM NaOH, hardly any ion signals could be assigned to clusters. These samples were challenging to measure due to the high salt concentration. The small number of identified cluster species in the 89 mM NaOH sample should therefore not be taken as a sign of the sample's monodispersity. Additionally, broad background signals were often observed around  $m/z$  1500 and 3000 for samples with 8.9 mM NaOH (Figure 5.8), but without knowing the charge, the mass of this species remains unknown.

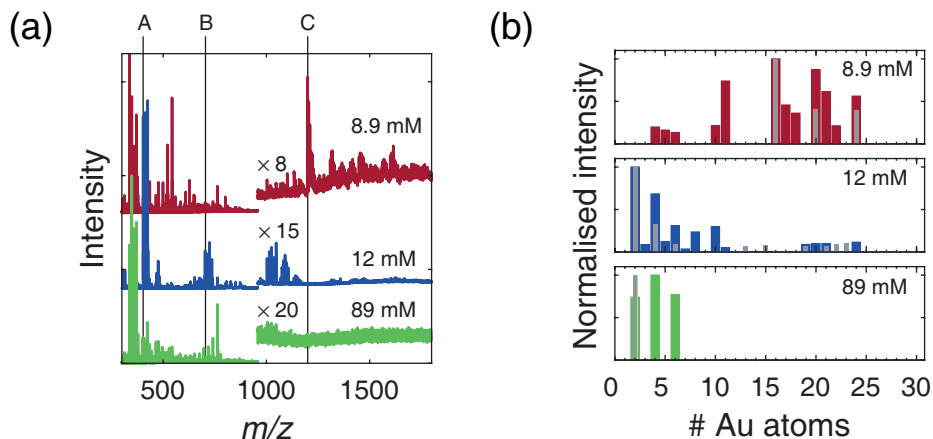


**Figure 5.6** (a) ESI-MS spectra of purified Au clusters with 8.9, 12 and 89 mM NaOH. Spectra have been magnified above  $m/z$  950. The three labelled cluster species A, B and C correspond to  $\text{Au}_2(\text{LA})_2^{2-}$ ,  $\text{Au}_4(\text{LA})_3^{2-}$  and  $[\text{Au}_{16}(\text{LA})_8^{2-} - 2\text{H}^+]^{4-}$ , respectively. (b) Histograms of all identified Au cluster species in the three spectra. Thinner grey bars are of unpurified samples.

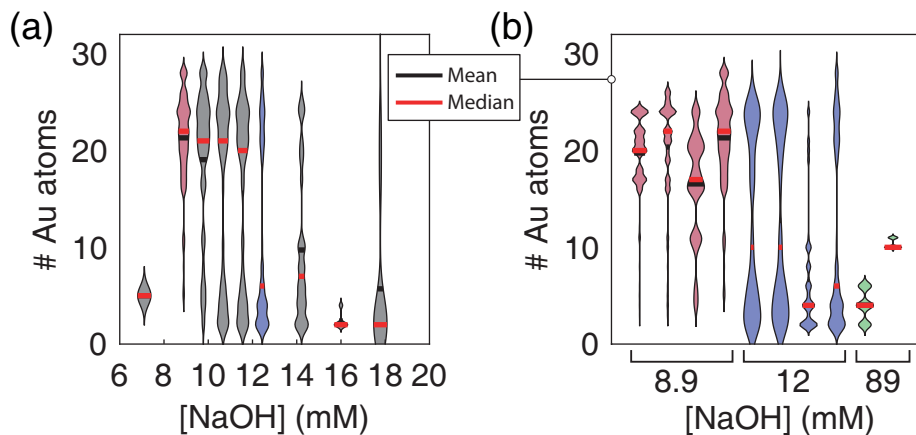


**Figure 5.7** (a) Normalised violin plots showing the size distributions of all identified clusters for samples with NaOH concentration between 7.1 and 18 mM. The mean and median cluster size are marked. Smaller clusters begin to dominate as the NaOH concentration increases. (b) Normalised violin plots for a number of different samples with 8.9, 12 and 89 mM NaOH showing that, despite polydispersity, the sample composition is reproducible.

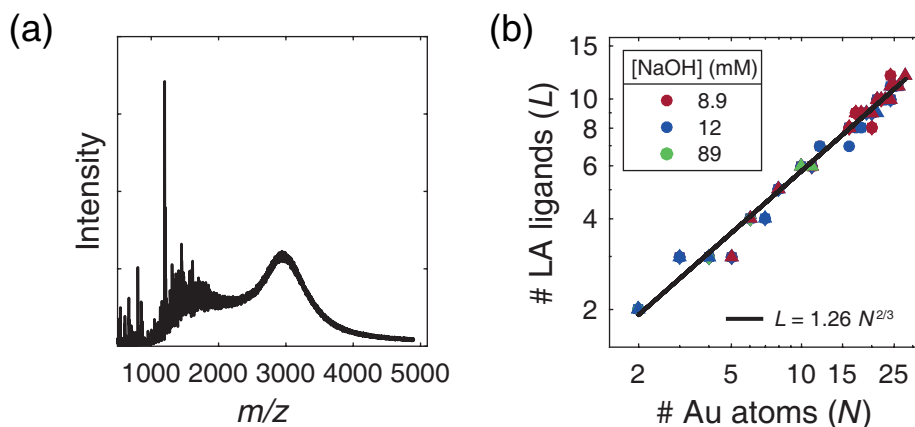


**Figure 5.8** (a) Mass spectrum of Au clusters with 8.9 mM NaOH, showing broad background signals around  $m/z$  1500 and 3000. The charges and thus masses of these species are unknown. The intense signal at  $m/z$  1200 is from  $[\text{Au}_{16}(\text{LA})_8]^{2-} - 2\text{H}^+$ . (b) The number of ligands scales with the number of gold atoms, following a power law with exponent  $2/3$ . Different plot markers indicate samples prepared on different days. The solid line is a power law fit.

The nano-scaling law proposed by Dass<sup>188</sup> was used to analyse the data further, Figure 5.8. When all identified cluster species are considered, a power law correlation  $L = mN^{2/3}$  is observed between the number of Au atoms,  $N$ , and the number of LA ligands,  $L$ .  $N$  and  $L$  can be considered as the volume and surface of the cluster, and the  $2/3$  scaling is also observed for Platonic solids. The coefficient  $m = 1.26$ . This is nearly identical to what was found for LA-capped Ag clusters (see Chapter 2). From the fact that the clusters obey the scaling law, we conclude that the identified species are clusters rather than aggregates of complexes. There is no constant ligand-to-metal ratio and the species do not follow the general formula  $[\text{Au}_z(\text{LA})_y]_n$ .

Overall, with ESI-MS we find smaller species than with SV-AUC. The largest identifiable cluster has around 25 Au atoms, and the numerous small clusters  $\text{Au}_{\leq 10}$  appear to be completely absent in SV-AUC. The small clusters probably absorb at lower wavelengths<sup>150</sup>, thus they may not be observed in SV-AUC at 484 nm. At 380 nm, a 1.5S species is observed, although the major component is still 3.5S. Differences in absorbance between species, as well as different stabilities, may explain some of the discrepancies between ESI-MS and SV-AUC. We tentatively assign the 3.5, 5.0 and 7.1S species to  $\text{Au}_{\sim 16}$ ,  $\text{Au}_{\sim 25}$  and the  $m/z$  3000 signal, respectively, although we stress that the assignment is far from certain.

### Characterisation and formation of synthesis intermediates

We now consider the synthesis process of the Au clusters in more detail, again focusing on samples with 8.9, 12 and 89 mM NaOH. At high pH, the reduction rate of  $\text{NaBH}_4$  is slowed down which may influence cluster composition.<sup>22,315</sup> However, the rate of the reduction step is not the only factor governing the cluster size distribution. As described, the synthesis proceeds via two steps. In the first step, Au(III) in the form of  $\text{HAuCl}_4$  solution is added to an aqueous solution of LA and NaOH, forming a synthesis intermediate. For our samples, the composition of the synthesis intermediate is also affected by the NaOH concentration.

UV-Vis absorption spectra of all synthesis intermediates, recorded 15 min after  $\text{HAuCl}_4$  addition, are featureless (see Figure 5.9), and samples do not luminesce under a handheld UV-lamp. The intermediates were further studied with SV-AUC and found to contain particles with broad size distributions (Figure 5.9) that depend on NaOH concentration. The 8.9 mM NaOH intermediate has an extremely broad size distribution, with a maximum around 9 S. This is significantly larger than what was observed for the corresponding cluster sample at the same wavelength. For the 12 mM NaOH intermediate, a bidisperse distribution is observed (1.3 and 2.7 S), while a 3.0 S species dominates in the 89 mM NaOH intermediate. In both cases, the cluster samples contained species with higher sedimentation coefficients than the intermediates.

UV-Vis spectra recorded in the sample cell after sedimentation show that free LA is present for all three NaOH concentrations. In the 8.9 mM NaOH intermediate, this is clearly the only small species, while for 12 and 89 mM NaOH there appears to be an additional small Au-containing species that sediments slowly. The precursor  $\text{AuCl}_4^-$ , which was found to have an absorption peak at 294 nm, is not present in any of the intermediates. However, in alkaline solution,  $\text{AuCl}_4^-$  can undergo hydrolysis to yield  $\text{AuCl}_{4-x}(\text{OH})_x^-$  which results in a disappearance of the absorption.<sup>316-318</sup> Based on SV-AUC and UV-Vis measurements, we cannot exclude the presence of any of these hydrolysed Au(III) species. For larger Au nanoparticles, the extent of  $\text{AuCl}_4^-$  hydrolysis has been found to influence the final particle size.<sup>319</sup>

We investigated whether modification of the 8.9 mM NaOH synthesis intermediate is possible by addition of NaOH right before the  $\text{NaBH}_4$  reduction step, to give final NaOH concentrations of 12 and 89 mM. The addition of NaOH resulted in a lightening of the yellow colour of the intermediate. UV-Vis absorption spectra of the final cluster samples are shown in Figure 5.10, together with samples prepared according to the standard protocol. The conversion appears to be mostly successful for the 12 mM NaOH sample although it has a high absorbance and the feature at 680 nm is still partially visible. For the 89 mM NaOH sample, the

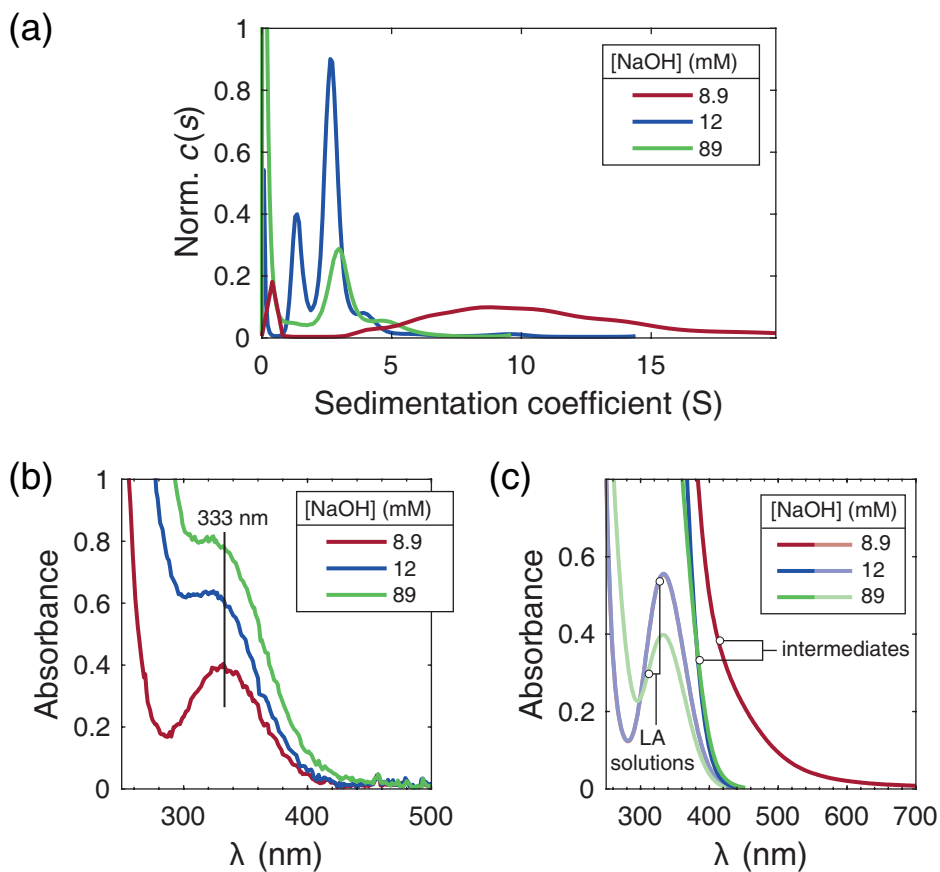


**Figure 5.9** (a) Sedimentation coefficient distributions of synthesis intermediates with 8.9, 12 and 89 mM NaOH. (b) UV-Vis spectra recorded in the sample cell after centrifugation, near the bottom of the cell. The absorption peak at 333 nm is from free LA. The pathlength for absorption is 12 mm. (c) UV-Vis absorption spectra of LA solutions and synthesis intermediates, 15 min after  $\text{HAuCl}_4$  addition. For LA solutions, the 8.9 and 12 mM NaOH spectra overlap.

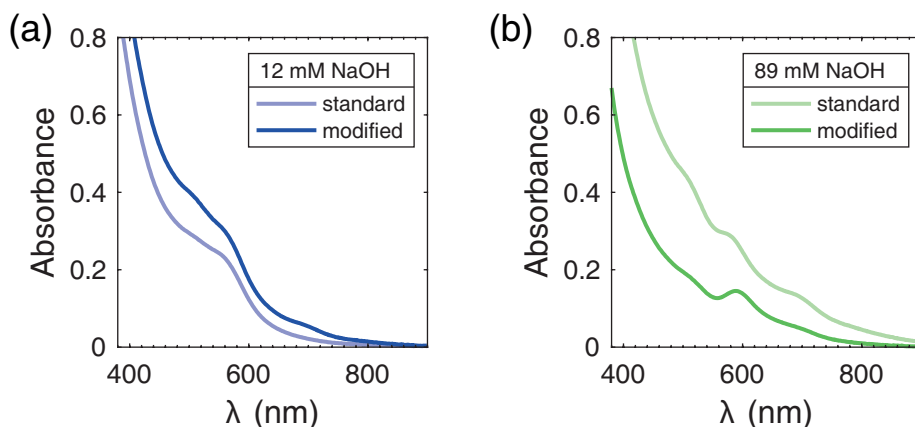


**Figure 5.10** UV-Vis absorption spectra of Au clusters with overall NaOH concentrations of (a) 12 and (b) 89 mM. Samples were prepared according to the standard synthesis protocol (light colours) and by adding NaOH to synthesis intermediates with 8.9 mM NaOH before reduction.

spectrum is very clearly different from the standard sample, with one pronounced absorption peak at 590 nm. From these experiments we conclude that the 8.9 and 89 mM NaOH synthesis intermediates contain different Au-species which cannot be interconverted by changing the NaOH concentration. Conversely, the 8.9 and 12 mM NaOH intermediates may contain similar Au-species that differ mostly in the extent of aggregation, which may be changed by changing the NaOH concentration. The slight turbidity of the 8.9 mM NaOH intermediate implies that some species are not fully desolved or that there is aggregation. The pH of the 8.9 mM NaOH intermediate, determined using pH paper, was found to be 6–7. This may not be high enough to fully deprotonate all LA ( $pK_a = 4.76$ <sup>320</sup>) and ensure complete solubility of the aggregated species. The 12 mM NaOH intermediate had a pH of around ~9. The intermediate-modified clusters were not studied further as their full characterisation is deemed beyond the scope of this thesis. Nevertheless, it opens up new synthesis routes for LA-protected Au clusters with potentially different sizes and optical properties.

Some interesting observations were made during the preparation of synthesis intermediates. All LA solutions are colourless, but upon addition of (yellow)  $\text{HAuCl}_4$  solution, colour changes are observed. For 89 mM NaOH, the solution becomes light yellow but the colour quickly fades. For 8.9 mM NaOH, a deep purple colour is briefly observed. Within a few seconds, this fades and the resulting synthesis intermediate is light yellow and slightly turbid. The sample

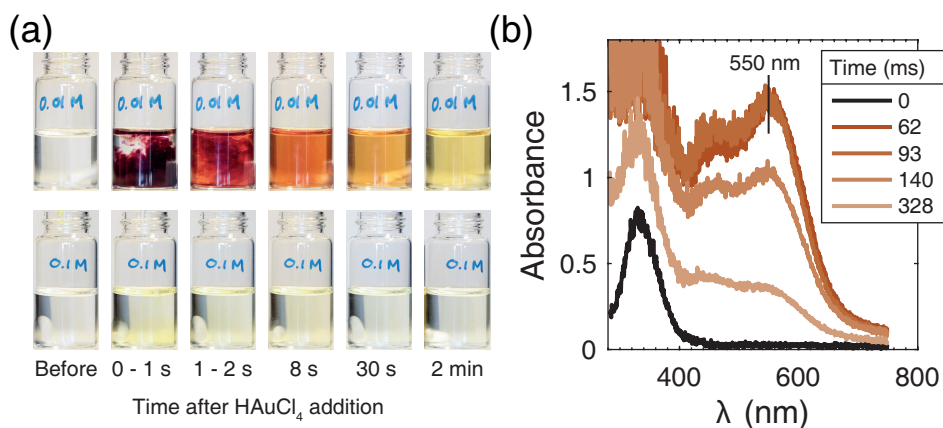


**Figure 5.11** (a) Photographs of LA solutions during addition of HAuCl<sub>4</sub> for samples with 8.9 and 89 mM NaOH (top and bottom, respectively). (b) UV-Vis absorption spectra recorded during addition of HAuCl<sub>4</sub> to LA solution with 8.9 mM NaOH. Addition occurs between 0 and 62 ms. The 0 ms spectrum shows the absorption spectrum of LA. Within 62 ms, a strong absorption peak around 550 nm is observed.

with 12 mM NaOH shows similar behaviour but the purple colour is less evident and fades more quickly. The purple colour observed during the formation of synthesis intermediates is the same as that typically seen for plasmonic Au nanoparticles (5–100 nm in size).<sup>7,321</sup> We recorded fast UV-Vis absorption spectra of the LA solution during addition of HAuCl<sub>4</sub> and found that a surface plasmon absorption peak indeed appears at 550 nm. Spectra and photographs can be found in Figure 5.11. Nanoparticle formation is fast, as the plasmon absorption is already present after < 60 ms. The plasmon resonance disappears within 1 min suggesting the Au nanoparticles also dissolve quickly.

The formation of the synthesis intermediates is not yet fully understood, but we offer some possible explanations for our observations. Upon addition of HAuCl<sub>4</sub> to the LA solution, there is locally a very high concentration of Au(III). Disulfides, like LA, are able to reduce Au(III) to Au(0)<sup>322</sup>, which could result in rapid formation of nanoparticles with low ligand-to-metal ratio. Next, through stirring and diffusion, the nanoparticles are distributed throughout the entire solution, whereupon the ligand-to-metal ratio increases to  $\sim 3 : 1$ . This may result in etching of the nanoparticles by LA to smaller species.<sup>191</sup> Furthermore, remaining Au(III)-complexes may oxidise Au(0) nanoparticles in a comproportionation reaction, resulting in Au(I).<sup>323</sup> Nanoparticle dissolution depends on the surface chemistry of the particle and all species present in solution, and the exact process may be more complex than described here.<sup>324</sup>

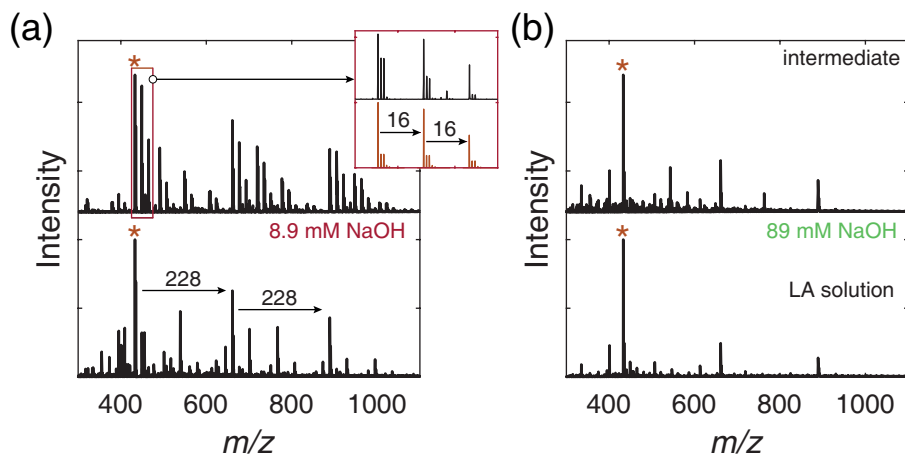


**Figure 5.12** Mass spectra for LA solutions (bottom) and synthesis intermediates (top) for 8.9 and 89 mM NaOH, (a) and (b), respectively. Ion signals marked with a red asterisk are at  $m/z$  433 and have been identified as  $[2 \text{LA} - 2 \text{H}^+ + \text{Na}]^-$ . An increase of 228 is consistent with addition of neutral  $[\text{LA} - \text{H}^+ + \text{Na}^+]$ . The inset shows a closer look at the new ion signals for the 8.9 mM synthesis intermediate (black). Theoretical spectra are shown in red. The  $m/z$  increase of 16 is consistent with addition of an oxygen atom.

Especially for the highest NaOH concentration we use, 89 mM, we expect that the redox reaction between  $\text{HAuCl}_4$  and LA competes with hydrolysis of  $\text{AuCl}_4^-$ , which gives  $\text{AuCl}_{4-x}(\text{OH})_x^-$ . At high pH, species with  $x = 3-4$  dominate.<sup>317,325</sup> This has an effect on the redox potential of Au(III).<sup>326</sup> Furthermore, we observe that the absorbance of LA solution is lower for 89 mM NaOH than for the other two concentrations (Figure 5.9), which may be due to degradation of the disulfide bond.<sup>327,328</sup> Together this may explain why nanoparticles are not formed for the 89 mM NaOH intermediate.

A redox reaction between  $\text{HAuCl}_4$  and LA implies that LA becomes oxidised. The oxidation of disulfides (RSSR) can result in the formation of numerous compounds, including thiosulfinates ( $\text{RS}(\text{O})\text{SR}$ ), thiosulfonates ( $\text{RSO}_2\text{SR}$ ) and disulfones ( $\text{RSO}_2\text{SO}_2\text{R}$ ), as well as sulfenic ( $\text{RSOH}$ ), sulfinic ( $\text{RSO}_2\text{H}$ ) and sulfonic acids ( $\text{RSO}_3\text{H}$ ) where disulfide bond cleavage occurs.<sup>328,329</sup> ESI-MS of synthesis intermediates with 8.9 mM NaOH did indeed show ion signals with mass 16 and 32 Da higher than those observed in LA solutions, see Figure 5.12. This could be due to 1 and 2 oxidations of LA. However, no ion signals belonging to Au-containing species could be identified for synthesis intermediates regardless of NaOH concentration.

Synthesis intermediates are clearly polydisperse, with sedimentation coefficients consistent with cluster-sized species (see Table 5.1). From the absence of pronounced absorption features and luminescence, we propose that the intermediates are Au(I) species, with possibly still some Au(III). This is in agreement with studies of aqueous thiolate-protected Au clusters. The NaOH concentration may affect which ligands bind to Au(I) (and Au(III)) and the extent to which these complexes aggregate. Further characterisation of synthesis intermediates with X-ray spectroscopy will be discussed in Chapter 7.

## 5.4 Conclusions

The size distribution and optical properties of Au clusters capped with lipoic acid (LA) were found to depend strongly on the NaOH concentration during synthesis. Three regimes were identified, with distinct UV-Vis absorption features. Interestingly, the excitation spectra of all samples show identical features. The cluster compositions were studied using mass spectrometry and analytical ultracentrifugation. Both techniques showed the cluster size distribution to be polydisperse, with the lowest NaOH concentration resulting in the largest clusters. However, while mass spectrometry identified cluster sizes up to Au<sub>~25</sub>, analytical ultracentrifugation identified significantly larger species (Au<sub>~45</sub>). The synthesis intermediates, formed by the initial reaction between HAuCl<sub>4</sub> and LA, were characterised with the same techniques to determine their composition. We suggest the intermediates consist of Au(I) and possibly Au(III) species, with different overall size distributions due to aggregation. Finally, the initial reaction between HAuCl<sub>4</sub> and LA results in the formation of large Au nanoparticles with surface plasmon absorption. These nanoparticles are highly unstable and disappear within minutes, possibly due to a comproportionation reaction with remaining Au(III).

## 5.5 Acknowledgements

We thank Dominique Thies-Weesie for analytical ultracentrifugation measurements and data analysis, Arjan Barendregt for help with mass spectrometry measurements, Patrick Chin for the use of the spectrometer and UV-Vis probe, and Mathew Hembury for useful discussions. This work was financially supported by the Debye Graduate Programme (NWO project 022.004.016), and ESRF Graduate Programme; the mass spectrometry research was performed within the framework of The Netherlands Organisation for Scientific Research (NWO) and supported by the large scale proteomics facility Proteins@Work (project 184.032.201) embedded in The Netherlands Proteomics Centre.



## X-ray spectroscopy of Au compounds

---

### Abstract

In this chapter we present  $L_3$ -edge X-ray absorption spectra of a number of Au compounds, recorded using High Energy Resolution Fluorescence Detection (HERFD). Spectral features depend on the oxidation state, the local geometry and the ligands of Au, which demonstrates the usefulness of X-ray spectroscopy for the characterisation of unknown compounds. Multiple scattering calculations were performed and found to reproduce the spectral features for most compounds. The calculations provided additional information on the nature of the electronic transitions. We further recorded Resonant Inelastic X-ray Scattering (RIXS) of these Au compounds by monitoring the emission from the valence states. These spectra could be reproduced with reasonable accuracy by ground state density of states calculations.

---



*"Y'know, it's very hard to talk quantum using a language originally designed to tell other monkeys where the ripe fruit is."*

— Terry Pratchett, *Night Watch*

## 6.1 Introduction

X-ray absorption spectroscopy (XAS) is a powerful, element-specific characterisation technique. It yields structural and electronic information, which can for instance be used to explain catalytic activity<sup>83,134</sup>, to study the speciation of heavy metals in environmental samples<sup>121,330</sup>, and to investigate the structure of metal-containing drugs in the body.<sup>331</sup> The spectrum is usually divided in two regions; Extended X-ray Absorption Fine Structure (EXAFS) and X-ray Absorption Near Edge Structure (XANES). From EXAFS, one can identify the nature of ligands, their coordination numbers and bond lengths. XANES gives information about the electronic structure, including oxidation numbers, and the local symmetry around the absorber.<sup>102,103</sup>

XANES and EXAFS have both been used to study noble metal clusters.<sup>332</sup> In particular, EXAFS has proved successful. It has been used to determine the location of dopants in bimetallic clusters<sup>248</sup> and to demonstrate<sup>333</sup> the unique bonding properties of  $\text{Au}_{36}(\text{SR})_{24}$  with face-centred cubic (fcc) structure. The element-selectivity of XAS is a great advantage compared to laboratory techniques such as for instance mass spectrometry, which may require purification. As the physical state of the sample is unimportant, EXAFS has been used to study the effect of solvation on  $\text{Au}_{25}$ <sup>223</sup> and  $\text{Au}_{38}$ <sup>288</sup> cluster structure. From EXAFS analysis, quantitative information can be obtained by fitting theoretical scattering properties to extract structural information. In contrast, the XANES region is often more difficult to understand. In many cases, spectra of unknown compounds are compared to spectra of reference compounds with known structures to search for similar spectral features.

This chapter describes  $L_3$ -edge XANES of Au reference compounds. These spectra are discussed in detail before considering XAS of Au clusters in Chapter 7. Five Au compounds are considered: bulk Au, AuCl, sodium aurothiomalate (an Au(I)-thiolate),  $\text{Au}_2\text{O}_3 \cdot x\text{H}_2\text{O}$  and  $\text{HAuCl}_4 \cdot 3\text{H}_2\text{O}$ . These compounds have different structures and oxidation states. High Energy Resolution Fluorescence Detected (HERFD) XANES was recorded to enhance the resolution, which resulted in multiple prominent features in each spectrum. The first feature, called the whiteline, mostly results from transitions of 2p electrons to empty 5d states. Its intensity is related to the number of 5d holes.<sup>112</sup> As expected, compounds with

Au in high oxidation states showed intense whitelines. We further found similar XANES spectra for compounds with similar coordination environments.

Self-consistent, full multiple scattering calculations were done and found to reproduce most of the spectral features, though the spherical potentials used in the muffin-tin approximation were found to limit the accuracy of the calculations for sodium aurothiomalate. Calculations were repeated for different dipole selection rules to determine the contributions of transitions to s and to d final states. The compounds were further studied with Resonant Inelastic X-ray Scattering (RIXS), where the resonant emission from valence orbitals was recorded. These spectra could be reproduced with reasonable accuracy by ground state density of states calculations. This chapter demonstrates how X-ray absorption and emission spectroscopy give information on the electronic structure and local geometry of the element of interest, which will be used in Chapter 7 for the study of Au clusters.

## 6.2 Experimental methods

### Chemicals

Au powder (99.95 %, 2  $\mu\text{m}$ ) was obtained from Goodfellow. Sodium aurothiomalate hydrate (Au(I)-thio),  $\text{Au}_2\text{O}_3 \cdot x\text{H}_2\text{O}$ , and  $\text{HAuCl}_4 \cdot 3\text{H}_2\text{O}$  ( $\geq 99.9\%$ ) were obtained from Sigma Aldrich. AuCl ( $\geq 99\%$ ) was purchased from Acros. Water was of Milli-Q quality, purified using a Millipore Direct-Q 3 water purification system.

### X-ray spectroscopy

Au  $L_3$ -edge XANES (11.92 keV) was recorded at beamline ID26 at the European Synchrotron Radiation Facility. The incident beam was selected using the (311) reflection from a double Si crystal monochromator. The spectrometer was equipped with a set of four Ge(555) analyser crystals to record High Energy Resolution Fluorescence Detected (HERFD) XANES. Masks were used to increase the resolution. The  $L\alpha_1$  fluorescence channel was monitored (9.71 keV). For Resonant Inelastic X-ray Scattering (RIXS), the spectrometer was equipped with a set of five Si(951) analyser crystals, with masks to maximise the resolution. The overall energy bandwidth was 0.5 eV for HERFD and 1.5 eV for RIXS.

Samples were measured as pellets, diluted with boron nitride or cellulose (typically 5 mg sample in 50–100 mg filler material). To minimise radiation damage, multiple short spectra were measured on different spots. To record RIXS maps, emission spectra were recorded at different excitation energies. For each point in the emission spectrum, a different spot on the sample was used. The total intensity recorded on each spot was used for normalisation.

Au(I)-thio was also measured in aqueous solution (1.5 mM for XANES and 7.5 mM for RIXS) using a liquid jet setup. The solution was pumped through a capillary to form a free-standing liquid jet in the focus of the beam. Below the jet, the liquid was collected and returned to the reservoir. The setup is shown in Figure 7.2. We attempted to record spectra of  $\text{HAuCl}_4 \cdot 3\text{H}_2\text{O}$  in solution, but this proved too susceptible to radiation damage.

**XANES analysis** The experimental spectra were compared to calculations using FEFF 9.6.<sup>106</sup> Preliminary calculations were done using the final state rule (FSR) for the core-hole, Hedin-Lundquist exchange model ( $ixc = 0$ ), full multiple scattering (FMS) and self-consistently calculated potentials (SCF). The radii for SCF and FMS were gradually increased until the spectrum no longer changed. Values of SCF and FMS radii can be found in Table 6.1. For Au, the calculation did not fully converge even at FMS radius 15 Å and there were still some minor changes up to around 15 eV above the edge. To keep the computational cost down, the FMS radius was not increased further. The final calculations were repeated without core-hole, which in some cases was found to give better agreement with experiment. The card UNFREEZEF was used to include f-electrons in the calculation. Spectral broadening was reduced with the EXCHANGE card to match the experimental high resolution spectra ( $vi0 = -2$  eV). By default, the dipole selection rule is used ( $\Delta l = \pm 1$ ). The individual contributions to the spectrum of d and s final states,  $\Delta l = +1$  and  $-1$ , respectively, were calculated using the MULTIPOLE card.

**Table 6.1** Radii of SCF and FMS, used for FEFF calculations.

Compound	SCF radius (Å)	FMS radius (Å)
Au	5.0	15.0*
HAuCl <sub>4</sub> · 3 H <sub>2</sub> O	4.0	7.0
Au(I)-thio	5.0	9.0
AuCl	5.0	9.0
Au <sub>2</sub> O <sub>3</sub>	4.0	9.0

\* The calculation did not fully converge.

Input files for calculations were generated using Atoms.<sup>334</sup> Crystallographic input files for Au, Au<sub>2</sub>O<sub>3</sub>, AuCl and HAuCl<sub>4</sub> · 3 H<sub>2</sub>O were obtained from the Inorganic Crystal Structure Database (ICSD)<sup>208</sup>, numbers 44362, 8014, 6052 and 414541, respectively. The crystal structure of Au(I)-thio was obtained from the Cambridge Structural Database<sup>335</sup>, number 1174744. Cs ions in this structure were replaced by Na ions in the calculation.

For Au(I)-thio, calculations were also done using FDMNES.<sup>120</sup> Atomic potentials, Fermi level, and charge transfer were calculated self-consistently, relativistic effects were taken into account, and the finite difference method was used to calculate potentials.<sup>212,213</sup> The real Hedin, Lundqvist and Von Barth exchange correlation potential was used. The core-hole is taken into account when calculating the absorption spectrum, but not for the self-consistency loop. That is, the electrons around the absorber do not instantly adjust to the presence of the photo-electron. A typical radius for calculation was 7 Å. This is somewhat lower than for FEFF calculations, as the finite difference method is more computationally demanding. The spectra were convoluted to apply an energy-dependent broadening, using default parameters (an arctangent function). The width of the core-hole was decreased to 0.50 eV and further broadened with a 1.0 eV Gaussian, to better match the experimental data. The

individual contributions to the spectrum of d and s final states,  $\Delta l = +1$  and  $-1$ , respectively, were calculated using *lplus1* and *lminus1* cards. Calculations were also done with the multiple scattering method with muffin-tin potentials.

## 6.3 Results and discussion

### HERFD-XANES of Au compounds

Experimental spectra of all five compounds are shown in Figure 6.1. HERFD spectra show an enhanced resolution compared to spectra recorded with total fluorescence yield (TFY). This results in more prominent spectral features for all five samples. In some cases, new features are observed, such as the small peak just above the whiteline in  $\text{HAuCl}_4 \cdot 3\text{H}_2\text{O}$ . Differences between samples are also more easily observed, which is of great importance when studying samples that are similar. We will consider only the HERFD spectra for analysis in this chapter.

The whiteline intensity clearly depends on the oxidation state. Formally, bulk Au has the electron configuration  $5d^{10}6s^1$ . However, there is hybridisation of s, p and d orbitals, giving a configuration of  $5d^{10-\delta}6sp^{1+\delta}$ .<sup>336</sup> This creates some empty states in the d-band, giving rise to the whiteline.<sup>112,114</sup> The whiteline intensity can be increased by oxidation<sup>337</sup> or bonding to electron-withdrawing ligands<sup>338</sup>, both

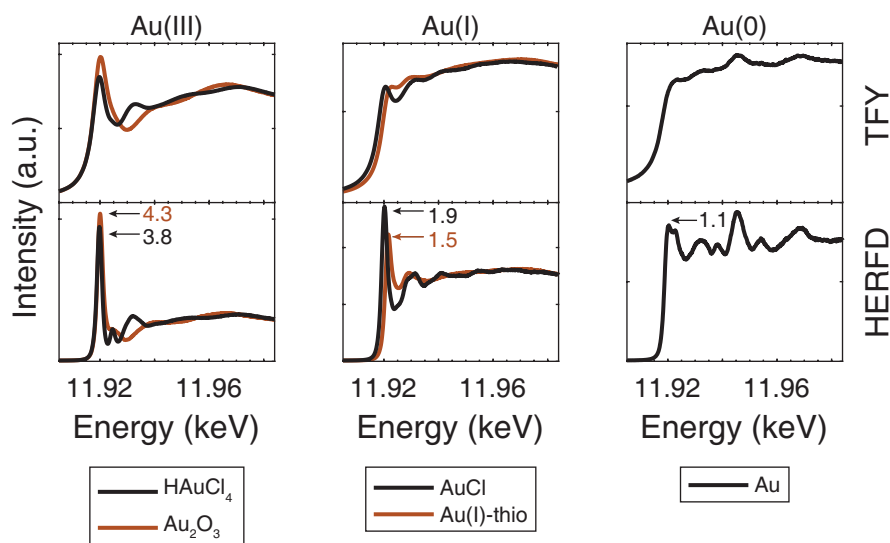


**Figure 6.1** XANES of the Au reference compounds, with three different formal oxidation states. Spectra are shown in HERFD (bottom) and total fluorescence yield (TFY, top). The numbers indicate the maximum whiteline intensity, relative to the post-edge.

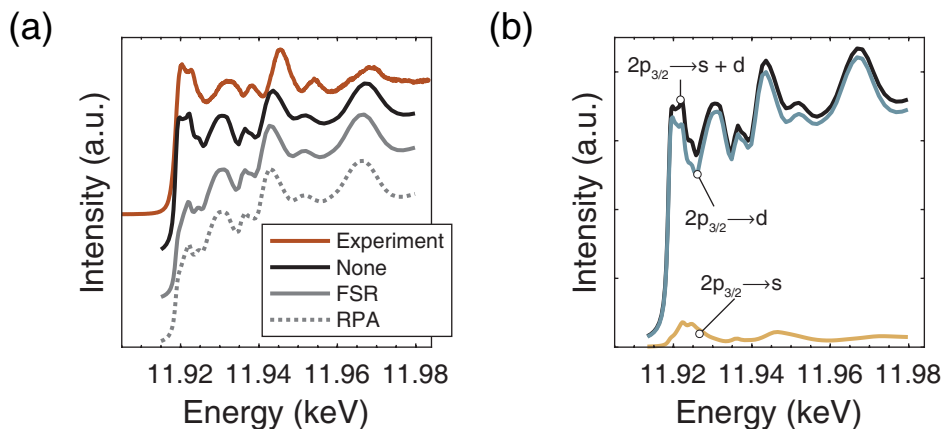


**Figure 6.2** (a) HERFD-XANES of bulk Au together with calculated spectra. The calculations were done with FEFF, using three different core-hole treatments: None (no core-hole), FSR (final state rule) and RPA (random phase approximation). (b) Calculated XANES of bulk Au for the dipole selection rules  $\Delta l = \pm 1$  (s+d final states, black),  $\Delta l = +1$  (d final states, blue) and  $\Delta l = -1$  (s final states, yellow).

of which create empty d-states. Charge redistribution in alloys may also affect the number of 5d electrons.<sup>339</sup>

We further observe some similarities between AuCl and Au(I)-thio, and between  $\text{Au}_2\text{O}_3 \cdot x\text{H}_2\text{O}$  and  $\text{HAuCl}_4 \cdot 3\text{H}_2\text{O}$ . In the first case, a broad, intense feature is present around 8 eV above the whitenline. In the latter case, there is a small shoulder or peak on the high energy side of the whitenline. The coordination geometry of Au compounds is closely related to the oxidation state, with Au(I) adopting linear coordination while Au(III) forms square planar complexes.<sup>340,341</sup> In the following section, the structure of each compound will be discussed in more detail and the experimental spectra will be compared with calculations.

**Bulk Au** Metallic gold has a face-centred cubic (fcc) structure, where each atom has a coordination number of 12 and bond lengths are 2.88 Å. The HERFD spectrum (Figure 6.2) is highly featured, and shows a weak whitenline. All spectral features are accurately reproduced by FEFF calculations. However, using the final state rule (FSR), where the core-hole is included and self-consistently screened, resulted in low calculated whitenline intensity. The best agreement was obtained when the calculation was done with no core-hole. Similar observations were made for  $L_3$ -edges of 3d metals.<sup>229</sup> A third way to calculate the core-hole is using the random phase approximation (RPA core-hole) where the screening of the

core-hole is determined from the dielectric function of the material.<sup>342</sup> However, this approach yields a spectrum is nearly identical to that with the FSR core-hole. Therefore the RPA core-hole was not considered further. The spectrum arises mainly from transitions to d-states, as seen when the calculation is performed using only the  $\Delta l = +1$  selection rule. Especially around the edge, there is also some contribution from s-states.

**Sodium aurothiomalate, Au(I)–thio** Thiolate-protected Au clusters have a large surface-to-volume ratio and their structures have been found to consist of a compact core surrounded not by thiolate ligands but rather by Au(I)-thiolate units.<sup>51</sup> Thus, the Au(I)-thiolate compound sodium aurothiomalate (chemical formula  $\text{NaO}_2\text{CCH}_2\text{CH}(\text{SAu})\text{CO}_2\text{Na} \cdot x\text{H}_2\text{O}$ , abbreviated Au(I)–thio) is expected to be a good reference compound for these Au atoms.

The structure of Au(I)-thio was determined with X-ray crystallography some twenty years ago.<sup>289</sup> The gold-sulfur backbone exists as a double-helical structure with two strands of ...–Au–S–Au–S–Au–S–... intertwined. The Au–S bond lengths are nearly all identical (2.289 Å and 2.285 Å). The Au–S–Au bond angle is 99.2°. In each unit cell, there are two inequivalent Au atoms that differ in their next-nearest neighbours. One of these, Au(**1**), has a Au–Au distance of 3.23 Å and an S–Au–S bond angle of 178.9°. The other, Au(**2**), has an S–Au–S bond angle of 169.4° and two O atoms at 3.35 Å. The helices of Au and S are surrounded by the ligand backbones, with carboxylic acid groups oriented outwards. The material contains counterions,  $\text{Cs}^+$  and  $\text{Na}^+$ , which are coordinated by these carboxylic acid groups, as well as by carboxylic acid groups of neighbouring helices. The centre-to-centre distance between two adjacent helices is around 15 Å. Other characterisation studies using EXAFS, wide-angle X-ray scattering and capillary zone electrophoresis found bond lengths and coordination numbers in agreement with this, although the double helix structure could not be observed with these techniques.<sup>290,331,343</sup> These studies also suggest that structure of the compound is similar in dilute solution and solid.

FEFF calculations were done for both Au sites. Results are shown in Figure 6.3, together with the experimental spectrum which shows a whitenline and one additional broad feature above the edge at 11.929 keV. Spectra are similar for the solid compound and the solution. For comparison with calculations, the solid is considered. Calculated spectra of the two Au sites are different, with the 11.929 keV feature best reproduced in the Au(**2**) site. The whitenline intensity is low for both calculations. Its intensity improves if the calculation is done without a core-hole, although this also results in a less prominent 11.929 keV feature.

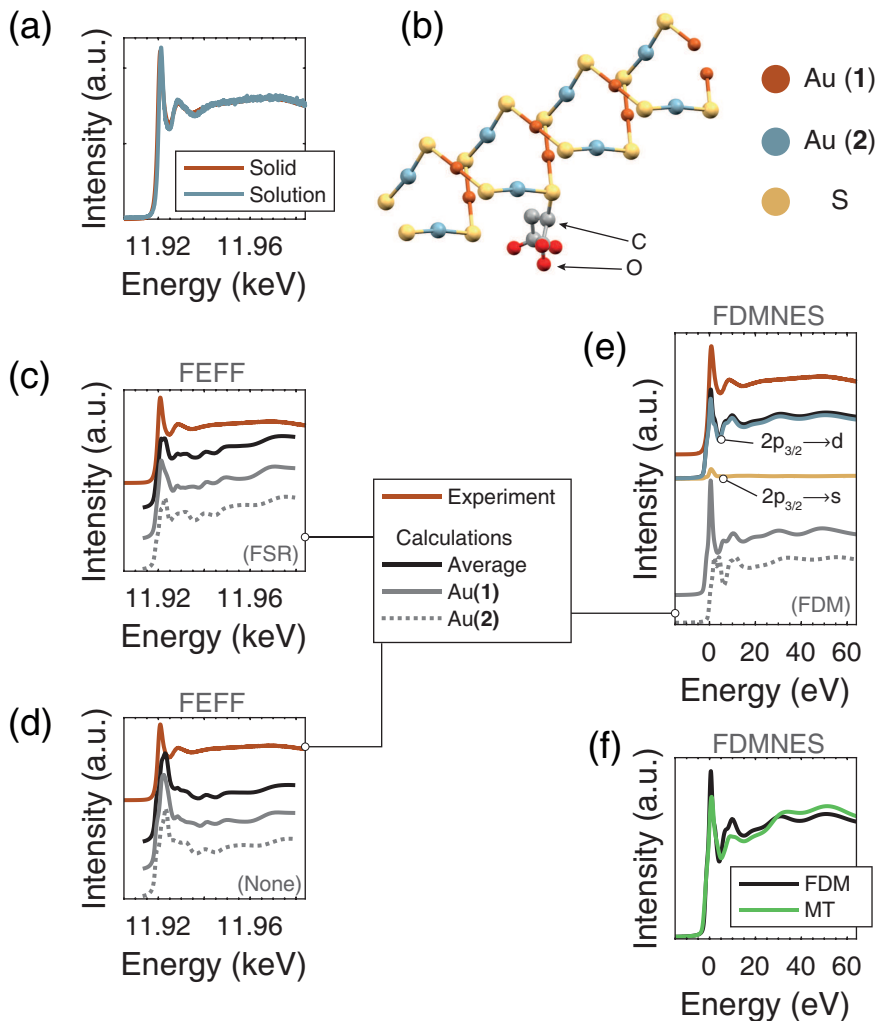


**Figure 6.3** (a) Experimental HERFD-XANES of Au(I)-thio in solution and as a solid. (b) Structure of the compound. For clarity, only one ligand backbone is shown, and the two Au sites have been given different colours. (c) FEFF calculations, using FSR (final state rule) core-hole. (d) FEFF calculations, without a core-hole. (e) FDMNES calculations, using the finite difference method (FDM). For the averaged spectrum, the individual contributions of  $\Delta l = -1$  and  $\Delta l = +1$  transitions are also shown (yellow and blue, respectively). (f) FDMNES calculations (average of the two Au sites) using FDM and the muffin-tin approximation (MT).

As Au(I)-thio is arguably the most important reference compound for thiolate-protected Au-clusters, the spectrum of Au(I)-thio was also calculated using FDMNES, which allows calculations using both a multiple scattering approach with spherical muffin-tin potentials, and the finite difference method, where the potentials can have any shape. FDMNES calculations show somewhat better agreement with experimental data. The agreement is good also when muffin-tin potentials are used. It may be that the core-hole effect is better described by the standard approach of FDMNES for this compound.

The default for all calculations is to calculate only dipolar transitions,  $\Delta l = \pm 1$ . To assign transitions, FDMNES calculations were also done using only the  $\Delta l = +1$  and only the  $\Delta l = -1$  selection rule, which calculates transitions to only d- and only s-states, respectively. As can be seen from Figure 6.3, nearly all spectral features are due to transitions to d-states. The exception is the whiteline, where  $2p_{3/2} \rightarrow 6s$  transitions have significant intensity. Formally, Au(I)-thio is  $5d^{10}6s^0$ . However, from density of states calculations, using FEFF, the ground state electron configuration is  $5d^9 6s^{0.8}$  (with remaining electron density in 6p, and some charge transfer to S atoms). Thus, the whiteline involves transitions to both 6s and 5d.

The average of the two crystallographic Au sites may not represent the actual average Au environment in our sample. The slight distortion away from linearity for Au(2) could be due to crystal packing. In order to crystallise the compound successfully, Cs ions had to be added which are not present in our sample. Moreover, our sample is hydrated which may affect next-nearest neighbours and long range order.

**AuCl** The Au atoms in AuCl are linearly coordinated to two Cl atoms, as is characteristic of Au(I) compounds.<sup>340,341</sup> The Au–Cl bonds are 2.30 Å. Next-nearest neighbours are four Au atoms at 3.32 Å. The HERFD spectrum of AuCl is shown in Figure 6.4. As with bulk Au, the whiteline intensity is only reproduced when the FEFF calculation is done without a core-hole. The experimental whiteline is intense, though lower than for Au<sub>2</sub>O<sub>3</sub> and HAuCl<sub>4</sub> as expected from the lower oxidation state. The whiteline intensity is also slightly lower than that of Au(I)-thio (see Figure 6.1). From density of states calculations, using FEFF, the ground state electron configuration was determined to be  $5d^{9.3} 6s^{0.9}$ . There is as good as no charge transfer to the Cl ligands, and therefore the total calculated electron count is higher than for Au(I)-thio. This explains why the calculations show AuCl with a less intense whiteline than Au(I)-thio.

It has been proposed that  $[\text{Au}(\text{I})\text{Cl}_2]^-$  species may be intermediates in the two-phase Brust-Schiffrin synthesis method for Au clusters.<sup>203</sup> While the protocol described in Chapter 5 takes place in one phase (water), a good understanding of  $[\text{Au}(\text{I})\text{Cl}_2]^-$  species may still be useful. It has been found that  $[\text{Au}(\text{I})\text{Cl}_2]^-$  species

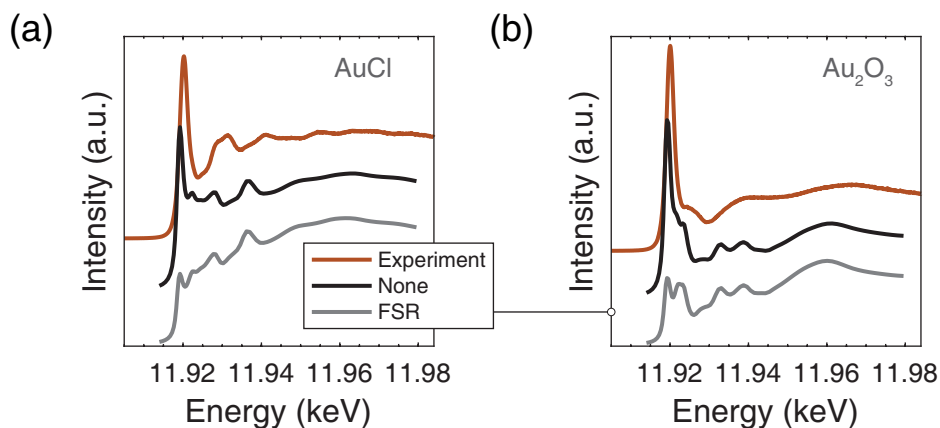


**Figure 6.4** HERFD-XANES of (a) AuCl and (b) Au<sub>2</sub>O<sub>3</sub>, together with calculated spectra. The calculations were done with FEFF, using two different core-hole treatments; FSR (final state rule) and None (no core-hole).

are metastable under ambient conditions. In aqueous solution, a significantly enhanced whiteline was observed, suggesting disproportionation to Au(III) and metallic Au.<sup>344</sup> In dichlorobenzene, instability of [Au(I)Cl<sub>2</sub>]<sup>-</sup> was found to be due to radiation damage.<sup>345</sup> During our measurements, we observed a ~5–10% decrease in whiteline intensity after 3 min. To avoid this radiation damage, multiple 5 s scans were recorded in different spots and later averaged to give the final spectrum in Figure 6.4.

**Au<sub>2</sub>O<sub>3</sub>** The Au atoms in Au<sub>2</sub>O<sub>3</sub> are formally Au(III) and adopt a square planar geometry with O ligands. The Au–O bonds are 1.93–2.07 Å. Each O atom is bound to two Au atoms, with an Au–O–Au bond angle of around 110°. The XANES spectrum of Au<sub>2</sub>O<sub>3</sub>, Figure 6.4, has an intense whiteline. FEFF calculations reproduce most features of this spectrum with reasonable accuracy. The whiteline intensity is low but it improves when the calculation is done without a core-hole. The Au<sub>2</sub>O<sub>3</sub> sample was used as provided by the supplier and is known to be hydrated. The preparation of stoichiometric Au<sub>2</sub>O<sub>3</sub> is difficult and involves high pressure.<sup>346</sup> Hydration could result in a disordered structure with different coordinates from the crystal structure, which reduces the validity of the calculations.

**HAuCl<sub>4</sub> · 3H<sub>2</sub>O** Chloroauric acid, HAuCl<sub>4</sub> · 3H<sub>2</sub>O, is used as precursor in the synthesis of gold clusters. It consists of AuCl<sub>4</sub><sup>-</sup> anions which adopt square planar geometry, with Au–Cl distances of 2.29 Å. The AuCl<sub>4</sub><sup>-</sup> anions form stacks which are staggered in such a way that each Au is axially coordinated by one Cl atom

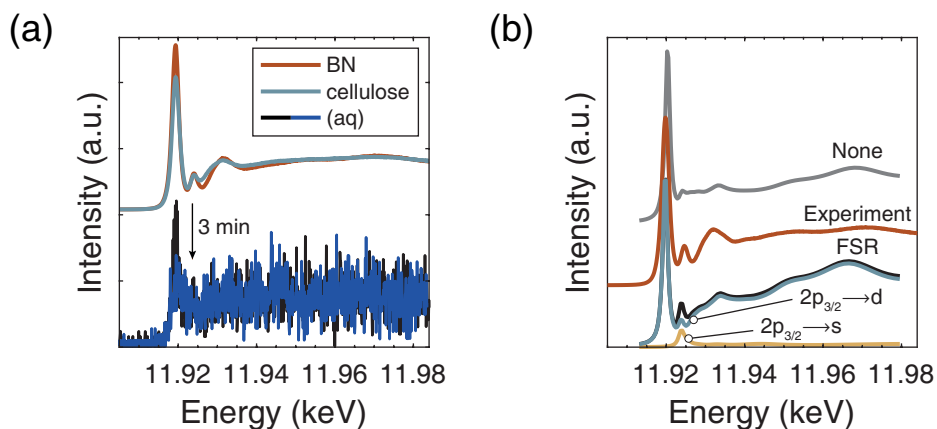


**Figure 6.5** (a) HERFD-XANES of  $\text{H[AuCl}_4] \cdot 3\text{H}_2\text{O}$ , in pellets of boron nitride and cellulose (top) and in solution (bottom). The latter damages quickly, as seen from the decrease in whiteline intensity after just a few minutes. (b) Comparison of the experimental XANES (red) with calculations. The calculations were done with FEFF, using two different core-holes treatments; FSR (final state rule, black) and None (no core-hole, grey). The dipole selection rule  $\Delta l = \pm 1$  was used. For the FSR core-hole, calculations were also done for the dipole selection rules  $\Delta l = +1$  (d final states, blue) and  $\Delta l = -1$  (s final states, yellow).

from each of the two neighbouring  $\text{AuCl}_4^-$  anions. This axial Au–Cl distance is 3.4 Å. The closest Au–O distance is around 4.5 Å.

The XANES spectrum of  $\text{H[AuCl}_4] \cdot 3\text{H}_2\text{O}$  is shown in Figure 6.5. The intensity of spectral features was found to be somewhat dependent on whether cellulose or boron nitride was used to prepare the pellets. The reason is not known; it may be that  $\text{H[AuCl}_4]$  reacts slowly with cellulose in a redox reaction.<sup>347</sup> The spectrum is accurately reproduced by FEFF calculations. Changing the core-hole from FSR to NONE resulted in a more intense whiteline, but somewhat worse agreement further from the edge. The intensity of the whiteline is due to  $2p_{3/2} \rightarrow 5d$  transitions, while transitions to 6s dominate for the second feature, 4 eV above the whiteline.

In the synthesis of Au clusters, an aqueous solution of  $\text{H[AuCl}_4]$  is used. A XANES measurement of this solution was not possible due to rapid radiation damage. The whiteline intensity decreased and within minutes the spectrum resembled that of bulk Au. The initially yellow solution became purple and showed a surface plasmon absorption at 540 nm, indicating the formation of larger nanoparticles. The liquid jet setup used was open to air which may accelerate radiation damage. A comparison of the spectra recorded in the first minute with the solid sample shows similar features, suggesting the geometry of Au in solid

and aqueous  $\text{HAuCl}_4$  are similar. Earlier studies of  $\text{AuCl}_4^-$  solutions suggest that the complex adopts a square planar geometry also in aqueous solution.<sup>325,348</sup> Two water molecules also coordinate axially, at a distance of around 2.5 Å. At high pH, exchange of  $\text{Cl}^-$  ligands with  $\text{OH}^-$  occurs, together with an increase in axial Au– $\text{OH}_2$  distance to 2.9 Å.

### RIXS of Au compounds

By detecting fluorescence from the valence orbitals rather than  $3d_{5/2}$  ( $L\alpha_1$  emission line), we can gain information on the valence states of the Au compounds. These are sensitive to local geometry and chemical environment.<sup>126,127</sup> The technique has been used to study for example U compounds<sup>349</sup>, to investigate the adsorption of CO on Pt nanoparticles<sup>133,350</sup>, and to study the effect of spin-orbit interactions on the ground state electronic structure of W and Re oxides.<sup>351</sup>

The RIXS process can be considered as a correlation function between empty and filled states according to the following equation<sup>352</sup>, derived from the Kramers-Heisenberg equation for the scattering cross section:

$$F(\Omega, \omega) \propto \int_{\varepsilon} d\varepsilon \frac{\rho(\varepsilon)\rho'(\varepsilon + \hbar\Omega - \hbar\omega)}{(\varepsilon - \hbar\omega)^2 + (\Gamma_{\text{int}}^2/4)} \quad (6.1)$$

where  $\hbar\Omega$  is the incident energy,  $\hbar\omega$  the emitted energy,  $\Gamma_{\text{int}}$  is the lifetime of the intermediate  $3d_{5/2}$  state and  $\rho$  and  $\rho'$  are the filled and empty Au 5d density of states (DOS) at energy  $\varepsilon$ , respectively. The Au 5d DOS was calculated for all compounds with FEFF, using input parameters as described earlier. Calculations were done for the ground state, without a core-hole. Only the 5d DOS is considered; for XANES the  $2p_{3/2} \rightarrow 5d$  transitions were found to contribute more to the spectrum than  $2p_{3/2} \rightarrow 6s$  (see for instance Figure 6.2). The use of the ground state electronic structure in Equation (6.1) implies that all interactions due to the photoexcitation process are neglected.

The intermediate state lifetime broadening is 5.54 eV.<sup>123</sup> The calculated RIXS maps are further broadened to take into account instrumental broadening of the monochromator and spectrometer, 0.5 and 0.3 eV, respectively, and by 0.01 eV to estimate the final state lifetime broadening.<sup>353</sup> The applied instrumental broadening is slightly sharper than the true broadening, to make it easier to distinguish features. The elastic peak has been added to the calculated spectra to facilitate comparison with experimental RIXS. The experimental spectra are shifted so that the elastic peak corresponds to 0 eV energy transfer. Experimental and calculated RIXS maps for all compounds are shown in Figures 6.6 to 6.10, together with the calculated

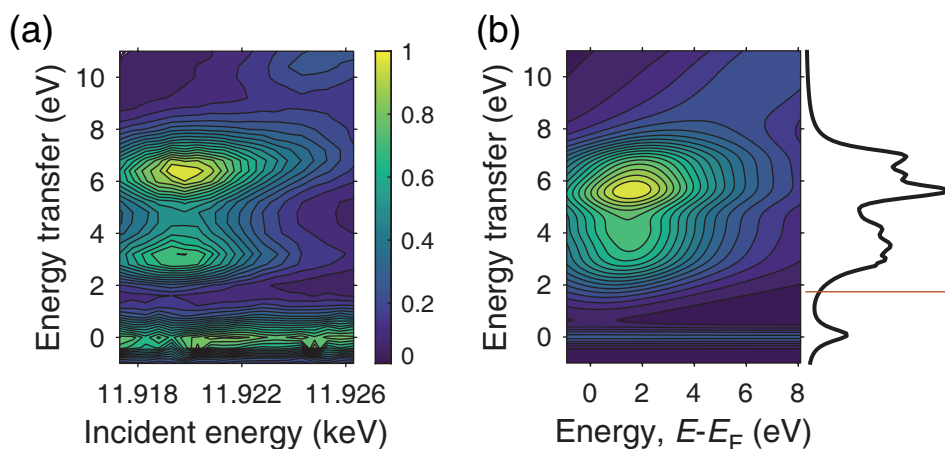


**Figure 6.6** RIXS of  $\text{H[AuCl}_4\text{]} \cdot 3\text{H}_2\text{O}$ , (a) experiment and (b) calculation. The ground state density of states is also shown. The red line indicates the Fermi level.

Au 5d DOS. This has been aligned with its maximum to the highest intensity of the calculated RIXS.

The energy difference between maxima in the occupied and unoccupied density of states determines the energy transfer value of RIXS features. This is observed clearly for  $\text{H[AuCl}_4\text{]}$  (Figure 6.6), where there is one maximum in the unoccupied DOS and two broad maxima in the occupied DOS. This gives two features in the RIXS, although the calculated splitting between them is too small, resulting in one intense peak and one shoulder. The experimental RIXS of the other Au(III) compound,  $\text{Au}_2\text{O}_3$ , is reasonably similar to that of  $\text{H[AuCl}_4\text{]}$  (Figure 6.7), although the two features are closer together and the energy resolution of the spectrometer is not sufficient to distinguish them. The calculated DOS is broad, resulting in a broad RIXS feature from Equation (6.1). While the shape of the RIXS feature is accurately reproduced by the calculation, the energy transfer position does not match the experimental.

There is excellent agreement between the experimental and calculated RIXS of bulk Au, both for the shape and energy transfer position of the feature, see Figure 6.8. As expected, the calculated Au 5d DOS shows that the d-band is nearly full, with the Fermi level positioned near the top.

The two other compounds, AuCl and Au(I)-thio, are both linearly coordinated Au(I). The similarities in their structures are reflected in their similar RIXS maps, with one intense feature. For Au(I)-thio, the position of the feature is the same for a solid and a solution sample. The peak is shifted  $\sim 1$  eV to lower energy

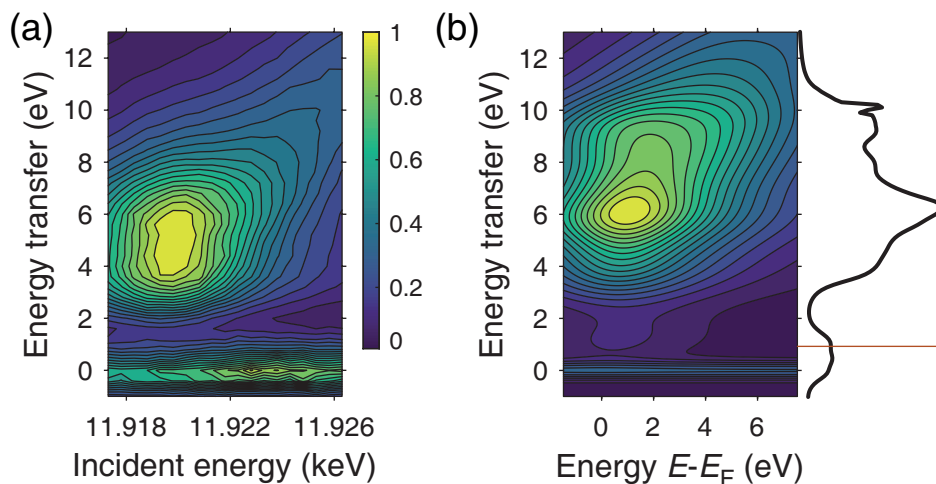


**Figure 6.7** RIXS of  $\text{Au}_2\text{O}_3$ , (a) experiment and (b) calculation. The ground state density of states is also shown. The red line indicates the Fermi level.

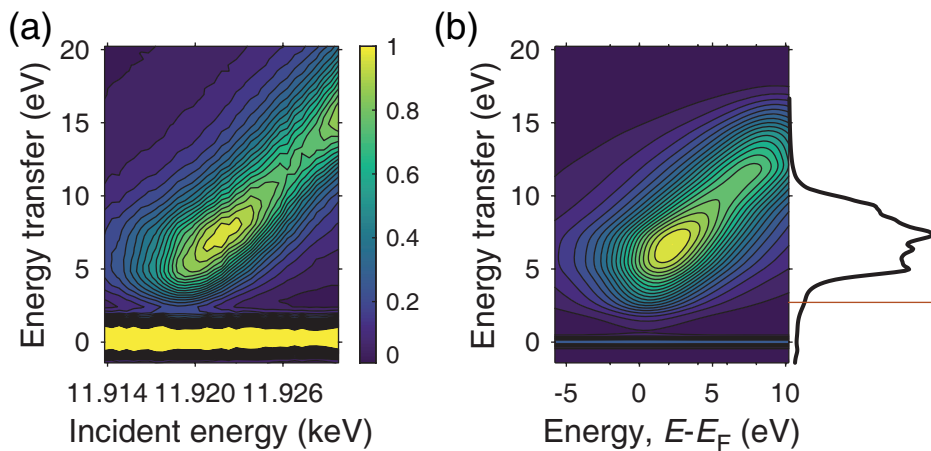


**Figure 6.8** RIXS of bulk Au, (a) experiment and (b) calculation. The ground state density of states is also shown. The red line indicates the Fermi level.

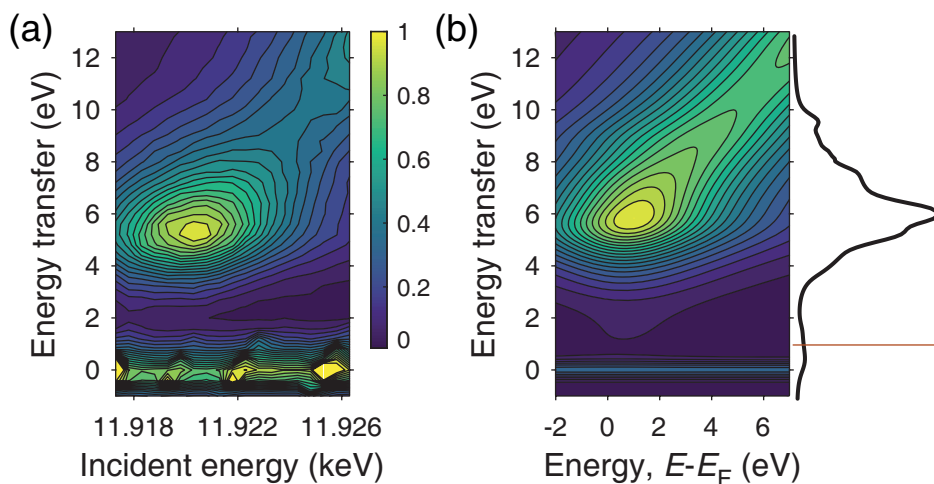


**Figure 6.9** RIXS of AuCl, (a) experiment and (b) calculation. The ground state density of states is also shown. The red line indicates the Fermi level.

transfer for AuCl. This shift is accurately reproduced by the calculations, as are the approximate energy transfer positions of the features. However, especially for Au(I)-thio, the calculated RIXS feature spreads along the diagonal rather than being more localised. Compared to for instance  $\text{HAuCl}_4$ , it can be seen that the Au(I)-thio Au 5d DOS has no distinct maxima in the unoccupied DOS.

It may be that the DOS calculations are not sufficiently accurate for most of these compounds. For instance, we calculated a higher 5d electron count for AuCl than for Au(I)-thio, despite the former having a more intense whiteline in the experimental XANES spectrum. It is also clear that the XANES calculations do not accurately reproduce all spectral features, for instance in the case of Au(I)-thio and AuCl. This may be related to the use of muffin-tin potentials. This approximation is less accurate for low-symmetry compounds such as linearly coordinated Au. FDMNES calculations using the finite difference method could improve the accuracy, although the hydrated and potentially distorted structures of  $\text{Au}_2\text{O}_3$  and Au(I)-thio remain an issue.

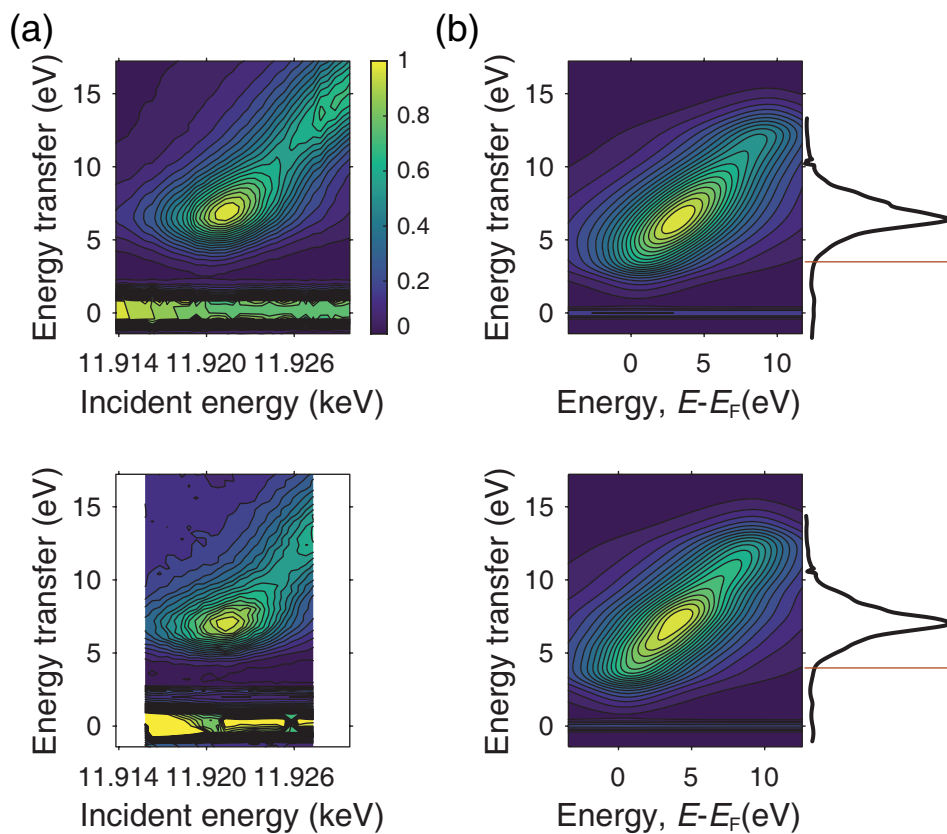


**Figure 6.10** RIXS of Au(I)-thio, (a) experiment, for both a solid (top) and solution (bottom) sample. (b) Calculation, for Au(1) (top) and Au(2) (bottom). The ground state density of states is also shown. The red line indicates the Fermi level. The experimental elastic peaks have been rescaled slightly for clarity.

## 6.4 Conclusions

X-ray absorption spectra, using High Energy Resolution Fluorescence Detection (HERFD), were recorded at the  $L_3$ -edge for a number of Au compounds with different oxidation states and different ligands. Most spectral features could be accurately reproduced using multiple scattering calculations, though more advanced calculation methods without the muffin-tin approximation were required for sodium aurothiomalate. The whiteline intensity depends on the oxidation state of the compound. From calculations it was determined that its intensity comes from both  $2p_{3/2} \rightarrow 5d$  and  $2p_{3/2} \rightarrow 6s$  transitions, with the former becoming more important for the higher oxidation states. We further recorded Resonant Inelastic X-ray Scattering (RIXS) by monitoring the emission from the valence states. These spectra could be reproduced with reasonable accuracy by ground state density of states calculations.

## 6.5 Acknowledgements

We thank Lucia Amidani, Pieter Glatzel and Sara Lafuerza for beamline support, and Hebatalla Elnaggar, Naud van Bunningen, Maarten Bransen, Mario Delgado-Jaime, Ties Haarman, Clara Garcia Yago, Stephan Pollitt and Lule Beqa for their help during the beamtimes. The ESRF is thanked for providing beamtime (proposals CH4593, IH-CH-1118 and CH5496). This work was financially supported by the Debye Graduate Programme (NWO project 022.004.016), and ESRF Graduate Programme.



## X-ray spectroscopy of Au clusters

---

### Abstract

The size distributions and optical properties of Au clusters capped with lipoic acid (LA) were previously found to depend on the NaOH concentration during synthesis. We further studied these samples with X-ray absorption and emission spectroscopy. All spectra had an intense whiteline and few prominent post-edge features; spectral features that are characteristic of an Au(I)-thiolate reference compound, but also of thiolate-protected Au clusters with  $\sim 20$  Au atoms. The intense whiteline arises from  $2p_{3/2} \rightarrow 5d$  transitions, with d-holes in Au caused by bonding to electron-withdrawing thiolates. Extended X-ray Absorption Fine Structure (EXAFS) was recorded of the sample with lowest NaOH concentration, and found an Au–Au coordination number of  $\sim 4$ , consistent with an average size of 20–40 Au atoms. The sample with highest NaOH concentration was found to contain some  $\text{AuCl}_{4-x}(\text{OH})_x^-$  species in addition to clusters. These species were also present in the synthesis intermediate of this sample, while the samples with lower NaOH resembled Au(I)-thiolates. This confirms that there is a reaction between LA and  $\text{HAuCl}_4$  at the start of the synthesis, before addition of the reducing agent, and that this reaction is inhibited at high NaOH concentrations.

---



*“There is nothing like looking, if you want to find something. You certainly usually find something, if you look, but it is not always quite the something you were after.”*

— J.R.R. Tolkien, *The Hobbit*

## 7.1 Introduction

The properties of noble metal clusters depend on their size and shape.<sup>15</sup> Different applications may require clusters with different sizes or properties<sup>354</sup>, necessitating the development of robust synthesis protocols for various clusters. Moreover, the study of different clusters may also answer fundamental questions about the origin of their size-dependent properties<sup>83,355</sup>, and how synthesis parameters may be tuned to yield desired sizes.<sup>30,76,78,80</sup>

In Chapter 5, we presented the synthesis and characterisation of Au clusters with lipoic acid (LA) and showed how the synthesis influences the cluster size. We described a two-step synthesis protocol that uses NaOH to ensure water-solubility of LA, as shown in Figure 7.1. In the first step, HAuCl<sub>4</sub> is added to an aqueous solution of LA with NaOH. This forms a synthesis intermediate. After 15 min, the intermediate is reduced by addition of NaBH<sub>4</sub> and the clusters are formed. The optical properties and size distributions of the clusters depend on the NaOH concentration, with three distinct NaOH concentration regimes. Typical NaOH concentrations were 8.9, 12 and 89 mM. The lowest NaOH concentration resulted in the largest clusters, but accurate size characterisation is challenging, partially due to the polydispersity of the clusters. From mass spectrometry and analytical ultracentrifugation, we estimate cluster sizes to be between 2–25 atoms, with some larger clusters (Au<sub>≤45</sub>) for the lowest NaOH concentration. The NaOH concentration was found to have an effect on the synthesis intermediate as well. For low NaOH concentrations, an initial reaction was observed between HAuCl<sub>4</sub> and LA, resulting in larger Au nanoparticles which quickly disappeared. Intermediates were even more challenging to characterise than clusters, with no Au species observed in mass spectrometry and no clear absorption features in UV-Vis spectroscopy.

There are still a number of unanswered questions about these Au clusters and their synthesis. What are the synthesis intermediates? How does NaOH affect their composition? Does NaOH influence the reduction step of the synthesis as well? Can we get more information on the composition of the clusters, to resolve the discrepancy between mass spectrometry and analytical ultracentrifugation?

In Chapter 6, we demonstrated the usefulness of X-ray absorption and emission spectroscopy in the analysis of various Au compounds. The intensity of the

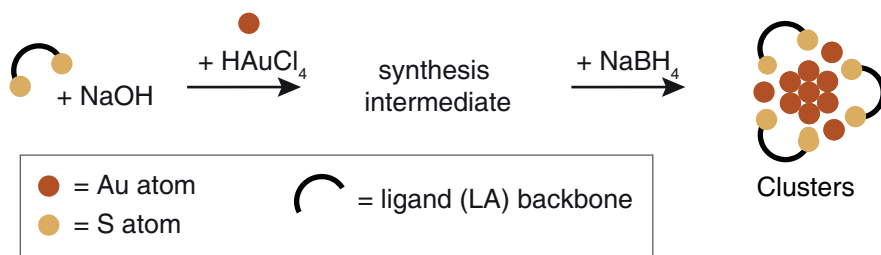


**Figure 7.1** Schematic representation of the synthesis of Au clusters capped with LA.

whiteline, the first peak in the X-ray Absorption Near Edge Spectrum (XANES), was found to be strongly dependent on oxidation state. Both nearest and next-nearest neighbours influence the intensity and position of features in the spectrum. In this chapter, we use X-ray spectroscopy to study Au clusters capped with LA, to get more information on their composition and the effect of NaOH on the synthesis.

Extended X-ray Absorption Fine Structure (EXAFS) of Au clusters with 8.9 mM NaOH reveals an average particle size of 20–40 atoms, consistent with what was found in Chapter 5. XANES spectra of Au clusters with 8.9 and 12 mM NaOH show an intense whiteline and few post-edge features, as is also observed for sodium aurothiomalate (Au(I)-thio), an Au(I) reference compound. However, the whitelines of the clusters are lower than that of Au(I)-thio, suggesting a lower average oxidation state. The spectrum of monodisperse Au<sub>25</sub>(SR)<sub>18</sub><sup>−</sup> has similar features, and calculated spectra of clusters with 18–25 Au atoms confirm that these spectral features are characteristic of thiolate-protected Au clusters due to their high surface-to-volume ratio. The intense whiteline arises from 2p<sub>3/2</sub> → 5d transitions, with d-holes in Au caused by bonding to electron-withdrawing thiolates. Overall, the X-ray absorption spectra of the clusters are consistent with cluster sizes of around 20 Au atoms, though the polydispersity of the sample make a conclusive assignment of spectral features impossible.

We further find that Au clusters with 89 mM NaOH contain AuCl<sub>4-x</sub>(OH)<sub>x</sub><sup>−</sup>, with oxidation state Au(III), in addition to LA-capped Au clusters. This sample therefore has a more intense whiteline and additional spectral features both in absorption and emission spectra. The AuCl<sub>4-x</sub>(OH)<sub>x</sub><sup>−</sup> species are also present in the synthesis intermediate of this sample, while the samples with 8.9 and 12 mM NaOH again resemble Au(I)-thiolates. There is clearly a reaction between LA and HAuCl<sub>4</sub> during the first step of the synthesis, which is inhibited at high NaOH concentrations. Finally, X-ray absorption spectra of synthesis intermediates are found to be remarkably similar to those of cluster samples, for which we offer a number of possible explanations.

## 7.2 Experimental methods

### Chemicals

$\text{HAuCl}_4 \cdot 3 \text{H}_2\text{O}$  ( $\geq 99.9\%$ ),  $\text{NaBH}_4$  (99%) and ( $\pm$ )- $\alpha$ -lipoic acid ( $\geq 99\%$ ) were purchased from Sigma Aldrich.  $\text{NaOH}$  ( $\geq 99.9\%$ ) was obtained from Roth. Water was of Milli-Q quality, purified using a Millipore Direct-Q 3 water purification system.

### Synthesis of Au clusters

10 mg lipoic acid (49  $\mu\text{mol}$ ) was placed in a 20 mL glass vial with water and a small amount of  $\text{NaOH}$  solution, with a total volume of 10.5 mL. Three concentrations of  $\text{NaOH}$  were investigated; 8.9, 12 and 89 mM. This corresponds to 0.5 mL 0.2 M, 0.7 mL 0.2 M and 0.5 mL 2 M  $\text{NaOH}$  in the synthesis. While stirring, 0.25 mL 68 mM  $\text{HAuCl}_4 \cdot 3 \text{H}_2\text{O}$  (17  $\mu\text{mol}$ ) was added to the LA solution, giving the synthesis intermediate. After 15 min, the synthesis intermediate was reduced with  $\text{NaBH}_4$  (1.7 mg in 0.5 mL water). Vials were wrapped in aluminium foil, kept closed except when adding reagents, and stirred throughout the synthesis, which was done at room temperature. Clusters were used without additional purification or concentration (except were explicitly noted), after stirring overnight. The samples before reduction, termed synthesis intermediates, were also studied. When describing these samples, the  $\text{NaOH}$  concentrations in the final volume are used. For experiments using the liquid jet setup, the synthesis was scaled up 5 $\times$ .

**Additional samples:  $\text{Au}_{25}(\text{SR})_{18}$  clusters and Au nanoparticles** Atomically monodisperse  $\text{Au}_{25}(\text{SR})_{18}^-$  clusters, where SR is 2-phenylethanethiolate, were provided by C. A. Hosier of Colorado State University. The clusters were prepared using a previously published synthesis<sup>235</sup> with tetrahydrofuran as the solvent. The purification protocol was slightly modified. After synthesis, the organic layer was isolated and concentrated. The clusters were then precipitated out of the concentrated organic layer by the addition of methanol. The resulting precipitate was washed twice more with methanol. A dichloromethane extraction of the precipitate followed by evaporation of the solvent afforded pure  $\text{Au}_{25}(\text{SR})_{18}^-$  nanoclusters as a brown oil. The counterion is tetraoctylammonium bromide. The clusters were characterised with UV-Vis spectroscopy and matrix-assisted laser desorption ionisation mass spectrometry to ensure their purity. This sample was used for X-ray absorption spectroscopy.

An aqueous solution of Au nanoparticles was provided by C. S. Wondergem of Utrecht University. The particles were prepared according to a standard protocol<sup>356</sup>, and consist of  $\sim 1.8$  nm Au cores capped with 4-(diphenylphosphino)-benzoic acid. The particle size was determined with transmission electron microscopy. This sample was used for X-ray emission spectroscopy.

### X-ray absorption and emission spectroscopy

Au L<sub>3</sub>-edge XANES (11.919 keV) was recorded at beamline ID26 at the European Synchrotron Radiation Facility. The incident beam was selected using the (311) reflection from a double Si crystal monochromator. The spectrometer was equipped with a set of four Ge(555) analyser crystals to record High Energy Resolution Fluorescence Detected (HERFD) XANES. Masks were used to increase the resolution. The L $\alpha_1$  fluorescence channel was monitored (9.71 keV). A liquid jet setup was used to minimise radiation damage. A schematic figure of the setup is shown in Figure 7.2. Samples of LA-capped Au clusters (5 $\times$  normal scale) were placed in a vial from which liquid was pumped through a capillary to form a free-standing liquid jet which was placed in the focus of the beam. Below the jet, the liquid was collected and returned to the vial.

For X-ray Emission Spectroscopy (XES), the spectrometer was equipped with a set of five Si(951) analyser crystals, with masks to maximise the resolution. The same liquid jet setup as for XANES was used, with one modification: a flow cuvette was included in the setup to record UV-Vis absorption spectra. This was done to monitor damage to the sample due to exposure to X-rays. Each sample was measured for  $\sim 1$  h for XANES and  $\sim 3.5$  h for XES. The excitation energy for XES was 11.922 keV for all samples, which corresponds to the whitenline. The emission spectra were shifted so that the elastic line corresponds to 0 eV energy transfer.

Additional XANES was recorded using a cryostat (KONTI, CryoVac) cooled with liquid He. The typical operating temperature was 40 K. Molecular mass cutoff filters (3 kDa, Amicon Ultra-4, Merck) were used to concentrate the LA-capped Au cluster solution around 30 $\times$ . Samples were placed in teflon holders with kapton windows and plunged into liquid nitrogen before being transferred to the cryostat. The Au<sub>25</sub>(SR)<sub>18</sub><sup>-</sup> clusters were dissolved in dichloromethane and dropcast on kapton tape, which was then fastened to the sample holder. To limit radiation damage, short scans were done on different spots. The time per scan was 5–30 s, depending on the sample.

**XANES analysis** XANES spectra were compared to those of reference compounds (see Chapter 6), and also to calculations. Calculations were done using FDMNES.<sup>120</sup> Atomic potentials, Fermi level, and charge transfer were calculated self-consistently, relativistic effects were taken into account, and the finite difference method was used to calculate potentials.<sup>212,213</sup> The real Hedin, Lundqvist and Von Barth exchange correlation potential was used. The radius for calculation was 6 Å. The spectra were convoluted to apply an energy-dependent broadening, using default parameters (an arctangent function). The width of the core-hole was decreased to 0.50 eV and further broadened with a 1.0 eV Gaussian, to better match the experimental data. The individual contributions to the spectrum of d and s final states,  $\Delta l = +1$  and  $-1$ , respectively, were calculated using *lplus1* and *lminus1* cards.

Spectra were calculated for four different clusters; Au<sub>18</sub>(SR)<sub>14</sub> with cyclohexanethiolate ligands<sup>357</sup>, Au<sub>25</sub>(SR)<sub>18</sub> with 2-phenylethanethiolate ligands<sup>53</sup>, and two different Au<sub>22</sub>(SCH<sub>3</sub>)<sub>18</sub> structures.<sup>162,358</sup> The first two structures were determined using single crys-

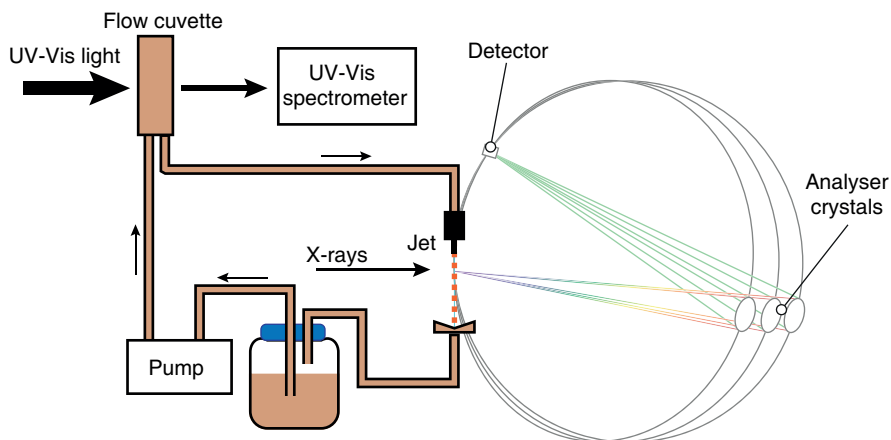


**Figure 7.2** Liquid jet setup with continuous flow for recording X-ray absorption spectroscopy. The sample is pumped from the reservoir first through a flow cuvette to record UV-Vis spectroscopy, then through a capillary nozzle to form a freestanding jet, where X-ray spectroscopy can be measured. The flow cuvette was not included for XANES experiments.

tal X-ray crystallography, while the latter were obtained from DFT calculations. Additional FDMNES calculations were done for  $\text{H}_2\text{O}\cdots\text{AuCl}_4\cdots\text{OH}_2$  and  $\text{H}_2\text{O}\cdots\text{Au}(\text{OH})_4\cdots\text{OH}_2$ , where the complex has a square planar geometry with Au–Cl and Au–O bonds of 2.29 and 1.97 Å, respectively. The axial Au $\cdots\text{OH}_2$  bonds were varied between 2.3–3.0 Å in the calculations.

## EXAFS

Au  $L_3$ -edge EXAFS was recorded at beamline BM26A (DUBBLE) of the European Synchrotron Radiation Facility.<sup>205</sup> The incident beam was selected using a Si(111) monochromator. The measurements were performed in fluorescence mode using an 8 element Ge detector. A cryostat cooled with liquid  $\text{N}_2$  (77 K) was used. A cluster sample with 8.9 mM NaOH was concentrated around 20 $\times$  using 3 kDa molecular mass cutoff filters (Amicon Ultra-4, Merck). Assuming no Au is lost, the final Au concentration was  $\sim 30$  mM. More dilute samples were also measured to check for self-absorption. The sample was sealed in kapton tape in a holder, then plunged into liquid nitrogen before being transferred to the cryostat. Additional room temperature EXAFS of samples with 8.9, 12 and 89 mM was recorded at beamline ID26, using the liquid jet setup described above.

**EXAFS analysis** EXAFS analysis was done using the Athena and Artemis software packages.<sup>207</sup> Scattering phases and amplitudes were calculated using FEFF for an Au atom on the surface of the icosahedral core in  $\text{Au}_{25}(\text{SR})_{18}$ .<sup>53</sup> To minimise the effect of multielectron excitations<sup>359,360</sup>, the background removal in Athena minimised peaks in the Fourier transformed EXAFS below  $R = 1.5$ .<sup>361</sup> Typical fit parameters were:  $k = 3.0\text{--}14.0 \text{ \AA}^{-1}$ ,

$R = 1.55\text{--}3.3 \text{ \AA}$ , using a Hanning window ( $dk = 1 \text{ \AA}^{-1}$ ) for the Fourier transformation and  $k = 1, 2, 3$  weighting. One parameter for the energy shift  $E_0$  was used for all paths. The amplitude reduction factor was not considered during fitting, that is,  $S_0^2 = 1$  was used. From fitting Au foil and an Au(I)-thio sample, and assuming transferability of  $S_0^2$ , we can estimate  $S_0^2 = 0.8$ .

### UV-Vis spectroscopy

Before and after XANES, UV-Vis absorption spectra were recorded of all samples using a Perkin Elmer Lambda 40. During measurements of XES, UV-Vis absorption spectra were recorded by pumping the solution through a Hellma 3-in-1 flow cuvette (product nr 176-766-15-40, 10 mm path length) which was built into the circuit just before the capillary. The excitation source was an Ocean Optics DH-2000-BAL lamp equipped with an Ocean Optics FVA-UV fiber optic variable attenuator, and transmitted light was detected using an Ocean Optics Maya 2000 Pro spectrometer. The attenuator was positioned between the lamp and flow cuvette to decrease the intensity of UV-Vis light, which was necessary to avoid saturation of the spectrometer. By recording a blank and dark spectrum, the absorbance of the sample was immediately calculated by the software (SpectraSuite).

## 7.3 Results and discussion

### EXAFS

Room temperature EXAFS was recorded of LA-capped Au clusters with 8.9, 12 and 89 mM NaOH, using the liquid jet setup. Spectra are shown in Figure 7.3. The Fourier transform shows only one major peak, consistent with the Au–S bond in Au(I)-thio. The lack of observable Au–Au bonding may be due to the high temperature, which leads to a dampening of the EXAFS oscillations. In clusters, the Debye-Waller factors of Au–Au are more temperature-dependent than those of Au–S.<sup>222</sup>

Therefore EXAFS of one cluster sample was also recorded at 77 K. The 8.9 mM NaOH sample was chosen, because from mass spectrometry and analytical ultracentrifugation (Chapter 5) we expect this to have the highest Au–Au coordination number. In addition, it is the only sample that does not contain a fraction of small clusters or Au complexes which are lost upon concentration with molecular mass cutoff filters (see Figure C.5). The low temperature allowed us to analyse EXAFS up to  $k = 14 \text{ \AA}^{-1}$ . A first fit was done using one Au–S and one Au–Au scattering path. Results of the fit are given in Table 7.1 and the fit is shown in Figure 7.4. The Au–Au coordination number is 0.8 (if  $S_0^2$  is considered, the coordination number becomes 1.0). This is similar to what was found for  $\text{Au}_{22}(\text{SR})_{18}$ <sup>162</sup>, which suggests

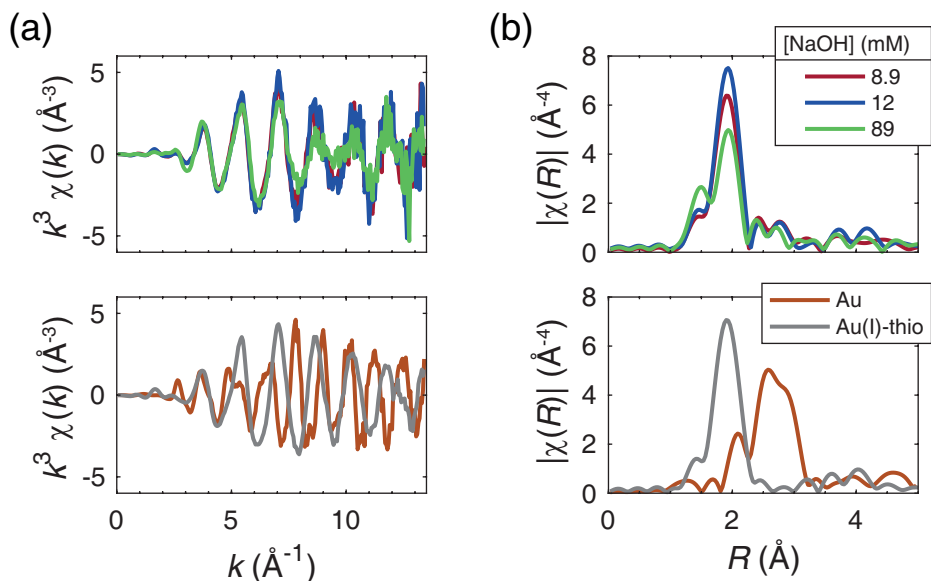


**Figure 7.3** Room temperature EXAFS of Au clusters with 8.9, 12 and 89 mM NaOH (top), as well as that of Au(l)-thio and bulk Au (bottom). All samples are measured as solutions in the liquid jet setup, except Au which was a solid. (a) and (b) show EXAFS in  $k$ -space and  $R$ -space, respectively.

an open structure with large staple motifs. However, the Fourier transformed EXAFS appears to show two Au–Au scattering paths, a feature that is not accurately reproduced by the fit.

Previous studies on thiolate-protected Au clusters have shown that there are two typical Au–Au bond distances. For  $\text{Au}_{25}(\text{SR})_{18}$ , these are around 2.78 and 2.95  $\text{\AA}$ .<sup>222,223</sup> The shorter bonds are from the central atom to the surface atoms of the icosahedral  $\text{Au}_{13}$  core, as well as between some adjacent surface atoms. The remaining bonds in  $\text{Au}_{13}$  are  $\sim 2.95$   $\text{\AA}$ . In addition,  $\text{Au}_{25}(\text{SR})_{18}$  contains  $\sim 3.15$   $\text{\AA}$  Au–Au bonds from the core to the Au atoms in staple motifs.<sup>223</sup> These aurophilic bonds have a high Debye-Waller factor and may be hard to observe even at low temperature.<sup>222</sup>

In accordance with these previous studies, we performed a fit with two Au–Au scattering paths. The experimental EXAFS is shown in Figure 7.5, together with the fit. Results of the fit are given in Table 7.2. With three rather than two scattering paths, the number of fit parameters increases which gives larger uncertainty in the fit results. Therefore the Debye-Waller factor of the long Au–Au path was fixed to  $1.5\times$  that of the short path. Based on previously reported Debye-Waller factors

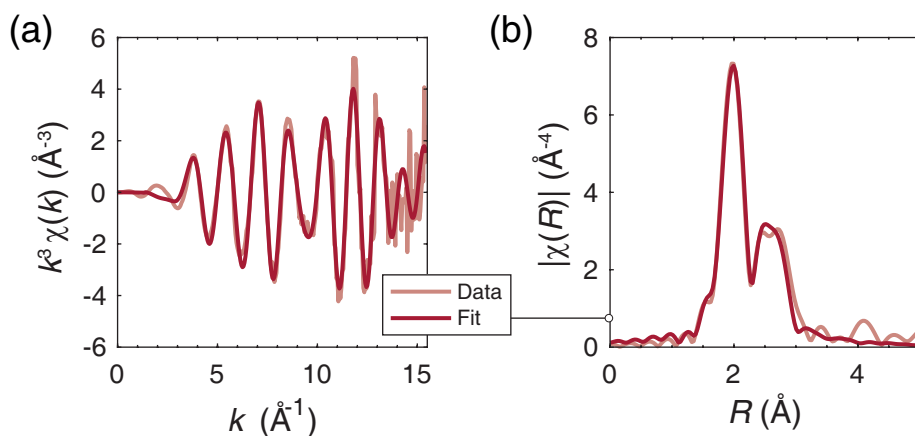


**Figure 7.4** EXAFS of Au clusters with 8.9 mM NaOH, in (a)  $k$ -space and (b)  $R$ -space, together with the fit to one Au–S and one Au–Au path. Results of the fit are given in Table 7.1.

**Table 7.1** Structural parameters of Au clusters with 8.9 mM NaOH at 77 K, from EXAFS analysis. CN is the coordination number,  $R$  the bond length,  $\sigma^2$  the Debye-Waller factor and  $E_0$  the energy shift. The fit is shown in Figure 7.4. For this fit, R-factor = 0.013 and reduced  $\chi^2 = 151$ . The amplitude reduction factor is not taken into account ( $S_0^2 = 1$ ) for the values in the table. From fitting of Au foil it was estimated to be 0.8.

Parameter	Au–S	Au–Au
CN	$1.38 \pm 0.18$	$0.80 \pm 0.45$
$R$ (Å)	$2.32 \pm 0.01$	$2.73 \pm 0.01$
$\sigma^2$ ( $10^{-3}$ Å <sup>2</sup> )	$1.79 \pm 0.97$	$2.64 \pm 2.17$
$E_0$ (eV)	$7.33 \pm 1.24$	

of thiolate-protected Au clusters<sup>222</sup>, this is a reasonable constraint. Furthermore, when the constraint was lifted, the fit results varied no more than 15%.

Au–Au coordination numbers are 1.8 and 1.7 for the short and long path, respectively (or 2.3 and 2.1 if  $S_0^2$  is taken into account). This is consistent with coordination numbers found for Au<sub>25</sub>(SR)<sub>18</sub> and Au<sub>38</sub>(SR)<sub>24</sub> clusters. Bond lengths and Debye-Waller factors are also consistent with previous reports on clusters of this size.<sup>222,223,288</sup> EXAFS results are in agreement with analytical ultracentrifugation and mass spectrometry studies (Chapter 5).

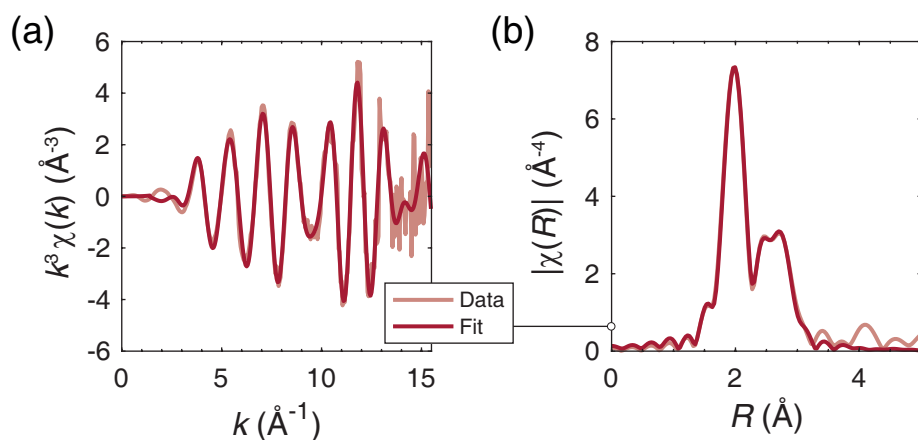


**Figure 7.5** EXAFS of Au clusters with 8.9 mM NaOH, in (a)  $k$ -space and (b)  $R$ -space, together with the fit to one Au–S and two Au–Au paths. Results of the fit are given in Table 7.2.

**Table 7.2** Structural parameters of Au clusters with 8.9 mM NaOH at 77 K, from EXAFS analysis. CN is the coordination number,  $R$  the bond length,  $\sigma^2$  the Debye-Waller factor and  $E_0$  the energy shift. The fit is shown in Figure 7.5. For this fit, R-factor = 0.0022 and reduced  $\chi^2 = 45$ . The amplitude reduction factor is not taken into account ( $S_0^2 = 1$ ) for the values in the table. From fitting of Au foil it was estimated to be 0.8.

Parameter	Au–S	Au–Au (1)	Au–Au (2)
CN	$1.23 \pm 0.10$	$1.82 \pm 0.42$	$1.65 \pm 0.58$
$R$ (Å)	$2.32 \pm 0.01$	$2.74 \pm 0.01$	$2.97 \pm 0.01$
$\sigma^2$ ( $10^{-3}$ Å <sup>2</sup> )	$1.08 \pm 0.53$	$5.81 \pm 0.95$	8.72*
$E_0$ (eV)		$7.96 \pm 0.62$	

\* Fixed to  $1.5 \times \sigma^2$  of Au–Au (1).

### XANES and XES of clusters

HERFD-XANES spectra of Au clusters with 8.9, 12 and 89 mM NaOH are shown in Figure 7.6. All three spectra show an intense whiteline and prominent features up to around 10 eV above the edge. Further above the edge, there are no prominent peaks, which is reasonable for small, disordered species.<sup>233,234</sup> The spectra resemble that of sodium aurothiomalate (Au(I)-thio, see Chapter 6). This will be discussed in more detail later.

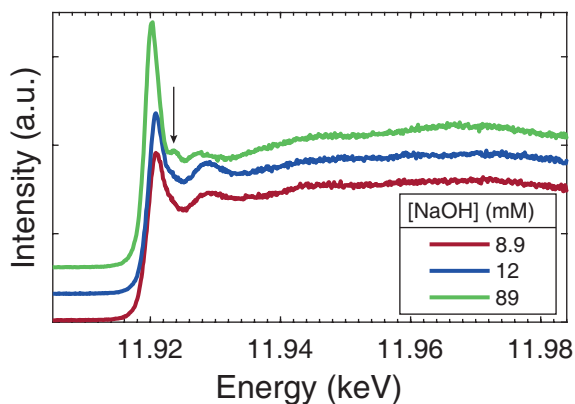


**Figure 7.6** HERFD-XANES of Au clusters with 8.9 and 12 mM NaOH. Spectra are shifted vertically to better observe all spectral features. The arrow indicates a shoulder in whiteline of the 89 mM spectrum.

The spectra of the three Au clusters show variation in the intensity of the first peak, the whiteline. As seen in Chapter 6, this peak arises mainly due to  $2p_{3/2} \rightarrow 5d$  transitions and its intensity depends on the number of d-holes.<sup>362</sup> In bulk Au, there is hybridisation of s, p and d orbitals, giving a configuration of  $5d^{10-\delta}6sp^{1+\delta}$ .<sup>336</sup> This creates some empty states in the d-band, giving rise to the whiteline.<sup>112,114</sup> An increased whiteline intensity is observed for oxidised compounds<sup>337,363</sup>, as can be seen in Figure 6.1. Bonding to electron-withdrawing ligands can also create d-holes.

However, the whiteline intensity can also change as the size of the Au particle is decreased. For bare Au nanoparticles on oxide supports, it was found that the intensity decreased with decreasing particle size.<sup>115</sup> This behaviour was independent of the type of support. Calculated density of states showed that a particle of just a few Au atoms has a narrower d-band at higher energy and a higher d electron density, compared to bulk Au. Lower whitelines than in bulk Au are also observed for 2 nm Au nanoparticles capped by dendrimers, which interact only weakly with Au. In contrast, when strongly interacting, electron-withdrawing thiolates were used, the whiteline intensity increased.<sup>364</sup> This effect was size-dependent, with whiteline intensity increasing with decreasing particle size.<sup>365</sup> Thus, for thiolate-protected clusters, an intense whiteline implies a larger fraction of Au atoms in staple motifs, so a smaller cluster.

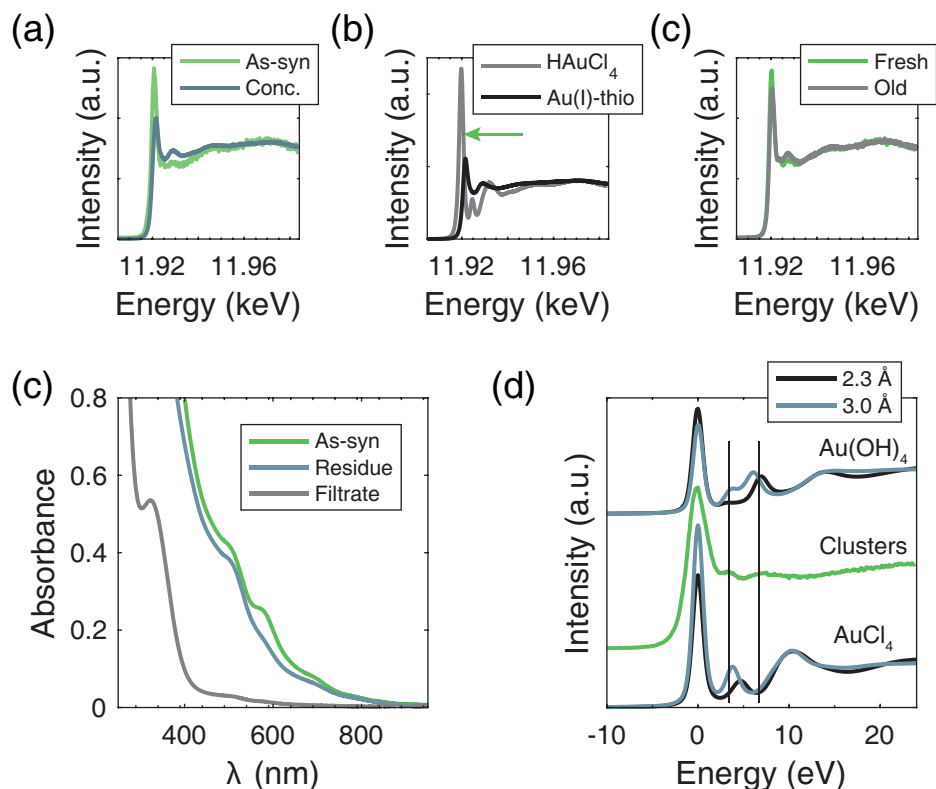


**Figure 7.7** (a) HERFD-XANES of Au clusters with 89 mM NaOH, as-synthesised and after concentration with molecular mass cutoff filters. Both samples were measured in the cryostat. (b) HERFD-XANES of HAuCl<sub>4</sub> and Au(I)-thio, for comparison. The green arrow indicates the maximum whiteline intensity of the as-synthesised clusters with 89 mM NaOH. (c) HERFD-XANES of a freshly prepared and a 6-day-old sample, measured in the liquid jet setup. (d) UV-Vis spectra of the as-synthesised clusters, as well as the residue and filtrate after concentration with molecular mass cutoff filters (the former corresponds to the concentrated sample). (e) FDMNES calculations of square planar AuCl<sub>4</sub> (bottom) and Au(OH)<sub>4</sub> (top) complexes, both with two axial H<sub>2</sub>O molecules, at 2.3 and 3.0 Å distance. The spectra are shifted so the whiteline maxima are aligned, and two features in the cluster spectrum are marked with vertical lines.

**The sample with 89 mM NaOH** While the 8.9 and 12 mM NaOH samples are nearly identical, the third sample is markedly different. The whiteline is more intense and has a shoulder 4 eV above the maximum. The spectrum is reminiscent of that of  $\text{HAuCl}_4$  or  $\text{Au}_2\text{O}_3$  (see Chapter 6). Both these compounds are formally Au(III) and adopt square planar geometry.  $\text{HAuCl}_4$  is the precursor for the Au cluster synthesis. The spectrum of the 89 mM NaOH sample changed upon concentration with molecular mass cutoff filters as seen in Figure 7.7: the whiteline intensity decreased and the shoulder on the whiteline disappeared, so that the spectrum resembles that of the two other clusters. Molecular mass cutoff filters remove small molecules from solution, such as excess ligands and solvent, thus effectively increasing the concentration of the heavier species. The UV-Vis spectrum of the sample hardly changed, however. Only a small amount of species absorbing in the visible (small clusters) pass through the filter. However, no luminescence was observed for the filtrate so this represents only a minor fraction of the total number of cluster species in the sample.

We attribute the similarity between spectra of  $\text{HAuCl}_4$  and clusters with 89 mM NaOH to the presence of  $\text{HAuCl}_4$ -like species in the as-synthesised cluster sample. These species are small enough to be removed with cutoff filters and do not absorb in the visible. Interestingly, the cluster sample was relatively stable in the X-ray beam: there were no noticeable changes in the X-ray absorption spectrum during the measurement (see Figures C.3 and C.4 and the discussion on radiation damage at the end of this chapter). This is in contrast to  $\text{HAuCl}_4$ , which was highly unstable in the liquid jet setup and within minutes of exposure to X-rays formed large, plasmonic nanoparticles, with a spectrum that resembled that of bulk Au. The 89 mM NaOH sample, on the other hand, was still stable with no change in whiteline intensity after around 1 h. At high NaOH concentrations, we expect hydrolysis of  $\text{AuCl}_4^-$  to occur, which gives  $\text{AuCl}_{4-x}(\text{OH})_x^-$ , where species with  $x = 3-4$  dominate.<sup>317,318</sup> The Au(III) species present in the 89 mM NaOH sample are therefore probably hydrolysed. The difference in ligand may affect the susceptibility of the compound to radiation damage. FDMNES calculations were done of  $\text{AuCl}_4^-$  and  $\text{Au}(\text{OH})_4^-$  complexes (Figure 7.7), both with square planar geometry and two axially coordinating  $\text{H}_2\text{O}$  molecules.<sup>348,366</sup> The features of the 89 mM NaOH cluster spectrum are accurately reproduced by the latter calculation in particular.

It was noted in Chapter 5 that the 89 mM NaOH sample was unstable, with a strong decrease in absorbance after just a few days. HERFD-XANES was therefore also done of a 6-day-old sample. Compared to the fresh (1-day-old) sample, this showed a decreased whiteline intensity, indicative of reduction or an increase in cluster size.

**Resonant X-ray emission spectroscopy of Au clusters** Resonant X-ray emission spectra were recorded of Au clusters with 8.9, 12 and 89 mM NaOH in the liquid jet setup. The X-ray emission comes from the valence orbitals and can thus be used to study the filled states. In this two-photon process, the net result is an excitation from valence to empty states, similar as in UV-Vis. The energy transfer is on the order of a few eV. The Au concentration in the cluster samples was too low to record a full RIXS plane within reasonable time, as was done in Chapter 6 for the reference compounds. We therefore recorded X-ray emission spectra at constant excitation energy, which corresponds to a vertical cut through the RIXS plane. Spectra are shown in Figure 7.8, together with those of reference compounds at the same excitation energy (11.922 keV). All three cluster samples have an intense peak at 7 eV. This feature is also present in the Au(I)-thio sample. The 89 mM NaOH sample has an additional shoulder at 4.5 eV, reminiscent of the spectra of Au<sub>2</sub>O<sub>3</sub> and HAuCl<sub>4</sub>. This confirms what was found from XANES; that this sample still contains some precursor. Finally, all three cluster samples have a shoulder at 16 eV, which is not present in Au(I)-thio or bulk Au. It is observed in the spectrum recorded of Au nanoparticles. These have a core size of ~1.8 nm and are capped by 4-(diphenylphosphino)benzoic acid, which binds to Au via its carboxylic acid group.

#### HERFD-XANES of Au cluster samples: Au(I)-thiolates or clusters?

Spectra of Au clusters with 8.9 and 12 mM NaOH, as well as the concentrated 89 mM sample, show similarities to that of Au(I)-thio. As discussed in Chapter 6, this reference compound consists of two intertwined strands of ...-Au-S-Au-S-.... The Au-S bonds are 2.29 Å, similar to those in thiolate-capped Au clusters.<sup>53,222</sup> The nearest Au-Au distance is 3.23 Å, which is similar to the distance between Au atoms in the icosahedral core and Au atoms in the staple motifs of Au<sub>25</sub>(SR)<sub>18</sub><sup>-</sup>.<sup>53</sup> The local environment of Au in Au(I)-thio is thus similar to that of Au in cluster staple motifs. A closer look at the spectra of Au(I)-thio and clusters with 8.9 and 12 mM NaOH (Figure 7.9) reveals some subtle differences, which implies the samples are not chemically and structurally identical. First, both clusters have lower whiteness, meaning Au atoms in the cluster samples have, on average, an oxidation state lower than Au(I). This suggests that part of the Au atoms are present as Au(0) in the core of a cluster. Second, the feature marked **A** in Figure 7.9 is at the same energy for Au(I)-thio and the 12 mM NaOH sample, while it is shifted around 0.5–1 eV to higher energy for the 8.9 mM NaOH sample. Third, both clusters show a weak post-edge feature at 11.945 keV (marked **B**) that is not as pronounced in Au(I)-thio. This is most easily observed in spectra of concentrated clusters, which are less noisy than the spectra recorded in the liquid jet.

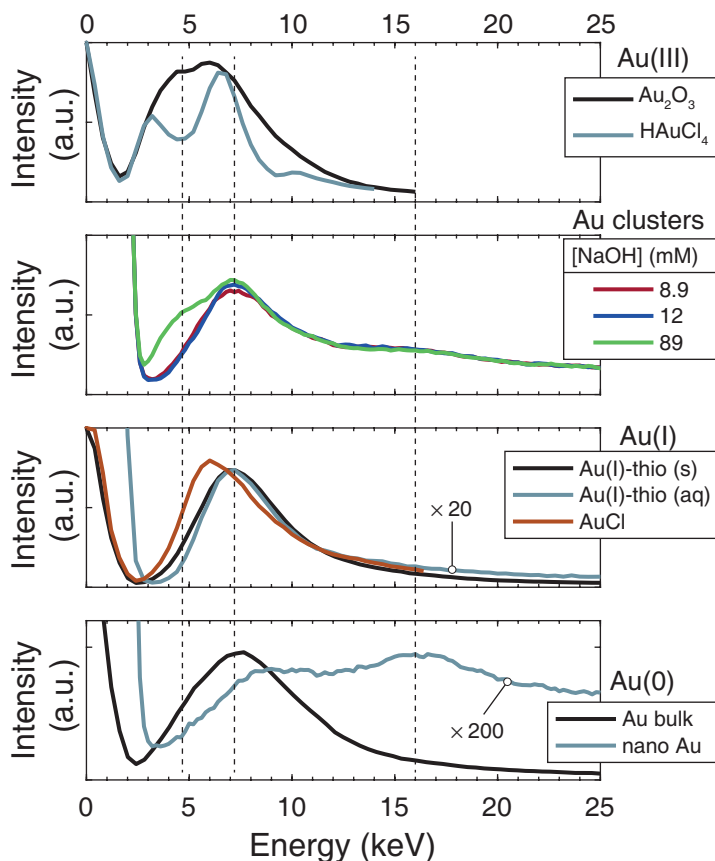


**Figure 7.8** X-ray emission spectra of Au clusters with 8.9, 12 and 89 mM NaOH, together with spectra of reference compounds. Vertical lines mark spectral features observed for the clusters. The nano Au sample consists of 1.8 nm Au particles, capped with 4-(diphenylphosphino)benzoic acid (a carboxylic acid). Where spectra of solid and aqueous samples have been plotted in the same graph, the intensity of the latter have been increased as these samples are dilute.

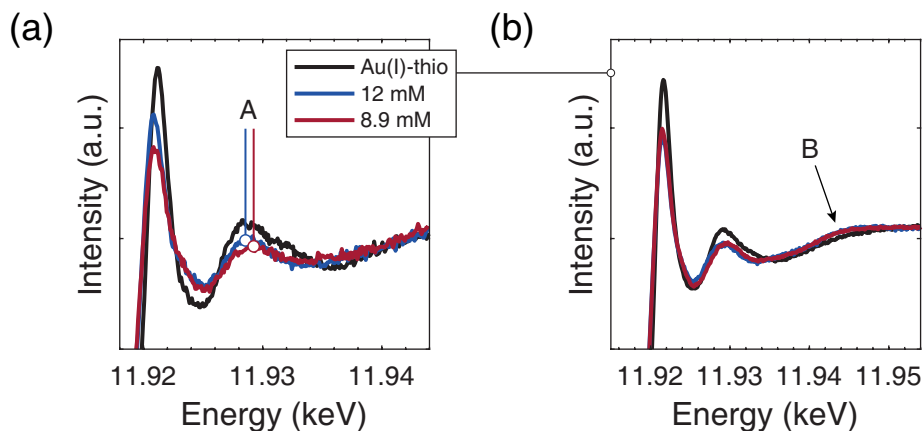


**Figure 7.9** (a) Close-up of HERFD-XANES around the edge, of Au clusters with 8.9 and 12 mM NaOH, together with Au(I)-thio. All samples are measured in the liquid jet setup, with the same Au concentration. Note the different energies for feature **A**. (b) Same, but for concentrated cluster samples, and solid Au(I)-thio. Samples were measured in the cryostat.

We further note that XANES spectra of Au clusters with 8.9 and 12 mM NaOH do not change upon concentration with molecular mass cutoff filters, as shown in Figure C.5. UV-Vis absorption spectra recorded before and after concentration are nearly identical as well. The filtrate of the 8.9 mM NaOH sample clearly contains only LA, while that of the 12 mM NaOH sample contains some other species that absorb around 300 nm. These may be Au(I)-thiolate complexes, or small clusters with  $\leq 10$  Au atoms.<sup>150</sup>

For these two clusters, the whiteline intensities varied somewhat, as shown in Figure 7.9. In the liquid jet, two samples were measured and the whiteline intensity of the 12 mM NaOH sample was consistently the highest, implying a smaller cluster. This is in agreement with what was found with mass spectrometry and analytical ultracentrifugation. However, the whiteline intensities of concentrated samples measured in the cryostat were similar. This was also the case for as-synthesised samples measured in the cryostat. For concentrated samples, UV-Vis spectra show that some Au(I)-complexes or small clusters are likely removed from the 12 mM sample during filtration. This may explain the decrease in whiteline. The as-synthesised sample measured in the cryostat was found to have a somewhat higher UV-Vis absorbance than usual, especially above 600 nm as is typically found for clusters with lower NaOH concentrations. This may explain its lower whiteline intensity, although we cannot conclusively say whether these whiteline intensities

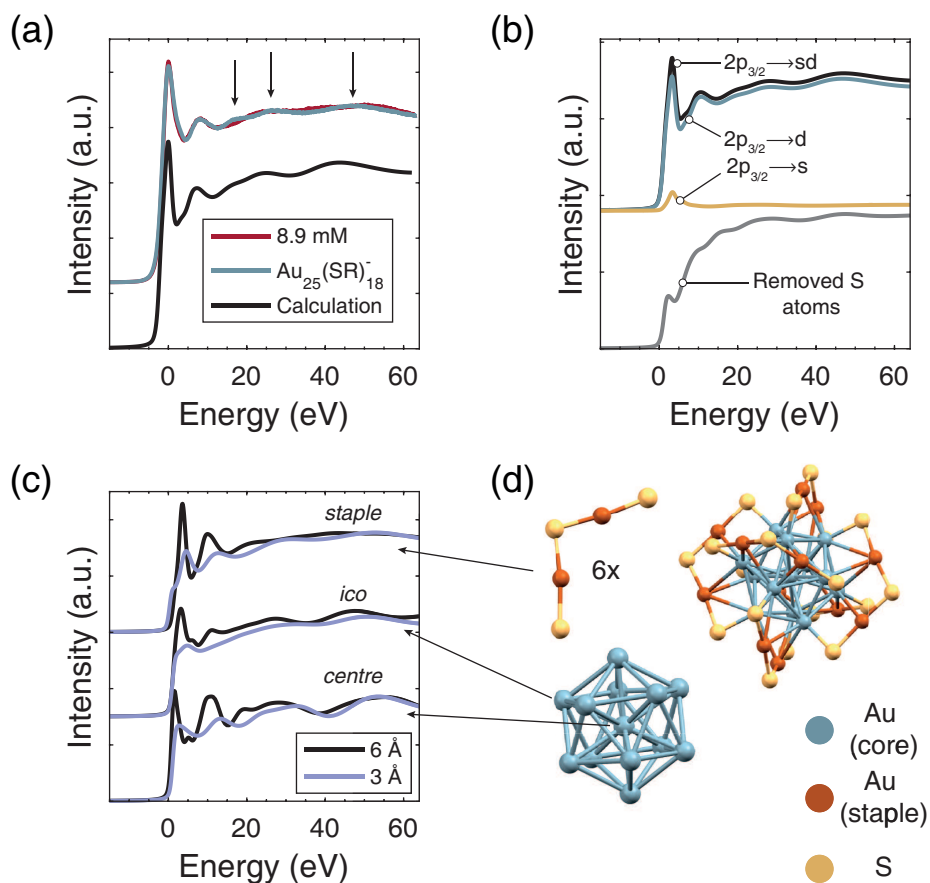


**Figure 7.10** (a) HERFD-XANES of Au<sub>25</sub>(SR)<sub>18</sub><sup>-</sup> and LA-capped clusters with 8.9 mM NaOH, together with the calculated spectrum of Au<sub>25</sub>(SR)<sub>18</sub><sup>-</sup>. Spectra are shifted so the whitelines overlap. Arrows mark post-edge features found in Au<sub>25</sub>. (b) Calculated spectrum of Au<sub>25</sub>(SR)<sub>18</sub><sup>-</sup> for the dipole selection rules  $\Delta l = \pm 1$  (s+d final states, black),  $\Delta l = +1$  (d final states, blue) and  $\Delta l = -1$  (s final states, yellow). Also shown is the calculated spectrum ( $\Delta l = \pm 1$ ) of the cluster with all S atoms removed (grey). (c) Calculated spectra of the *centre*, *ico* and *staple* sites of Au<sub>25</sub>(SR)<sub>18</sub><sup>-</sup>, calculated with 3 and 6 Å radii. (d) The structure of Au<sub>25</sub>(SR)<sub>18</sub><sup>-</sup>. Also shown are the Au<sub>13</sub> core and an SR-(Au-SR)<sub>2</sub> staple motif. For clarity, Au atoms in the core and staple motifs have been given different colours, and ligand backbones have been omitted.

truly reflect the average cluster size of the sample, or whether there is some natural variation between samples with the same NaOH concentration.

From the similarity between the clusters and Au(I)-thio, it is tempting to assume that the clusters contain a large fraction of Au(I)-thiolates and are thus much smaller than found in Chapter 5 or by EXAFS analysis. However, this is not necessarily the case. As can be seen in Figure 7.10, the intense whitenline and first post-edge feature are also present in the spectrum of  $\text{Au}_{25}(\text{SR})_{18}^-$ . This spectrum is further compared to results of FDMNES calculations. All spectral features of  $\text{Au}_{25}(\text{SR})_{18}$  are accurately reproduced. By performing the calculation for  $l \rightarrow l + 1$  and  $l \rightarrow l - 1$  dipole selection rules, we see that the whitenline intensity is mostly due to  $2p_{3/2} \rightarrow 5d$  transitions, with only a minor contribution from  $2p_{3/2} \rightarrow 6s$ . A calculation with the overall dipole selection rule  $l \rightarrow l \pm 1$  for the same cluster with all S atoms removed shows a dramatic reduction in whitenline intensity. This clearly illustrates that the intense whitenline of thiolate-capped Au clusters is due to bonding to electron-withdrawing thiolate ligands. The  $\text{Au}_{25}$  cluster consists of an icosahedral  $\text{Au}_{13}$  core surrounded by six  $\text{SR}-(\text{Au}-\text{SR})_2$  staple motifs. There are 36 Au-S bonds. The cluster has three unique sites; *centre* (1 site), *ico* (12 sites) and *staple* (12 sites). Spectra of the three different sites are also shown in Figure 7.10, for two different radii of the calculation. At 3 Å, only nearest neighbours are taken into account, while at 6 Å the staple motifs are also included in the calculation of the *centre* spectrum.

As the structures of LA-capped Au clusters are unknown, we performed FDMNES calculations for a number of Au cluster model systems. In addition to  $\text{Au}_{25}(\text{SR})_{18}$ , they are  $\text{Au}_{18}(\text{SR})_{14}$  with cyclohexanethiolate ligands<sup>357</sup>, and two different  $\text{Au}_{22}(\text{SCH}_3)_{18}$  structures<sup>162,358</sup>, which were both obtained from DFT calculations. The structures are shown in Figure 7.11.

The  $\text{Au}_{18}(\text{SR})_{14}$  cluster consists of a bi-octahedral  $\text{Au}_9$  core protected by three different types of staple motifs; one  $\text{SR}-(\text{Au}-\text{SR})_4$ , one  $\text{SR}-(\text{Au}-\text{SR})_2$  and three  $\text{SR}-\text{Au}-\text{SR}$ . The overall cluster shape is somewhat elongated, and it has 28 Au-S bonds. The first  $\text{Au}_{22}(\text{SCH}_3)_{18}$  structure, hereafter called **(1)**, has a prolate  $\text{Au}_8$  core surrounded by two  $\text{SR}-(\text{Au}-\text{SR})_3$  and two  $\text{SR}-(\text{Au}-\text{SR})_4$  staple motifs.<sup>162</sup> The structure of  $\text{Au}_{22}(\text{SCH}_3)_{18}$  **(2)** consists of a bitetrahedral  $\text{Au}_7$  core surrounded by a ring-shaped  $\text{Au}_6(\text{SR})_6$  complex and three  $\text{SR}-(\text{Au}-\text{SR})_3$  staple motifs.<sup>358</sup> Structures **(1)** and **(2)** have elongated and triangular shapes, respectively, both with 36 Au-S bonds. It has been proposed that the longer staple motifs found in these clusters, compared to  $\text{Au}_{25}$ , are necessary to protect the small cores of these clusters.<sup>367</sup> LA has two S-atoms which most likely both bind to the Au core.<sup>66</sup> These two S atoms can participate in the same staple motif or in different ones, further increasing the number of possible structures.<sup>368</sup>

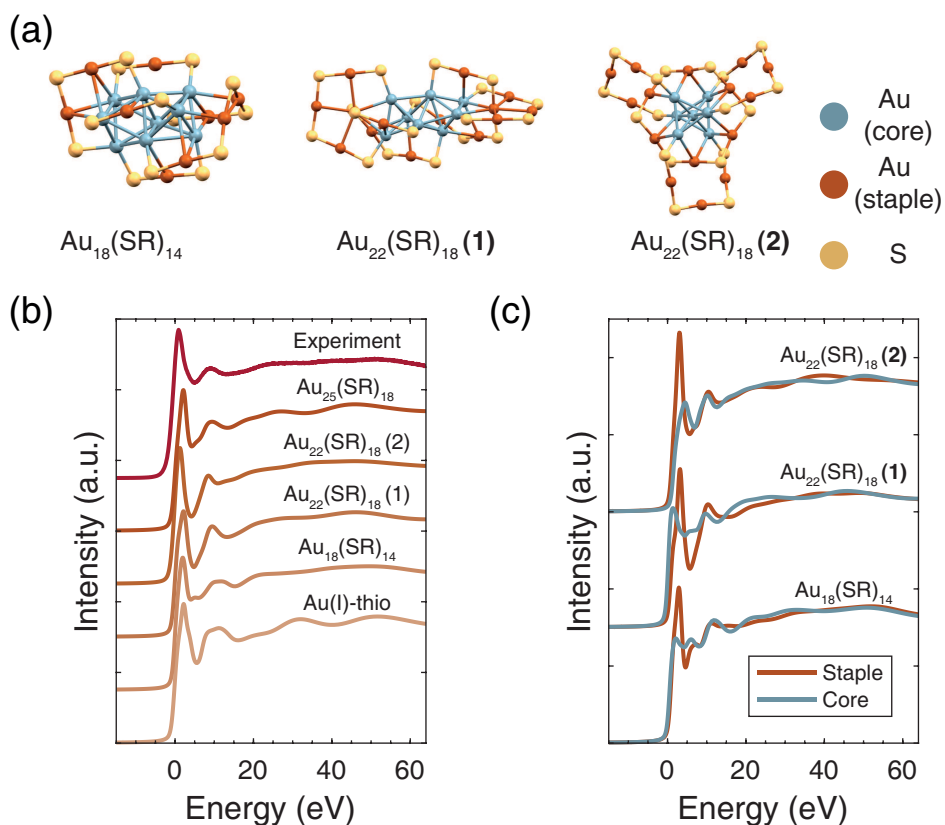


**Figure 7.11** (a) Structures of three thiolate-protected Au clusters. For clarity, Au atoms in the core and staple motifs have been given different colours, and ligand backbones have been omitted. (b) FDMNES calculations of the three clusters in (a), as well as  $\text{Au}_{25}(\text{SR})_{18}$  and Au(I)-thio. The experimental spectrum of Au clusters with 8.9 mM NaOH is also shown. All spectra are aligned to the edge (maximum of the first derivative). (c) FDMNES calculations of the three clusters shown in (a), for a *core* and a *staple* site.

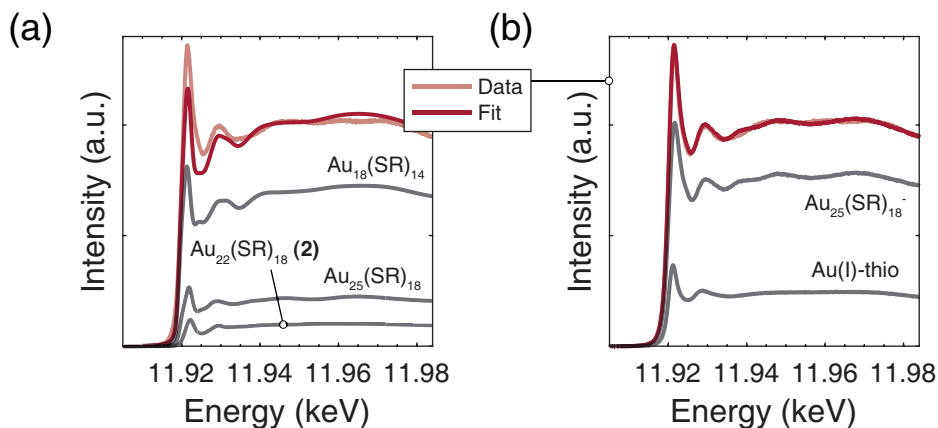


**Figure 7.12** (a) Fit of a 8.9 mM NaOH Au cluster sample, to calculated spectra of  $\text{Au}_{25}(\text{SR})_{18}$ ,  $\text{Au}_{22}(\text{SR})_{18}$  (2) and  $\text{Au}_{18}(\text{SR})_{14}$ , contributions of which are shown in grey.  $\text{Au}_{22}(\text{SR})_{18}$  (1) was included in the fit but had a weight of 0. (b) Fit of the same spectrum to experimental spectra of Au(I)-thio and  $\text{Au}_{25}(\text{SR})_{18}^-$ .

The calculated HERFD-XANES spectra of these three clusters are shown in Figure 7.11. For comparison, calculated spectra of  $\text{Au}_{25}(\text{SR})_{18}$  and Au(I)-thio are also shown, together with the recorded spectrum of clusters with 8.9 mM NaOH. All calculated spectra show an intense whiteline and a broader feature  $\sim 7$  eV higher. The post-edge features vary from cluster to cluster, but also depend on the site of the Au atom. While each cluster contains a number of (near-) equivalent sites, such as the 12 *ico* sites in  $\text{Au}_{25}(\text{SR})_{18}$ , and the *staple* Au sites of each cluster, this still leaves potentially dozens of different Au sites in a polydisperse cluster sample. This may lead to an almost featureless post-edge. As an example, we performed a linear combination fit of the calculated spectra to the measured spectrum of a sample (8.9 mM NaOH), which can be seen in Figure 7.12. While the intensity around the edge is not accurately reproduced, the fit does show the nearly flat post-edge. The spectrum of the 8.9 mM NaOH sample was also fitted to experimental spectra of Au(I)-thio and  $\text{Au}_{25}(\text{SR})_{18}^-$ . A good fit is obtained with a 76 % contribution of  $\text{Au}_{25}$ . While not conclusive identification of cluster species, these calculations and fits show that, despite similarities to Au(I)-thio, our experimental spectra are also consistent with cluster sizes of  $\sim 20$  Au atoms.

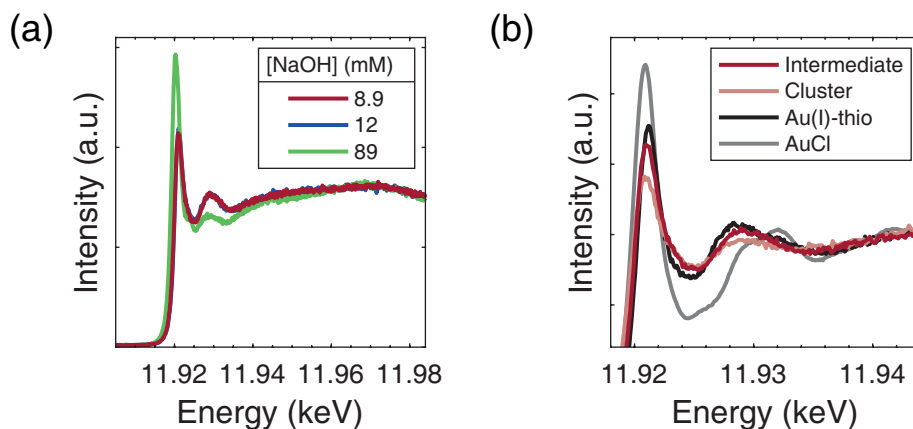


**Figure 7.13** (a) HERFD-XANES of synthesis intermediates, for three NaOH concentrations. (b) HERFD-XANES of a 8.9 mM NaOH Au cluster sample and synthesis intermediate, together with Au(I)-thio and AuCl.

### HERFD-XANES of synthesis intermediates: the synthesis mechanism

HERFD-XANES was also recorded of the synthesis intermediates. Spectra are shown in Figure 7.13. These spectra show the same main features as the clusters; for 8.9 and 12 mM NaOH, the spectra resemble that of Au(I)-thio while the 89 mM sample has features reminiscent of  $\text{HAuCl}_4$  and  $\text{Au}_2\text{O}_3$ . For all three NaOH concentrations, the intermediates showed a higher whiteline intensity than the clusters. The whiteline intensities of synthesis intermediates with 8.9 and 12 mM NaOH are nearly identical, and lower than that of Au(I)-thio. This implies that intermediates are more oxidised, or have more Au–S bonds than the clusters, although the differences are small.

Synthesis intermediates with 8.9 and 12 mM NaOH have nearly identical spectra, though the cluster samples had slightly different spectral features. This implies that the reduction step of the synthesis is also influenced by the NaOH concentration. At high pH, the reduction rate of  $\text{NaBH}_4$  is slowed down which may influence cluster composition.<sup>22,315</sup> As was proposed in Chapter 5, there is a major difference between the synthesis intermediates of 8.9 and 89 mM NaOH samples, with the latter containing a significant fraction of (hydrolysed)  $\text{HAuCl}_4$  precursor. The spectra also confirm that there is a reaction between  $\text{HAuCl}_4$  and LA at low NaOH concentrations, giving Au(I) species as intermediates.

It is generally accepted that Au(I) species are intermediates in the synthesis of Au clusters, although the nature of the ligands varies. It has been proposed that

intermediates in the two-phase Brust-Schiffrin synthesis are Au(I)-halides rather than Au(I)-thiolates, with the latter present only in water.<sup>203,306,307</sup> As can be seen from Figure 7.13, spectra of our synthesis intermediates show better agreement with Au(I)-thio than with AuCl. It should be noted that the AuCl sample was measured as a solid rather than in solution. Solvation may change the spectrum somewhat. Nevertheless, our findings are consistent with reports of Au(I)-thiolates being present as intermediates of aqueous Au clusters.

Intriguingly, while clusters and synthesis intermediates were found to possess different optical properties and size distributions, their HERFD-XANES spectra are nearly identical. This implies that the average environment of Au atoms hardly changes upon reduction of the synthesis intermediates. There are a number of possible explanations. First, it may be that the addition of NaBH<sub>4</sub> only reduces a fraction of the intermediates. However, this is not supported by analytical ultracentrifugation of clusters and intermediates (Figures 5.4 and 5.9), which are clearly different. Moreover, we estimate the molar extinction coefficient at 510 nm of the cluster samples to be  $\sim 5 \times 10^3 \text{ M}^{-1}\text{cm}^{-1}$ , which is the same order of magnitude that was found for monodisperse Au<sub>25</sub>(SR)<sub>18</sub><sup>-</sup>.<sup>178</sup> A second possibility is that the intermediates are already partially reduced, with average oxidation state between Au(I) and Au(0), and so already contain some clusters. We deem this unlikely, as no sign of clusters is observed from mass spectrometry or UV-Vis spectroscopy. Exposure to X-rays may reduce Au(I) in the intermediates, but we see no evidence of this in our X-ray absorption spectra (see also the discussion on radiation damage below). Finally, the size polydispersity of the synthesis intermediates may result in an averaging out of post-edge features, just as with the clusters. Even clusters with  $\sim 20$  Au atoms have spectra with intense whitelines (Figure 7.11) and their X-ray absorption spectra thus resemble Au(I)-thio due to the large fraction of surface Au atoms. Differences between clusters and intermediates may be too subtle to observe clearly with XAS.

**A note on radiation damage** Exposure of samples to intense X-rays may lead to radiation damage. This was observed for HAuCl<sub>4</sub>. In solution, the intense whiteline that is characteristic of this compound disappeared within minutes, and spectral features of bulk Au appeared. UV-Vis measurements of the solution later confirmed the presence of large, plasmonic Au nanoparticles. When a solid HAuCl<sub>4</sub> sample was measured, a rapid reduction in whiteline intensity was also observed. To obtain a high-quality spectrum, multiple short (5 s) spectra were measured on different spots, and later averaged. Radiation damage of solid (frozen) Au cluster samples was minimised in the same way.

First, the intensity of the whitenline was monitored with  $< 1$  s time resolution to determine the typical timescale for radiation damage. Multiple XANES scans were then performed, each shorter than this timescale, on different spots. Au clusters in the liquid jet setup are not continuously exposed to X-rays because the solution is pumped through the jet. However, even brief exposure may lead to formation of radicals in water, which may damage the sample further.<sup>369</sup> A typical scan length for HERFD-XANES was 30 s, repeated for 1 h. The first and last scans were compared to check for radiation damage, and UV-Vis absorption spectra were recorded of the samples before and after exposure to X-rays. Results are given in Figures C.1 to C.3. The X-ray spectra hardly changed during the measurement, but UV-Vis spectra show dramatic differences, especially for samples with high NaOH concentrations and synthesis intermediates. However, these UV-Vis spectra were not recorded immediately after the experiments. The samples were stored for several hours after XAS before recording UV-Vis, and it may be that X-ray induced damage progressed further during this time.

For the XES experiments, a flow cuvette was built into the liquid jet setup which allowed us to record UV-Vis absorption spectra during X-ray spectroscopy. In this case, the change in the UV-Vis absorption spectrum during exposure to X-rays was less than for HERFD, despite a much longer (4 h) overall exposure time (Figure C.4). We therefore judge that the X-ray spectra of clusters presented in this chapter represent mostly undamaged samples. The changes observed by *ex situ* UV-Vis spectroscopy could be due to gradual radiation damage, which continues after the XAS measurement is finished, for instance due to radical formation. *In situ* UV-Vis absorption spectra are not available for the synthesis intermediates, but based on the lack of changes in the XANES spectrum, we propose radiation damage is limited for the intermediates as well.

## 7.4 Conclusions

X-ray absorption spectroscopy was used to study Au clusters capped with lipoic acid. Three samples with different NaOH concentrations were studied, which had previously been found to have different size distributions and optical properties. EXAFS was recorded of the sample with lowest NaOH concentration, which contains the biggest clusters. An overall Au–Au coordination of  $\sim 4$  was found, consistent with an average size of 20–40 Au atoms. HERFD-XANES of the three cluster samples found spectral features similar to those of an Au(I)-thiolate reference compound, with an intense whitenline and few prominent post-edge features. This implies a significantly smaller cluster size. However, XANES of monodisperse Au<sub>25</sub>(SR)<sub>18</sub> clusters, as well as FDMNES calculations of Au clusters with 18–25 Au

atoms, show that these spectral features are also characteristic of thiolate-protected Au clusters. The intense whitenline arises from  $2p_{3/2} \rightarrow 5d$  transitions, with d-holes in Au caused by bonding to electron-withdrawing thiolates. HERFD-XANES spectra of the clusters are thus consistent with cluster sizes of around 20 Au atoms, though the polydispersity of the sample made a more conclusive assignment of spectral features impossible.

The sample with highest NaOH concentration was found to contain some  $\text{AuCl}_{4-x}(\text{OH})_x^-$  species in addition to clusters, resulting in a more intense whitenline and additional spectral features both in absorption and emission spectra. These species are also present in the synthesis intermediate of this sample, while the samples with lower NaOH resemble Au(I)-thiolates. This confirms that there is a reaction between lipoic acid and  $\text{HAuCl}_4$  at the start of the synthesis, before addition of the reducing agent, and that this reaction is inhibited at high NaOH concentrations.

## 7.5 Acknowledgements

We thank Lucia Amidani, Pieter Glatzel, Sara Lafuerza and Alessandro Longo for beamline support; and Hebatalla Elnaggar, Naud van Bunningen, Maarten Bransen, Mario Delgado-Jaime, Ties Haarman, Clara Garcia Yago, Stephan Pollitt and Lule Beqa for their help during the beamtimes. The ESRF and NWO are thanked for providing beamtime (proposals CH4593, IH-CH-1118., CH5496 and IH-CH-1345). Chris Hosier and Katinka Wondergem are thanked for providing additional samples. This work was financially supported by the Debye Graduate Programme (NWO project 022.004.016), and ESRF Graduate Programme.

## Additional spectra; gold clusters

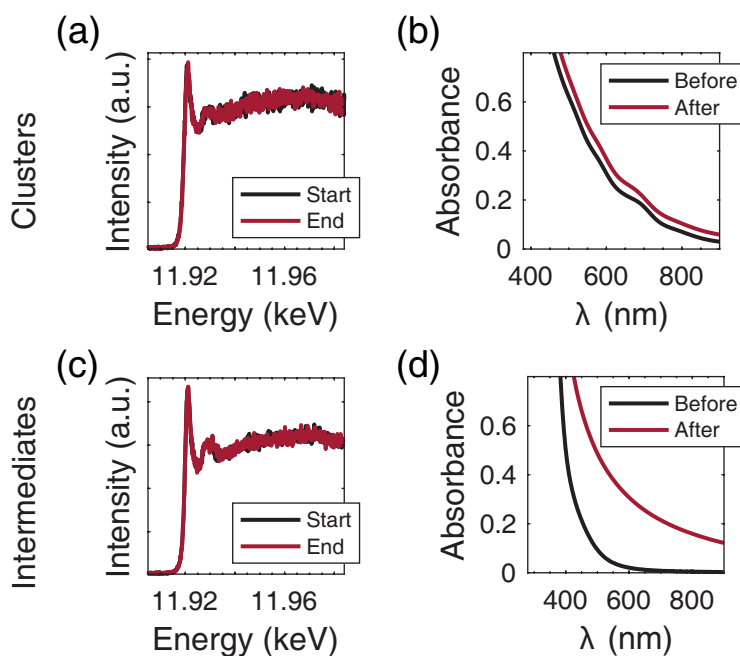


**Figure C.1** Effect of radiation damage during XAS measurements, for clusters with 8.9 mM NaOH. (a) XANES spectra at the start and end of the experiment. (b) UV-Vis absorption spectra before and after recording XANES. See also Figure C.4. In (c) and (d), the same is shown for the synthesis intermediate.

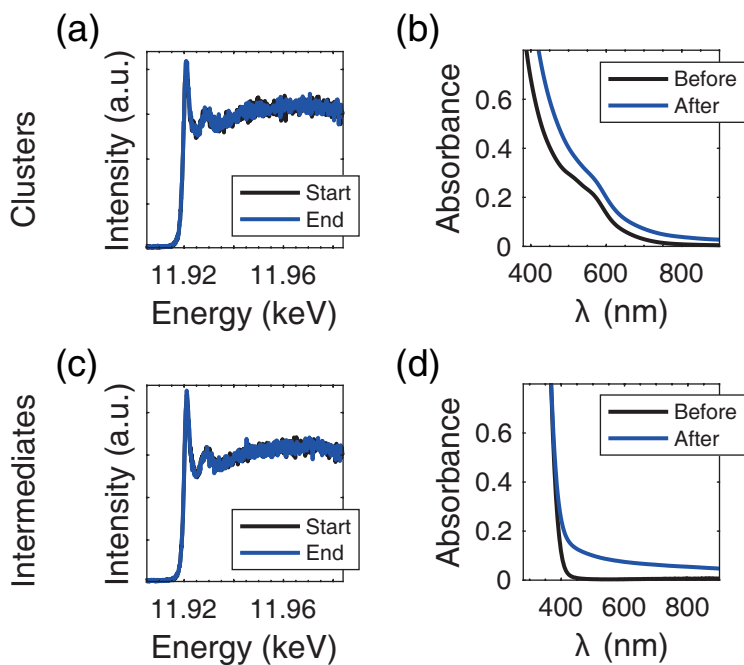


**Figure C.2** Effect of radiation damage during XAS measurements, for clusters with 12 mM NaOH. (a) XANES spectra at the start and end of the experiment. (b) UV-Vis absorption spectra before and after recording XANES. See also Figure C.4. In (c) and (d), the same is shown for the synthesis intermediate.

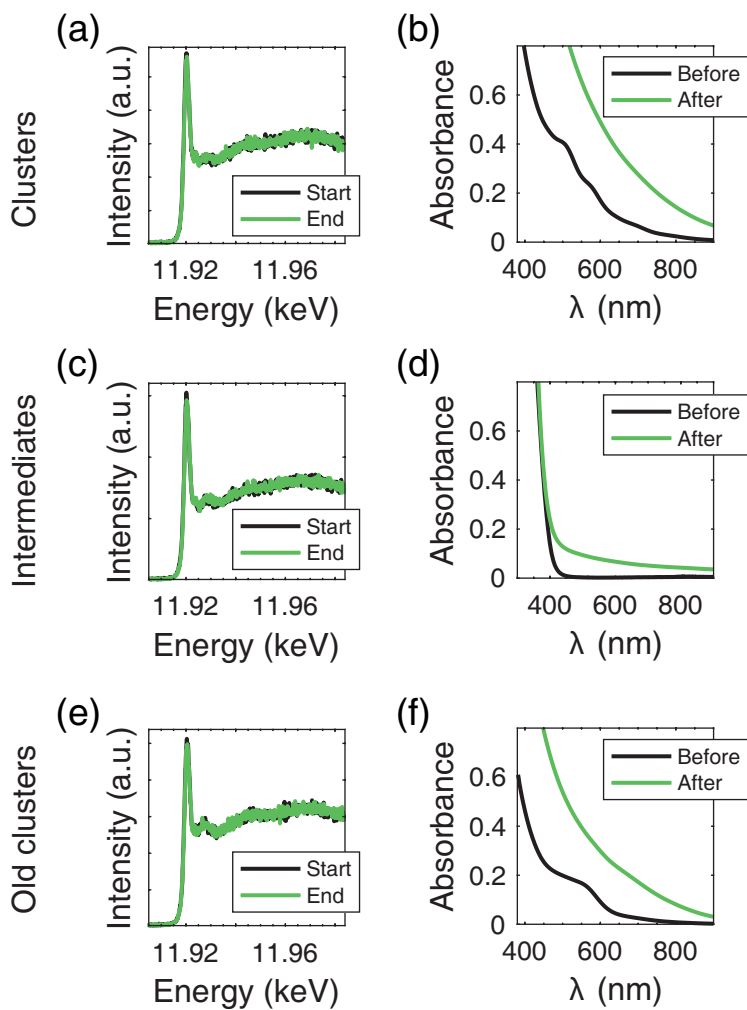


**Figure C.3** Effect of radiation damage during XAS measurements, for clusters with 89 mM NaOH. (a) XANES spectra at the start and end of the experiment. (b) UV-Vis absorption spectra before and after recording XANES. See also Figure C.4. In (c) and (d), the same is shown for the synthesis intermediate, and in (e) and (f) for clusters a few days after synthesis.

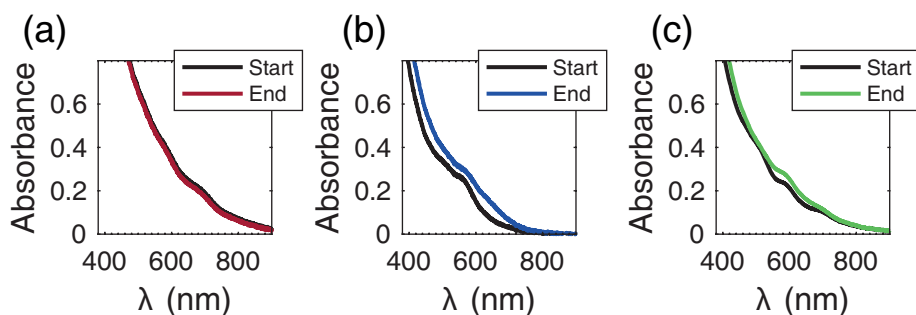


**Figure C.4** Effect of radiation damage during XES measurements, for clusters with (a), (b) and (c): 8.9, 12 and 89 mM NaOH, respectively. UV-Vis spectroscopy was recorded in situ using a flow cuvette built into the liquid jet setup.

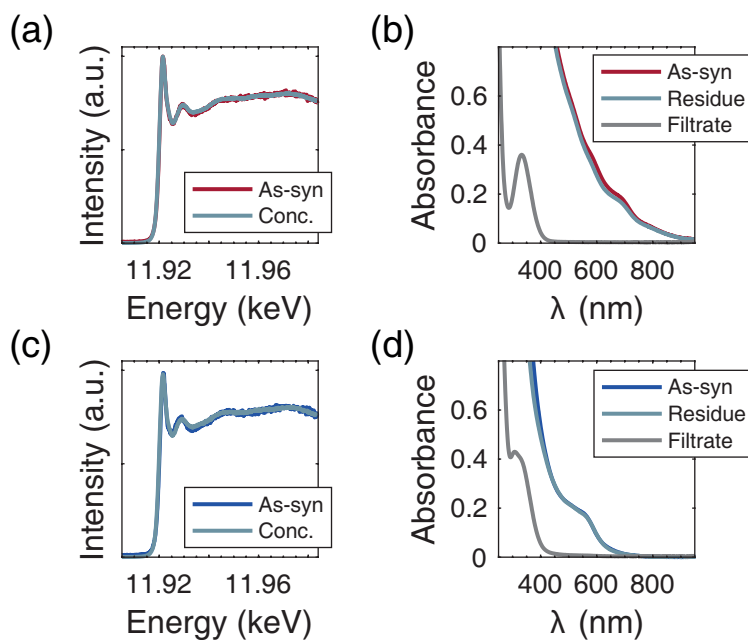
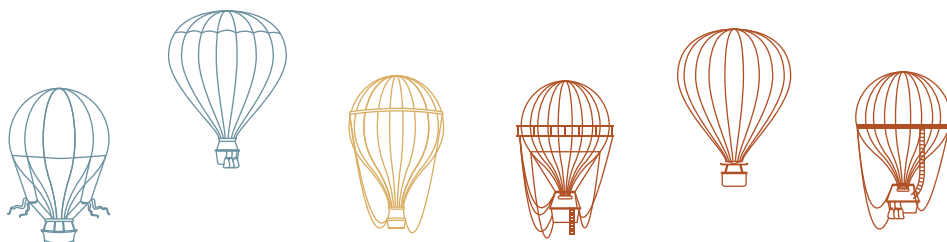


**Figure C.5** (a) HERFD-XANES of Au clusters with 8.9 mM NaOH, as-synthesised and after concentration with molecular mass cutoff filters. (b) UV-Vis spectra of the as-synthesised 8.9 mM NaOH clusters, as well as the residue and filtrate after concentration with molecular mass cutoff filters (the former corresponds to the concentrated sample). Figures (c) and (d) show the same for a 12 mM NaOH sample. XANES spectra were recorded in the cryostat.

## Summary and outlook

*“Don’t adventures ever have an end? I suppose not. Someone else always has to carry on on the story.”*

— J.R.R. Tolkien, *The Fellowship of the Ring*



Gold and silver nanoclusters with sizes up to  $\sim 100$  atoms have unique properties not found in bulk materials or in larger nanoparticles. They resemble molecules rather than metals. Their potentially atomic monodispersity allows for correlation between size, shape and structure on the one hand, and properties such as stability and luminescence on the other. For instance, the emergence of metallicity and surface plasmon resonance has been observed to occur at  $\sim 150$  atoms.<sup>17,18</sup> Clusters also have potential applications in diverse fields such as catalysis<sup>81</sup> and biomedicine.<sup>354</sup>

This thesis describes the synthesis and characterisation of aqueous gold and silver clusters. A graphical summary is given in Figure 8.1. Lipoic acid (LA) is used as the ligand for the clusters described in this thesis. LA is a disulfide which binds to Au and Ag in a bidentate fashion. Most studies of thiolate-protected noble metal clusters have used monodentate ligands; with dithiolates, clusters with different structures<sup>69</sup> and thus different properties can be obtained<sup>70</sup>, for instance increased luminescence intensity.<sup>71</sup>

Pure silver clusters with LA can be prepared in a one-pot synthesis which yields atomically monodisperse clusters without any purification. This is described in **Chapter 2**. Monodispersity was demonstrated with sedimentation

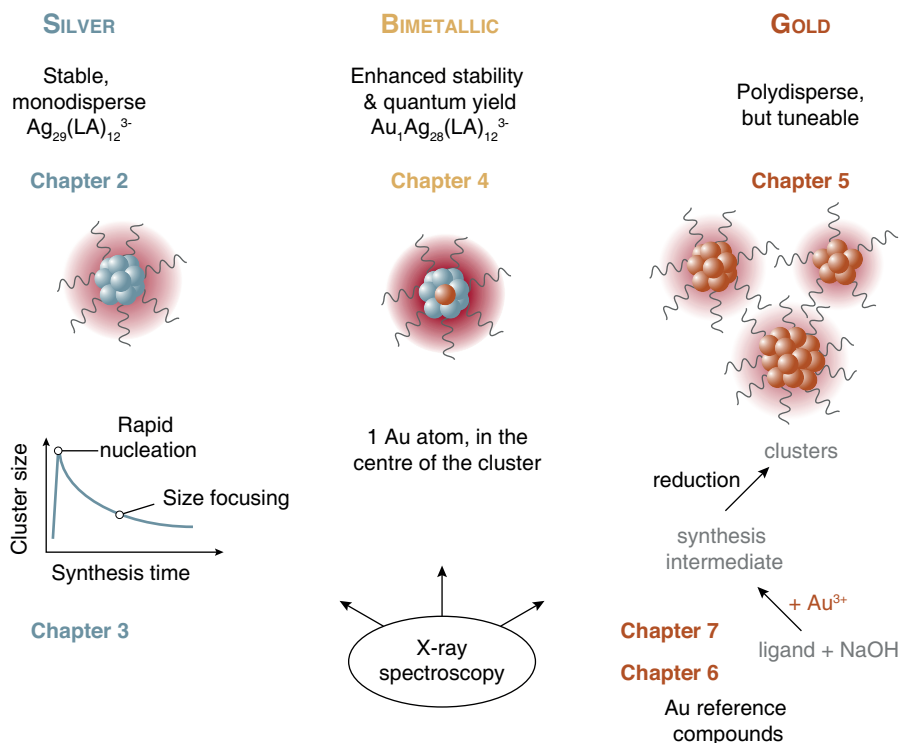


**Figure 8.1** Graphical summary of this thesis.

velocity analytical ultracentrifugation (SV-AUC). The cluster composition was determined with electrospray ionisation mass spectrometry (ESI-MS) and found to be  $\text{Ag}_{29}(\text{LA})_{12}^{3-}$ . The clusters show bright red luminescence with a quantum yield of nearly 3%. When stored in the dark, the clusters remain luminescent for up to 18 months. The clusters degrade slowly, forming larger non-luminescent species. This degradation is reversible, which has not been observed for other thiolate-protected silver clusters.

In **Chapter 3** we present new insights into the synthesis mechanism of  $\text{Ag}_{29}$  clusters.  $\text{Ag}_{29}$  clusters are prepared by the addition of a strong reducing agent ( $\text{NaBH}_4$ ) to an aqueous solution containing reduced LA and  $\text{AgNO}_3$ . Within minutes of  $\text{NaBH}_4$  addition, the synthesis solution turns black, after which it gradually lightens to a reddish orange as the clusters are formed. Using a combination of experimental techniques, we show that after an initial rapid reduction, particles with  $\sim 100$  Ag atoms are formed, which slowly decrease in size until only  $\text{Ag}_{29}$  clusters remain. ESI-MS experiments show  $\text{Ag}_{29}(\text{LA})_{12}^{3-}$  clusters are present at low concentrations shortly after the solution turns black.

The signal-to-noise ratio of this ion signal increases over time, as does the intensity of the cluster luminescence. No other cluster species could be identified from mass spectrometry during the synthesis, except small amounts of Ag<sub>28</sub> and Ag<sub>26</sub>.

Further information was obtained from X-ray spectroscopy, an element-selective characterisation technique that does not require extensive sample purification. Both Extended X-ray Absorption Fine Structure (EXAFS) and X-ray Absorption Near Edge Structure (XANES) regions of the spectrum were investigated. These studies show the presence of larger nanoparticles (estimated size ~ 100 Ag atoms) in the first hour after NaBH<sub>4</sub> addition. We also demonstrate that oxygen plays an important role in the etching of these larger species to Ag<sub>29</sub>.

**Chapter 4** describes bimetallic clusters, prepared by adding a small amount of HAuCl<sub>4</sub> during the synthesis of Ag<sub>29</sub>(LA)<sub>12</sub><sup>3-</sup>. Doping with a few percent gold increases the stability of the clusters while the quantum yield is enhanced to 8%. This was attributed to an increase in the radiative decay rate. ESI-MS shows that there is a preference for monodoped clusters, Au<sub>1</sub>Ag<sub>28</sub>(LA)<sub>12</sub><sup>3-</sup>. Using XANES and EXAFS, it was found that the Au atom is preferentially located in the centre of the cluster. Only a small fraction of Au atoms is present as Au-thiolates or on the surface of the Au<sub>1</sub>Ag<sub>28</sub> clusters. The Au–S bond of these species is shorter than the Ag–S bond in Ag<sub>29</sub>. Doping of surface sites of Ag<sub>29</sub> with Au may therefore induce structural distortions which decreases the stability of the clusters. This could explain why the Au atom preferentially occupies the centre of the cluster.

Doping of Ag<sub>29</sub> with more than a few percent of Au does not lead to the formation of stable clusters. Pure Au clusters with LA can be prepared, but as demonstrated in **Chapter 5**, these are not atomically monodisperse. However, the average size and optical properties can be tuned. The synthesis proceeds in two steps. The first is the formation of a synthesis intermediate by addition of HAuCl<sub>4</sub> to an aqueous solution of LA and NaOH. The second step is the reduction of the synthesis intermediate with NaBH<sub>4</sub>. The clusters show red and near-infrared luminescence with a quantum yield of 0.2–0.3%. UV-Vis absorption features vary depending on the NaOH concentration. With ESI-MS and SV-AUC, we found that this is related to the cluster size distribution. A lower NaOH concentration corresponds to a larger average cluster size, although somewhat smaller clusters were observed with ESI-MS than with SV-AUC.

After showing X-ray spectra of Au reference compounds in **Chapter 6**, an X-ray spectroscopy study of these clusters is described in **Chapter 7**. XANES shows spectral features similar to those of an Au(I) thiolate compound, with an intense whiteline and few prominent post-edge features. However, we found that this does not necessarily mean that the concentration of clusters is low, or that they are smaller than expected. Similar spectral features were also found in Au<sub>25</sub>(SR)<sub>18</sub><sup>-</sup>

and, by calculating spectra of different  $\text{Au}_x(\text{SR})_y$  clusters, these features could be attributed to bonding of Au to electron-withdrawing thiolates. Low temperature EXAFS clearly demonstrates the presence of Au–Au bonds in the clusters with lowest NaOH concentration.

In **Chapters 5 and 7**, we also study the synthesis intermediates in more detail. We demonstrate, using mass spectrometry and fast UV-Vis absorption spectroscopy, that there is a reaction between  $\text{HAuCl}_4$  and LA at low NaOH concentrations, resulting in the formation of large, unstable Au nanoparticles. This reaction is inhibited at high NaOH concentrations, where it must compete with hydrolysis of  $\text{HAuCl}_4$ . The resulting  $\text{AuCl}_{4-x}(\text{OH})_x^-$  species ( $x = 3-4$ ) may be less reactive towards LA. Both synthesis intermediates and clusters with high NaOH concentration were found to contain  $\text{AuCl}_{4-x}(\text{OH})_x^-$ .

Together with the straightforward synthesis, the high luminescence quantum yield of Ag and Au clusters with LA makes them promising candidates for applications such as sensing of heavy metal ions<sup>85,86</sup> and *in vivo* biomedical imaging<sup>89,90</sup> to localise tumors. Different applications require clusters with different properties. The optical properties of our clusters can be tuned by the addition of Au to  $\text{Ag}_{29}$  clusters, and by varying the NaOH concentration for Au clusters. The carboxylic acid group of LA can also be functionalised to create polymeric or zwitterionic ligands.<sup>72,73,298-300</sup> This is not investigated in this thesis, but studies have shown that modification of the ligand can affect for instance the cluster solubility, as well as its luminescence intensity and colour.

The stability of  $\text{Ag}_{29}$  clusters after purification remains an issue for potential applications. Removal of excess ligands by extraction with butanol leads to cluster degradation after just one week. Modification of the ligand may improve the stability, for instance by cross-linking of the ligand shell, or by encapsulation in a protein.<sup>171</sup> It may also be worthwhile to investigate how storage conditions affect the cluster stability. All experiments in this thesis were done on cluster solutions. The isolation of clusters as pure solids may allow for long-term storage, as well as investigations into the effect of solvation, which can influence reactivity and structure.<sup>288</sup> Furthermore, the exact structure of  $\text{Ag}_{29}(\text{LA})_{12}^{3-}$  remains unknown. Single crystal X-ray crystallography of this cluster would be an important step, if crystals can be grown. This is often challenging for flexible, water-soluble ligands such as glutathione<sup>357</sup>; LA ligands may have similar issues. If the structure of  $\text{Ag}_{29}(\text{LA})_{12}^{3-}$  can be determined, this will allow a better comparison with its organosoluble counterpart  $\text{Ag}_{29}(\text{BDT})_{12}(\text{TPP})^{3-}$  (BDT, 1,3-benzenedithiol; TPP, triphenylphosphine)<sup>56</sup> to explain their differences and similarities. Moreover, knowing the structure of  $\text{Ag}_{29}(\text{LA})_{12}^{3-}$  facilitates fundamental studies into the origin of its strong red luminescence, which is still not fully understood.<sup>91,370</sup>

The polydispersity of the Au clusters with LA has to some extent impeded the interpretation of experimental results. ESI-MS and SV-AUC results can not easily be compared, and XANES spectra show featureless post-edge regions. Isolation of one cluster size would be a significant improvement. The effect of temperature and solvent during synthesis has not been investigated in great detail, but may be useful parameters that can be varied in trying to obtain clusters with higher monodispersity. The modification of synthesis intermediates before reduction, as shown in Figure 5.10, also opens up further possibilities. If a one-pot synthesis of monodisperse Au clusters with LA is not feasible, purification techniques such as size-exclusion chromatography<sup>371</sup>, thin-layer chromatography<sup>372</sup>, and polyacrylamide gel electrophoresis<sup>373</sup> could be used to isolate different cluster sizes and study them separately with ESI-MS, SV-AUC and optical spectroscopy.

Many of the conclusions presented in this thesis are based on X-ray spectroscopy studies. EXAFS and XANES were used to demonstrate that the synthesis of Ag<sub>29</sub> clusters proceeds via larger particles, that the Au atom in Au<sub>1</sub>Ag<sub>28</sub> is preferentially located in the centre of the cluster, that synthesis intermediates of Au clusters are Au(I)-thiolates, and that Au cluster samples with high NaOH concentration contain AuCl<sub>4-x</sub>(OH)<sub>x</sub><sup>-</sup> species. A great advantage of X-ray spectroscopy is that it is element-selective. It enables us to study for instance only the Au dopant in bimetallic clusters, or all Ag species during the synthesis of Ag<sub>29</sub>. Solids, solutions, mixtures and disordered species can all be measured, and no purification is necessary to remove excess salts or ligands because these are invisible in X-ray spectroscopy. EXAFS analysis is relatively straightforward and can be used to obtain information on neighbouring atoms; including bond lengths and coordination numbers.<sup>102</sup> From XANES one can get information on oxidation state and local geometry, but analysis is often more complicated and may require more extensive calculations or comparison with reference compounds, as demonstrated in **Chapter 6**.

X-ray absorption spectroscopy can be used to study structural and electronic properties of Au clusters<sup>332</sup>, and how these change for instance upon solvation<sup>288</sup>, with temperature<sup>222</sup>, upon doping<sup>248</sup>, or with increasing cluster size.<sup>374</sup> In many cases, the differences between XANES spectra of clusters are minimal. In this thesis, we use High Energy Resolution Fluorescence Detection (HERFD) to record XANES with increased resolution, which results in more prominent spectral features and greater differences between samples. To the best of our knowledge, this is the first HERFD-XANES study of thiolate-protected noble metal clusters. We have recently recorded HERFD-XANES of atomically monodisperse, thiolate-protected Au clusters with sizes between Au<sub>25</sub> and Au<sub>~500</sub>. Of this, only Au<sub>25</sub> spectra are

presented in this thesis (**Chapter 7**), but we will analyse the remaining part of this data in the near future.

Finally, we propose that (HERFD-)XANES, possibly in combination with EXAFS or X-ray emission spectroscopy, could be a useful tool for studying the synthesis mechanism of organosoluble thiolate-protected Au clusters. The intermediates present in these syntheses are usually considered to be Au(I)-thiolates<sup>91</sup>, although recent work has suggested that Au(I)-halides are a more likely candidate in the absence of water.<sup>203,306,307</sup> A detailed X-ray spectroscopy study may shed light on this. This would require samples at different stages in the synthesis, with different solvents and other reaction conditions, as well as a large number of reference Au(I)-thiolate and Au(I)-halide compounds.

# Samenvatting voor een algemeen publiek

*“Ubygde kraftverker,  
ukjente stjerner –  
skap dem, med skånet livs  
dristige hjerner!”*

---

— Nordahl Grieg,  
*Til Ungdommen*

## Klein is fijn

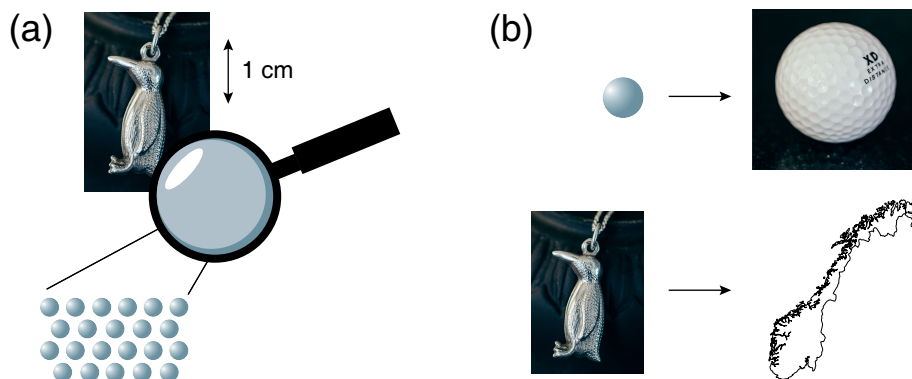
De wereld om ons heen bestaat uit atomen, de bouwstenen van de scheikunde. Er bestaan ruim honderd verschillende atoomsoorten. Atomen zijn onvoorstelbaar klein. De afgebeelde zilveren hanger in Figuur A bestaat uit meer atomen dan er sterren zijn in ons sterrenstelsel of mieren op aarde.

Atomen zijn eigenlijk net pinguïns.\* En wel hierom: er zijn verschillende soorten, ze zijn net iets kleiner dan je denkt, ze variëren een beetje in grootte en sommige soorten zitten het liefst met duizenden miljarden bij elkaar in een grote groep. Pinguïns staan bij elkaar in een groep om warm te blijven tijdens de Antarctische winter. Hoe meer burens, hoe warmer. Voor metaal-atomen zoals goud en zilver is het gunstig omringd te zijn door zo veel mogelijk andere atomen. Atomen aan het oppervlak van een metaaldeeltje hebben andere eigenschappen dan atomen in het midden. Ze zijn chemisch reactiever, net als pinguïns aan de buitenrand. Die hebben het kouder en zijn dus onrustiger.

De eigenschappen van een materiaal als goud of zilver zijn daarom ook afhankelijk van het aantal atomen. In het dagelijks leven zien we dit effect nauwelijks. Een stuk zilver van 1 kg heeft dezelfde eigenschappen (kleur, smeltpunt, dichtheid) als een stuk van 1 g. Het effect treedt pas op als een significant deel van de atomen op het oppervlak zit, dus voor kleine deeltjes. Zo neemt bijvoorbeeld het smeltpunt van goud af voor deeltjes kleiner dan 20 nanometer. Een nanometer (afgekort nm) is een miljardste van een meter. Deeltjes met afmeting tot 100 nm noemt men nanodeeltjes. Dat komt overeen met ongeveer vijftigmiljoen atomen.

---

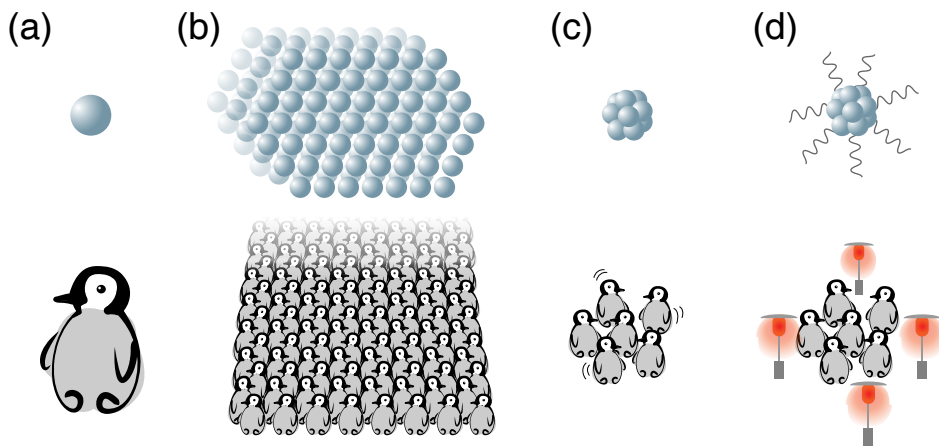
\*Deze vergelijking werkt vast ook met andere dieren maar zoals iedereen weet zijn pinguïns de beste dieren.



**Figuur A** (a) Een voorwerp dat we met het blote oog kunnen zien, zoals een zilveren hanger in de vorm van een pinguïn, bestaat uit een haast ontelbaar aantal atomen. (b) Honderdmiljoen keer uitvergroot zal elk van die atomen ongeveer zo groot zijn als een golfbal. De hanger zelf is dan groot genoeg om heel Noorwegen te bedekken.

De kleinste nanodeeltjes, van ongeveer 1–2 nm, bestaan uit slechts enkele tientallen of honderden atomen. Deze nanodeeltjes noemen we ook wel nanoclusters of gewoon clusters. Clusters zijn typisch opgebouwd uit complete schillen van atomen rond 1 centraal atoom. Eén atoom meer of minder kan daarom veel uitmaken voor de stabiliteit. Dankzij het verschil in stabiliteit kunnen we groepen clusters maken waarvan alle clusters even groot zijn (monodisperse deeltjes): clusters van andere grootte zijn immers instabiel. Dit in tegenstelling tot grotere nanodeeltjes, die we alleen kunnen maken als mengsel van groottes (polydisperse deeltjes), bijvoorbeeld  $(20 \pm 1)$  nm. De eigenschappen van zilver- en goudclusters zijn anders dan die van een groot stuk zilver en goud en ook anders dan die van grotere nanodeeltjes. Ze kunnen ze bijvoorbeeld licht van één kleur absorberen, om vervolgens uit te zenden in een andere kleur. Dit noemen we luminescentie.

De clusters in dit proefschrift zijn opgelost in water en kunnen vrij bewegen. Ze kunnen dus ook tegen elkaar aanbotsen. Om te voorkomen dat twee of meer clusters samengroeien tot een groter nanodeeltje, zijn ze omringd door liganden. Liganden zijn moleculen die sterk binden aan metaal-atomen. De liganden stabiliseren de atomen aan het oppervlak en vormen een barrière die de clusters beschermt, zoals geïllustreerd in Figuur B. Als ligand gebruiken we liponzuur. Dit bevat twee zwavelatomen die sterk binden aan goud en zilver. Het biedt daarom een efficiënte bescherming.



**Figuur B** (a) We kunnen metaal-atomen vergelijken met pinguïns. (b) Een groot blok metaal komt overeen met een enorme groep pinguïns. Bijna alle pinguïns zijn omringd door warme buren. Een groot blok metaal is daarom stabiel. (c) Bij een klein nanodeeltje, een cluster, is het percentage atomen aan het oppervlak hoog. In pinguïntaal: de meeste pinguïns hebben het koud. (d) Liganden kunnen binden aan het oppervlak en zo de cluster stabiliseren. Het is alsof je terrasverwarmers om een klein groepje pinguïns zet.

## Hoe maak je nanoclusters?

Het klinkt misschien moeilijk: deeltjes maken met slechts enkele tientallen metaal-atomen met daaromheen ook nog eens liganden, maar het maken van nanoclusters is relatief eenvoudig. We noemen dit proces synthese. Eerst zorgen we voor losse zilver- of goudatomen. Dit doen we door een zout als zilvernitraat op te lossen in water. Alle metaal-atomen zijn hier aanwezig als ionen (geladen atomen) die elkaar afstoten. Vervolgens mengen we deze oplossing met een oplossing van liganden. Vaak reageren de metaalionen en liganden met elkaar en vormen chemische bindingen. We weten alleen niet precies welke samenstelling dit mengsel heeft. We noemen dit mengsel overigens een syntheseintermediair. Het is een tussenproduct op weg naar ons doel, de clusters. De volgende stap is het toevoegen van een reductor. De reductor neemt de lading van de ionen weg zodat de metaal-atomen bij elkaar kunnen komen om nanodeeltjes te maken. De liganden zorgen er voor dat de deeltjes niet te groot worden.

Om nanoclusters van een bepaalde grootte te maken kun je bijvoorbeeld het type ligand variëren of de verhouding tussen liganden en metaal-atomen. Ook kunnen het oplosmiddel en de temperatuur een rol spelen. Soms wordt een mengsel van clusters gevormd en is het nodig om het mengsel te zuiveren om één

specifieke grootte te isoleren. Dit proberen wij in dit proefschrift zo veel mogelijk te vermijden. Het is juist interessant om te zien welke groottes je krijgt onder bepaalde omstandigheden.

## Hoe kun je nanoclusters bestuderen?

Nanoclusters en atomen zijn te klein om met het blote oog of zelfs met een microscoop te zien. In plaats daarvan gebruiken we analysetechnieken als spectroscopie, waar we de interactie tussen de clusters en elektromagnetische straling bestuderen. Zichtbaar licht en röntgenstraling zijn voorbeelden van elektromagnetische straling. We gebruiken in dit proefschrift beide vormen van straling.

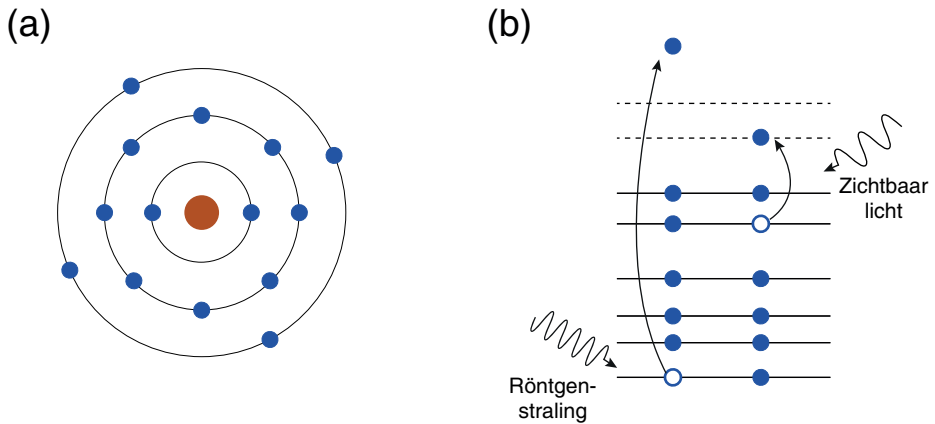
Om het principe van spectroscopie te begrijpen moeten we eerst kijken naar de (enigszins versimpelde) interne structuur van atomen. Die bestaan uit een atoomkern met daaromheen elektronen in verschillende banen. Er zijn ook lege banen. Een baan staat voor een bepaalde hoeveelheid energie. Dat is de bindingsenergie van het elektron. Banen met hoge bindingsenergie, dicht bij de kern, worden als eerste opgevuld. Elektronen zitten dus vast om de atoomkern. Het is mogelijk om een elektron naar een lege baan te brengen (of zelfs helemaal uit het atoom te slaan). Hier is evenveel of meer energie dan de bindingsenergie voor nodig. Dit proces wordt excitatie genoemd. De energie die nodig is voor het excitatieproces is afkomstig uit elektromagnetische straling. De oude baan van het elektron kan vervolgens worden opgevuld door een ander elektron. Hier komt de energie juist weer bij vrij. Deze energie kan vrijkomen als licht maar ook als warmte.

In een molecuul of een cluster is de situatie iets ingewikkelder omdat er meer dan één atoomkern aanwezig is. De zwakst gebonden elektronen kunnen in een baan om meer dan één atoomkern zitten<sup>†</sup> en de banen zijn daarom ingewikkelder. Het principe blijft echter hetzelfde.

Zichtbaar licht heeft genoeg energie om de zwak gebonden elektronen te exciteren. Het licht zelf wordt geabsorbeerd in dit proces. Bij een spectroscopisch experiment kijken we welke kleuren licht worden geabsorbeerd door de clusters. Ook kunnen we de processen die na excitatie plaatsvinden bestuderen, bijvoorbeeld emissie van licht. Dat wil zeggen dat we meten welke kleuren licht worden uitgezonden door de clusters nadat we er met blauw of UV-licht op schijnen. Het resultaat van deze metingen geven we grafisch weer in een spectrum, dat laat zien hoeveel licht van iedere energie (kleur) wordt geabsorbeerd of uitgezonden. Deze absorptie- en emissiespectra zijn een soort vingerafdrukken. Veranderingen in de spectra kunnen wijzen op veranderingen in de grootte of de structuur van de

---

<sup>†</sup>Dit is een chemische binding.



**Figuur C** (a) Een atoom bestaat uit een kern (rood) met daaromheen elektronen (blauw). De elektronen zitten vast in banen met een bepaalde bindingsenergie. (b) Schematische weergave van de bindingsenergie van de elektronen. Hoe lager de streep, hoe hoger de bindingsenergie. De golvende pijlen stellen elektromagnetische straling voor. Zichtbaar licht kan de zwak gebonden elektronen exciteren (rechts), terwijl röntgenstraling energie-rijk genoeg is om ook de sterkst gebonden elektronen te exciteren (links). In dit voorbeeld wordt het rechter elektron geëxciteerd naar een lege baan (stippellijn) terwijl het linker elektron helemaal wordt losgeslagen uit het atoom.

clusters. Ook is het mogelijk de verhouding tussen geabsorbeerd en uitgezonden licht uit te rekenen en zo de efficiëntie van de luminescentie te bepalen.

Röntgenstraling is energierijker dan zichtbaar licht. De hoge energie is voldoende om de sterkst gebonden elektronen te exciteren. Voor deze elektronen geldt dat de bindingsenergie sterk afhankelijk is van de atoomsoort. Het is daarom mogelijk om een absorptiespectrum op te nemen van bijvoorbeeld alleen zilver. Een oplossing van zilverclusters bevat naast zilveratomen namelijk ook andere atomen zoals zwavel, koolstof, zuurstof, natrium en waterstof. Deze zitten in de liganden, in het oplosmiddel, of in de toegevoegde reductor. Maar deze atomen zijn onzichtbaar in het röntgenabsorptiespectrum van zilver omdat we daar alleen kijken naar de energieën rond de bindingsenergie van elektronen in zilver. Deze bindingsenergie hangt een beetje af van de omgeving van het zilveratoom. De spectra van verschillende zilververbindingen zijn daarom verschillend. Zo kunnen we bepalen of een stof zilverclusters bevat, of zilvernitraat, of metallisch zilver. Het is zelfs mogelijk met röntgenspectroscopie te achterhalen hoeveel buuratomen er zijn, wat voor soort atomen dit zijn, hoe ver weg ze zitten. Met behulp van röntgenspectroscopie is het daarom mogelijk informatie te krijgen over de grootte,

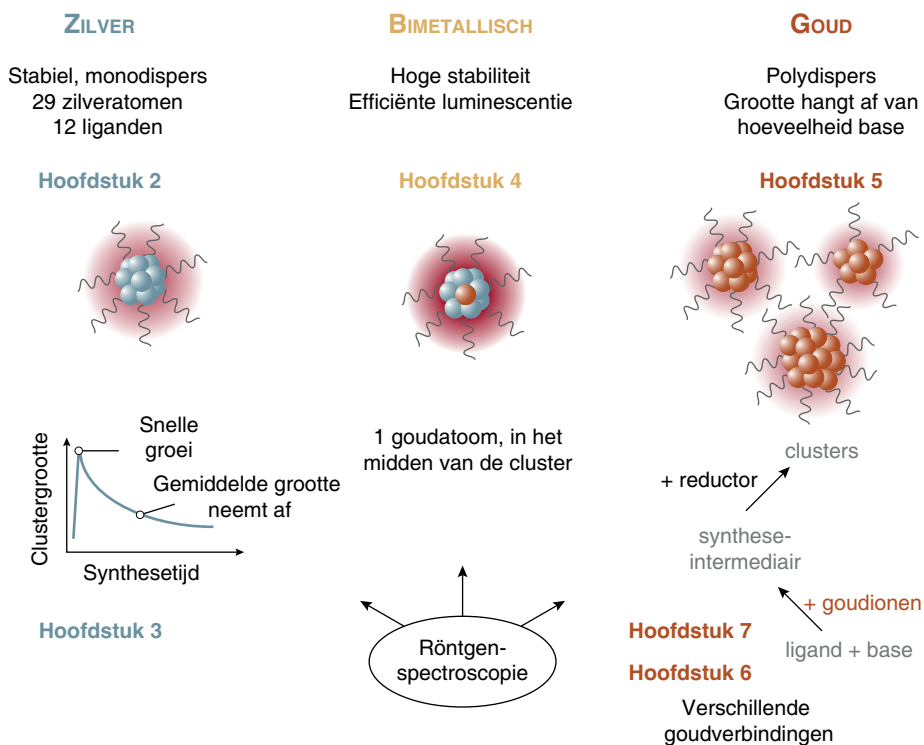
structuur en samenstelling van clusters, zelfs tijdens de synthese en zonder dat de clusteroplossing hoeft te worden gezuiverd om andere atomen weg te halen.

Twee andere technieken die in dit proefschrift gebruikt worden om clusters te analyseren zijn analytische ultracentrifugering en massaspectrometrie. In massaspectrometrie worden de clusters gasvormig gemaakt. De clusters zijn geladen en kunnen daarom worden geaccelereerd met behulp van elektrische of magnetische velden. We kunnen de snelheid waarmee een cluster beweegt meten. Die snelheid is afhankelijk van de massa en de lading van de clusters. De massa's van goudatomen, zilveratomen en liganden zijn bekend. Het is daarom mogelijk uit een massaspectrum de samenstelling van een cluster te bepalen. In analytische ultracentrifugering centrifugereren we de clusteroplossing bij hoge snelheid. Zware, compacte deeltjes sedimenteren sneller dan kleine, net als een pinguïn sneller valt dan een veer. De sedimentatiesnelheid van de clusters kan worden gemeten en hieruit krijgen we informatie over de grootte, de vorm en de massa van de clusters. Ook is het mogelijk te bepalen of de clusters monodispers zijn.

## In dit proefschrift

In dit proefschrift beschrijven we experimenten over nanoclusters van zilver en goud. Ook hebben we bimetallische nanoclusters bestudeerd. Die bestaan uit zilver en goud. De experimenten uit dit proefschrift zijn samengevat in Figuur D. In **Hoofdstuk 2** beschrijven we de synthese van zilverclusters. Deze clusters luminesceren rood, met een efficiëntie van ongeveer 3%. Met behulp van massaspectrometrie en analytische ultracentrifugering kunnen we de massa van één enkele cluster bepalen. Hieruit blijkt dat deze clusters precies 29 zilveratomen en 12 liganden hebben. Grotere of kleinere clusters worden niet gevormd. In **Hoofdstuk 3** proberen we uit te zoeken hoe de synthese leidt tot clusters met precies 29 atomen. Met behulp van röntgenspectroscopie zien we dat er in eerste instantie deeltjes met ongeveer honderd zilveratomen worden gevormd. Deze gaan vervolgens langzaam kapot, waarschijnlijk omdat de liganden kleine stukjes afbreken. Deze kleine stukjes kunnen vervolgens samengroeien tot grotere deeltjes. Dit proces gaat door tot alle clusters 29 atomen hebben.

Het tweede deel van dit proefschrift (**Hoofdstuk 4**) gaat over zilverclusters met een klein beetje goud. De zilveratomen in de cluster kunnen worden vervangen door goudatomen. Deze goudatomen kunnen plaatsnemen in het midden van de zilvercluster of aan het oppervlak waar er ook een binding is met de liganden. Het blijkt dat de cluster waar slechts één van de 29 zilveratomen is vervangen door goud stabiel is dan clusters met meer goudatomen en ook stabiel is dan clusters van puur zilver. Daarom worden vooral clusters met 1 goudatoom en 28



**Figuur D** Een grafische samenvatting van dit proefschrift.

zilveratomen gevormd. Het goudatoom bevindt zich in het midden van de cluster. Dit heeft grote invloed op de eigenschappen van de cluster. Naast de stabiliteit neemt bijvoorbeeld ook de intensiteit van de luminescentie toe. Dit komt omdat de cluster met goud sneller luminesceert dan de zilvercluster, zodat er minder tijd is voor de geabsorbeerde energie om verloren te gaan als warmte.

In het derde deel van het proefschrift bestuderen we goudclusters. Deze clusters zijn polydispers. Echter is het wel mogelijk om de gemiddelde grootte van de clusters aan te passen door de hoeveelheid base tijdens de synthese te variëren. Hierdoor kunnen ook clusters met verschillende eigenschappen worden gemaakt. In **Hoofdstuk 5** beschrijven we hoe deze clusters worden gemaakt en proberen we hun grootte te bepalen met massaspectrometrie en analytische ultracentrifugering. Dit is lastiger dan voor de zilverclusters, omdat er meerdere groottes aanwezig zijn. We gebruiken daarom ook röntgenspectroscopie. Dit wordt beschreven in **Hoofdstuk 7**. Röntgenspectra zijn soms lastig te analyseren en interpreteren. Vaak worden daarom ook spectra opgenomen van stoffen waarvan de samenstelling bekend is. Vergelijkbare spectra zijn vaak het gevolg van

vergelijkbare structuur of chemische samenstelling. In **Hoofdstuk 6** bespreken we daarom ook de röntgenspectra van een vijftal goudmaterialen. Dit helpt ons om de röntgenspectra van de clusters beter te begrijpen. We zien dat er al vroeg in de synthese een reactie optreedt tussen het goudionen en de liganden. Deze reactie neemt al een deel van de lading van de ionen weg. Er wordt waarschijnlijk een verbinding gevormd met om en om goudionen en liganden. Bij de laatste stap van de reactie worden de clusters gevormd. Echter, bij een hoge concentratie base vindt de eerste reactie tussen goudionen en liganden niet plaats. In de uiteindelijke clusteroplossing is daarom nog een beetje goudzout aanwezig.

## Maar waarom?

Het onderzoek in dit proefschrift is fundamenteel, dat wil zeggen dat het wordt gedaan zonder een directe toepassing. Het doel van de experimenten is niet het ontwikkelen van een vliegende auto of een nieuw medicijn maar het verkrijgen van kennis over de eigenschappen van nanoclusters. We doen dit onderzoek omdat we nieuwsgierig zijn en nanomaterialen beter willen begrijpen.

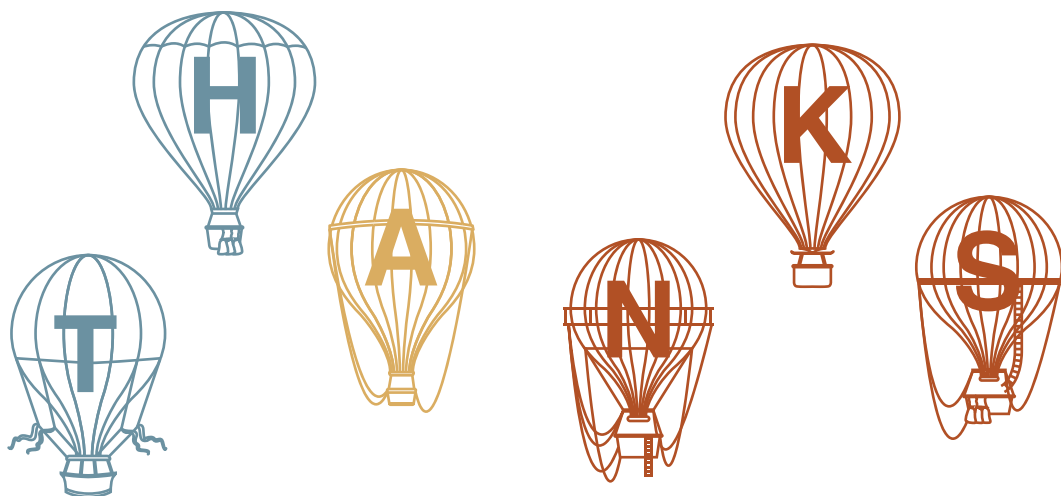
Dat betekent natuurlijk niet dat het onderzoek verder zinloos is. De nanoclusters hebben vele mogelijke toepassingen. Nanodeeltjes van verschillende metalen worden veel gebruikt als katalysatoren. Dat zijn stoffen die chemische reacties sneller en efficiënter te laten verlopen. Van een aantal nanoclusters is de structuur bekend. Dit kan nuttig zijn voor het begrip van katalytische processen. Ook is het aangetoond dat de luminescentie van nanoclusters zeer gevoelig kan zijn voor de omgeving. Bijvoorbeeld neemt de intensiteit van de luminescentie van onze zilverclusters sterk af in de aanwezigheid van kwik, zelfs bij extreem lage concentraties. Het is daarom mogelijk de clusterluminescentie te gebruiken om de hoeveelheid kwik in drinkwater te bepalen. Met de juiste liganden kunnen nanoclusters ook binden aan kankercellen. De luminescentie van de clusters kan in de toekomst wellicht worden gebruikt worden om de locatie van tumoren te bepalen.

Het is natuurlijk niet zeker dat de clusters die beschreven zijn in dit proefschrift geschikt zijn voor deze toepassingen, of dat deze toepassingen ook echt praktisch haalbaar zijn. Wel is het zeker dat er nooit toepassingen voor nanomaterialen zullen zijn als niemand eerst nanomaterialen maakt en bestudeert.

## Acknowledgements

*"I don't know half of you half as well as I should like; and I like less than half of you half as well as you deserve."*

— J.R.R. Tolkien, *The Fellowship of the Ring*



While my name is the only one on the cover of this book, dozens of people contributed towards this work. First and foremost, I want to thank my promotor Frank de Groot. Thank you for your support and encouragement, and for giving me the freedom and independence to research my own favourite topics. I've enjoyed our meetings, which usually went from science to holidays to politics to history and somehow back to science again. I also want to thank my copromotor, Pieter Glatzel. Thanks for hosting me at the ESRF, and for all you've taught me about X-ray spectroscopy. It's been a great pleasure working with you, and I will continue to try doing *great science*.

During my PhD I have had the privilege to supervise Maarten Bransen and Naud van Bunningen, who are respectively the best bachelor student and the best master student I have ever supervised. Naud, your work forms a fundamental part of Chapter 4. Figure 4.3 for example contains hours and hours of your hard work, each individual sample represented nicely by one marker. I want to give you one last +1 for that, even if we never figured out which phase of the moon

## Acknowledgements

was most beneficial for the synthesis of bimetallic clusters. Maarten, none of your experiments made it into this thesis because you were way too independent. I hope the recent revival of the mass spectrometry aspect of your research will yield some new insights. Thank you both for joining me on beamtime (especially Naud who did it twice).

I was introduced to the wonderful world of nanoclusters by Patrick Chin. Patrick, thanks for the great supervision and collaboration during my master's research, your continued enthusiasm and of course for the loan of your spectrometer. For his enthusiasm for this project, I also want to thank Andries Meijerink who supervised my master's research and kept up the collaboration. Cluster characterisation would not have been possible without the help of Dominique Thies-Weesie and Arjan Barendregt. Arjan, thanks for your help with recording mass spectra, and the endless supply of capillaries and needles. I like to think I've gotten a bit better at breaking the tips over the past four years. Dominique, thank you for the ultracentrifugation measurements and careful analysis. I loved working with you, and I hope we can collaborate on more projects.

From the ESRF I would like to thank the amazing staff of ID26 where I got to spend nearly a year and a half. In particular, I want to thank Lucia Amidani, who introduced me to the beamline and helped me with my first experiments. Thank you also for driving me to the station and sorting out my train ticket when I really needed it. Many thanks also to Sara Lafuerza and Blanka Detlefs, the best local contacts a scientist could wish for. Also thanks to Tim Bohdan, Rafal Baran and Mauro Rovezzi for their help. Magda Piskorz, thanks for the fun nightshifts, although I hope I never again have to measure such a tiny sample. Anurag Kawde, thanks for being a great roommate! Same goes for Matteo Rossi, and sorry for all the times the mess on my desk decided to invade yours. I also spent a couple of beamtimes at BM26A. Alessandro Longo, thank you for your help with measurements and data analysis. It was a pleasure working with you!

From Utrecht, I could not have wished for better colleagues than those in the ~~X-ray spectroscopy group~~ Rayman family, the greatest bunch of scientists, superheroes and human beings on this planet. Mustafa al Samarai, my first neighbour, thank you for welcoming me into the group and taking me on my first beamtimes, and of course the amazing visit to Yosemite. Boyang Liu, thank you for your kindness and hospitality, and the 企鵝. Also my best regards to your amazing wife and of course Photon. Next, the master of magnetite, the ruler of rotations, the sovereign of soft and hard X-rays, my partner in ~~erime~~ beamtime and fellow grandma: the one and only Hebatalla Elnaggar. Heba, you are amazing. Despite your beamtimes being on the difficult side, they were fantastic because we did them together. Thank you for the tea breaks, the laughter, the chocolate, the daily

penguin emails and the nightshift exercises. And good luck with writing your thesis! I look forward to calling you Dr Heba. Then we can do postdocs together. Or build a spaceship and explore the universe. Or I could come to Egypt so we can ride camels (don't worry, I'll go first). Thanks also for being my paranymp! One person stands out in our group for having a horrible taste in elements. I am talking of course about Ties Haarman. Ties, despite your irrational obsession with vanadium, I want to thank you for being the most relaxed person in our group. Our beamtimes, and PhDs in general, were a lot more bearable because you were never stressed. Thanks also to Dasha for barbecues and Russian hospitality, and say hello to Erixs for me! The Rayman team consists of slightly messed-up superheroes, such as our Iron(II,III)man who works with cobalt: Ru-Pan Wang. Thank you for the endless supply of M&M's, the oolong from Taiwan, and of course your jokes. Your sense of humour may be somewhat hidden but it is nevertheless excellent. Just don't set off any firealarms during my defence. Please. Our most adventurous superhero is without a doubt Federica Frati. I wish I could join you on beamtime to Taiwan, and go to Hong Kong together afterwards. Though maybe I won't eat *all* the food. Thanks for the hospitality, and may there always be an endless supply of good books and guinea pigs in your life. Ahmed Ismail, I loved exploring Zurich together! Thanks for the many awesome science discussions we had. Don't do too many beamtimes! The top superheroes in the group are of course Mahnaz Ghiasi and Mario Delgado-Jaime. Mahnaz, it's incredible how so much kindness can be packed into such a small person! Mario, enjoy Mexico and please, please *please* start the Surfing & Spectroscopy Summer School soon! Or, alternatively, become president of the world. I can't think of a more suitable person. Thank you for the amazing dinners you cooked for all of us! One amazing Rayman member even made it to Mars: Myrtille Hunault. Congratulations on becoming a beamline scientist and thanks for introducing me to Bellissimo. Yohei Uemura, you were a latecomer to the group so you missed out on all the liquid jet fun! But maybe we can do some EXAFS together in the future. Patric Zimmermann, thank you for the many excellent talks and work discussions that helped me understand X-ray spectroscopy better. Also thanks to Lieven Folkertsma for being brave enough to join this crazy group as a student.

I want to thank and rethank everyone in the Rayman family for making the blood, sweat and tears of this PhD fun (you can put CTM<sub>4</sub>Chicken in whichever category you think is most appropriate). Thank you for the many coffee/tea breaks, dinners, parties, excursions, and of course for great science. Dear fellow descendants of X-ray Bill: you are the best, and I hope you will never be far away. Beam on!

## Acknowledgements

Due to the time-consuming and travel-intense nature of our experiments (and no doubt some radiation damage that makes us too socially awkward for the rest of the world), the X-ray group has always been a bit isolated from the rest of Inorganic Chemistry and Catalysis. Nevertheless I have enjoyed my time here. A big thank you must go to Katinka Wondergem, my fellow gold enthusiast and Disney fan, not to mention wedding dress designer extraordinaire. There's no one I'd rather blow myself up with while baking macarons. Thank you for being my paronymph. Many thanks also to the other ICC ladies! Suzanne Verkleij and Marjolein Velthoen; let's do weird things to our hair again sometime. Nazila Masoud, thanks for being my fumehood neighbour (and sorry for the mess). Thank you all for the great bachelorette party you organised, I will cherish the penguin onesie forever. Sandra Constant, thanks for the fun trip to the zoo to see the penguins (when we managed to drag Heba away from the pandas). Thanks also to my friendly 5th floor colleagues, Fang Liu and José Moya-Cancino. Best of luck with your writing. Baira Donoeva, Giorgio Totarella and Remco Dalebout; thanks for the fun beamtime together. Special thanks also to the ICC technical and administrative staff who keep the labs and group running smoothly. In particular I want to thank Dymph Serrée, who sorted out all the administrative issues I encountered even before I started this PhD.

Wenjin Xu, thanks for the fun discussions about silver nanoclusters, and good luck with your experiments! Mathew Hembury, I thoroughly enjoyed having someone in our building to discuss clusters with, especially from a more biochemical point of view. You even brought along a student, Erik Hebels, who helped out with quantum yield determinations. Erik, thank you also for the fun EXAFS nightshifts. Many thanks also to John Rehr for making FEFF calculations more fun and less frustrating.

I was fortunate enough to attend the International Symposium on Monolayer Protected Clusters 2017 in Ascona, which is probably the best conference I have ever attended, thanks to the brilliant, talented and lovely people there. Hannu Häkkinen, thank you for inviting me to Finland to visit your group! Who knows, it might not be my last visit. Alvaro Muñoz Castro, I will visit you in Chile some day to see penguins. Clara Garcia Yago, Stephan Pollitt and Lule Beqa; thank you for making samples and joining my beamtime! A big thank you also to Chris Hosier! One of your samples actually made it into the thesis! Thanks also for the fun time at ChemCYS. I really enjoyed your visit to the Netherlands. We will definitely drop by Colorado in the future, possibly with a suitcase full of chocolate!

I don't think I would have studied chemistry without the International Chemistry Olympiad. A big thank you to the organisers and all participants of the 40th IChO in Budapest! Thanks also the organisers the Norwegian chemistry olympiad,

without whom I would never have made it to the IChO. Of course, I would not have gone to the finals of Kjemiolympiaden without three excellent high school chemistry teachers at Follo: Lars Arve Larsen, Liv Ellen Vold and Johan Xt Olsen. Tusen takk! Ik heb het afgelopen jaar met groot plezier meegedaan aan de Science Battle. Suzanne Streefland en René Broeders, bedankt voor jullie enthousiasme! Ik heb veel van jullie geleerd.

Ik wil ook mijn familie bedanken voor hun steun. What ho, tally pip pip! Pap, je hebt hierbij toestemming om maximaal 1 keer per maand de “two doctors” grap te maken. Mamma, æ glede mæ te neste del av Rhine & Wine, vi må husk å ta med Kvikk Lunsj (og kanskje ta oss en is, eller to, eller tre). Tim en Stein, ook jullie hebben bijgedragen aan dit proefschrift. Tim, mijn vroege interesse in wetenschap komt deels omdat jij vroeger astronaut wilde worden en ik dus als zevenjarige alle planeten in het zonnestelsel moest leren en samen met jou Star Trek moest/mocht kijken. Live long and prosper! Verder is mijn schoonfamilie de beste schoonfamilie. Jan, Nanny, Ellen, Job, Ivo, Edina: bedankt voor de gezelligheid, de Sinterklaasvieringen en de gigantische hoeveelheden thee.

Jasper, bedankt dat je FzBL bent. Speciaal voor jou heb ik een aantal rode panda's verstoppt in dit proefschrift. You've dragged me up Mount Doom. Now let's go on an adventure!

— Marte, Utrecht 2018

## List of publications

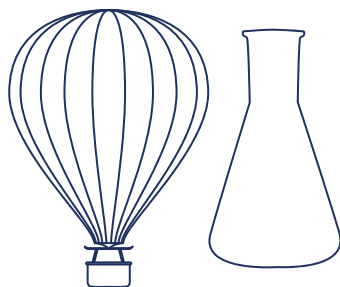
This thesis is based on the following publications:

- M. van der Linden, D. M. E. Thies-Weesie, H. Elnaggar, A. J. van Bunningen, M. Bransen, A. Longo, L. Amidani, P. Glatzel, and F. M. F. de Groot, **Size tuneability of Au clusters with lipoic acid**, in preparation. [Chapters 5 and 7]
- M. van der Linden, A. J. van Bunningen, L. Amidani, P. Glatzel, A. Meijerink, and F. M. F. de Groot, **Single atom doping of silver nanoclusters**, in preparation. [Chapter 4]
- M. van der Linden, A. J. van Bunningen, M. U. Delgado-Jaime, B. Detlefs, P. Glatzel, A. Longo, and F. M. F. de Groot, **Synthesis mechanism of Ag<sub>29</sub> nanoclusters**, in preparation. [Chapter 3]
- M. van der Linden, A. Barendregt, A. J. van Bunningen, P. T. K. Chin, D. M. E. Thies-Weesie, F. M. F. de Groot, and A. Meijerink, **Characterisation, degradation and regeneration of luminescent Ag<sub>29</sub> clusters in solution**, *Nanoscale*, vol. 8, no. 47, pp. 19901-19909, 2016. [Chapter 2]

## Other publications

- M. van der Linden, C. I. Garcia Yago, L. Beqa, T. Haarman, S. Pollitt, C. A. Hosier, P. Window, K. Sokołowska, V. Saarnio, T. Lahtinen, S. Yamazoe, P. Glatzel, and F. M. F. de Groot, **High-resolution X-ray absorption spectra of size-selected Au-thiolate clusters**, in preparation. [partially based on Chapter 7]
- L. Amidani, K. Korthout, J. J. Joos, M. van der Linden, H. F. Sijbom, A. Meijerink, D. Poelman, P. F. Smet, and P. Glatzel, **Oxidation and luminescence quenching of europium in BaMgAl<sub>10</sub>O<sub>17</sub> blue phosphors**, *Chem. Mater.*, vol. 29, no. 23, pp. 10122-10129, 2017.
- A. Bunschoten, P. T. K. Chin, T. Buckle, M. van der Linden, A. Barendregt, M. A. Verheijen, and F. W. B. van Leeuwen, **Receptor-Targeted Luminescent Silver Bionanoparticles**, *Eur. J. Inorg. Chem.*, vol. 2016, no. 18, pp. 3030-3035, 2016.
- M. van der Linden, B. O. Conchúir, E. Spigone, A. Niranjana, A. Zaccone, and P. Cicuta, **Microscopic Origin of the Hofmeister Effect in Gelation Kinetics of Colloidal Silica**, *J. Phys. Chem. Lett.*, vol. 6, no. 15, pp. 2881-2887, 2015.
- J. van Rijssel, M. van der Linden, J. D. Meeldijk, R. J. A. van Dijk-Moes, A. P. Philipse, and B. H. Ern e, **Spatial Distribution of Nanocrystals Imaged at the Liquid-Air Interface**, *Phys. Rev. Lett.*, vol. 111, no. 10, p. 108302, 2013.

- P. T. K. Chin, M. van der Linden, E. J. van Harten, A. Barendregt, M. T. M. Rood, A. J. Koster, F. W. B. van Leeuwen, C. de Mello Donega, A. J. R. Heck, and A. Meijerink, **Enhanced luminescence of Ag nanoclusters via surface modification**, *Nanotechnology*, vol. 24, no. 7, p. 075703, 2013.



## Conference contributions

Oral presentations:

- **From silver ions to atomically monodisperse Ag<sub>29</sub> clusters**, International Conference on X-ray Absorption Fine Structure (XAFS), Kraków, Poland, July 2018.
- **Mechanism of gold nanocluster synthesis unravelled by X-ray spectroscopy**, Chemistry Conference for Young Scientists (ChemCYS), Blankenberge, Belgium, February 2018.
- **Single atom doping of monodisperse clusters**, Physics@Veldhoven, Veldhoven, the Netherlands, January 2018.
- **Unravelling the synthesis mechanism of ligand-protected silver nanoclusters**, CHAINS conference, Veldhoven, the Netherlands, December 2016.
- **Luminescent gold clusters studied by X-ray spectroscopy**, ESRF Science and Student Days, Val Cenis-Lanslebourg, France, October 2016. Awarded prize for best presentation.

Invited talk:

- **Shooting X-rays at nanoclusters: a high-energy approach to unravelling structures and synthesis mechanisms**, Nanoseminar, University of Jyväskylä, October 2017.

## Publications and conferences

### Selected poster presentations:

- **Tuneable synthesis of gold nanoclusters studied by optical and X-ray spectroscopy**, International Symposium on Monolayer Protected Clusters (ISMPC), Monte Verità, Switzerland. August 2017.
- **Gold nanoclusters with tuneable size: multi-technique characterisation**, International Conference on Vacuum Ultraviolet and X-ray Physics (VUVX), Zürich, Switzerland, July 2016.
- **Ultrasmall noble metal nanoclusters**, Methods in Molecular Energy Research: Theory and Spectroscopy, summer school, Gelsenkirchen, Germany, August 2015.
- **Highly stable luminescent Ag nanoclusters**, CHAINS conference, Veldhoven, the Netherlands, November 2014.

## About the author

Marte van der Linden was born in Utrecht on 14<sup>th</sup> April 1989. She moved to Norway as a child, and graduated from Orkdal vidaregåande skole in 2008, with mathematics, physics and chemistry as her chosen subjects. She qualified for the Norwegian national olympiads in both physics and chemistry, and won a place on the team representing Norway at the 40<sup>th</sup> International Chemistry Olympiad in Budapest. Here, she met Jasper Landman, on whom she played a practical joke that was picked up by C&EN.\*

Marte went on to study chemistry at Utrecht University, obtaining her bachelor's degree (cum laude) in 2011. Her bachelor's thesis was done at the Van 't Hoff Laboratory for Physical and Colloid Chemistry, under the supervision of Ben Ern  and Jos van Rijssel. During this time, she was a member of the board of ANSA Nederland & Belgia, a group for Norwegian students abroad. She went on to obtain her master's degree in chemistry from Utrecht University (cum laude) in 2013. Her master's thesis on the characterisation of silver nanoclusters was supervised by Andries Meijerink and Patrick Chin, and was awarded the KNCV Golden Master Award for best chemistry master's thesis in the Netherlands. She also spent five months at the Cavendish laboratory in Cambridge, studying the gelation of colloidal silica. This internship project was supervised by Pietro Cicuti.

She started her PhD in 2014, under the supervision of Frank de Groot and Pieter Glatzel. The project was a collaboration between Utrecht University and the European Synchrotron Radiation Facility. Currently, she is a postdoc in the group of Frank de Groot.

In her spare time, Marte enjoys mountain hiking and nature photography. Her favourite animals are penguins.



---

\*See <http://cenblog.org/2008/07/hint-21/>

About the author

## Bibliography

- 1 E. Roduner, Chem. Soc. Rev. **35**, 583 (2006).
- 2 K. Koga, T. Ikeshoji, and K.-i. Sugawara, Phys. Rev. Lett. **92**, 115507 (2004).
- 3 K. J. Taylor, C. L. Pettiette-Hall, O. Cheshnovsky, and R. E. Smalley, J. Chem. Phys. **96**, 3319 (1992).
- 4 I. Laoufi, M.-C. Saint-Lager, R. Lazzari, J. Jupille, O. Robach, S. Garaudée, G. Cabailh, P. Dolle, H. Cruguel, and A. Bailly, J. Phys. Chem. C **115**, 4673 (2011).
- 5 J. T. Miller, A. J. Kropf, Y. Zha, J. R. Regalbuto, L. Delannoy, C. Louis, E. Bus, and J. A. van Bokhoven, J. Catal. **240**, 222 (2006).
- 6 C. Burda, X. Chen, R. Narayanan, and M. A. El-Sayed, Chem. Rev. **105**, 1025 (2005).
- 7 V. Amendola, R. Pilot, M. Frascioni, O. M. Maragò, and M. A. Iatì, J. Phys. Condens. Matter **29**, 203002 (2017).
- 8 J. Jortner, Zeitschrift für Phys. D Atoms, Mol. Clust. **24**, 247 (1992).
- 9 H. Fröhlich, Physica **4**, 406 (1937).
- 10 R. Kubo, J. Phys. Soc. Japan **17**, 975 (1962).
- 11 R. Jin, Nanoscale **7**, 1549 (2015).
- 12 I. Díez and R. H. A. Ras, Nanoscale **3**, 1963 (2011).
- 13 Y. Lu and W. Chen, Chem. Soc. Rev. **41**, 3594 (2012).
- 14 M. Zhu, C. M. Aikens, M. P. Hendrich, R. Gupta, H. Qian, G. C. Schatz, and R. Jin, J. Am. Chem. Soc. **131**, 2490 (2009).
- 15 R. Jin, Nanoscale **2**, 343 (2010).
- 16 R. L. Johnston, Philos. Trans. Math. Phys. Eng. Sci. **356**, 211 (1998).
- 17 I. Chakraborty, J. Erusappan, A. Govindarajan, K. S. Sugi, T. Udayabhaskararao, A. Ghosh, and T. Pradeep, Nanoscale **6**, 8024 (2014).
- 18 Y. Negishi, T. Nakazaki, S. Malola, S. Takano, Y. Niihori, W. Kurashige, S. Yamazoe, T. Tsukuda, and H. Häkkinen, J. Am. Chem. Soc. **137**, 1206 (2015).
- 19 R. Jin, S. Zhao, Y. Xing, and R. Jin, CrystEngComm **18**, 3996 (2016).
- 20 I. Chakraborty and T. Pradeep, Chem. Rev. **117**, 8208 (2017).
- 21 Y. Lu, W. Wei, and W. Chen, Chinese Sci. Bull. **57**, 41 (2012).
- 22 X. Yuan, B. Zhang, Z. Luo, Q. Yao, D. T. Leong, N. Yan, and J. Xie, Angew. Chemie Int. Ed. **53**, 4623 (2014).
- 23 A. Desireddy, B. E. Conn, J. Guo, B. Yoon, R. N. Barnett, B. M. Monahan, K. Kirschbaum, W. P. Griffith, R. L. Whetten, U. Landman, and T. P. Bigioni, Nature **501**, 399 (2013).
- 24 U. Kreibig and M. Vollmer, *Optical Properties of metal clusters* (Springer, 1995).
- 25 J. Zheng, P. R. Nicovich, and R. M. Dickson, Annu. Rev. Phys. Chem. **58**, 409 (2007).
- 26 I. Chakraborty, A. Govindarajan, J. Erusappan, A. Ghosh, T. Pradeep, B. Yoon, R. L. Whetten, and U. Landman, Nano Lett. **12**, 5861 (2012).

## BIBLIOGRAPHY

- 27 D. Crasto and A. Dass, *J. Phys. Chem. C* **117**, 22094 (2013).
- 28 G. Natarajan, A. Mathew, Y. Negishi, R. L. Whetten, and T. Pradeep, *J. Phys. Chem. C* **119**, 27768 (2015).
- 29 A. George, K. S. Asha, A. C. Reber, S. R. Biltek, A. F. Pedicini, A. Sen, S. N. Khanna, and S. Mandal, *Nanoscale* **7**, 19448 (2015).
- 30 R. Jin, H. Qian, Z. Wu, Y. Zhu, M. Zhu, A. Mohanty, and N. Garg, *J. Phys. Chem. Lett.* **1**, 2903 (2010).
- 31 T. P. Martin, *Phys. Rep.* **273**, 199 (1996).
- 32 E. G. Noya, J. P. Doye, D. J. Wales, and A. Aguado, *Eur. Phys. J. D* **43**, 57 (2007).
- 33 R. L. Johnston, *Atomic and Molecular Clusters*, 1st ed. (Taylor & Francis, 2002).
- 34 B. Yoon, P. Koskinen, B. Huber, O. Kostko, B. von Issendorff, H. Häkkinen, M. Moseler, and U. Landman, *ChemPhysChem* **8**, 157 (2007).
- 35 I. Katakuse, T. Ichihara, Y. Fujita, T. Matsuo, T. Sakurai, and H. Matsuda, *Int. J. Mass Spectrom. Ion Process.* **67**, 229 (1985).
- 36 W. A. de Heer, *Rev. Mod. Phys.* **65**, 611 (1993).
- 37 K. R. Krishnadas, A. Baksi, A. Ghosh, G. Natarajan, and T. Pradeep, *Nat. Commun.* **7**, 13447 (2016).
- 38 L. G. AbdulHalim, N. Kothalawala, L. Sinatra, A. Dass, and O. M. Bakr, *J. Am. Chem. Soc.* **136**, 15865 (2014).
- 39 T.-R. Tero, S. Malola, B. Koncz, E. Pohjolainen, S. Lautala, S. Mustalahti, P. Permi, G. Groenhof, M. Pettersson, and H. Häkkinen, *ACS Nano* **11**, 11872 (2017).
- 40 K. Salorinne, S. Malola, O. A. Wong, C. D. Rithner, X. Chen, C. J. Ackerson, and H. Häkkinen, *Nat. Commun.* **7**, 10401 (2016).
- 41 Y. Yu, S. Y. New, J. Xie, X. Su, and Y. N. Tan, *Chem. Commun.* **50**, 13805 (2014).
- 42 A. Pandya, A. N. Lad, S. P. Singh, and R. Shanker, *RSC Adv.* **6**, 113095 (2016).
- 43 X.-K. Wan, Z.-W. Lin, and Q.-M. Wang, *J. Am. Chem. Soc.* **134**, 14750 (2012).
- 44 P. A. Bartlett, B. Bauer, and S. J. Singer, *J. Am. Chem. Soc.* **100**, 5085 (1978).
- 45 G. Salassa, A. Sels, F. Mancin, and T. Bürgi, *ACS Nano* **11**, 12609 (2017).
- 46 M. Walter, J. Akola, O. Lopez-Acevedo, P. D. Jadzinsky, G. Calero, C. J. Ackerson, R. L. Whetten, H. Grönbeck, and H. Häkkinen, *Proc. Natl. Acad. Sci. U. S. A.* **105**, 9157 (2008).
- 47 M. A. Tofanelli and C. J. Ackerson, *J. Am. Chem. Soc.* **134**, 16937 (2012).
- 48 M. A. Tofanelli, K. Salorinne, T. W. Ni, S. Malola, B. Newell, B. Phillips, H. Häkkinen, and C. J. Ackerson, *Chem. Sci.* **7**, 1882 (2016).
- 49 H. Häkkinen, M. Walter, and H. Grönbeck, *J. Phys. Chem. B* **110**, 9927 (2006).
- 50 D.-e. Jiang, M. L. Tiago, W. Luo, and S. Dai, *J. Am. Chem. Soc.* **130**, 2777 (2008).
- 51 H. Häkkinen, *Nat. Chem.* **4**, 443 (2012).
- 52 P. D. Jadzinsky, G. Calero, C. J. Ackerson, D. A. Bushnell, and R. D. Kornberg, *Science* **318**, 430 (2007).
- 53 M. W. Heaven, A. Dass, P. S. White, K. M. Holt, and R. W. Murray, *J. Am. Chem. Soc.* **130**, 3754 (2008).
- 54 J. Akola, M. Walter, R. L. Whetten, H. Häkkinen, and H. Grönbeck, *J. Am. Chem. Soc.* **130**, 3756 (2008).

- 55 H. Yang, Y. Wang, H. Huang, L. Gell, L. Lehtovaara, S. Malola, H. Häkkinen, and N. Zheng, *Nat. Commun.* **4**, 2422 (2013).
- 56 L. G. AbdulHalim, M. S. Bootharaju, Q. Tang, S. Del Gobbo, R. G. AbdulHalim, M. Eddaoudi, D.-e. Jiang, and O. M. Bakr, *J. Am. Chem. Soc.* **137**, 11970 (2015).
- 57 X.-K. Wan, J.-Q. Wang, Z.-A. Nan, and Q.-M. Wang, *Sci. Adv.* **3**, e1701823 (2017).
- 58 Z. Wu and R. Jin, *Nano Lett.* **10**, 2568 (2010).
- 59 Y. Chen, C. Zeng, D. R. Kauffman, and R. Jin, *Nano Lett.* **15**, 3603 (2015).
- 60 D. M. P. Mingos, *Inorg. Chem.* **21**, 464 (1982).
- 61 C. Zeng, Y. Chen, G. Li, and R. Jin, *Chem. Mater.* **26**, 2635 (2014).
- 62 J.-i. Nishigaki, R. Tsunoyama, H. Tsunoyama, N. Ichikuni, S. Yamazoe, Y. Negishi, M. Ito, T. Matsuo, K. Tamao, and T. Tsukuda, *J. Am. Chem. Soc.* **134**, 14295 (2012).
- 63 C. Zeng, C. Liu, Y. Pei, and R. Jin, *ACS Nano* **7**, 6138 (2013).
- 64 M. S. Bootharaju, C. P. Joshi, M. J. Alhilaly, and O. M. Bakr, *Chem. Mater.* **28**, 3292 (2016).
- 65 M. S. Bootharaju, V. M. Burlakov, T. M. D. Besong, C. P. Joshi, L. G. AbdulHalim, D. M. Black, R. L. Whetten, A. Goriely, and O. M. Bakr, *Chem. Mater.* **27**, 4289 (2015).
- 66 B. Garcia, M. Salomé, L. Lemelle, J.-L. Bridot, P. Gillet, P. Perriat, S. Roux, and O. Tillement, *Chem. Commun.* **0**, 369 (2005).
- 67 S. Roux, B. Garcia, J.-L. Bridot, M. Salomé, C. Marquette, L. Lemelle, P. Gillet, L. Blum, P. Perriat, and O. Tillement, *Langmuir* **21**, 2526 (2005).
- 68 W. Hou, M. Dasog, and R. W. J. Scott, *Langmuir* **25**, 12954 (2009).
- 69 Z. Tang, B. Xu, B. Wu, M. W. Germann, and G. Wang, *J. Am. Chem. Soc.* **132**, 3367 (2010).
- 70 A. Ghosh, D. Ghosh, E. Khatun, P. Chakraborty, and T. Pradeep, *Nanoscale* **9**, 1068 (2017).
- 71 Z. Tang, T. Ahuja, S. Wang, and G. Wang, *Nanoscale* **4**, 4119 (2012).
- 72 F. Aldeek, M. A. H. Muhammed, G. Palui, N. Zhan, and H. Mattoussi, *ACS Nano* **7**, 2509 (2013).
- 73 M. A. H. Muhammed, F. Aldeek, G. Palui, L. Trapiella-Alfonso, and H. Mattoussi, *ACS Nano* **6**, 8950 (2012).
- 74 M. Brust, M. Walker, D. Bethell, D. J. Schiffrin, and R. Whyman, *J. Chem. Soc. Chem. Commun.* , 801 (1994).
- 75 J. B. Tracy, G. Kalyuzhny, M. C. Crowe, R. Balasubramanian, J.-P. Choi, and R. W. Murray, *J. Am. Chem. Soc.* **129**, 6706 (2007).
- 76 M. Zhu, E. Lanni, N. Garg, M. E. Bier, and R. Jin, *J. Am. Chem. Soc.* **130**, 1138 (2008).
- 77 Z. Wu, J. Suhan, and R. Jin, *J. Mater. Chem.* **19**, 622 (2009).
- 78 C. Liu, G. Li, G. Pang, and R. Jin, *RSC Adv.* **3**, 9778 (2013).
- 79 X. Meng, Z. Liu, M. Zhu, and R. Jin, *Nanoscale Res. Lett.* **7**, 277 (2012).
- 80 Z. Wu, M. A. MacDonald, J. Chen, P. Zhang, and R. Jin, *J. Am. Chem. Soc.* **133**, 9670 (2011).
- 81 G. Li and R. Jin, *Acc. Chem. Res.* **46**, 1749 (2013).
- 82 M.-b. Li, S.-k. Tian, and Z. Wu, *Chinese J. Chem.* **35**, 567 (2017).
- 83 J. Liu, K. S. Krishna, Y. B. Losovyj, S. Chattopadhyay, N. Lozova, J. T. Miller, J. J. Spivey, and C. S. S. R. Kumar, *Chem. A Eur. J.* **19**, 10201 (2013).
- 84 L. Shang, S. Dong, and G. U. Nienhaus, *Nano Today* **6**, 401 (2011).
- 85 C. Niu, Q. Liu, Z. Shang, L. Zhao, and J. Ouyang, *Nanoscale* **7**, 8457 (2015).

## BIBLIOGRAPHY

- 86 B. Adhikari and A. Banerjee, *Chem. Mater.* **22**, 4364 (2010).
- 87 L. Shang, L. Yang, F. Stockmar, R. Popescu, V. Trouillet, M. Bruns, D. Gerthsen, and G. U. Nienhaus, *Nanoscale* **4**, 4155 (2012).
- 88 N. Mohammed, A. Baidya, V. Murugesan, A. A. Kumar, M. A. Ganayee, J. S. Mohanty, K. C. Tam, and T. Pradeep, *ACS Sustain. Chem. & Eng.* **4**, 6167 (2016).
- 89 X. Wu, X. He, K. Wang, C. Xie, B. Zhou, and Z. Qing, *Nanoscale* **2**, 2244 (2010).
- 90 X. Wang, H. He, Y. Wang, J. Wang, X. Sun, H. Xu, W. M. Nau, X. Zhang, and F. Huang, *Chem. Commun.* **52**, 9232 (2016).
- 91 R. Jin, C. Zeng, M. Zhou, and Y. Chen, *Chem. Rev.* **116**, 10346 (2016).
- 92 K. L. D. M. Weerawardene and C. M. Aikens, *J. Am. Chem. Soc.* **138**, 11202 (2016).
- 93 K. Pyo, V. D. Thanthirige, K. Kwak, P. Pandurangan, G. Ramakrishna, and D. Lee, *J. Am. Chem. Soc.* **137**, 8244 (2015).
- 94 Z. Luo, X. Yuan, Y. Yu, Q. Zhang, D. T. Leong, J. Y. Lee, and J. Xie, *J. Am. Chem. Soc.* **134**, 16662 (2012).
- 95 A. Baksi, A. Ghosh, S. K. Mudedla, P. Chakraborty, S. Bhat, B. Mondal, K. R. Krishnadas, V. Subramanian, and T. Pradeep, *J. Phys. Chem. C* **121**, 13421 (2017).
- 96 C. Zeng and R. Jin, *Chem. Asian J.* **12**, 1839 (2017).
- 97 W. C. Röntgen, *Sitzungsberichte der Würzburg. Phys. Gesellschaft* **9**, 132 (1895).
- 98 R. F. Mould, *Phys. Med. Biol.* **40**, 1741 (1995).
- 99 H. G. J. Moseley, *London, Edinburgh, Dublin Philos. Mag. J. Sci.* **26**, 1024 (1913).
- 100 R. Cesareo, in *Ullmann's Encyclopedia of Industrial Chemistry* (American Cancer Society, 2010).
- 101 F. M. F. de Groot and A. Kotani, *Core level spectroscopy of solids* (CRC Press, Boca Raton, 2008).
- 102 M. Newville, *Rev. Mineral. Geochemistry* **78**, 33 (2014).
- 103 J. Penner-Hahn, in *Compr. Coord. Chem. II*, edited by J. A. McCleverty and T. J. Meyer (Elsevier, 2003) 2nd ed., pp. 159–186.
- 104 G. S. Henderson, F. M. F. de Groot, and B. J. A. Moulton, *Rev. Mineral. Geochemistry* **78**, 75 (2014).
- 105 D. E. Sayers, E. A. Stern, and F. W. Lytle, *Phys. Rev. Lett.* **27**, 1204 (1971).
- 106 J. J. Rehr, J. J. Kas, F. D. Vila, M. P. Prange, and K. Jorissen, *Phys. Chem. Chem. Phys.* **12**, 5503 (2010).
- 107 P. A. M. Dirac, *Proc. R. Soc. A.* **114**, 243 (1927).
- 108 P. Glatzel and A. Juhin, in *Local Struct. Characterisation Inorg. Mater. Ser.*, edited by D. W. Bruce, D. O'Hare, and R. I. Walton (Wiley, New York, 2014) pp. 89–171.
- 109 F. de Groot, *Coord. Chem. Rev.* **249**, 31 (2005).
- 110 F. de Groot, G. Vankó, and P. Glatzel, *J. Phys. Condens. Matter* **21**, 104207 (2009).
- 111 N. F. Mott, *Proc. Phys. Soc. A* **62**, 416 (1949).
- 112 F. Lytle, P. S. P. Wei, R. B. Gregor, G. H. Via, and J. H. Sinfelt, *J. Chem. Phys.* **70**, 4849 (1979).
- 113 D. H. Pearson, C. C. Ahn, and B. Fultz, *Phys. Rev. B* **47**, 8471 (1993).
- 114 F. W. Lytle, *J. Catal.* **43**, 376 (1976).
- 115 J. A. van Bokhoven and J. T. Miller, *J. Phys. Chem. C* **111**, 9245 (2007).
- 116 G. N. George and M. L. Gorbaty, *J. Am. Chem. Soc.* **111**, 3182 (1989).

- 117 J. A. Kirby, D. B. Goodin, T. Wydrzynski, A. S. Robertson, and M. P. Klein, *J. Am. Chem. Soc.* **103**, 5537 (1981).
- 118 R. Sarangi, *Coord. Chem. Rev.* **257**, 459 (2013).
- 119 J. J. Rehr, J. J. Kas, M. P. Prange, A. P. Sorini, Y. Takimoto, and F. Vila, *Comptes Rendus Phys.* **10**, 548 (2009).
- 120 O. Bunău and Y. Joly, *J. Phys. Condens. Matter* **21**, 345501 (2009).
- 121 M. F. Lengke, B. Ravel, M. E. Fleet, G. Wanger, R. A. Gordon, and G. Southam, *Environ. Sci. Technol.* **40**, 6304 (2006).
- 122 P. Glatzel and U. Bergmann, *Coord. Chem. Rev.* **249**, 65 (2005).
- 123 J. L. Campbell and T. Papp, *At. Data Nucl. Data Tables* **77**, 1 (2001).
- 124 K. Hämäläinen, D. P. Siddons, J. B. Hastings, and L. E. Berman, *Phys. Rev. Lett.* **67**, 2850 (1991).
- 125 F. M. F. de Groot, M. H. Krisch, and J. Vogel, *Phys. Rev. B* **66**, 195112 (2002).
- 126 E. Gallo and P. Glatzel, *Adv. Mater.* **26**, 7730 (2014).
- 127 M. Rovezzi and P. Glatzel, *Semicond. Sci. Technol.* **29**, 023002 (2014).
- 128 C. J. Pollock and S. DeBeer, *J. Am. Chem. Soc.* **133**, 5594 (2011).
- 129 A. Kotani and S. Shin, *Rev. Mod. Phys.* **73**, 203 (2001).
- 130 L. J. P. Ament, M. van Veenendaal, T. P. Devereaux, J. P. Hill, and J. van den Brink, *Rev. Mod. Phys.* **83**, 705 (2010).
- 131 P. Glatzel, M. Sikora, G. Smolentsev, and M. Fernández-García, *Catal. Today* **145**, 294 (2009).
- 132 P. Carra, M. Fabrizio, and B. T. Thole, *Phys. Rev. Lett.* **74**, 3700 (1995).
- 133 P. Glatzel, T.-C. Weng, K. Kvashnina, J. Swarbrick, M. Sikora, E. Gallo, N. Smolentsev, and R. A. Mori, *J. Electron Spectros. Relat. Phenomena* **188**, 17 (2013).
- 134 J. A. van Bokhoven, C. Louis, J. T. Miller, M. Tromp, O. V. Safonova, and P. Glatzel, *Angew. Chemie Int. Ed.* **45**, 4651 (2006).
- 135 O. V. Safonova, M. Tromp, J. A. van Bokhoven, F. M. F. de Groot, J. Evans, and P. Glatzel, *J. Phys. Chem. B* **110**, 16162 (2006).
- 136 D. R. Mortensen, G. T. Seidler, A. S. Ditter, and P. Glatzel, *J. Phys. Conf. Ser.* **712**, 012036 (2016).
- 137 "easyXAFS," <http://easyxafs.com/>.
- 138 T. K. Sham and M. L. Rivers, *Rev. Mineral. Geochemistry* **49**, 117 (2002).
- 139 E. J. Finehout and K. H. Lee, *Biochem. Mol. Biol. Educ.* **32**, 93 (2004).
- 140 R. M. Ewing, P. Chu, F. Elisma, H. Li, P. Taylor, S. Climie, L. McBroom-Cerajewski, M. D. Robinson, L. O'Connor, M. Li, R. Taylor, M. Dharsee, Y. Ho, A. Heilbut, L. Moore, S. Zhang, O. Ornatsky, Y. V. Bukhman, M. Ethier, Y. Sheng, J. Vasilescu, M. Abu-Farha, J.-P. Lambert, H. S. Duetzel, I. I. Stewart, B. Kuehl, K. Hogue, K. Colwill, K. Gladwish, B. Muskat, R. Kinach, S.-L. Adams, M. F. Moran, G. B. Morin, T. Topaloglou, and D. Figeys, *Mol. Syst. Biol.* **3**, 89 (2007).
- 141 Y. Lu and W. Chen, *Anal. Chem.* **87**, 10659 (2015).
- 142 I. N. Serdyuk, N. R. Zaccai, and J. Zaccai, *Methods in Molecular Biophysics: Structure, Dynamics, Function*, 1st ed. (Cambridge University Press, Cambridge, 2007).
- 143 P. Brown and C. Djerassi, *Angew. Chemie Int. Ed.* **6**, 477 (1967).
- 144 Y. Negishi, W. Kurashige, Y. Niihori, T. Iwasa, and K. Nobusada, *Phys. Chem. Chem. Phys.* **12**, 6219 (2010).

## BIBLIOGRAPHY

- 145 S. Knoppe, A. C. Dharmaratne, E. Schreiner, A. Dass, and T. Bürgi, *J. Am. Chem. Soc.* **132**, 16783 (2010).
- 146 H. Qian, Y. Zhu, and R. Jin, *J. Am. Chem. Soc.* **132**, 4583 (2010).
- 147 J. B. Fenn, M. Mann, C. K. Meng, S. F. Wong, and G. M. Whitehouse, *Science* **246**, 64 (1989).
- 148 T. G. Schaaff, G. Knight, M. N. Shafigullin, R. F. Borkman, and R. L. Whetten, *J. Phys. Chem. B* **102**, 10643 (1998).
- 149 T. G. Schaaff and R. L. Whetten, *J. Phys. Chem. B* **104**, 2630 (2000).
- 150 Y. Negishi, K. Nobusada, and T. Tsukuda, *J. Am. Chem. Soc.* **127**, 5261 (2005).
- 151 L. Patiny and A. Borel, *J. Chem. Inf. Model.* **53**, 1223 (2013).
- 152 R. P. Carney, J. Y. Kim, H. Qian, R. Jin, H. Mehenni, F. Stellacci, and O. M. Bakr, *Nat. Commun.* **2**, 335 (2011).
- 153 C. S. W. Koehler, *Today's Chem. Work*, 63 (2003).
- 154 T. R. Patel, D. J. Winzor, and D. J. Scott, *Methods* **95**, 55 (2016).
- 155 G. J. Howlett, A. P. Minton, and G. Rivas, *Curr. Opin. Chem. Biol.* **10**, 430 (2006).
- 156 P. H. Brown and P. Schuck, *Biophys. J.* **90**, 4651 (2006).
- 157 J. L. Cole, J. W. Lary, T. Moody, and T. M. Laue, *Methods Cell Biol.* **84**, 143 (2008).
- 158 P. Schuck, *Biophys. J.* **78**, 1606 (2000).
- 159 H. Zhao, C. A. Brautigam, R. Ghirlando, and P. Schuck, *Curr. Protoc. Protein Sci.* **71**, 20.12.1 (2013).
- 160 O. M. Bakr, V. Amendola, C. M. Aikens, W. Wenseleers, R. Li, L. Dal Negro, G. C. Schatz, and F. Stellacci, *Angew. Chemie Int. Ed.* **48**, 5921 (2009).
- 161 B. A. Ashenfelter, A. Desireddy, S. H. Yau, T. Goodson, and T. P. Bigioni, *J. Phys. Chem. C* **119**, 20728 (2015).
- 162 Y. Yu, Z. Luo, D. M. Chevrier, D. T. Leong, P. Zhang, D.-e. Jiang, and J. Xie, *J. Am. Chem. Soc.* **136**, 1246 (2014).
- 163 A. Mathew, E. Varghese, S. Choudhury, S. K. Pal, and T. Pradeep, *Nanoscale* **7**, 14305 (2015).
- 164 Z. Tang, B. Xu, B. Wu, D. A. Robinson, N. Bokossa, and G. Wang, *Langmuir* **27**, 2989 (2011).
- 165 L. Shang, N. Azadfar, F. Stockmar, W. Send, V. Trouillet, M. Bruns, D. Gerthsen, and G. U. Nienhaus, *Small* **7**, 2614 (2011).
- 166 X. Le Guevel, O. Tagit, C. E. Rodriguez, V. Trouillet, M. P. Leal, and N. Hildebrandt, *Nanoscale* **6**, 8091 (2014).
- 167 W.-T. Chen, Y.-J. Hsu, and P. V. Kamat, *J. Phys. Chem. Lett.* **3**, 2493 (2012).
- 168 P. T. K. Chin, M. van der Linden, E. J. van Harten, A. Barendregt, M. T. M. Rood, A. J. Koster, F. W. B. van Leeuwen, C. de Mello Donega, A. J. R. Heck, and A. Meijerink, *Nanotechnology* **24**, 075703 (2013).
- 169 L. Shang, R. M. Dörlich, V. Trouillet, M. Bruns, and G. U. Nienhaus, *Nano Res.* **5**, 531 (2012).
- 170 I. Russier-Antoine, F. Bertorelle, R. Hamouda, D. Rayane, P. Dugourd, v. Sanader, V. Bonačić-Koutecký, P.-F. Brevet, and R. Antoine, *Nanoscale* **8**, 2892 (2016).
- 171 A. Bunschoten, P. T. K. Chin, T. Buckle, M. van der Linden, A. Barendregt, M. A. Verheijen, and F. W. B. van Leeuwen, *Eur. J. Inorg. Chem.* **2016**, 3030 (2016).
- 172 Y. Levi-Kalisman, P. D. Jadzinsky, N. Kalisman, H. Tsunoyama, T. Tsukuda, D. A. Bushnell, and R. D. Kornberg, *J. Am. Chem. Soc.* **133**, 2976 (2011).

- 173 X. Yuan, Q. Yao, Y. Yu, Z. Luo, X. Dou, and J. Xie, *J. Phys. Chem. Lett.* **4**, 1811 (2013).
- 174 M. Zhu, W. T. Eckenhoff, T. Pintauer, and R. Jin, *J. Phys. Chem. C* **112**, 14221 (2008).
- 175 K. Rurack and M. Spieles, *Anal. Chem.* **83**, 1232 (2011).
- 176 R. Sens and K. H. Drexhage, *J. Lumin.* **24-25**, 709 (1981).
- 177 J. R. Rumble (ed.), "CRC Handbook of Chemistry and Physics," (2017).
- 178 L. M. Tvedte and C. J. Ackerson, *J. Phys. Chem. A* **118**, 8124 (2014).
- 179 L. Shang and S. Dong, *Chem. Commun.* **0**, 1088 (2008).
- 180 J. Sharma, H.-C. Yeh, H. Yoo, J. H. Werner, and J. S. Martinez, *Chem. Commun.* **46**, 3280 (2010).
- 181 A. Mathew, P. R. Sajanlal, and T. Pradeep, *J. Mater. Chem.* **21**, 11205 (2011).
- 182 A. Baksi, M. S. Bootharaju, X. Chen, H. Häkkinen, and T. Pradeep, *J. Phys. Chem. C* **118**, 21722 (2014).
- 183 K. Zheng, X. Yuan, K. Kuah, Z. Luo, Q. Yao, Q. Zhang, and J. Xie, *Chem. Commun.* **51**, 15165 (2015).
- 184 X. Le Guével, C. Spies, N. Daum, G. Jung, and M. Schneider, *Nano Res.* **5**, 379 (2012).
- 185 B. Michen, C. Geers, D. Vanhecke, C. Endes, B. Rothen-Rutishauser, S. Balog, and A. Petri-Fink, *Sci. Rep.* **5**, 9793 (2015).
- 186 I. Moreels, J. C. Martins, and Z. Hens, *ChemPhysChem* **7**, 1028 (2006).
- 187 D. M. Black, G. Robles, P. Lopez, S. B. H. Bach, M. M. Alvarez, and R. L. Whetten, *Anal. Chem.* **90**, 2010 (2018).
- 188 A. Dass, *Nanoscale* **4**, 2260 (2012).
- 189 K. M. Harkness, Y. Tang, A. Dass, J. Pan, N. Kothalawala, V. J. Reddy, D. E. Cliffler, B. Demeler, F. Stellacci, O. M. Bakr, and J. A. McLean, *Nanoscale* **4**, 4269 (2012).
- 190 H. G. Fijolek, P. González-Duarte, S. H. Park, S. L. Suib, and M. J. Natan, *Inorg. Chem.* **36**, 5299 (1997).
- 191 C.-A. J. Lin, T.-Y. Yang, C.-H. Lee, S. H. Huang, R. A. Sperling, M. Zanella, J. K. Li, J.-L. Shen, H.-H. Wang, H.-I. Yeh, W. J. Parak, and W. H. Chang, *ACS Nano* **3**, 395 (2009).
- 192 S. Huang, C. Pfeiffer, J. Hollmann, S. Friede, J. J.-C. Chen, A. Beyer, B. Haas, K. Volz, W. Heimbrot, J. M. Montenegro Martos, W. Chang, and W. J. Parak, *Langmuir* **28**, 8915 (2012).
- 193 I. Chakraborty and T. Pradeep, *Nanoscale* **6**, 14190 (2014).
- 194 A. Mathew and T. Pradeep, *Part. Part. Syst. Charact.* **31**, 1017 (2014).
- 195 L. G. AbdulHalim, S. Ashraf, K. Katsiev, A. R. Kirmani, N. Kothalawala, D. H. Anjum, S. Abbas, A. Amassian, F. Stellacci, A. Dass, I. Hussain, and O. M. Bakr, *J. Mater. Chem. A* **1**, 10148 (2013).
- 196 Y. Yu, X. Chen, Q. Yao, Y. Yu, N. Yan, and J. Xie, *Chem. Mater.* **25**, 946 (2013).
- 197 H. Qian, Y. Zhu, and R. Jin, *ACS Nano* **3**, 3795 (2009).
- 198 H. Qian and R. Jin, *Chem. Mater.* **23**, 2209 (2011).
- 199 M. Zhu, H. Qian, and R. Jin, *J. Am. Chem. Soc.* **131**, 7220 (2009).
- 200 M. M. Alvarez, J. T. Khoury, T. G. Schaaff, M. Shafiqullin, I. Vezmar, and R. L. Whetten, *Chem. Phys. Lett.* **266**, 91 (1997).
- 201 C. J. Ackerson, P. D. Jadzinsky, and R. D. Kornberg, *J. Am. Chem. Soc.* **127**, 6550 (2005).
- 202 R. P. Briñas, M. Hu, L. Qian, E. S. Lyman, and J. F. Hainfeld, *J. Am. Chem. Soc.* **130**, 975 (2008).
- 203 P. J. G. Goulet and R. B. Lennox, *J. Am. Chem. Soc.* **132**, 9582 (2010).

## BIBLIOGRAPHY

- 204 Y. Yu, Q. Yao, Z. Luo, X. Yuan, J. Y. Lee, and J. Xie, *Nanoscale* **5**, 4606 (2013).
- 205 S. Nikitenko, A. M. Beale, A. M. Van Der Eerden, S. D. Jacques, O. Leynaud, M. G. O'Brien, D. Detollenaere, R. Kaptein, B. M. Weckhuysen, and W. Bras, *J. Synchrotron Rad.* **15**, 632 (2008).
- 206 K. V. Klementev, *J. Phys. D. Appl. Phys.* **34**, 209 (2001).
- 207 B. Ravel and M. Newville, *J. Synchrotron Rad.* **12**, 537 (2005).
- 208 "Inorganic Crystal Structure Database," <https://icsd.fiz-karlsruhe.de/>.
- 209 M. D. Hanwell, D. E. Curtis, D. C. Lonie, T. Vandermeersch, E. Zurek, and G. R. Hutchison, *J. Cheminform.* **4**, 17 (2012).
- 210 S. T. Korhonen, A. M. Beale, M. A. Newton, and B. M. Weckhuysen, *J. Phys. Chem. C* **115**, 885 (2011).
- 211 J. C. Woicik, B. Ravel, D. A. Fischer, and W. J. Newburgh, *J. Synchrotron Rad.* **17**, 409 (2010).
- 212 P. R. Amestoy, A. Guermouche, J. Y. L'Excellent, and S. Pralet, *Parallel Comput.* **32**, 136 (2006).
- 213 S. A. Guda, A. A. Guda, M. A. Soldatov, K. A. Lomachenko, A. L. Bugaev, C. Lamberti, W. Gawelda, C. Bressler, G. Smolentsev, A. V. Soldatov, and Y. Joly, *J. Chem. Theory Comput.* **11**, 4512 (2015).
- 214 J. P. Wilcoxon, J. E. Martin, and P. Provencio, *J. Chem. Phys.* **115**, 998 (2001).
- 215 N. Xia, J. Yang, and Z. Wu, *Nanoscale* **7**, 10013 (2015).
- 216 M. van der Linden, A. Barendregt, A. J. van Bunningen, P. T. K. Chin, D. M. Thies-Weesie, F. M. F. de Groot, and A. Meijerink, *Nanoscale* **8**, 19901 (2016).
- 217 A. C. Dharmaratne, T. Krick, and A. Dass, *J. Am. Chem. Soc.* **131**, 13604 (2009).
- 218 Z. Luo, V. Nachammai, B. Zhang, N. Yan, D. T. Leong, D.-e. Jiang, and J. Xie, *J. Am. Chem. Soc.* **136**, 10577 (2014).
- 219 A. Jentys, *Phys. Chem. Chem. Phys.* **1**, 4059 (1999).
- 220 R. E. Benfield, *J. Chem. Soc. Trans.* **88**, 1107 (1992).
- 221 G. A. Simms, J. D. Padmos, and P. Zhang, *J. Chem. Phys.* **131**, 214703 (2009).
- 222 S. Yamazoe, S. Takano, W. Kurashige, T. Yokoyama, K. Nitta, Y. Negishi, and T. Tsukuda, *Nat. Commun.* **7**, 10414 (2016).
- 223 M. A. MacDonald, D. M. Chevrier, P. Zhang, H. Qian, and R. Jin, *J. Phys. Chem. C* **115**, 15282 (2011).
- 224 O. Šipr, F. Rocca, and G. Dalba, *J. Synchrotron Rad.* **6**, 770 (1999).
- 225 T. Miyamoto, H. Niimi, Y. Kitajima, T. Naito, and K. Asakura, *J. Phys. Chem. A* **114**, 4093 (2010).
- 226 T. K. Sham, *Phys. Rev. B* **31**, 1888 (1985).
- 227 J. D. Padmos and P. Zhang, *J. Phys. Chem. C* **116**, 23094 (2012).
- 228 H. Yamaguchi, A. Kido, T. Uechi, and K. Yasukouchi, *Bull. Chem. Soc. Jpn.* **49**, 1271 (1976).
- 229 A. I. Nesvizhskii and J. J. Rehr, *J. Synchrotron Rad.* **6**, 315 (1999).
- 230 Y. Joly, *Phys. Rev. B* **63**, 125120 (2001).
- 231 J. Ohyama, K. Teramura, Y. Higuchi, T. Shishido, Y. Hitomi, K. Aoki, T. Funabiki, M. Kodera, K. Kato, H. Tanida, T. Uruga, and T. Tanaka, *Phys. Chem. Chem. Phys.* **13**, 11128 (2011).
- 232 J. Ohyama, K. Teramura, Y. Higuchi, T. Shishido, Y. Hitomi, K. Kato, H. Tanida, T. Uruga, and T. Tanaka, *ChemPhysChem* **12**, 127 (2011).
- 233 J. Ohyama, K. Teramura, T. Shishido, Y. Hitomi, K. Kato, H. Tanida, T. Uruga, and T. Tanaka, *Chem. Phys. Lett.* **507**, 105 (2011).

- 234 Y. M. Yiu, P. Zhang, and T. K. Sham, in *Tech. Proc. 2003 Nanotechnol. Conf. Trade Show, Vol. 3* (Nano Science and Technology Institute <https://www.nsti.org/procs/Nanotech2003v3/4>, 2003) pp. 183–186.
- 235 J. F. Parker, J. E. F. Weaver, F. McCallum, C. A. Fields-Zinna, and R. W. Murray, *Langmuir* **26**, 13650 (2010).
- 236 T. A. Dreier and C. J. Ackerson, *Angew. Chemie* **127**, 9381 (2015).
- 237 T. A. Dreier, W. S. Compel, O. A. Wong, and C. J. Ackerson, *J. Phys. Chem. C* **120**, 28288 (2016).
- 238 N. Cathcart, P. Mistry, C. Makra, B. Pietrobon, N. Coombs, M. Jelokhani-Niaraki, and V. Kitaev, *Langmuir* **25**, 5840 (2009).
- 239 X. Yuan, M. I. Setyawati, A. S. Tan, C. N. Ong, D. T. Leong, and J. Xie, *NPG Asia Mater.* **5**, e39 (2013).
- 240 S. Wang, X. Meng, A. Das, T. Li, Y. Song, T. Cao, X. Zhu, M. Zhu, and R. Jin, *Angew. Chemie Int. Ed.* **53**, 2376 (2014).
- 241 T.-y. Zhou, L.-p. Lin, M.-c. Rong, Y.-q. Jiang, and X. Chen, *Anal. Chem.* **85**, 9839 (2013).
- 242 X. Le Guével, V. Trouillet, C. Spies, K. Li, T. Laaksonen, D. Auerbach, G. Jung, and M. Schneider, *Nanoscale* **4**, 7624 (2012).
- 243 S. Wang, S. Jin, S. Yang, S. Chen, Y. Song, J. Zhang, and M. Zhu, *Sci. Adv.* **1**, e1500441 (2015).
- 244 R. Ferrando, J. Jellinek, and R. L. Johnston, *Chem. Rev.* **108**, 845 (2008).
- 245 R. Jin and K. Nobusada, *Nano Res.* **7**, 285 (2014).
- 246 H. Qian, D.-e. Jiang, G. Li, C. Gayathri, A. Das, R. R. Gil, and R. Jin, *J. Am. Chem. Soc.* **134**, 16159 (2012).
- 247 Y. Niihori, W. Kurashige, M. Matsuzaki, and Y. Negishi, *Nanoscale* **5**, 508 (2013).
- 248 S. L. Christensen, M. A. MacDonald, A. Chatt, P. Zhang, H. Qian, and R. Jin, *J. Phys. Chem. C* **116**, 26932 (2012).
- 249 M. A. Tofanelli, T. W. Ni, B. D. Phillips, and C. J. Ackerson, *Inorg. Chem.* **55**, 999 (2016).
- 250 D.-e. Jiang and S. Dai, *Inorg. Chem.* **48**, 2720 (2009).
- 251 M. S. Bootharaju, C. P. Joshi, M. R. Parida, O. F. Mohammed, and O. M. Bakr, *Angew. Chemie Int. Ed.* **55**, 922 (2016).
- 252 X. Dou, X. Yuan, Q. Yao, Z. Luo, K. Zheng, and J. Xie, *Chem. Commun.* **50**, 7459 (2014).
- 253 X. Yuan, X. Dou, K. Zheng, and J. Xie, *Part. Part. Syst. Charact.* **32**, 613 (2015).
- 254 X. Dou, X. Yuan, Y. Yu, Z. Luo, Q. Yao, D. T. Leong, and J. Xie, *Nanoscale* **6**, 157 (2014).
- 255 H. Yang, Y. Wang, J. Yan, X. Chen, X. Zhang, H. Häkkinen, and N. Zheng, *J. Am. Chem. Soc.* **136**, 7197 (2014).
- 256 K. R. Krishnadas, A. Ghosh, A. Baksi, I. Chakraborty, G. Natarajan, and T. Pradeep, *J. Am. Chem. Soc.* **138**, 140 (2016).
- 257 K. R. Krishnadas, A. Baksi, A. Ghosh, G. Natarajan, A. Som, and T. Pradeep, *Acc. Chem. Res.* **50**, 1988 (2017).
- 258 Y. Negishi, K. Munakata, W. Ohgake, and K. Nobusada, *J. Phys. Chem. Lett.* **3**, 2209 (2012).
- 259 E. Gottlieb, H. Qian, and R. Jin, *Chem. Eur. J.* **19**, 4238 (2013).
- 260 Y. Negishi, T. Iwai, and M. Ide, *Chem. Commun.* **46**, 4713 (2010).
- 261 C. Kumara and A. Dass, *Nanoscale* **4**, 4084 (2012).

## BIBLIOGRAPHY

- 262 C. Kumara and A. Dass, *Nanoscale* **3**, 3064 (2011).
- 263 Y. Yu, Q. Yao, T. Chen, G. X. Lim, and J. Xie, *J. Phys. Chem. C* **120**, 22096 (2016).
- 264 V. R. Jupally and A. Dass, *Phys. Chem. Chem. Phys.* **16**, 10473 (2014).
- 265 G. Soldan, M. A. Aljuhani, M. S. Bootharaju, L. G. AbdulHalim, M. R. Parida, A.-H. Emwas, O. F. Mohammed, and O. M. Bakr, *Angew. Chemie Int. Ed.* **55**, 5749 (2016).
- 266 K. R. Krishnadas, D. Ghosh, A. Ghosh, G. Natarajan, and T. Pradeep, *J. Phys. Chem. C* **121**, 23224 (2017).
- 267 J. Yan, H. Su, H. Yang, S. Malola, S. Lin, H. Häkkinen, and N. Zheng, *J. Am. Chem. Soc.* **137**, 11880 (2015).
- 268 X. Liu, J. Yuan, C. Yao, J. Chen, L. Li, X. Bao, J. Yang, and Z. Wu, *J. Phys. Chem. C* **121**, 13848 (2017).
- 269 T. Udayabhaskararao, Y. Sun, N. Goswami, S. K. Pal, K. Balasubramanian, and T. Pradeep, *Angew. Chemie Int. Ed.* **51**, 2155 (2012).
- 270 Z. Wu, *Angew. Chemie Int. Ed.* **51**, 2934 (2012).
- 271 Z. Wu, M. Wang, J. Yang, X. Zheng, W. Cai, G. Meng, H. Qian, H. Wang, and R. Jin, *Small* **8**, 2028 (2012).
- 272 D. R. Kauffman, D. Alfonso, C. Matranga, H. Qian, and R. Jin, *J. Phys. Chem. C* **117**, 7914 (2013).
- 273 C. Kumara, C. M. Aikens, and A. Dass, *J. Phys. Chem. Lett.* **5**, 461 (2014).
- 274 J. R. Lakowicz, *Principles of Fluorescence Spectroscopy*, 3rd ed. (Springer Science, New York, 2006).
- 275 A. Grinvald and I. Z. Steinberg, *Anal. Biochem.* **59**, 583 (1974).
- 276 K. L. D. M. Weerawardene and C. M. Aikens, *J. Phys. Chem. C* **122**, 2440 (2018).
- 277 M. Zhou, J. Zhong, S. Wang, Q. Guo, M. Zhu, Y. Pei, and A. Xia, *J. Phys. Chem. C* **119**, 18790 (2015).
- 278 Y. Hong, J. W. Y. Lam, and B. Z. Tang, *Chem. Commun.* **0**, 4332 (2009).
- 279 N. Goswami, Q. Yao, Z. Luo, J. Li, T. Chen, and J. Xie, *J. Phys. Chem. Lett.* **7**, 962 (2016).
- 280 J. J. Velázquez, V. K. Tikhomirov, L. F. Chibotaru, N. T. Cuong, A. S. Kuznetsov, V. D. Rodríguez, M. T. Nguyen, and V. V. Moshchalkov, *Opt. Express* **20**, 13582 (2012).
- 281 C. M. Marian, *Wiley Interdiscip. Rev. Comput. Mol. Sci.* **2**, 187 (2012).
- 282 P. Atkins, J. de Paula, and J. Keeler, *Atkins' Physical Chemistry*, 11th ed. (Oxford University Press, Oxford, 2018).
- 283 M. S. Bootharaju, S. M. Kozlov, Z. Cao, M. Harb, M. R. Parida, M. N. Hedhili, O. F. Mohammed, O. M. Bakr, L. Cavallo, and J.-M. Basset, *Nanoscale* **9**, 9529 (2017).
- 284 A. I. Frenkel, *Chem. Soc. Rev.* **41**, 8163 (2012).
- 285 S. Yamazoe, W. Kurashige, K. Nobusada, Y. Negishi, and T. Tsukuda, *J. Phys. Chem. C* **118**, 25284 (2014).
- 286 J. Liu, K. S. Krishna, C. Kumara, S. Chattopadhyay, T. Shibata, A. Dass, and C. S. S. R. Kumar, *RSC Adv.* **6**, 25368 (2016).
- 287 A. Shivhare, K. E. Lee, Y. Hu, and R. W. J. Scott, *J. Phys. Chem. C* **119**, 23279 (2015).
- 288 M. A. MacDonald, P. Zhang, N. Chen, H. Qian, and R. Jin, *J. Phys. Chem. C* **115**, 65 (2011).
- 289 R. Bau, *J. Am. Chem. Soc.* **120**, 9380 (1998).
- 290 R. C. Elder, K. Ludwig, J. N. Cooper, and M. K. Eidsness, *J. Am. Chem. Soc.* **107**, 5024 (1985).
- 291 A. Manceau, C. Lemouchi, M. Rovezzi, M. Lanson, P. Glatzel, K. L. Nagy, I. Gautier-Luneau, Y. Joly, and M. Enescu, *Inorg. Chem.* **54**, 11776 (2015).

- 292 J. Timoshenko, A. Shivhare, R. W. J. Scott, D. Lu, and A. I. Frenkel, *Phys. Chem. Chem. Phys.* **18**, 19621 (2016).
- 293 S. Malola and H. Häkkinen, *J. Phys. Chem. Lett.* **2**, 2316 (2011).
- 294 S. Malola, L. Lehtovaara, and H. Häkkinen, *J. Phys. Chem. C* **118**, 20002 (2014).
- 295 J. Fan, Y. Song, J. Chai, S. Yang, T. Chen, B. Rao, H. Yu, and M. Zhu, *Nanoscale* **8**, 15317 (2016).
- 296 R. Juarez-Mosqueda, S. Malola, and H. Häkkinen, *Phys. Chem. Chem. Phys.* **19**, 13868 (2017).
- 297 P. Schwerdtfeger, H. L. Hermann, and H. Schmidbaur, *Inorg. Chem.* **42**, 1334 (2003).
- 298 D. Mishra, F. Aldeek, E. Lochner, G. Palui, B. Zeng, S. Mackowski, and H. Mattoussi, *Langmuir* **32**, 6445 (2016).
- 299 G. Pramanik, J. Humpolickova, J. Valenta, P. Kundu, S. Bals, P. Bour, M. Dracinsky, and P. Cigler, *Nanoscale* **10**, 3792 (2018).
- 300 Y. Chen, D. M. Montana, H. Wei, J. M. Cordero, M. Schneider, X. Le Guével, O. Chen, O. T. Bruns, and M. G. Bawendi, *Nano Lett.* **17**, 6330 (2017).
- 301 L. Shang, F. Stockmar, N. Azadfar, and G. U. Nienhaus, *Angew. Chemie Int. Ed.* **52**, 11154 (2013).
- 302 M. C. Alonso, L. Trapiella-Alfonso, J. M. C. Fernandez, R. Pereiro, and A. Sanz-Medel, *Biosens. Bioelectron.* **77**, 1055 (2016).
- 303 E. Porret, L. Sancey, A. Martín-Serrano, M. I. Montañez, R. Seeman, A. Yahia-Ammar, H. Okuno, F. Gomez, A. Ariza, N. Hildebrandt, J.-B. Fleury, J.-L. Coll, and X. Le Guével, *Chem. Mater.* **29**, 7497 (2017).
- 304 X. Le Guevel, O. Tagit, C. E. Rodríguez, V. Trouillet, M. Pernia Leal, and N. Hildebrandt, *Nanoscale* **6**, 8091 (2014).
- 305 Q. Yao, Y. Yu, X. Yuan, Y. Yu, J. Xie, and J. Y. Lee, *Small* **9**, 2696 (2013).
- 306 L. Zhu, C. Zhang, C. Guo, X. Wang, P. Sun, D. Zhou, W. Chen, and G. Xue, *J. Phys. Chem. C* **117**, 11399 (2013).
- 307 B. M. Barngrover and C. M. Aikens, *J. Am. Chem. Soc.* **134**, 12590 (2012).
- 308 L. Korson, W. Drost-Hansen, and F. J. Millero, *J. Phys. Chem.* **73**, 34 (1969).
- 309 I. M. Smallwood, *Handbook of Organic Solvent Properties*, 1st ed. (Hallsted, New York, 1996).
- 310 J. Jiang, C. V. Conroy, M. M. Kvetny, G. J. Lake, J. W. Padelford, T. Ahuja, and G. Wang, *J. Phys. Chem. C* **118**, 20680 (2014).
- 311 H. P. Erickson, *Biol. Proced. Online* **11**, 32 (2009).
- 312 M. Koskinen, P. O. Lipas, and M. Manninen, *Zeitschrift für Phys. D Atoms, Mol. Clust.* **35**, 285 (1995).
- 313 X.-B. Li, H.-Y. Wang, X.-D. Yang, Z.-H. Zhu, and Y.-J. Tang, *J. Chem. Phys.* **126**, 084505 (2007).
- 314 N. B. Singh and U. Sarkar, *Cogent Chem.* **1**, 1076713 (2015).
- 315 M. M. Kreevoy and J. E. C. Hutchins, *J. Am. Chem. Soc.* **94**, 6371 (1972).
- 316 I. V. Mironov and E. V. Makotchenko, *J. Solution Chem.* **38**, 725 (2009).
- 317 P. J. Murphy and M. S. LaGrange, *Geochim. Cosmochim. Acta* **62**, 3515 (1998).
- 318 K. Paclawski and K. Fitzner, *Metall. Mater. Trans. B* **35**, 1071 (2004).
- 319 S. Wang, K. Qian, X. Bi, and W. Huang, *J. Phys. Chem. C* **113**, 6505 (2009).
- 320 L. J. Reed, I. C. Gunsalus, G. H. F. Schnakenberg, Q. F. Soper, H. E. Boaz, S. F. Kern, and T. V. Parke, *J. Am. Chem. Soc.* **73**, 1267 (1953).

## BIBLIOGRAPHY

- 321 S. Eustis and M. A. El-Sayed, *Chem. Soc. Rev.* **35**, 209 (2006).
- 322 C. F. Shaw III, M. P. Cancro, and P. L. Witkiewicz, *Inorg. Chem.* **19**, 3198 (1980).
- 323 P. J. G. Goulet, A. Leonardi, and R. B. Lennox, *J. Phys. Chem. C* **116**, 14096 (2012).
- 324 S. K. Misra, A. Dybowska, D. Berhanu, S. N. Luoma, and E. Valsami-Jones, *Sci. Total Environ.* **438**, 225 (2012).
- 325 F. Farges, J. A. Sharps, and G. E. Brown, *Geochim. Cosmochim. Acta* **57**, 1243 (1993).
- 326 M. Wuihthschick, A. Birnbaum, S. Witte, M. Sztucki, U. Vainio, N. Pinna, K. Rademann, F. Emmerling, R. Kraehnert, and J. Polte, *ACS Nano* **9**, 7052 (2015).
- 327 T. M. Florence, *Biochem. J.* **189**, 507 (1980).
- 328 I. V. Koval, *Russ. Chem. Rev.* **63**, 735 (1994).
- 329 W. E. Savige and J. A. MacLaren, in *The chemistry of organic sulfur compounds*, edited by N. Kharasch and C. Y. Meyers (Pergamon Press, London, 1966) 1st ed., Chap. 15, pp. 367–402.
- 330 A. Manceau, C. Lemouchi, M. Enescu, A.-C. Gaillot, M. Lanson, V. Magnin, P. Glatzel, B. A. Poulin, J. N. Ryan, G. R. Aiken, I. Gautier-Luneau, and K. L. Nagy, *Environ. Sci. Technol.* **49**, 9787 (2015).
- 331 R. C. Elder and M. K. Eidsness, *Chem. Rev.* **87**, 1027 (1987).
- 332 P. Zhang, *J. Phys. Chem. C* **118**, 25291 (2014).
- 333 D. M. Chevrier, A. Chatt, P. Zhang, C. Zeng, and R. Jin, *J. Phys. Chem. Lett.* **4**, 3186 (2013).
- 334 B. Ravel, *J. Synchrotron Rad.* **8**, 314 (2001).
- 335 C. R. Groom, I. J. Bruno, M. P. Lightfoot, and S. C. Ward, *Acta Crystallogr. Sect. B* **72**, 171 (2016).
- 336 L. F. Mattheiss and R. E. Dietz, *Phys. Rev. B* **22**, 1663 (1980).
- 337 A. Pantelouris, G. Küper, J. Hormes, C. Feldmann, and M. Jansen, *J. Am. Chem. Soc.* **117**, 11749 (1995).
- 338 N. Weiher, E. Bus, L. Delannoy, C. Louis, D. E. Ramaker, J. T. Miller, and J. A. van Bokhoven, *J. Catal.* **240**, 100 (2006).
- 339 D. T. Jiang, T. K. Sham, P. R. Norton, and S. M. Heald, *Phys. Rev. B* **49**, 3709 (1994).
- 340 M. C. Gimeno, in *Mod. Supramol. Gold Chem. Gold-Metal Interact. Appl.*, edited by A. Laguna (Wiley-Blackwell, Weinheim, Germany, 2008) 1st ed., Chap. 1, pp. 1–63.
- 341 F. Mohr, ed., *Gold Chemistry: Applications and Future Directions in the Life Sciences* (Wiley-Blackwell, Weinheim, Germany, 2009).
- 342 J. J. Kas, K. Jorissen, and J. J. Rehr, in *X-Ray Absorpt. X-Ray Emiss. Spectrosc. Theory Appl.*, edited by J. A. van Bokhoven and C. Lamberti (Wiley-Blackwell, 2016) 1st ed., Chap. 3, pp. 51–72.
- 343 R. C. Elder, W. B. Jones, Z. Zhao, J. G. Dorsey, and K. Tepperman, *Met. Based. Drugs* **1**, 363 (1994).
- 344 M. F. Lengke, B. Ravel, M. E. Fleet, G. Wanger, R. A. Gordon, and G. Southam, *Can. J. Chem.* **85**, 651 (2007).
- 345 S.-Y. Chang, A. Uehara, S. G. Booth, K. Ignatyev, J. F. W. Mosselmans, R. A. W. Dryfe, and S. L. M. Schroeder, *RSC Adv.* **5**, 6912 (2015).
- 346 N. Weiher, E. A. Willneff, C. Figulla-Kroschel, M. Jansen, and S. L. M. Schroeder, *Solid State Commun.* **125**, 317 (2003).
- 347 Z.-m. Qi, H.-s. Zhou, N. Matsuda, I. Honma, K. Shimada, A. Takatsu, and K. Kato, *J. Phys. Chem. B* **108**, 7006 (2004).
- 348 X. Chen, W. Chu, D. Chen, Z. Wu, A. Marcelli, and Z. Wu, *Chem. Geol.* **268**, 74 (2009).

- 349 K. O. Kvashnina, Y. O. Kvashnin, J. R. Vegelius, A. Bosak, P. M. Martin, and S. M. Butorin, *Anal. Chem.* **87**, 8772 (2015).
- 350 P. Glatzel, J. Singh, K. O. Kvashnina, and J. A. van Bokhoven, *J. Am. Chem. Soc.* **132**, 2555 (2010).
- 351 N. Smolentsev, M. Sikora, A. V. Soldatov, K. O. Kvashnina, and P. Glatzel, *Phys. Rev. B* **84**, 235113 (2011).
- 352 J. Jiménez-Mier, J. van Ek, D. L. Ederer, T. A. Callcott, J. J. Jia, J. Carlisle, L. Terminello, A. Asfaw, and R. C. Perera, *Phys. Rev. B* **59**, 2649 (1999).
- 353 S. A. Miller, J. M. Womick, J. F. Parker, R. W. Murray, and A. M. Moran, *J. Phys. Chem. C Lett.* **113**, 9440 (2009).
- 354 Z. Luo, K. Zheng, and J. Xie, *Chem. Commun.* **50**, 5143 (2014).
- 355 M. Zhou, C. Zeng, Y. Chen, S. Zhao, M. Y. Sfeir, M. Zhu, and R. Jin, *Nat. Commun.* **7**, 13240 (2016).
- 356 S. E. Crawford, C. M. Andolina, A. M. Smith, L. E. Marbella, K. A. Johnston, P. J. Straney, M. J. Hartmann, and J. E. Millstone, *J. Am. Chem. Soc.* **137**, 14423 (2015).
- 357 A. Das, C. Liu, H. Y. Byun, K. Nobusada, S. Zhao, N. Rosi, and R. Jin, *Angew. Chemie Int. Ed.* **54**, 3140 (2015).
- 358 Y. Pei, J. Tang, X. Tang, Y. Huang, and X. C. Zeng, *J. Phys. Chem. Lett.* **6**, 1390 (2015).
- 359 R. E. Benfield, A. Filippini, D. T. Bowron, R. J. Newport, and S. J. Gurman, *J. Phys. Condens. Matter* **6**, 8429 (1994).
- 360 A. Filippini, *Physica B. Condens. Matter* **208-209**, 29 (1995).
- 361 C. Hennig, *Phys. Rev. B* **75**, 035120 (2007).
- 362 A. N. Mansour, J. W. Cook, and D. E. Sayers, *J. Phys. Chem.* **88**, 2330 (1984).
- 363 R. E. Benfield, D. Grandjean, M. Kröll, R. Pugin, T. Sawitowski, and G. Schmid, *J. Phys. Chem. B* **105**, 1961 (2001).
- 364 P. Zhang and T. K. Sham, *Appl. Phys. Lett.* **81**, 736 (2002).
- 365 P. Zhang and T. K. Sham, *Phys. Rev. Lett.* **90**, 245502 (2003).
- 366 K. Paclawski, D. A. Zajac, M. Borowiec, C. Kapusta, and K. Fitzner, *J. Phys. Chem. A* **114**, 11943 (2010).
- 367 D. E. Jiang, W. Chen, R. L. Whetten, and Z. Chen, *J. Phys. Chem. C* **113**, 16983 (2009).
- 368 R. Ueno and H. Yao, *Colloids Surf. A* **426**, 39 (2013).
- 369 R. Roots and S. Okada, *Radiat. Res.* **64**, 306 (1975).
- 370 J. Zheng, C. Zhou, M. Yu, and J. Liu, *Nanoscale* **4**, 4073 (2012).
- 371 S. Knoppe, J. Boudon, I. Dolamic, A. Dass, and T. Bürgi, *Anal. Chem.* **83**, 5056 (2011).
- 372 A. Ghosh, J. Hassinen, P. Pulkkinen, H. Tenhu, R. H. A. Ras, and T. Pradeep, *Anal. Chem.* **86**, 12185 (2014).
- 373 K. Kimura, N. Sugimoto, S. Sato, H. Yao, Y. Negishi, and T. Tsukuda, *J. Phys. Chem. C* **113**, 14076 (2009).
- 374 M. A. MacDonald, P. Zhang, H. Qian, and R. Jin, *J. Phys. Chem. Lett.* **1**, 1821 (2010).